

Microwave Ablation System Design for Cancer Applications

Submitted to the Graduate School of Natural and Applied Sciences
in partial fulfillment of the requirements for the degree of

Doctor of Philosophy

in Electrical and Electronics Engineering

by

Caner MURAT

ORCID 0000-0001-9251-9149

July, 2023

This is to certify that we have read the thesis **Microwave Ablation System Design for Cancer Applications** submitted by **Caner Murat**, and it has been judged to be successful, in scope and in quality, at the defense exam and accepted by our jury as a DOCTORAL THESIS.

APPROVED BY:

Advisor: **Prof. Dr. Adnan Kaya**
Izmir Katip Celebi University

Committee Members:

Prof. Dr. Merih Palandoken
Izmir Katip Celebi University

Prof. Dr. Mustafa Secmen
Yasar University

Prof. Dr. Emine Yesim Zoral
Dokuz Eylul University

Assoc. Prof. Dr. Mumin Alper Erdogan
Izmir Katip Celebi University

Date of Defense: July 19, 2023

Declaration of Authorship

I, **Caner MURAT**, declare that this thesis titled **Microwave Ablation System Design for Cancer Applications** and the work presented in it are my own. I confirm that:

- This work was done wholly or mainly while in candidature for the Doctoral degree at this university.
- Where any part of this thesis has previously been submitted for a degree or any other qualification at this university or any other institution, this has been clearly stated.
- Where I have consulted the published work of others, this is always clearly attributed.
- Where I have quoted from the work of others, the source is always given. This thesis is entirely my own work, with the exception of such quotations.
- I have acknowledged all major sources of assistance.
- Where the thesis is based on work done by myself jointly with others, I have made clear exactly what was done by others and what I have contributed myself.

Date: 19.07.2023

Microwave Ablation System Design for Cancer Applications

Abstract

This doctoral thesis focuses on the design of a microwave ablation (MWA) system that incorporates Non-Foster Circuits (NFC) and a microwave power amplifier (PA) to enhance power transfer efficiency and profit in various cancer treatments. The study extensively examines the MWA applicators, PA and NFC structures independently in the initial sections, followed by proposing, analytically demonstrating, and experimentally verifying association between these phenomena. This interconnection presents a promising perspective for cancer therapy through minimally invasive approaches and resulting in predictable designs. Notably, an active impedance matching circuit is devised to adjust the amplifier's impedance, compensating for losses and enabling stable operation in novel applications, thereby facilitating efficient treatment protocols.

The present investigation primarily concentrates on the development of a novel microwave applicator operating at 2.45 GHz within the Industrial, Scientific, and Medical (ISM) band. The aim is to attain a temperature rise exceeding 60 °C on the tumor surfaces through tissue recipe, in vitro, ex vivo and in vivo study. The investigation into the utilization of multiple applicators reveals that it leads to a larger ablation zone and higher homogeneity, making it more suitable for treating larger tumor lesions. Furthermore, PA and NFC connection improve the MWA system requirements about 319 %, 33 % and 225 % for output power, gain and power added efficiency, respectively. The study proves that MWA supplemented with pulsed electromagnetic field (PEMF), induces a significant reduction in cell proliferation of nearly 40 % with heightened apoptosis rates in breast cancer cells. The outcomes of the experiment provide robust evidence affirming the benefit of the suggested MWA system indicating its potential to become a dedicated device for tumor treatment.

Keywords: microwave ablation, power amplifier, non foster circuit, active impedance matching, 3D tissue recipe, in vitro, ex vivo in vivo, cancer

Kanser Uygulamaları İçin Mikrodalga Ablasyon Sistemi Tasarımı

ÖZ

Bu doktora tezi, çeşitli kanser tedavilerinde güç aktarım verimliliğini ve etkisini artırmak için foster olmayan devreleri (NFC) ve bir mikrodalga güç amplifikatörünü (PA) içeren bir mikrodalga ablasyon (MWA) sisteminin tasarımına odaklanmaktadır. Çalışma, MWA uygulayıcılarını, PA ve foster olmayan yapıları ilk bölümlerde bağımsız olarak kapsamlı bir şekilde incelemekte, ardından bu fenomenler arasındaki ilişkiyi önermekte, analitik olarak göstermekte ve deneysel olarak doğrulamaktadır. Bu bağlantı, minimal invaziv yaklaşımlar yoluyla kanser tedavisi için umut verici bir perspektif sunmakta ve öngörülebilir tasarımlarla sonuçlanmaktadır. Özellikle, amplifikatörün empedansını ayarlamak, kayıpları telafi etmek ve yeni uygulamalarda kararlı çalışmayı sağlamak ve böylece verimli tedavi protokollerini kolaylaştırmak için aktif bir empedans eşleştirme devresi tasarlanmıştır.

Bu araştırma öncelikle Endüstriyel, Bilimsel ve Tıbbi (ISM) bandında 2.45 GHz frekansında çalışan verimli bir mikrodalga aplikatörün geliştirilmesine odaklanmaktadır. Amaç doku tarifi, in vitro, ex vivo ve in vivo çalışma üzerinden tümörlerin yüzeyinde 60 °C'yi aşan bir sıcaklık artışı elde etmektir. Çoklu aplikatörlerin kullanımına ilişkin araştırma, bunun daha büyük bir ablasyon bölgesi ve daha yüksek homojenliğe yol açtığını ve daha büyük tümör lezyonlarının tedavisi için daha uygun olduğunu göstermiştir. Ayrıca, PA ve NFC bağlantısı MWA sisteminin gereksinimlerini çıkış gücü, kazanç ve güç katma verimliliği için sırasıyla % 319, % 33 ve % 225 oranında iyileştirmiştir. Çalışma, darbeli elektromanyetik alan (PEMF) ile desteklenen MWA, meme kanseri hücrelerinde artan apoptoz oranları ile hücre çoğalmasında yaklaşık % 40'luk önemli bir azalmaya neden olduğunu göstermektedir. Deneyin sonuçları, önerilen MWA sisteminin etkinliğini doğrulayan sağlam kanıtlar sunmakta ve tümör tedavisi için özel bir cihaz olma potansiyelini göstermektedir.

Anahtar Kelimeler: mikrodalga ablasyon, güç amplifikatörü, foster olmayan devre, aktif empedans uyumlandırma, 3B doku tarifi, in vitro, ex vivo, in vivo, kanser

To my family

Acknowledgment

In the realisation of this study, I would like to thank and express my gratitude to Prof. Dr. Adnan KAYA, who has shared his valuable knowledge with me, who spared his precious time whenever I consulted him, who patiently and with great interest offered me more than he could do to be useful to me, who I could go to him without hesitation whenever I had any problems, who did not spare his smiling face and sincerity from me, and who fulfilled the status of a valuable and consultant teacher who I think I will benefit from the valuable information he gave me in my future professional life.

I would like to thank my beloved family for supporting me during my thesis studies, and my esteemed teacher Prof. Dr. Merih PALANDÖKEN, who shared her knowledge and experience at every stage of my thesis study, in the planning and progress of the protocol.

This study was financially supported by Izmir Katip Celebi University, Scientific Research Projects Fund (BAP) through the 2021-TDR-FEBE-0013 research project and the Scientific and Technological Research Council of Turkey (TUBITAK) under Project 117E811.

Table of Contents

Declaration of Authorship	ii
Abstract	iii
Öz	iv
Acknowledgment.....	vi
Table of Contents	vii
List of Figures	x
List of Tables.....	xviii
List of Abbreviations.....	xxi
List of Symbols	xxiii
1 Introduction	1
1.1 Motivation and Research Problem.....	1
1.2 Thesis Organization and Novel Contribution	5
1.3 Background on Cancer Treatment Techniques.....	6
1.4 MWA Technology for Cancer Treatment.....	11
1.5 MWA System Requirement.....	14
2 Computational Analysis for MWA Applicator Design	17
2.1 RTMWAP Design and Optimization in In Vitro.....	22
2.2 3DPMWAP Design and Optimization in In Vitro.....	34
2.3 MMWAP Design and Optimization in Ex Vivo.....	47
3 Non-Foster Circuit Implementation for Active Matching in MWA System	55
3.1 Theoretical Background of Non-Foster Reactance.....	56
3.2 Simulation Results and Practical Application of NFC	60

3.3	Empirical Measurement Results of NIC.....	62
3.4	Active Impedance Matching Techniques Utilizing Non-Foster NIC.....	68
4	MWA System Design.....	73
4.1	Microwave Power Amplifier Design Utilizing a 400 W HEMT	73
4.2	Overview on Microwave Power Amplifier Design	74
4.3	QORVO 400W HEMT Nonlinear Model Evaluation	77
4.3.1	Current-Voltage Simulation of Nonlinear HEMT Model.....	78
4.3.2	Assessing Nonlinear HEMT Model via Load Pull Analysis	80
4.4	Design Technique for Optimization of QPD350	82
4.5	Simulation-Based Analysis of QPD350 Design	87
4.6	Manufacturing Process of the Proposed QPD350	93
4.7	Evaluating QPD350 Performance in MWA Study	99
4.8	MWA System Interface and Embedded Design	108
5	Ablation Zone Analysis on 3D Phantom Model	114
5.1	Studies on 3D Kidney Phantom.....	117
5.2	Ablation Zone Analysis on 3D Breast Phantom	121
5.3	MWA Studies on 3D Pancreas Electrical Model.....	126
5.4	MWA Studies on 3D Lung Electrical Model	129
5.5	MWA Studies on 3D Liver Electrical Model	132
6	In Vitro and Ex Vivo Experimental Study of Designed Applicators.....	135
6.1	RTMWAP for In Vitro Breast Cancer Ablation	136
6.2	In Vitro Breast Cancer Ablation Using 3DMWAP	140
6.3	Ex Vivo Experimental Study of MMWAP	145
6.3.1	Experimental Return Loss Measurement.....	146
6.3.2	Electric Field and SAR Performances in Near Field	146
6.3.3	Ablation Performances of MMWAP over Single Applicator.....	147
6.4	MWA and PEMF Studies on Prostate Cancer	151

6.4.1. Cell Lines and Culture Conditions.....	155
6.4.2. Wound Healing/Migration Assay	156
6.5 MWA Study on Pancreas Cancer	157
7 In Vivo Experimental Study	162
7.1 MWA and PEMF Applications.....	163
7.1.1. MWA Application Using MFMWAP.....	163
7.1.2. MWA Application Using CA20L1	166
7.1.3. MWA Application with the Use of CSA	168
7.1.4. NiTi Loop Antenna Application with MWA Application.....	170
7.1.5. In Vivo PEMF Application with Helmholtz Coil Pair.....	173
7.2 Histopathological Evaluation.....	174
7.3.1 Macroscopic Evaluation.....	174
7.3.2 Microscopic Evaluation	175
7.3 Paraffin Tissue Tracking.....	176
7.3.1. Histopathological Staining.....	176
7.3.2. Indirect Immunohistochemistry Staining.....	177
7.3.3. TUNEL Painting	179
7.4 Statistical Analysis.....	180
7.4.1 Macroscopic Findings.....	180
7.4.2. Hematoxyline Eosin Signs	182
7.4.3. Reproduction Findings.....	184
7.4.4. Cell Death Findings	186
7.5 Result and Discussion	188
8 Conclusion.....	193
References	196
Appendices	216
Curriculum Vitae	235

List of Figures

Figure 1.1 MWA treatment of kidney cancer (a) tomography, (b) images outside the organism and (c) cancer stages	2
Figure 1.2 Cancer treatment history	10
Figure 1.3 (a) Microwave ablation application and (b) applicator.....	11
Figure 1.4 Frequency spectrum of electromagnetic waves [58]	12
Figure 1.5 MWA system block diagram	14
Figure 2.1 Designed MWA applicator for cancer treatment (a) HTIMWAP, (b) RTMWAP, (c) 3DPMWAP, (d) CA20L1, (e) MMWAP, (f) MFMWAP.....	20
Figure 2.2 RTMWAP sections and material information.	22
Figure 2.3 The effect of the dielectric radiator length of the RTMWAP on the S parameter.....	25
Figure 2.4 The effect of length of cylinder of dielectric radiator on S11	26
Figure 2.5 The effect of shaft length of RTMWAP on the S11	26
Figure 2.6 Invasive microwave ablation system model setup. (b) Optimized S parameter of numerically computed reflector type MW probe.....	29
Figure 2.7 Electric field-distance graph (a) in y-axis and (b) in z-axis with corresponding simulation setup. Electric field distribution (c) on x and (d) on y plane.	31
Figure 2.8 (a) SAR pattern, (b) PLD, (c) electric and (d) magnetic energy densities of 1.76 g tumorous cell which is exposed to microwave power emitted by reflector type microwave applicator in the presence of 15 W microwave power excitation.	32
Figure 2.9 (a) Section and length information, (b) diameter and material information and (c) installation of fabricated 3D printed microwave ablation probe	36

Figure 2.10 Proposed microwave applicator theoretical model.....	38
Figure 2.11 Simulated curves of reflection coefficient, S11, of proposed microwave probe for different values of (a) l_d , (b) l_i and c) l_s	39
Figure 2.12 (a) Simulation model, and (b) reflection coefficient comparison of cases with/without tumor cells near the cone section of 3D printed MWA probe.....	40
Figure 2.13 (a) Numerical computation model for the calculation of the electric field strength inside and on the surface of breast tumor cells. Electric field distributions are respectively along: (b) y-axis, and (d) z-axis. Electric field distributions on: (c) x plane, and (e) y plane.....	41
Figure 2.14 SAR value of tumor sample under (a) 1 W and (b) 46 W microwave input power of proposed probe placed on the petri dishes. SAR value of tumor sample under (a) 1 W and (b) 46 W microwave input power of proposed probe inserted in the petri dishes.	43
Figure 2.15 CST Thermal Transient Solver results of tumor after 20 min exposure emitted by 3DPMWAP (a) outside, and (b) inside the MCF7 cells culture.	45
Figure 2.16 Numerically computed S11-distributions of proposed microwave probe inside / outside regions of the breast tumor tissue.	45
Figure 2.17 (a) Microwave ablation system block diagram (b) system component ..	47
Figure 2.18 MMWAP structure inside the chicken liver model	48
Figure 2.19 The return loss values of single coaxial slot antenna and 1:3 power divider in the presence of MMWAP connection inside the chicken liver model.....	51
Figure 2.20 Electric field distributions in chicken liver under 0.5 W gaussian sine input power emitted by (a) coaxial slot antenna (b) MMWAP.....	52
Figure 2.21 Numerical SAR distributions in 125 g chicken liver model with (a) coaxial slot antenna (b) MMWAP usage.....	53
Figure 3.1 Negative capacitance principle from (a) S11 and (b) impedance.....	57
Figure 3.2 Linville based NFC equivalent model [141].	58
Figure 3.3 MWA system simplified model including NFC [142].	59
Figure 3.4 (a) Schematic, (b) layout and (b) fabricated prototype of NFC.....	61

Figure 3.5 Block diagram illustrating the experimental measurement setup of NIC.	62
Figure 3.6 S11 and Series Reactance of Non Foster NIC, $V_{cc}=12V$	63
Figure 3.7 Series Capacitance of Non Foster NIC changing feeding voltage	64
Figure 3.8 Steady state temperature distribution measurement of the NIC circuit under various feeding voltages: (a) 6 V, (b) 8 V, (c) 10 V, and (d) 12 V for 30 s.....	65
Figure 3.9 Transient temperature graph of the NIC circuit under various feeding voltages: (a) 6 V, (b) 8 V, (c) 10 V, and (d) 12 V for 30 s.....	66
Figure 3.10 (a) Schematic, (b) simulated S11 with/without NFM, (c) experimental setup, (d) experimental S11 with NFM varaying feeding voltage using MFMWAP	68
Figure 3.11 High power measurement setup using MFMWAP with NFC matching.	69
Figure 3.12 Input power versus output powers of (a) PA, (b) OCS (c) NIC and (d) feeding current when $V_{cc}= 3 V$, $V_{cc}= 4 V$ and $V_{cc}=5 V$	70
Figure 3.13 Input power versus output powers of (a) PA, (b) OCS (c) NIC and (d) feeding current when $V_{cc}= 12 V$, and $V_{cc}=14 V$	71
Figure 4.1 Angelov model for QORVO GAN technology	77
Figure 4.2 Simulation setup generating drain current versus drain voltage curve.....	78
Figure 4.3 Drain current versus drain voltage curve of QPD2795	79
Figure 4.4 Circuit schematic for generating load pull output of QPD2795	80
Figure 4.5 Load pull contour of QPD2795 at 2.4 GHz fundamental frequency.....	81
Figure 4.6 Capacitance simulations of ATC capacitors from DC to 3 GHz.....	83
Figure 4.7 Proposed QPD350 in schematic view.....	86
Figure 4.8 Reflection and transmission coefficients of QPD350 at 2.45 GHz.	87
Figure 4.9 Output power, PAE and Gain of proposed PA.....	89
Figure 4.10 Output power versus input power graph of proposed PA.	90
Figure 4.11 Power spectrum of harmonics graph of proposed PA	91
Figure 4.12 Input versus output (a) voltage and (b) current of QPD350.....	92

Figure 4.13 (a) Layout and (b) fabricated prototype of proposed QPD350.....	97
Figure 4.14 Experimental measurement setup including the microwave ablation of in vitro prostate cancer using QPD350.	99
Figure 4.15 (a) Drain current versus drain-source voltage graph and (b) drain current versus transistor temperature graph of proposed MWPA.....	100
Figure 4.16 The algorithm for determining stability, including the K- Δ test.	101
Figure 4.17 Stability determination graph via K- Δ test.....	102
Figure 4.18 Input and output stability circles of NIC, $V_{cc}=12$ V.....	103
Figure 4.19 S21 measurement result of QPD350, $V_{GS}=-2.9$ V.....	104
Figure 4.20 (a) Block diagram, (b) output power, (c) gain and (d) PAE of QPD350 with Foster Matching	105
Figure 4.21 (a) Block diagram, (b) output power, (c) gain and (d) PAE of QPD350 with Non-Foster Matching	106
Figure 4.22 Clock configuration of embedded design.....	109
Figure 4.23 (a) Hardware architecture and (b) pin configuration of the embedded system design for MWA	110
Figure 4.24 MWA system interface.....	112
Figure 4.25 MWA system prototype.....	113
Figure 5.1 Anatomic model (a), (d), (g), (k), (o); 3D electrical equivalent model (b), (e), (h)-(i), (l)-(m), (p)-(n) and real organ view of kidney, breast, pancreas, lung and liver, respectively	115
Figure 5.2 (a) Preparing 3D kidney phantom (b) and experimental setup.....	117
Figure 5.3 Temperature distribution resulting from the application of (a) 10 W, (b) 25 W, (c) 50 W and (d) 80 W microwave power to the 3D kidney phantom model for 6 minutes.	118
Figure 5.4 Time-dependent temperature measurement results of the kidney recipe	119
Figure 5.5 Temperature distribution as a result of applying (a) 10 W, (b) 25 W, (c) 50 W and (d) 80 W microwave power to the 3D kidney recipe for 6 minutes.	120

Figure 5.6 (a) 3D breast cancer phantom model (b) experimental measurement setup	121
Figure 5.7 (a) CA20L1, (b) MMWAP and (c) S11 experimental measurement results when these two applicator were immersed in a breast cancer phantom model.	122
Figure 5.8 Experimental measurement setup ablation of pancreas recipe under microwave power exposure	126
Figure 5.9 (a) Pancreas recipe with the measurement including (b) temperature distribution after 30 s microwave exposure, (c) Time-dependent temperature measurement results of the 3D pancreas phantom model (d) temperature histogram.....	127
Figure 5.10 Time-dependent measurement results of the electric field (a) and radiated microwave power (b) at different distances from the pancreas recipe.....	128
Figure 5.11 Experimental measurement setup ablation of lung recipe under microwave power exposure	129
Figure 5.12 (a) Lung recipe with the measurement including (b) temperature distribution after 30s microwave exposure, (c) Time-dependent temperature measurement results (d) temperature histogram.	130
Figure 5.13 Time-dependent measurement results of the electric field (a) and radiated microwave power (b) at different distances from the lung recipe.	131
Figure 5.14 Experimental measurement setup ablation of liver recipe under microwave power exposure	132
Figure 5.15 (a) Liver recipe with the measurement including (b) temperature distribution after 30 s microwave exposure, (c) Time-dependent temperature measurement results of that recipe (d) temperature histogram.	133
Figure 5.16 Time-dependent measurement results of the electric field (a) and radiated microwave power (b) at different distances from the liver recipe.	134
Figure 6.1 (a) Fabricated reflector type microwave applicator and (b) S parameter of reflector type microwave applicator placed inside the tumor sample.....	136

Figure 6.2 Microwave ablation system (a) block diagram, (b) experimental setup containing PA (Power Amplifier), MWS (Microwave Source), DC (Directional Coupler), PS (Direct Current Power Supply), BS (Biological Sample), TC (Thermal Camera), EFP (Electric Field Probe), PA (Spectrum Analyzer) and MWP (Microwave Probe).....	137
Figure 6.3 Temperature distribution (a) outside (b) inside the petri dishes containing tumor sample that exposed to the microwave power emitted by reflector type microwave applicator up to 10 minutes and (c) temperature histogram in breast cancer.	138
Figure 6.4 S-parameter measurement results of 3D printed MWA Applicator with petri dishes placed on the petri dishes containing MCF7 cells without direct contact.	141
Figure 6.5 Microwave ablation experimental setup.....	141
Figure 6.6 (a) Thermal camera view and (b) temperature profile inside the petri dishes along the distance from 3DPMWAP of MCF7 cells after 20 min exposure. ..	142
Figure 6.7 Transient temperature of MCF7 cells during 20 min exposure to microwave power.....	143
Figure 6.8 Weight measurements of microwave probes made of: (a) ABS, and (b) aluminum	144
Figure 6.9 Microwave ablation ex vivo experimental setup using MMWAP	145
Figure 6.10 Return loss measurement of MMWAP immersed in chicken liver	146
Figure 6.11 (a) Ex vivo chicken liver thermal measurement setup in single slot antenna immersion (b) real time temperature data of single slot antenna usage measured by each thermocouple (c) ex vivo chicken liver thermal measurement setup in MMWAP immersion (d) real time temperature data measured of MMWAP usage by each thermocouple.	149
Figure 6.12 Ablation zone measurements of 118 g ex vivo chicken liver with (a) single coaxial slot antenna and (b) MMWAP usage	150
Figure 6.13 Treatment application on prostate cancer including MWA and PEMF	151

Figure 6.14 Thermal camera measurements results of (a) Group 1, (b) Group 2, (c) Group 3, (d) Group 4 and Group 5 at the time of the highest prostate cancer surface temperatures.....	152
Figure 6.15 Time dependent temperature measurement of (a) Group 1, Group 2 and Group 3; (b) Group 4 and Group 5	153
Figure 6.16 MWA results of prostate cancer	156
Figure 6.17 Treatment application on pancreas cancer including MWA	157
Figure 6.18 Maximum temperature of pancreas cancer with 75 W microwave power	158
Figure 6.19 Time dependent temperature measurement of MWA Group and Control Group	159
Figure 7.1 MWA application of rats	162
Figure 7.2 (a) MWA application using MFMWAP on D6 label BALB/c. (b) Thermal camera measurement, and (c) temperature distribution in percent after 30 s of that application with (d) time dependent temperature measurement result.	164
Figure 7.3 (a) Height, and (b) width of tumor size in D6 label mice after MWA ...	165
Figure 7.4 (a) Microwave ablation application using CA20L1 on D9 label BALB/c. (b) Thermal camera measurement, and (c) temperature distribution in percent after 15 s of that application with (d) time dependent temperature measurement result.....	166
Figure 7.5 Tumor diameter measurement in mice ablated with CA20L1.....	167
Figure 7.6 (a) Microwave ablation application using CSA on D24 label BALB/c. (b) Thermal camera measurement, and (c) temperature distribution in percent after 12 s of that application with (d) time dependent temperature measurement result.	168
Figure 7.7 Tumor diameter measurement in mice ablated with CSA.....	169
Figure 7.8 (a) MWA application using Niti Loop Antenna on D21 label BALB/c. (b) Thermal camera measurement, and (c) temperature distribution in percent after 6 s of that application with (d) time dependent temperature measurement result.	170

Figure 7.9 Tumor diameter measurement in mice ablated with NiTi Loop Antenna	171
Figure 7.10 (a) PEMF application on BALB/c with Helmholtz coil pair and (b) : Measurement of tumor size in mice treated with PEMF with Helmholtz coil pair.	173
Figure 7.11 4T1 Appearance of (a) semiconfluent and (b) confluent cancer cells in 4T1 cell sequence culture for breast cancer model.....	174
Figure 7.12 MWA-PEMF applications in; (a) Group 1, (b) Group 2, (c) Group 3, (d) Group 4, (e) Group 5, (f) Group 6, (g) Group 7, (h) Group 8.....	175
Figure 7.13 T41 Small and large magnification images of HE histochemistry staining after MWA-PEMF applications in groups with breast cancer (a) Group 1, (b) Group 2, (c) Group 3, (d) Group 4, (e) Group 5, (f) Group 6, (g) Group 7, (h) Group 8	183
Figure 7.14 Ki67 immunohistochemistry staining images after MWA-PEMF applications in groups with T41 breast cancer (a) Group 1, (b) Group 2, (c) Group 3, (d) Group 4, (e) Group 5, (f) Group 6, (g) Group 7, (h) Group 8	184
Figure 7.15 T41 TUNEL marking images after microwave thermal ablation-PEMF applications in groups with breast cancer; (a) Group 1, (b) Group 2, (c) Group 3, (d) Group 4, (e) Group 5, (f) Group 6, (g) Group 7, (h) Group 8	187

List of Tables

Table 1.1 Estimated new cancer cases and deaths in 2023, United States [26].....	3
Table 1.2 Ex vivo and In vitro studies in literature.....	13
Table 1.3 Gain and loss informatin of component in proposed MWA System.....	16
Table 2.1 Proposed microwave probe performance comparison with the alternative microwave probe designs in literature	19
Table 2.2 Parameter optimization results of proposed applicator	21
Table 2.3 Optimized parameters of RTMWAP	24
Table 2.4 Parameter optimization results of proposed applicator	27
Table 2.5 Material properties of breast cancer and PTFE at 2.45 GHz [114-116]	28
Table 2.6 Optimized parameters of reflector type microwave applicator.....	33
Table 2.7 Proposed dimensions of the 3DPMWAP.....	37
Table 2.8 Electromagnetic radiation performances of 3DPMWAP in electrical and thermal properties given breast cancer and distilled water [130-132]	42
Table 2.9 SAR values of 1.76 g breast cancer with changing distance between 3DPMWAP and tumorous cell.....	44
Table 2.10 Optimized dimensions of MMWAP	49
Table 2.11 Material information of MWA components at 2.45 GHz. [133–136]	49
Table 2.12 Applicator performances table on 125 g chicken liver	54
Table 3.1 Optimized parameters of Non Foster NIC	60
Table 3.2 Performance table of NIC at 2.45 GHz.....	67
Table 4.1 MWPA designs studied in last 15 years.....	75
Table 4.2 Lumped elements used in QPD350.....	84

Table 4.3 Optimized parameters of proposed MWPA.....	85
Table 4.4 Properties of commonly used materials in QPD350 design	94
Table 4.5 Substrate properties of commercially available Rogers substrates.....	95
Table 5.1 Dielectric and thermal properties of kidney, breast, pancreas, lung and liver at 2.45 GHz	116
Table 5.2 Experimental measurement results on a 3D kidney phantom model.....	120
Table 5.3 Electric field measurement results with the MMWAP and CA20L1	123
Table 5.4 Temperature measurement results of the MMWAP and CA20L1 at the end of 150 s.....	124
Table 5.5 Experimental measurement results on a 3D pancreas recipe.....	128
Table 5.6 Experimental measurement results on a 3D lung recipe.....	131
Table 5.7 Experimental measurement results on a 3D liver recipe.....	134
Table 6.1 Applicator performances table on 125 g chicken liver	147
Table 6.2 MWA and PEMF assay results on prostate cancer	154
Table 6.3 MWA and PEMF assay results on pancreas cancer.....	160
Table 7.1 Microwave thermal ablation-PEMF applications and groups [177].....	163
Table 7.2 In vivo experimental parameters and temperature analysis results according to antenna type [177].....	172
Table 7.3 Tissue tracking protocol.....	176
Table 7.4 H&E staining protocol	177
Table 7.5 Immunohistochemical staining protocol in room temperature	178
Table 7.6 T41 Morphometric analyses after microwave thermal ablation-PEMF applications in breast cancer groups (Mean 95% Confidence Interval)	181
Table 7.7 Morphometric analysis of HE stains (Mean 95% Confidence Interval)..	182
Table 7.8 T41 Morphometric analyses after microwave thermal ablation-PEMF applications in breast cancer groups (Mean 95% Confidence Interval)	185

Table 7.9 Morphometric analysis of reproduction findings (Mean 95% Confidence Interval).....	186
Table 7.10 T41 Morphometric analyses of cell death finding after MWA-PEMF application (Mean 95% Confidence Interval).....	188

List of Abbreviations

PA	Power Amplifier
LNA	Low Noise Amplifier
ISM	Industrial, Scientific, and Medical
CST	Computer Simulated Technology
MWA	Microwave Ablation
HTIMWAP	Helix Tipped Thin Microwave Ablation Probe
RTMWAP	Reflector Type Microwave Ablation Probe
3DPMWAP	3D Printed Microwave Ablation Probe
CA20L1	Commercially Available 20 cm Length Ablation Applicator
MMWAP	Multiple Microwave Ablation Prob
MFMWAP	Marble Filled NiTi Tipped Microwave Ablation Probe
QPD350	350 W Microwave Power Applifier Proposed In This Thesis
FDA	Food and Drug Administration
DC	Direct Current
AC	Alternating Current
SAR	Spechific Absorption Rate
PTFE	Poly Tetra Fluoro Ethylene
ABS	Akrilonitril Bütadien Stiren
VSWR	Voltage Standing Wave Ratio
NFC	Non-Foster Circuit
NIC	Negative Impedance Converter
OCS	Open Circuit Stub

List of Symbols

ϵ_r	Relative dielectric constant
μ_r	Relative permeability
σ	Electrical Conductivity [S/m]
ω	Angular frequency [rad/s]
k_T	Thermal Conductivity [W/(m.K)]
c_p	Specific Heat [kJ/(kg·K)]
ρ	Density[kg/m ³]
Γ	Reflection Coefficient
β	Propagation Constant [m ⁻¹]
Z_0	Characteristic Impedance [Ω]
RL	Return Loss
T	Temperature [°C]
Q_h	Heat loss [W]

Chapter 1

Introduction

1.1 Motivation and Research Problem

Cancer is one of the most important problems which is basically defined as uncontrolled cell proliferation in unpredictable ways [1-2]. One in three women and one in two men suffer from various types of cancer in United States [3]. Due to the high fatality rate associated with the majority of cancer diagnoses, there has been a notable surge in research endeavors pertaining to cancer treatment in recent times [4].

Microwave ablation (MWA) process is a minimally invasive, non-ionizing method based on the cellular level heating of the region to be ablated with the high-power localized microwave energy for cancer treatment [5]. Microwave ablation technique operating within 2.4–2.5 GHz industrial, scientific, and medical (ISM) band is minimally invasive and improved solution method for the cancer treatment [6–8]. The interaction of high microwave power with tumorous tissue causes cellular cytotoxicity with the temperature above 42 °C or the loss of cellular viability by raising the core temperature above 60 °C [8–15]. For that purpose, it is necessary to heat the ablation zone up to nearly 60 °C while avoiding the temperature to exceed beyond that temperature. Otherwise, it results in the surgery duration and death risk that to increase [16–18]. In order to generate microwave power that is required to quickly heat tumorous cells around 60 °C, it is necessary to constrain the electromagnetic radiation around the section of the microwave ablation probe contacting the biological target directly. If the heating process-based tumor cell ablation is performed with conventional heating systems, the heated region warms up by heat radiation, convection, and conduction mechanisms. Materials under convectional heating processes are heated up from an external heat source in one direction. However, in

MWA systems, the exposed cancer region is heated directly with the interaction to the interior polar molecules and charged particles of the tissue because of microwave power. Therefore, microwave heating-based ablation treatment is characterized to be internal, efficient, and environmentally friendly heating methodology [19–23].

In clinical application, healthy tissues can be damaged by radiating tumorous tissue from a non-directional electromagnetic field source. To remove the tumor tissue from the surrounding healthy tissue, an applicator that creates a directional radiation pattern that allows to reduce thermal injury to adjacent organs is needed [24] Most of the microwave ablation applicator design based on linear antenna such as monopole, dipole or slot antenna because of providing enough wide frequency bandwidth which, is able to avoid the reflection due to the possible changes of radiating impedance in biological medium under heating process [25]. However, that antennas provide an omnidirectional heating pattern leading to relatively low directivity in ablation zone. One of the novelty of this thesis is integrating reflector antenna into the classical linear antenna so that design a microwave applicator with increasing directivity in ablation region. Thus, the novel microwave applicator has both advantages of the wide operating frequency bandwidth and high electromagnetic field localization in undesirable tumorous tissue.

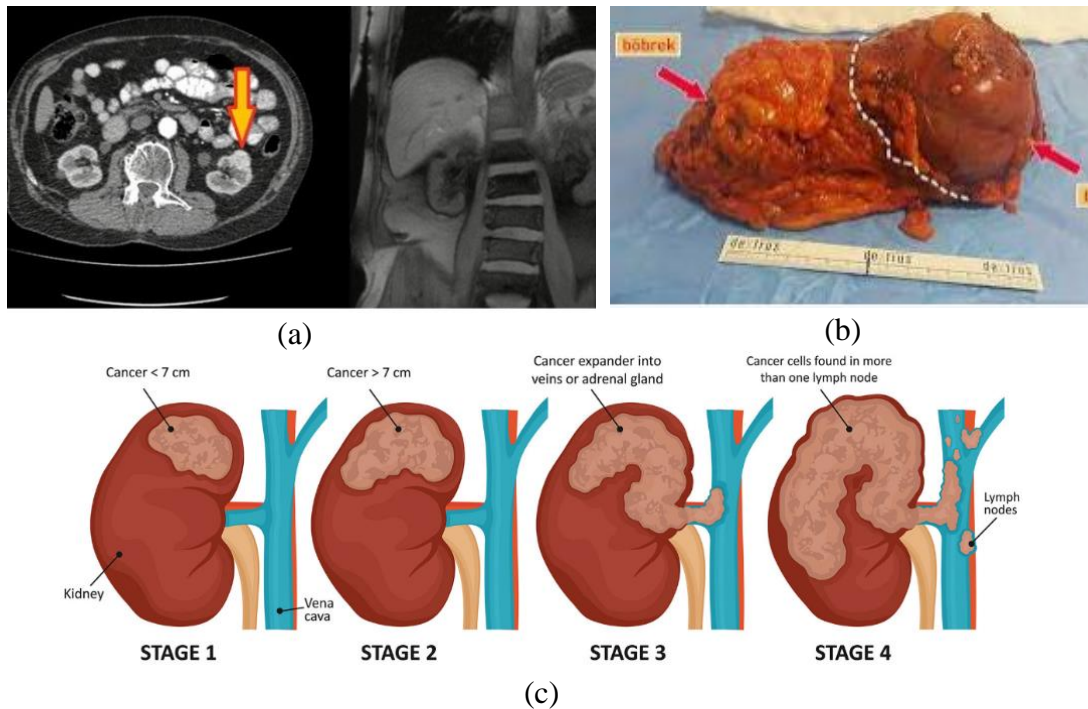


Figure 1.1: MWA treatment of kidney cancer (a) tomography, (b) images outside the organism and (c) cancer stages

The American Cancer Society annually projects the incidence and mortality rates of cancer within the United States. To achieve this, they collate and scrutinize the most current data on the population-based prevalence and outcomes of cancer using incidence data gathered by central cancer registries and mortality data compiled by the National Center for Health Statistics. Table 1.1 presents the projected number of new cases of invasive cancer in the US for 2023, which totals approximately 2 million [26].

Table 1.1: Estimated new cancer cases and deaths in 2023, United States [26]

Cancer site	Case	Death	Mortality rate (%)
Tongue	18,040	11,580	64.19
Mouth	14,820	2,940	19.84
Pharynx	20,070	3,090	15.4
Esophagus	21,560	16,120	74.77
Stomach	26,500	11,130	42
Small intestine	12,070	2,070	17.15
Colon and Rectum	153,020	52,550	34.34
Anus	9,760	1,870	19.16
Liver	41,210	29,380	71.29
Gallbladder	12,220	4,510	36.91
Pancreas	64,050	50,550	78.92
Larynx	12,380	3,820	30.86
Lung and bronchus	238,340	127,070	53.31
Larynx	12,380	3,820	30.86
Skin	104,930	12,470	11.88
Breast	300,590	43,700	14.54
Uterine	80,160	17,340	21.63
Ovary	19,710	13,270	67.33
Prostate	288,300	34,700	12.04
Testis	9,190	470	5.11
Kidney and renal pelvis	81,800	14,890	18.20
Brain and other nervous system	24,810	18,990	76.54
Thyroid	43,720	2,120	4.85
Lymphoma	89,380	21,080	23.58
Myeloma	35,730	12,590	35.24
Leukemia	59,610	23,710	39.78

Table 1.1 provides numerical estimates for new cancer cases and deaths in the United States in 2023, based on data from 2005-2019 for incidence and 2006-2020 for mortality. The estimated number of new cases of invasive cancer is 1,958,310 excluding basal cell and squamous cell skin cancer and in situ carcinoma except urinary bladder, with 55,720 cases of female breast ductal carcinoma in situ and 89,070 cases of melanoma in situ expected. The total number of deaths from cancer in 2023 is estimated to be around 609,640, with colon and rectal cancer deaths combined due to misclassification, and potentially more deaths than cases due to issues with recording underlying causes of death. The greatest number of deaths are from cancers of the lung, prostate and breast which are studied in this thesis [26].

Since 1990s, there has been a consistent and noteworthy decrease in cancer mortality rates, leading to an overall reduction of 33 % and the prevention of approximately 4 million cancer-related deaths. This encouraging progress can be attributed to various factors, including a decrease in smoking rates and increased screening procedures. Moreover, the advancement of treatment options, such as adjuvant chemotherapies for colon and breast cancers, has also played a pivotal role in the reduction of mortality rates. Additionally, recent developments in targeted therapy and immunotherapy have further expedited the decrease in lung cancer mortality rates, even surpassing the decline in incidence rates. These novel treatment breakthroughs have also positively impacted the management of complex cancers, including non-small cell lung cancer and metastatic melanoma. Nonetheless, there is concern regarding the mounting incidence of breast, prostate, and uterine corpus cancers, which display a marked racial disparity in mortality rates and are amenable to early detection [26].

The estimated number of new cancer cases and deaths can provide insights into the potential demand and market size for microwave ablation systems designed for various cancer types, including those that have high mortality rates such as lung, prostate, breast, and colorectal cancer. Additionally, understanding the trends in cancer incidence and mortality rates can aid in identifying areas where there may be an unmet need for new or improved cancer treatments, including those that utilize microwave ablation technology. In this thesis, a microwave ablation system design is proposed for microwave ablation systems operating in ISM band at 2.45 GHz with numerical computation, experimental studies and optimization.

1.2 Thesis Organization and Novel Contribution

Chapter 1 highlights the significance of cancer as the motivation for the thesis, provides a concise overview of previous studies addressing the issue, discusses the role of microwave ablation as a proposed cancer treatment method, and outlines the system design requirements for this technique.

Chapter 2 focuses on the design of applicators, which serve the function of electromagnetic radiation in the microwave ablation system. These designs are optimized using the CST Microwave Studio, a 3D numerical computing program. The optimization process aims to achieve a low reflection coefficient, high directivity electric field emission, and incorporates simulations of SAR and transient temperatures to gather preliminary information about the targeted cells for ablation.

Chapter 3 introduces an active impedance matching circuit for the applicator structures, whose design parameters are determined through simulations. This circuit employs an innovative non-Foster negative impedance converter circuit to ensure efficient energy transfer to various cancer cells with minimal reflection loss. By providing impedance matching across a wide frequency band, the circuit minimizes changes in applicator impedance caused by radiation impedance, thus reducing energy loss that could occur when connecting the high-powered applicator to the amplifier.

In Chapter 4, the power amplifier (PA), a critical component in the design of the MWA system. Using AWR Microwave Office, a 2D electronic circuit design program, the chapter discusses the optimization of output power, gain, and power added efficiency. Design parameters derived from the optimization process are used to fabricate the PA, which is subsequently tested both with and without impedance matching.

In Chapter 5, designed MWA applicators in 3D tissue equivalent models were studied for ablation zone detection. Chapter 6 focused on the detection of ablation zones using MWA applicators on ex vivo bovine liver, as well as performing survival analysis on microscope images to evaluate the effects of MWA application on cancer cells in an in vitro environment. In Chapter 7, the ablation application was performed with in vivo mouse group and the MWA system was tested through the final phase stage. Finally, concluding remarks are presented in Chapter 8.

1.3 Background on Cancer Treatment Techniques

Cancer has been a significant health concern throughout human history, and the treatment of cancer has evolved over time. This thesis provides an overview of the history of cancer treatment, including its ancient origins, developments in the 19th and 20th centuries, and current research.

In ancient times, cancer treatment often involved the use of herbal remedies and surgical procedures. For example, Hippocrates, the famous Greek physician, described the surgical removal of breast tumors in the 4th century BCE. Indian physicians also used plants and minerals to treat cancers [27]. However, cancer was often seen as a death sentence in ancient times, and the impact of these treatments was limited.

During the Middle Ages, cancer treatment was primitive and often ineffective. The understanding of the disease was limited, and the treatments were often based on superstitious beliefs rather than scientific evidence. One common approach to treating cancer during this time was the use of toxic substances such as arsenic. These substances were believed to have therapeutic properties and were often used to treat a range of illnesses, including cancer. However, the use of toxic substances to treat cancer during the Middle Ages was not without risks. One major problem was the high risk of infection, which limited the effectiveness of surgical procedures. Infection was a significant concern in the pre-antibiotic era, and many patients who underwent surgery for cancer died as a result of postoperative infection. Moreover, the use of toxic substances like arsenic could also cause harm to patients. Arsenic was a known poison and exposure to high levels of the substance could lead to serious health problems. In addition, the use of such toxic substances could have unintended consequences, such as damaging healthy tissue or causing the cancer to spread more quickly [28].

The 19th century saw significant advances in cancer treatment, with the development of new techniques and technologies that paved the way for more effective therapies. One of the most important developments during this period was the discovery of anesthesia and antiseptics. These breakthroughs made surgery safer and more effective, enabling surgeons to remove cancerous tumors with greater precision and reduced risk of infection [29]. Another significant development during this period was

the discovery of X-rays in 1895, which led to the development of radiation therapy as a cancer treatment. Radiation therapy uses high-energy radiation to kill cancer cells and shrink tumors. By the early 1900s, radiation therapy was a standard treatment for certain types of cancer, including breast and skin cancer [30]. Radiation therapy has continued to evolve over the years, with new technologies and techniques being developed to make the treatment more effective and less harmful to healthy tissue. For example, modern radiation therapy techniques such as intensity-modulated radiation therapy and stereotactic body radiation therapy use advanced computer software to deliver highly targeted doses of radiation to cancerous tumors, while minimizing exposure to surrounding healthy tissue [31].

In the mid-20th century, chemotherapy was developed, with the discovery of chemicals that could kill cancer cells. Chemotherapy was developed in the 1940s when researchers discovered that certain chemicals could kill rapidly dividing cells, including cancer cells [32]. Hormone therapy, which involves the use of drugs to block the production of hormones that stimulate cancer growth, was also developed around this time. Hormone therapy, which involves the use of drugs to block the production of hormones that stimulate cancer growth, was also developed in the mid-20th century. Researchers discovered that certain cancers, such as breast and prostate cancer, rely on hormones to grow and spread [33]. By blocking the production or action of these hormones, hormone therapy can slow or stop the growth of cancer cells. Hormone therapy can be given orally or by injection and is typically used in combination with other treatments such as chemotherapy or radiation therapy. Both chemotherapy and hormone therapy have undergone significant advancements since their initial development, with new drugs and treatment regimens being developed to improve their effectiveness and reduce side effects. For example, targeted therapies are a type of chemotherapy that target specific molecules or proteins on cancer cells, minimizing damage to healthy cells [34]. Similarly, new types of hormone therapy, such as aromatase inhibitors, have been developed that can effectively block the production of hormones that stimulate the growth of certain types of cancer.

DC ablation, also known as direct current ablation or DC cardioversion, is a medical procedure used to correct abnormal heart rhythms, such as atrial fibrillation or ventricular tachycardia. It involves the use of an electric shock to reset the heart's

electrical activity and restore a normal rhythm. The history of DC ablation can be traced back to the early 20th century, when scientists first discovered the electrical activity of the heart. In the 1930s, a Swedish physician named Rune Elmqvist developed the first external defibrillator, which used direct current to shock the heart and restore a normal rhythm. However, these early defibrillators were large and cumbersome, and were only used in hospitals. In the 1950s, Dr. Paul Zoll, an American cardiologist, developed the first portable defibrillator, which was small enough to be used outside of hospitals. This innovation made it possible to use DC ablation to treat patients with heart rhythm disorders in emergency situations (NIH, 2020). Over the years, DC ablation technology has continued to evolve, with new devices being developed that are smaller, more portable, and more effective at restoring normal heart rhythms [35]. Today, DC ablation is a common and effective treatment for many types of heart rhythm disorders and is widely used in hospitals and emergency medical services around the world [34].

Laser ablation, also known as laser surgery or laser therapy, is a minimally invasive procedure that uses a laser to remove or destroy abnormal or cancerous tissue [36]. The use of lasers in medicine dates back to the 1960s when the first laser was invented by Theodore Maiman [37]. However, it wasn't until the 1980s that laser ablation began to be used as a treatment for cancer. One of the earliest applications of laser ablation in cancer treatment was in the treatment of cervical cancer. In the 1980s, researchers began using laser ablation to remove abnormal cells from the cervix [38]. This procedure, known as laser conization, was found to be highly effective and resulted in a high cure rate for early-stage cervical cancer. In the years that followed, laser ablation began to be used in the treatment of other types of cancer. For example, laser ablation has been used to treat skin cancer, lung cancer, and prostate cancer [39–40]. In many cases, laser ablation is used as a primary treatment for early-stage cancers or as a secondary treatment for cancers that have not responded to other therapies. One of the advantages of laser ablation is its precision. Because lasers can be focused on specific areas of tissue, they can be used to remove or destroy cancerous cells without damaging surrounding healthy tissue [39]. This precision also reduces the risk of complications and side effects associated with other types of cancer treatments, such as surgery and radiation therapy. Today, laser ablation continues to be an important tool in the fight against cancer. Ongoing research and development are focused on

improving the effectiveness and safety of laser ablation, as well as expanding its use to treat a wider range of cancers.

In the 1970s, immunotherapy emerged as a new approach to treating cancer. This treatment involves boosting the body's immune system to help fight cancer cells. One of the first immunotherapy drugs developed was interleukin-2 (IL-2), which was approved by the US Food and Drug Administration (FDA) in 1992 for the treatment of advanced kidney cancer [41]. IL-2 stimulates the production of immune cells, including T-cells and natural killer cells, which attack cancer cells. Since then, other immunotherapy drugs have been developed and approved for use in various types of cancer. Examples of such drugs include checkpoint inhibitors, such as ipilimumab and pembrolizumab, which block the signals that cancer cells use to evade the immune system, and chimeric antigen receptor (CAR) T-cell therapy, which involves modifying a patient's own T-cells to specifically target cancer cells. Immunotherapy has shown great promise in treating cancer and has led to long-term remission in some patients, particularly those with advanced or metastatic disease. However, it is not effective for all types of cancer or all patients, and there can be significant side effects associated with treatment [42].

In 1997, radiofrequency ablation (RFA) was developed as a minimally invasive alternative to surgery for the treatment of liver tumors. The technique involves the insertion of a needle-like electrode into the tumor, which is then heated using high-frequency electrical currents to destroy the cancer cells. [43]. In the radiofrequency ablation (RFA) system, unlike the direct current ablation system, the electromagnetic wave created by using alternating current in the 350 kHz-1 MHz frequency range as an energy source, instead of high-voltage discharge, destroys the targeted area [44]. RFA causes tissue protein denaturation and disruption of membrane integrity in an exposure time of 4-6 minutes when the temperature of the ablation site is 50 °C or 60 °C [45]. Radio frequency ablation (RFA) has been shown to be clinically effective in the treatment of tumors smaller than 3 centimeters. RFA has since been used to treat tumors in other parts of the body, such as the lungs and kidneys. The procedure is typically performed under local anesthesia and can often be done on an outpatient basis. It has been shown to be effective in treating small tumors and can be used as a standalone treatment or in combination with other treatments, such as chemotherapy

or radiation therapy. One of the advantages of RFA is that it is a minimally invasive procedure that can be performed with a very small incision. This can result in less pain, shorter hospital stays, and a faster recovery time compared to traditional surgery. RFA has also been shown to have a low rate of complications. Despite these advantages, RFA is not suitable for all types of tumors. It may not be effective for larger tumors or tumors located in certain parts of the body. In addition, there is a risk of complications, such as bleeding or infection, as with any invasive procedure. [46–48].

More recently, MWA has emerged as an alternative to RFA. MWA uses microwave energy to heat and destroy cancerous tissue. MWA uses high-frequency electromagnetic waves to heat and destroy cancerous tissue, and it is believed to be more effective than RF ablation for larger tumors and those located near blood vessels [49]. Microwave ablation has also been found to be faster and require fewer treatments than RFA [50]. The technique of MWA involves the use of a small probe that is inserted into the tumor under image guidance. The probe emits electromagnetic waves that create friction within the tumor tissue, causing the cells to heat up and die [51]. Because electromagnetic waves can penetrate deeper into tissue than the electrical current used in RFA, MWA is considered more effective for larger tumors [50]. MWA has been found to be a safe and effective treatment option for a variety of tumors, including liver, lung, and kidney tumors [52–53]. Compared to other ablative techniques such as RFA and cryoablation, microwave ablation has also been associated with a lower incidence of complications, such as bleeding and infections [51]. Timeline of cancer treatment is indicated in Figure 1.2.

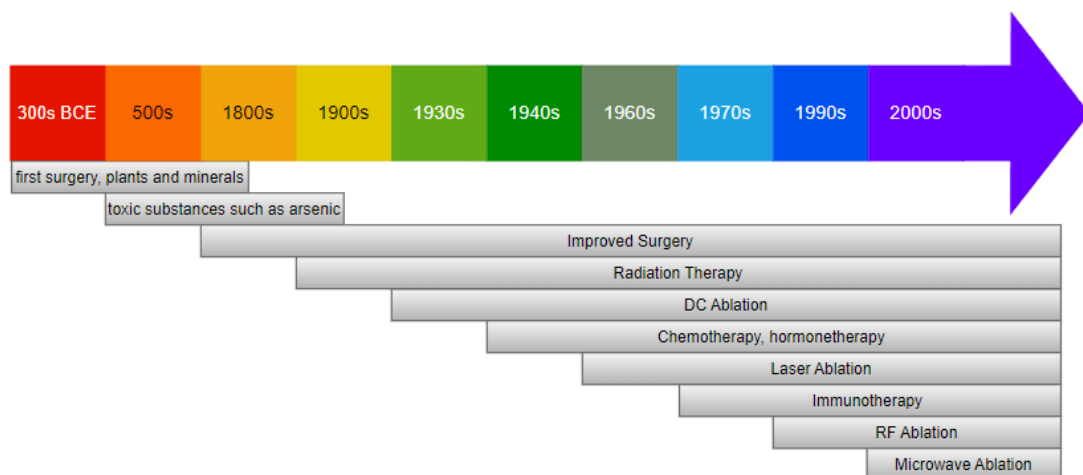


Figure 1.2: Cancer treatment history

1.4 MWA Technology for Cancer Treatment

MWA is a minimally invasive technique used to destroy tumors such as liver, lung, kidney, and bone [54]. Microwave ablation uses electromagnetic waves in the microwave range to generate heat and destroy cancer cells. MWA has advantages over other ablation techniques because it generates heat faster and is more efficient in destroying cancer cells [55]. MWA works by delivering high-frequency electromagnetic waves into the tumor tissue. Microwaves generate heat and cause the tumor cells to undergo thermal necrosis as shown in Figure 1.3 [56]. MWA can be performed using either a single or multiple antennas, which are inserted into the tumor under imaging guidance [55]. The antenna emits microwave energy that creates a zone of coagulation necrosis around the tip of the antenna. The size of the zone depends on the power and duration of the microwave energy delivered.



Figure 1.3: (a) Microwave ablation application and (b) applicator

Microwave ablation has several advantages over other ablation techniques. It generates heat faster and is more efficient in destroying cancer cells [55]. It also causes less damage to the surrounding tissues and has a lower risk of complications such as bleeding or infection [56]. The procedure can be performed under local anesthesia, and patients usually recover quickly and can return to their normal activities within a few days. Microwave ablation is used to treat various types of tumors, including liver, lung, kidney, and bone tumors. In liver cancer, microwave ablation is used as an alternative to surgery in patients who are not candidates for surgery due to the location or size of the tumor. In lung cancer, microwave ablation is used as a curative treatment for early-stage tumors or as a palliative treatment for advanced-stage tumors while in bone tumors, microwave ablation is used to reduce pain and improve function [54].

The mechanism of microwave ablation is based on the principles of dielectric heating, which refers to the heating of a material due to the interaction of electromagnetic waves with its polar molecules. Cancer cells have a higher water content than surrounding healthy tissue, and therefore, absorb more microwave energy, resulting in selective heating of the cancer cells while preserving the surrounding healthy tissue. The absorption of microwave energy causes rapid oscillation of the water molecules in the cancer cells, leading to frictional heating and subsequent thermal damage to the cancer cells [13]. In accordance with the information presented in Figure 1.4, the placement and role of the microwave within its corresponding frequency spectrum is illustrated.

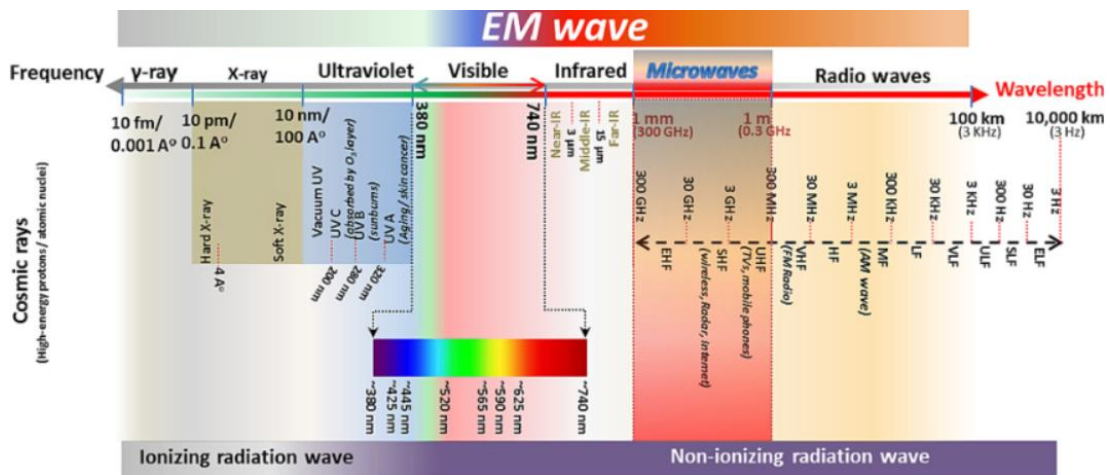


Figure 1.4: Frequency spectrum of electromagnetic waves [58]

When the heating operation is carried out with conventional heating systems, the target region is heated by three distinct mechanisms such as heat radiation, convection, and conduction. Materials are heated in one direction from an external heat source while high energy microwave heating systems heat the materials exposed by the localized microwave power with the direct interaction to the internal polar molecules and charged material particles. Consequently, microwave heating is characterized by efficient, internal, and environmentally friendly heating techniques [59–63]. Additionally, it is necessary to heat the ablation zone up nearly 60 °C to reduce the surgery duration and correspondingly reduce pain [64–66]. The studies in the literature were taken as reference for the success of the microwave ablation system to define MWA system parameters. Ex vivo and in vitro studies conducted since 2006 were compiled in and Table 1.2.

Tablo 1.2: Ex vivo and In vitro studies in literature

Ref.	Year	MWA System	Subject	Ablation region (mL)
[67]	2006	2.45 GHz, 150 W, 20 min	Bovine (ex vivo)	16.5–372.0
[68]	2012	2.45 GHz, 30 W, 10 min	Bovine (ex vivo)	19.8
[69]	2012	2.45 GHz, 105 W, 5 min	Pig (ex vivo)	11.1– 42.3
[70]	2012	2.45 GHz, 135 W, 16 min	Bovine (ex vivo)	-
[71]	2013	915 MHz - 2.45 GHz	Bovine (ex vivo)	17.1 – 57.5
[72]	2013	915 MHz, 45 W, 7 min	Bovine (ex vivo)	7.3 ± 2.1
[73]	2013	915 MHz, 60 W, 10 min	Bovine (ex vivo)	21.30 ± 0.95
[74]	2014	2.45 GHz, 100 W, 10 min	Bovine (ex vivo)	50.8
[75]	2015	2.45 GHz, 40 W, 10 min	Bovine (ex vivo)	1.02–25.60
[76]	2015	2.45 GHz, 60 W, 10 min	Bovine (ex vivo)	51.46
[77]	2015	2.45 GHz, 100 W, 5 min	Bovine (ex vivo)	49.29
[78]	2015	915 MHz, 82 W 675 s	Bovine (ex vivo)	15.33 ± 3.4
[79]	2015	2.45 GHz 28 W, 17 min	Pig (ex vivo)	232 ± 28
[80]	2015	2.45 GHz, 45 W, 10 min	Bovine (ex vivo)	2.47
[81]	2015	40 W, 10 min	Bovine (ex vivo)	-
[82]	2016	915 MHz 50 W, 5 min	Pig (ex vivo)	32.1 ± 5.5;
[82]	2016	2.45 GHz, 50 W, 5 min	Pig (ex vivo)	32.1 ± 5.5;
[83]	2016	2.45 GHz, 130 W, 30 min	Pig (ex vivo)	3.2–274.2
[84]	2007	2.45 GHz, 100 W, 8 min	Pig (in vitro)	33. ±17.3; 92±6.5
[85]	2009	2.45 GHz, 100 W, 4 min	Pig (in vitro)	–
[86]	2011	2.45 GHz, 60 W, 15 min	Pig (in vitro)	21.1
[87]	2014	45 W, 10 min	Pig (in vitro)	–
[88]	2015	2.45 GHz, 80 W, 2 min	Sheep (in vitro)	–
[89]	2012	2.45 GHz, 140 W, 10 min	Pig (in vitro)	–
<i>This Work</i>		<i>2.45 GHz, 20 W, 5 min</i>	<i>Bovine (ex vivo)</i>	<i>24.45</i>

In Table 1.2, the input signal parameters of the MWA system (such as frequency, waveform, application time and magnetic field intensity) have been optimized for use in cancer treatment. When the results obtained were compiled, it was aimed to observe the cases of reducing proliferation in cancerous cells, while not having a significant effect on non-cancerous cells. Based on the information in Table 1.2, a MWA system capable of applying a microwave power of up to 100 W was created and it was aimed to reach the steady state temperature of 60 °C for the ablated tumor cell cultures.

1.5 MWA System Requirement

MWA systems are complex and require several components for their proper functioning. While the three fundamental components of the system are the microwave generator, power distribution system, and applicator antenna, optional components such as a solid-state power amplifier, directional coupler, spectrum analyzer or microwave power sensor, computer, temperature sensor, and thermal camera may also be necessary for gathering data and controlling the system. The selection and configuration of the components will depend on the specific clinical application and user feedback, as MWA systems continue to evolve and emerge in the marketplace.

A microwave ablation system consists of three fundamental components: the microwave generator, the power distribution system, and the applicator antenna. The microwave generator is the crucial part of the system, responsible for generating microwave energy at a specific frequency and power level. The generator may be a standalone unit or integrated with the power distribution system. The frequency of microwave energy can range from 900 MHz to 2.45 GHz, and the power level can range from a few watts to several hundred watts. The generator may also feature different modes of operation, such as continuous wave, pulsed wave, or modulated wave, depending on the specific clinical application [55]. The block diagram of proposed MWA system is indicated in Figure 1.5.

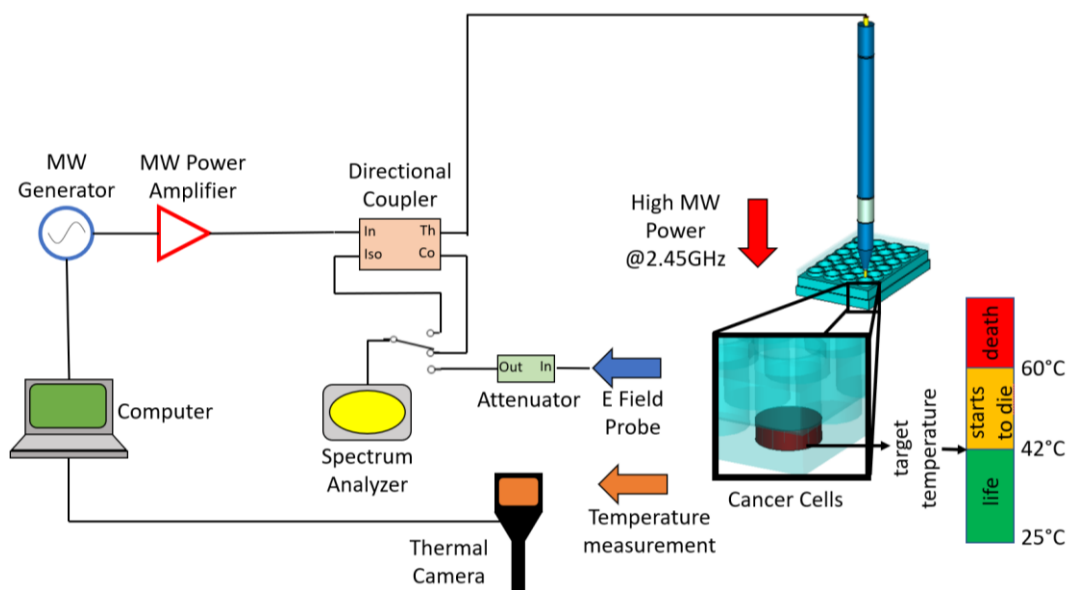


Figure 1.5: MWA system block diagram

The power distribution system is responsible for delivering the microwave energy from the generator to the applicator antenna. It may be a simple cable or a more complex system featuring components to govern the phase, amplitude, and duty cycle of multiple antennas. The power distribution system may also include a solid-state power amplifier to increase the power level of the microwave energy. This is necessary because the microwave generator typically generates a low-power signal that needs to be amplified to achieve the desired level of energy required for ablation.

The applicator antenna is the component that transfers the microwave energy into the tissue, causing heating and destruction of the tumor cells. The antenna may adopt different designs, such as monopole, dipole, or helical, depending on the specific clinical application. Each design has its own advantages and disadvantages, such as the ability to produce a specific shape or size of ablation zone.

In addition to these fundamental components, there are several optional components that may be needed for the proper functioning of the microwave ablation system as indicated in Figure 1.5. For instance, a directional coupler and spectrum analyzer or microwave power sensor may be needed to measure the microwave power delivered to the tissue accurately. This is important for ensuring that the desired level of energy is delivered to the target tissue and avoiding the risk of overheating or under-treatment. A computer is also needed to gather data and control the entire system. The computer may be used to monitor the temperature of the tissue during the ablation process using a temperature sensor, which is placed inside the tissue to provide time-dependent temperature data. Additionally, a thermal camera may be used to provide spatial temperature data, allowing the physician to visualize the ablation zone and ensure that the tumor cells are adequately destroyed.

In addition to the components mentioned in Figure 1.5, an electric field measurement (EFM) probe may also be used in microwave ablation systems. This probe is used to measure the electric field strength in tissue during the ablation process, providing feedback to the system to ensure that the desired field strength is being achieved. The EFM probe consists of a small metallic tip that is inserted into the tissue and connected to a measuring instrument, such as an oscilloscope or spectrum analyzer. As microwave energy is delivered to the tissue, the EFM probe measures the strength of the electric field, which is directly proportional to the amount of energy being

delivered. Using the EFM probe, the ablation process can be monitored in real-time and adjust the system parameters as needed to achieve the desired ablation zone. This allows for greater precision and control during the procedure, potentially leading to better treatment outcomes and reduced risk of complications.

Microwave attenuators may also be used in a microwave ablation system to control the power level of the microwave energy delivered to the tissue. Attenuators work by reducing the power level of the microwave signal that is passed through them, allowing for fine-tuning of the energy delivered to the tissue. This can be particularly useful in cases where the tissue is located near critical structures, as the attenuation can help prevent damage to these structures by limiting the amount of energy delivered to the surrounding tissue. Microwave attenuators are available in both fixed and variable configurations, with the latter allowing for greater flexibility in power adjustment. The use of microwave attenuators in a microwave ablation system can help to ensure precise control over the ablation process and improve patient outcomes. In this thesis, 50 dB microwave attenuator on the power level of 100 W is connected to the input port of spectrum analyzer to avoid it damaging from high power. The budget table of the system given in Figure 1.5 is given in Table 1.3.

Tablo 1.3: Gain and loss informatin of component in proposed MWA System

Component	Gain/loss (dB)
Signal Hound Vector Signal Generator (VSG)	-0.1
CA2906 RF kable (VSG-LNA)	-0.42
Microwave Low Noise Amplifier	39.2
CA2912 RF kable (LNA-PA)	-0.78
Microwave Power Amplifier (PA)	19.6
CA2912 RF kable (PA-Directional Coupler)	-0.78
CNCR Directional Coupler	-1.46
CA3439 RF kable (Directional Coupler -MWA Applicator)	-1.12
EMC Near Field Probe	-0.1
CA2924 RF kable (Near Field Probe – Attenuator)	-1.19
Anritsu Spektrum Analyzer	-0.32

In Tablo 1.3 low noise amplifier and microwave power amplifier exhibit nearly 60 dB gain, However, the RF cables using in the power transmission part of that system diminish aproximately 4.5 dB of output power. When the whole system is together, it creates a large gain value and output power.

Chapter 2

Computational Analysis for MWA Applicator Design

For the applicator section of MWA systems in literature, a triaxial microwave ablation antenna operating in 2.45 GHz ISM band have been introduced by Brace et al. for ex vivo ablation at 50 W power level In 2005 [90]. Laeseke et al. have presented three coherently driven triaxial probes at 2.45 GHz for breast cancer treatment with 90 W input power in 2009 [91]. In 2010, Cavagnaro et al. have proposed a closed tip interstitial antenna validated in ex vivo bovine liver ablation at 2.45 GHz [92]. In 2014, Gentili et al. have proposed a switched mode 100 W multi applicator containing four microwave ablation applicators at 2.45 GHz for the surgical operation [93]. Luyen et al. have suggested 1.95 GHz balun free coax fed helical antenna at 42 W to create localized SAR pattern in the ablation region [94]. A dipole fed by a balanced parallel-wire transmission line antenna operating at 2.45 GHz have been presented by Mohtashami et al. in 2018, conducting an ex vivo experiment on a egg white at a power level of 25 W [95]. In 2018, Muntoni et al. have proposed 434 MHz antenna in order to heat rhabdomyosarcomas tumors about 7-8 °C above the body temperature [96]. In 2019, Fallahi et al. have designed a microwave loop antenna for global endometrial ablation enabling conformal ablation of uterine cavities operating at 915 MHz [97]. A numerical computation of 2.45 GHz interstitial microwave applicator, which is designed to be used in vivo application, have been performed by Hall et al., In 2020 [98]. In 2020, Manop et al. proposed coaxial triple slot antenna for the liver tumor cell ablation at 20 W input power level [99]. Moreover Chalermwisutkul et al. have used the capacitive loading methodology at the radiating end section of the microwave probe for the conventional impedance matching technique of inductive impedance of microwave probe with the capacitive top loading [100].

In addition, it is essential to heat up the ablation region into temperature of about 42°C in order to decrease the surgery duration and, as a result, reduce the pain [101–102]. Therefore, to generate a microwave power to heat the tumorous cells above 42°C, it is essential to localize the electromagnetic radiation at the end of MWA probe. In this regard, in MWA systems, Longo et al., in 2003, has proposed a coaxial antenna with miniaturized choke for minimally invasive microwave ablation applications operating at 2.45 GHz with a power level of 25 W [103]. In 2008, Gentili and Linari have presented a 2.45 GHz temperature sensor integrated microwave applicator under 20 W input power [104]. A floating sleeve dipole antenna operating at 1.9 GHz has been presented by Luyen et al. in 2014 for the use of ex vivo experiments under power level of 42 W [105]. In 2014, Gentili et al. has proposed a switched mode 2.45 GHz microwave multi probe ablation applicator for the open surgical thermoablative treatments by feeding four microwave ablation applicators in an array form up to 100 W [100]. In 2015, McWilliams et al. has introduced a directional interstitial antenna operating at 2.45 GHz ISM band for ex vivo ablation at 80 W power level [101]. Luyen et al. has presented 1950 MHz balun-free coax fed helical antenna at 42 W for the minimally invasive microwave ablation by providing localized SAR pattern [102]. In 2017, the same authors, have put forward an invasiveness of coax-fed MWA antenna at 10 GHz operation frequency with performing ex vivo porcine liver experiment at 30 W [106]. The same year, Gas et al. has designed a 2.45 GHz multi-slot coaxial antenna with numerical computation in human soft tissues [107]. Fallahi has put forward a microwave loop antenna operating at 915 MHz for menorrhagia treatment at a nominal microwave power level of 60 W in next year [108]. The same year, a dual mode coaxial slot applicator operating at 5.8 GHz is presented by Reimann et al. on liver sample with the power level 20 W [109]. In 2020, Yang et al. has proposed a 2.45 GHz Giuseppe Peano fractal phased array antenna with the microwave ablation experiment on tissue mimicking gel [110]. In 2021, Ashour et al. has presented shifted 1T-ring based applicator for the ablation of hepatocellular carcinoma using 6 W microwave power [111]. Considering the microwave ablation applicators designed in mentioned above studies with the operation frequencies ranging from 915 MHz up to 7 GHz at various power levels between 10 W and 100 W and the successful results obtained with these applicators on ex vivo experiments.

Table 2.1: Proposed microwave probe performance comparison with the alternative microwave probe designs in literature

Ref. No.	Freq. (MHz)	S_{11} (dB)	Study Area	Power (W)	Time (min)	T_{abl} (°C)	SAR (W/kg)
[90]	2450	-15	Ex vivo	50	7	80	N.A
[91]	2450	N.A	Ex vivo	90	5	111	N.A
[92]	2450	-14	Ex vivo	60	10	>60	1
[93]	2450	-15	Ex vivo	100	10	80	8
[94]	1950	-18	Ex vivo	42	5	>60	0.6
[95]	10000	-28	Ex vivo	25	5	>60	0.2
[96]	434	-24	Numeric	25	20	42	1
[97]	915	-20	Ex vivo	60	3	90	14
[98]	2450	-6.6	Numeric	1	0.16	40	N.A
[99]	2450	N.A	In vitro	20	10	65.9	N.A
[100]	2450	-20	<i>Ex vivo</i>	25	2	65	4
[101]	2450	-24	<i>Ex vivo</i>	20	15	70	0.1
[102]	1950	N.A	<i>Ex vivo</i>	42	10	60	0.3
[103]	2450	-15	<i>Ex vivo</i>	100	10	80	8
[104]	2450	-39	<i>Ex vivo</i>	80	10	52	N.A
[105]	1950	-30	<i>Ex vivo</i>	42	10	N.A	0.3
[106]	10000	-28	<i>Ex vivo</i>	30	5	60	0.2
[107]	2450	-23	<i>Ex vivo</i>	21	N.A	110	N.A
[108]	915	-7	<i>In vivo</i>	60	3	70	N.A
[109]	5800	-15	<i>Ex vivo</i>	20	2	60	N.A
[110]	2450	-30	<i>In vitro</i>	50	3	57	N.A
[111]	2450	-20	<i>Ex vivo</i>	6	10	110	N.A
This Work	2450	-27	<i>In vitro</i> (outside)	46	20	45	0.26
	2450	-18	<i>In vitro</i> (inside)	46	20	98	6.33

SAR values are considered under 1 W microwave excitation

Based on the research findings presented in the Table 2.1, it was deemed suitable to develop a MWA applicator characterized by minimal reflection losses, capable of operating within a power range of 0-100 W at a frequency of 2.45 GHz. The applicator structures designed during the course of the thesis are depicted in Figure 2.1.

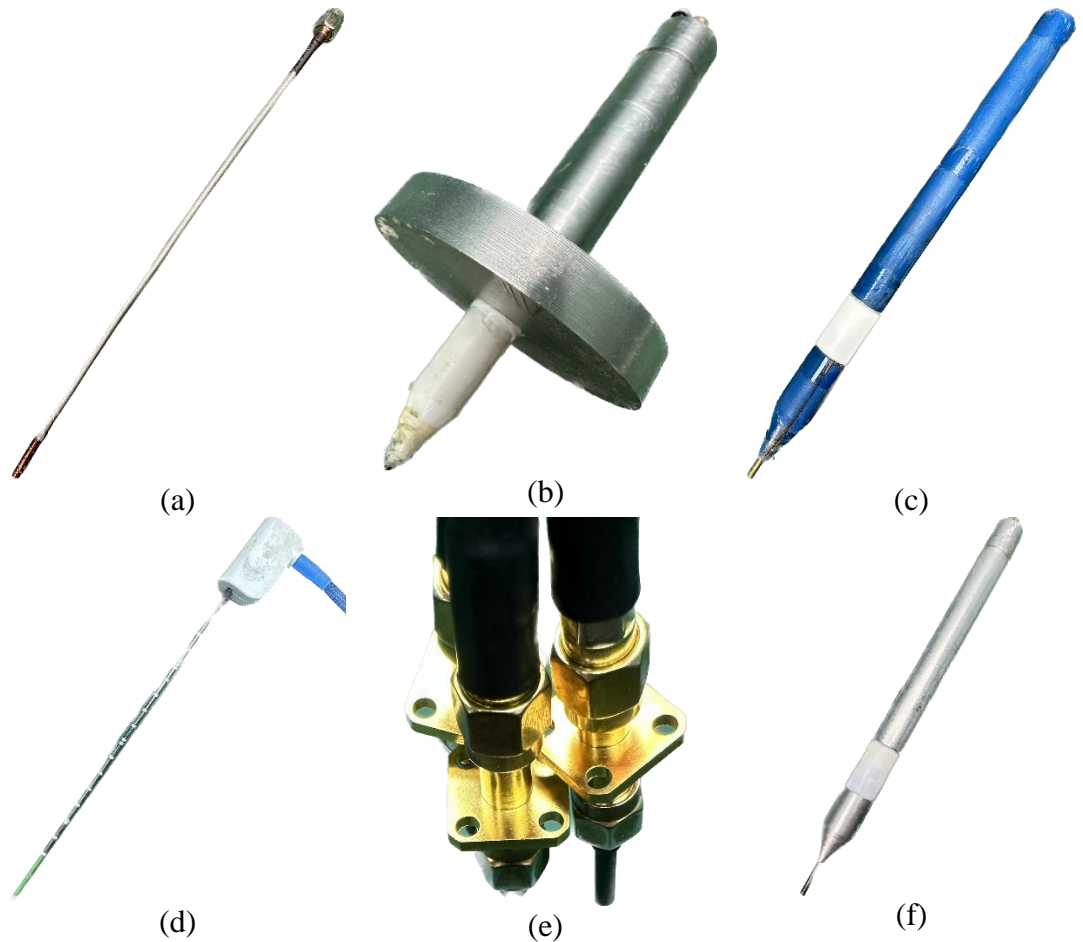


Figure 2.1: Designed MWA applicator for cancer treatment (a) HTIMWAP, (b) RTMWAP, (c) 3DPMWAP, (d) CA20L1, (e) MMWAP, (f) MFMWAP

The depicted applicators in Figure 2.1 exhibit variations in terms of their dimensions, utilization, manufacturing techniques, and material advancements. Within Figure 2.1, the following designs have been developed: in Figure 2.1(a) the Helix Tipped Thin Microwave Ablation Probe (HTIMWAP), in Figure 2.1(b) the Reflector Type Microwave Ablation Probe (RTMWAP), in Figure 2.1(c) the 3D Printed Microwave Ablation Probe (3DPMWAP), in Figure 2.1(d) Commercially Available 20 cm Length Microwave Ablation Applicator (CA20L1), in Figure 2.1(e) the Multiple Microwave Ablation Probe (MMWAP), and in Figure 2.1(f) the Marble Filled NiTi Tipped Microwave Ablation Probe (MFMWAP). HTIMWAP possesses enhanced profit in accessing anatomically challenging regions of the body, and it facilitates high-intensity energy transmission through its helix-shaped antenna structure during low-power operations. Conversely, RTMWAP proves more suitable for delivering high-power, localized microwave energy in cancer types situated in close proximity to the upper

layers of the skin, such as breast cancer. The 3DPMWAP design, which offers improved ease of fabrication and accessibility to materials, is also employed in similar cancer cases. CA20L1 was used from time to time in the experimental stages in order to compare the ablation performances of the designed microwave applicators. When dealing with larger lesions, the CSABMWAP design presents a more logical choice. Lastly, the MFMWAP design capitalizes on the advantageous properties of the biocompatible and electrically/mechanically efficient NiTi material, incorporating marble a low-loss dielectric substance into the applicator structure. Among these designs, Section 2.1 focuses on the RTMWAP, Section 2.2 discusses the 3DPMWAP, and Section 2.3 examines the CSABMWAP. Information on the function of these applicators is summarised in Table 2.2.

Table 2.2: Parameter optimization results of proposed applicator

Applicator	Utilization	Manufacturing Technique	Material Advancements
HTIMWAP	Accessing challenging body regions	Helix-shaped antenna structure	Generic copper usage
RTMWAP	Localized microwave energy delivery	Reflector structure integration	Teflon coated copper usage
3DPMWAP	Cancer cases with improved fabrication	3D printing technology	Cheap, light easily accessible
CA20L1	Experimental performance comparison	Commercially available applicator	Biocompatible ceramic usage
MMWAP	Dealing with larger lesions	Coaxial slot antenna structure	Generic copper usage
MFMWAP	Incorporating advantageous materials	NiTi material with marble filling	biocompatible and efficient materials

These advantages encompass enhanced accessibility to anatomically challenging body regions, precise delivery of localized energy, streamlined fabrication processes, benchmarking capabilities, effective management of larger lesions, and utilization of advantageous materials. These applicators were utilized in cancer types characterized by the specifications outlined in the applicator summary table, as documented in Table 2.2. Subsequently, this chapter introduces simulation studies exploring innovative approaches within the scope of these applicators, while subsequent chapters delve into the utilization of other structures.

2.1 RTMWAP Design and Optimization in In Vitro

In high power microwave ablation systems, it is beneficial to design an microwave applicator whose one port reflection parameter is as small as possible to avoid the high reflected power into the microwave power generator section. Therefore, the resonance frequency of microwave applicator has to be in ISM band at 2.45 GHz for microwave ablation systems. In addition to the obligation of possibly small reflected power, the designed microwave applicator has to emit the localized electromagnetic radiation in order for the high microwave power to penetrate through into the ablation zone for the desired temperature level in the tumorous tissue. In an attempt to design the applicator emitting the localized electromagnetic radiation, a RTMWAP is proposed by placing the circular aluminium disk on the upper side of the dielectric radiator section in a form of reflector as shown in Figure 2.2. The reflector part could also be structured with various different shapes in the forms of triangular pyramid, parabola and tapering cylinder instead of circular disc. However, circular disc geometry is preferred to be the reflector section due to its convenience in structural manufacturing. The reflecting section prevents the backscattered electromagnetic field at the dielectric radiator section from affecting the overall microwave operation performance.

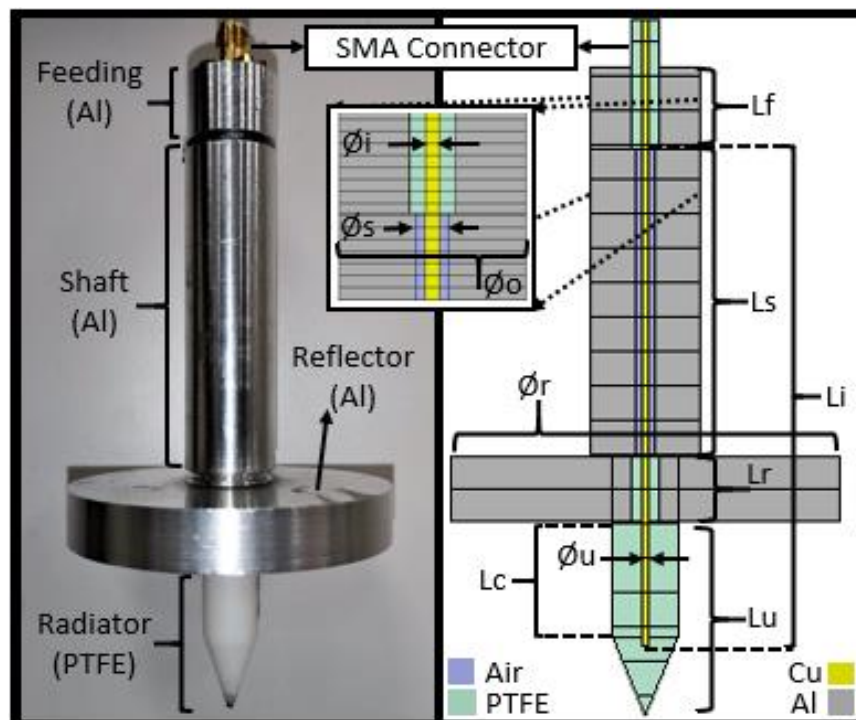


Figure 2.2: RTMWAP sections and material information.

The depicted Figure 2.2 illustrates a crucial probe section and reflector structure known as the dielectric radiator. This dielectric radiator section is designed in a conical geometry and fabricated using biocompatible PTFE (polytetrafluoroethylene) material. Its purpose is to facilitate the emission of electromagnetic radiation. The implementation of the dielectric radiator allows for the successful penetration into tumor tissues without the risk of surgical contamination during surgical procedures, thereby ensuring a safe and effective approach.

The microwave applicator employed in this study is characterized by a reflector configuration, comprising both a transmission line and an antenna section. While the dielectric radiator section serves as the antenna component, the feeding shaft and reflector sections serve as the transmission components. These sections are implemented using a coaxial waveguide structure, thereby enabling the dominant mode of wave propagation to be the transverse electromagnetic (TEM) mode. Nonetheless, at higher operational frequencies surpassing the cut-off frequency defined by Equation (2.1), both transverse electric (TE) and transverse magnetic (TM) modes also manifest themselves [112]

$$f_c = \frac{c}{\pi(r_o + r_i)\sqrt{\epsilon_r}} \quad (2.1)$$

Where f_c is the cutoff frequency, c is the speed of light in free space, ϵ_r is the dielectric constant used in probe structure, r_i is the inner conductor diameter and r_o is the outer dielectric diameter of transmission line structures. In order to avoid for higher order modes in the transmission line sections of proposed microwave applicator, 2.45 GHz operation frequency should be less than the cut off frequency. After calculating the dimensions and materials limitations of microwave applicator sections in coaxial waveguide form, exact dimensions are calculated in Equation (2.2) and Equation (2.3) which, are valid in TEM mode propagation [113]

$$Z_o = \sqrt{\frac{L}{C}} = \frac{1}{2\pi} \sqrt{\frac{\mu}{\epsilon}} \ln \frac{r_o}{r_i} = \frac{60}{\sqrt{\epsilon_r}} \ln \frac{r_o}{r_i} \quad (2.2)$$

$$\Gamma = \frac{Z_{0s} - Z_{0f}}{Z_{0s} + Z_{0f}} \quad (2.3)$$

Where L is the series inductance and C is the shunt capacitance of probe sections based on transmission lines and Γ is the reflection coefficients due to the connection of probe sections have the feature coaxial waveguide. Z_{0s} and Z_{0f} are the characteristic impedances of shaft and feeding section respectively, μ and ϵ are the constitutive parameters of dielectric material between the inner conductor diameter (r_i) and outer dielectric diameter (r_o) of each probe section in coaxial waveguide form. The feeding section of microwave applicator is designed to be fit the 180C sma connector whose outer dielectric diameter is 4.2 mm and inner conductor diameter is 1.3 mm. Similarly, the dielectric diameter of reflector section is also designed to be 4.2 mm because the PTFE material is between the inner and outer conductor as in feeding section. In addition, the inner conductor of sma connector extends along the whole applicator length without a mechanical discontinuity for the constitution of durable piece. the inner conductor diameter of shaft section is also 1.3 mm. Therefore, from Equation (2.2) and Equation (2.3), the optimum outer conductor diameter must be 3 mm for minimizing the reflection between the 50 Ω sma connector, feeding and shaft sections.

Numerical computations are done to obtain the optimized parameters of the RTMWAP for minimum return loss at 2.45 GHz. The optimized geometric parameters of the RTMWAP are shown in Table 2.3 where L_c is defined as the length of cylinder in dielectric radiator section, L_u is the length of dielectric radiator and L_s is the shaft length. In order to determine the optimized geometry of RTMWAP, numerically computed return loss for different geometric parameters is extensively investigated in Figure 2.3, Figure 2.4 and Figure 2.5.

Table 2.3: Optimized parameters of RTMWAP

Lengths and Diameters	Unit (mm)
Inner conductor diameter ($\text{\O}i$)	1.3
Inner conductor length (L_i)	86
Feeding length (L_f)	12.5
Inner diameter of shaft ($\text{\O}s$)	3
Outer diameter of shaft ($\text{\O}o$)	17
Shaft length (L_s)	60
Reflector outer diameter ($\text{\O}r$)	60
Reflector length (L_r)	10
Dielectric radiator length (L_u)	30
Dielectric radiator diameter ($\text{\O}u$)	10
Length of cylinder of dielectric radiator (L_c)	18

In the microwave ablation systems, the main aim is to transport the electromagnetic energy generated at the high power microwave source section to the target tissue to be ablated with the microwave performance parameters of high transmission coefficient, high electric field penetration and correspondingly high microwave power absorption in the biological sample. Firstly, in order to design the microwave applicator with high transmission coefficient, S11 numerical computations for various dielectric radiator lengths have been performed and S11 results are shown in Figure 2.3.

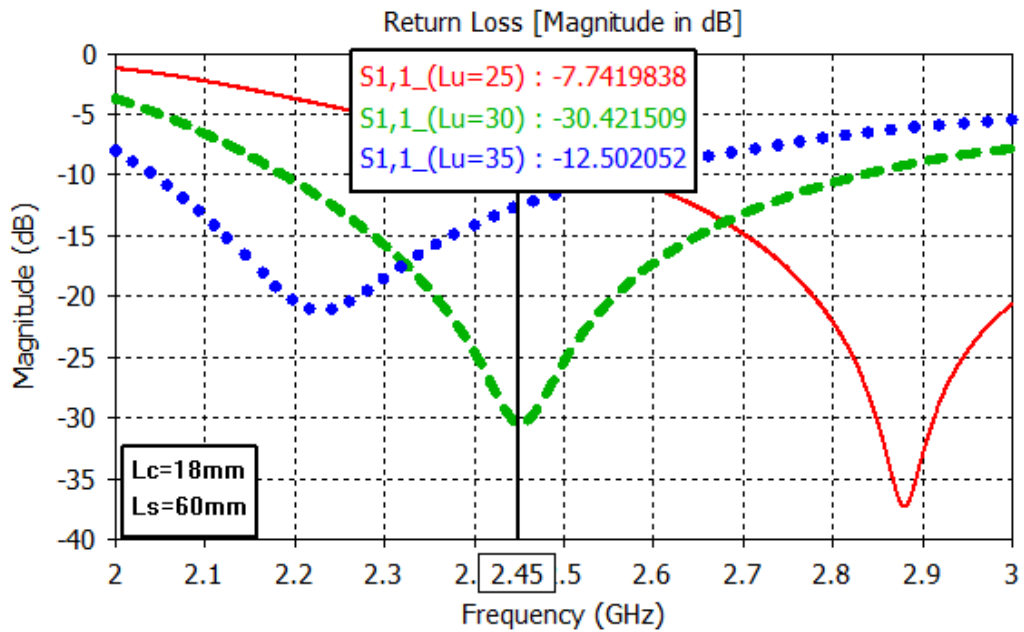


Figure 2.3: The effect of the dielectric radiator length of the RTMWAP on the S parameter.

The S11 results of the RTMWAP dielectric radiator are -7.31 dB, -30.42 dB and -12.57 dB for the different dielectric radiator lengths of 20 mm, 30 mm and 40 mm, respectively. Considering the numerical calculation results shown in Figure 2.3, the dielectric radiator length of proposed RTMWAP is selected to be 30 mm in order to obtain the resonance frequency at 2.45 GHz.

The resonance frequency of proposed microwave applicator with minimum return loss at 2.45 GHz ISM band has to be adjustable in order to compensate the frequency shifts from the fabrication process or biological tumorous cells placed near the dielectric radiator section during the ablation process. In Figure 2.4 the numerical computations are done in order to find out the effect of shape of the dielectric radiator section on the resonance frequency.

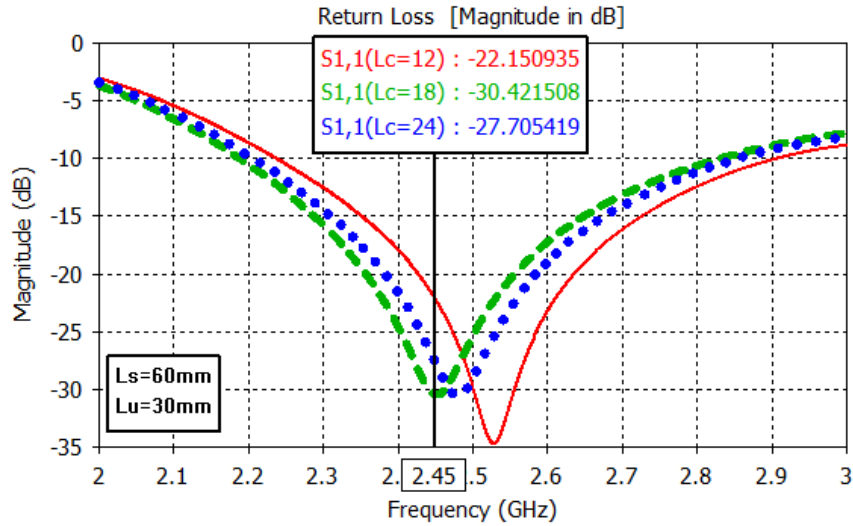


Figure 2.4: The effect of length of cylinder of dielectric radiator on S11

As deduced from the numerical computation result indicated in Figure 2.4 changing the cylinder ratio of proposed probe by 6 mm results into approximately 30 - 70 MHz resonance frequency shift. Thus, the fine adjustment in the resonance frequency can be accomplished by changing the dielectric radiator modules of different length of cylinder. The cylinder length of dielectric radiator section of RTMWAP is selected to be 18 mm since the resonance frequency is the center frequency of ISM band, 2.45 GHz with the relatively low return loss value of -30.42 dB. Since the shaft section of the RTMWAP is designed to serve for handheld operation during the surgical operation, it is necessary to decide the proper shaft length. Because the average handling length varies from 50 mm to 70 mm, the numerical computations are performed by changing the shaft length of RTMWAP as shown in Figure 2.5.

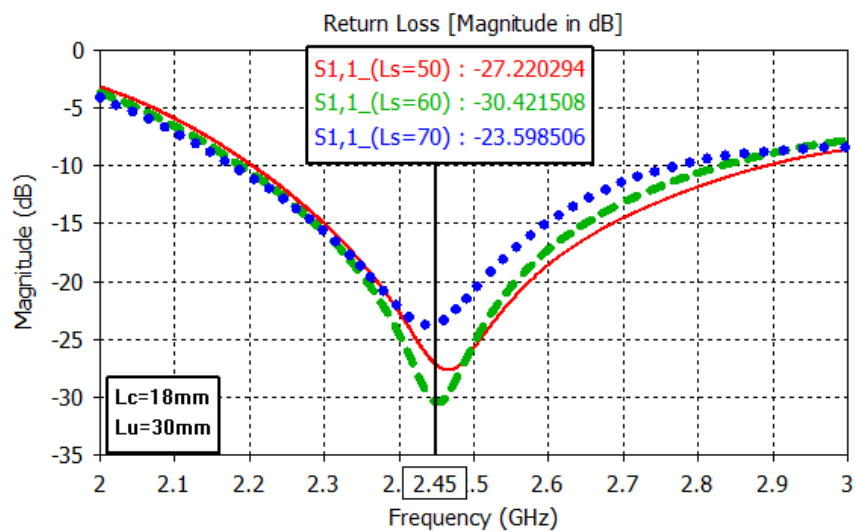


Figure 2.5: The effect of shaft length of RTMWAP on the S11

The S11 results of the RTMWAP are -27.22 dB, -30.42 dB and -23.6 dB for the different shaft lengths of 50 mm, 60 mm and 70 mm, respectively. As it can be deduced from the numerical calculation results shown in Figure 2., the S parameter does not have significant dependence on shaft length due to the shielding effect of the reflecting section. Therefore, the shaft length of reflector type microwave applicator is selected to be 60 mm since the return loss of the reflector type microwave applicator is minimum at 2.45 GHz desired operating frequency. Numerical calculations without reflector structure have also been performed to calculate the improvement in the electromagnetic radiation performance of proposed applicator by the integration of the reflector structure into the probe geometry. In addition to the numerical S11 computations of purposed applicator with and without reflector structure, the average electric field in tumor volume and microwave power absorbed under 15 W microwave power excitation by the tumorous tissue are also calculated via the evaluation of field statistics tool in CST Microwave Studio. The parameter optimization results of reflector type microwave applicator are indicated in Table 2.4.

Table 2.4: Parameter optimization results of proposed applicator

Lu (mm)	Lc (mm)	Ls (mm)	Without reflector			With reflector		
			S11 (dB)	Average E Field (V/m)	Ptumor (mW)	S11 (dB)	Average E Field (V/m)	Ptumor (mW)
30	18	60	-6.96	293	106	-30.42	449	357
35	18	60	-8.07	201	68	-12.50	312	288
30	12	60	-3.70	250	50	-22.15	433	222
30	18	60	-6.96	293	106	-30.42	449	357
30	24	60	-3.88	206	46	-27.71	416	202
30	18	50	-3.79	234	74	-27.22	432	204
30	18	60	-6.96	293	106	-30.42	449	357
30	18	70	-9.11	167	91	-23.60	383	189

As shown in Table 2.4, integrating the reflector structure into the classical monopole antenna structure improve the average electric field and absorbed microwave power in tumor volume by nearly 50 % and 250 % respectively under the same geometric parameters and MWA system model setup. The geometric parameters of reflector type microwave applicator have been determined according to the optimization results to obtain the minimum return loss, maximum electric field and power absorption in the tumor sample. The optimized parameters of dielectric radiator and the reflector sections are determined to be 30 mm, 18 mm and 60 mm for Lu, Lc and Ls,

respectively. Nevertheless, the minor changes in the optimized parameters do not lead the remarkable degradation in the applicator performances. Therefore, the each section of the proposed microwave applicator is fabricated in a form of having the capability of each section to be screwed to one another in order to modify the geometric parameters of respective sections if necessary. Even though the optimized radiator length capable of the annihilation of tumor up to 30 mm in depth, deeper tumorous tissues can be ablated with the proper invasion by mounting a longer radiator section due to the ease of structural assembly. Therefore, an invasive ablation application can be conveniently achieved by ensuring the reflector structure not to contact to the biological medium in addition to choosing the biocompatible PTFE in the dielectric radiator section.

While designing a probe to be utilized in microwave ablation systems, it is required to consider the reflection coefficient of the reflector type microwave applicator not to be affected by the tumorous cells located in the nearfield region. Therefore, the proposed reflector type microwave applicator is simulated in the Time Domain solver of CST Microwave Studio with the tumor sample in petri dishes to be located around the dielectric radiator section as shown in Figure 2.. The electrical and thermal properties of tumorous tissue and PTFE which is the material of dielectric radiator inserted in petri dishes indicated in Table 2.5.

Table 2.5: Material properties of breast cancer and PTFE at 2.45 GHz [114-116]

Dielectric Materials	Breast Cancer	PTFE
Relative Permittivity	55.26	2.1
Relative Permeability	1	1
Electrical Conductivity (S/m)	2.70	0.002
Thermal Conductivity (W/(m·°C))	0.28	0.2
Specific Heat (kJ/(kg·°C))	3.5	1
Density (kg/m ³)	1250	2200

As can be seen from Table 2.5, breast cancer and PTFE differ in terms of electrical properties. According to Equation (2.6), since electrical conductivity is directly proportional to the absorbed microwave power consumed, breast cancer absorbs approximately 14 thousand times more microwave power than PTFE in the probe structure. In this way, the power of the microwave effect spent in the probe is extremely small, while the power spent in the targeted tumour area is extremely large.

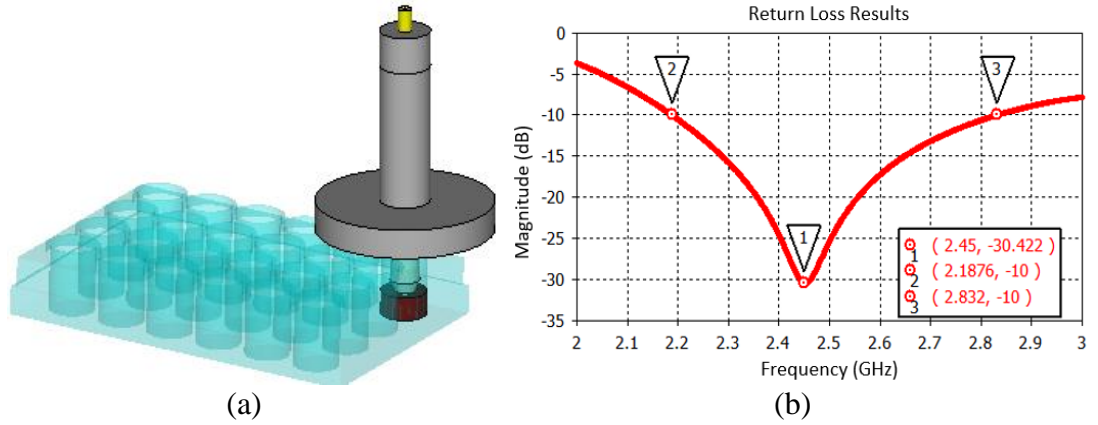


Figure 2.6: Invasive microwave ablation system model setup. (b) Optimized S parameter of numerically computed reflector type MW probe.

As concluded from Figure 2.6(b), the reflector type microwave applicator is operated in 2.4-2.5 GHz ISM band with the numerically calculated S11 value smaller than -25 dB in the existence of tumorous cells around the end region of the dielectric radiator portion. Detailed numerical calculations of reflector type microwave probe with optimized parameters has been performed in CST Microwave Studio Finite Integration Technique by dividing the geometric structures nearly 238000 hexahedral mesh elements. Calculation of each mesh elements are based on the Maxwell Time-Harmonic Equations to obtain the electromagnetic radiation performance of microwave applicator in lossy breast cancer medium. The numerical calculations including electromagnetic radiation performance of microwave probe which are electric field distribution, SAR and PLD, electric and magnetic energy densities in the tumor sample have been calculated under 15 W microwave input power feeding the microwave applicator with waveguide port at SMA connector section.

After pointing out the proposed microwave probe is operating in ISM band with very small reflection coefficient for effective power transfer to tumorous cell in Figure 2.6, the numerical calculations have been performed to figure out the electric field distribution inside the tumorous cells. The electric field distribution in the tumor sample has been computed by using Helmholtz Time-Harmonic Wave Equation shown in Equation (2.4) [117]

$$k_0^2 \left(\epsilon_r - \frac{j\sigma}{\omega\epsilon_0} \right) \mathbf{E} = 0 \quad (2.4)$$

Where E [V/m] is the electric field intensity, ω [rad/s] is the angular frequency of propagating wave, k_0 [m^{-1}] and ϵ_0 [F/m] are the wavenumber and the permittivity of free space, ϵ_r is the real part of relative permittivity, σ [S/m] is the electrical conductivity of tumorous tissue under microwave power exposure. The calculated E field distribution around the surface of the tumorous cells to be ablated indicated in Figure 2.7.

As shown in Figure 2.7(a) and Figure 2.7(c), the tumorous tissue absorbs the electric field emitted by the proposed microwave ablation applicator, which can be deduced from the fact that in the vertical axis the electric field of 10045 V/m reduces down to 378 V/m inside the tumor sample. Because the dielectric constant and electrical conductivity of the tumor tissue are comparably greater than the nearby located material, the more electric flux lines are highly concentrated inside the tumor sample with the result of decreasing electric field level due to the higher electrical conductivity as indicated in Figure 2.7(b) and Figure 2.7(d) Therefore, it is expected that the proposed reflector type microwave applicator causes quite less damage to the healthy tissue during the ablation process. In addition to the electric field distribution, SAR and power loss density are also numerically calculated from Equation (2.5) [118] and Equation (2.6) [119]

$$SAR = \frac{\sigma |\mathbf{E}|^2}{2\rho} \text{ [W/kg]} \quad (2.5)$$

$$PLD = \frac{\sigma |\mathbf{E}|^2}{2} \text{ [W/m}^3\text{]} \quad (2.6)$$

The term "Specific Absorption Rate" (SAR) refers to the rate at which electromagnetic fields are absorbed by breast cancer cells. In the context of microwave exposure, it is essential to consider the Power Loss Density (PLD), the electrical conductivity (σ), and the density (ρ) of the breast cancer cells. Additionally, the electric field intensity (E), emitted by a microwave applicator, plays a crucial role. By examining the simulated SAR value and power loss density illustrated in Figure 2.7, one can ascertain the dissipated localized microwave power within the tumorous cell. This dissipation occurs as a result of heat generation, which is attributed to the high electrical conductivity of the cell.

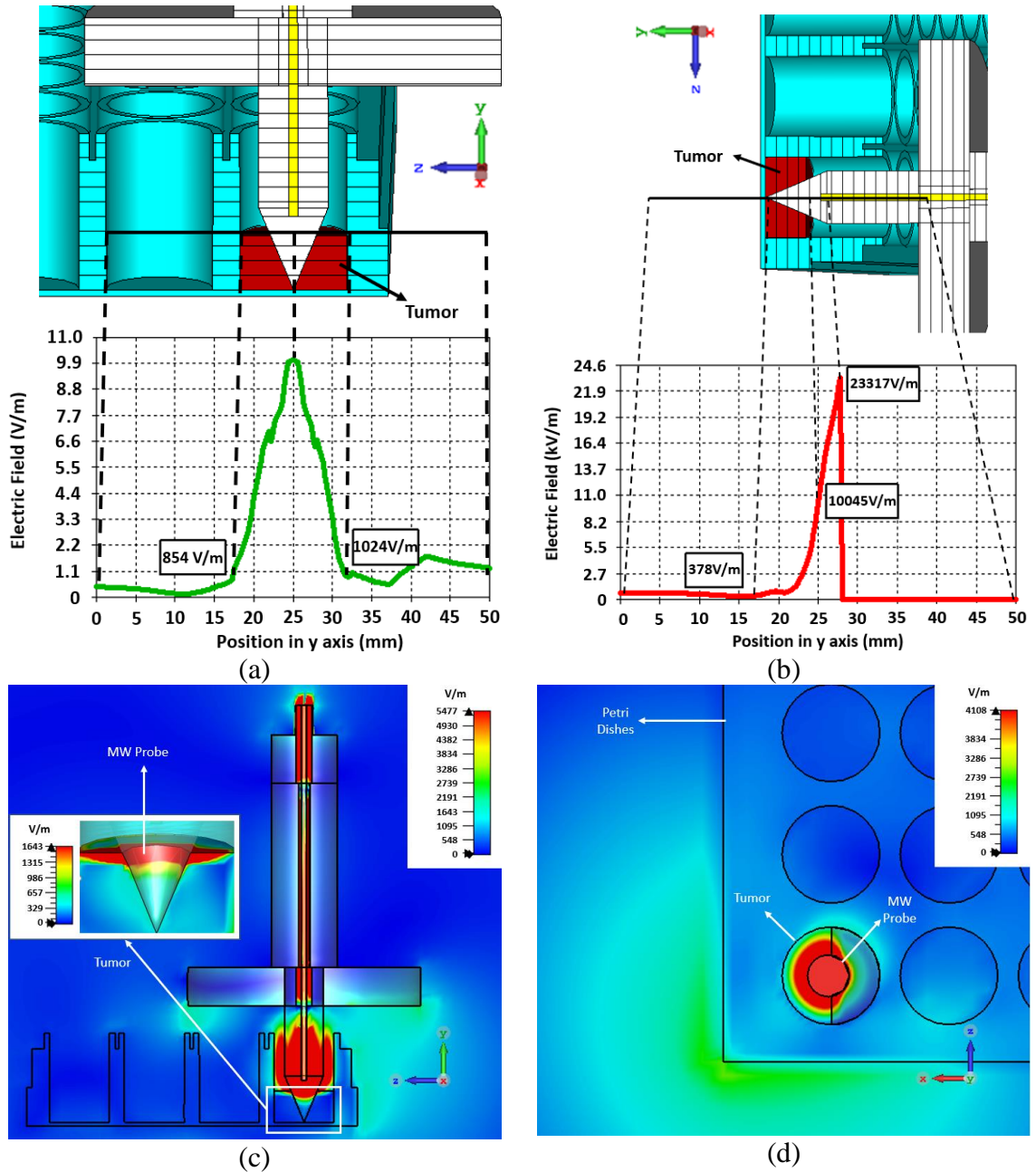


Figure 2.7: Electric field-distance graph (a) in y-axis and (b) in z-axis with corresponding simulation setup. Electric field distribution (c) on x and (d) on y plane.

As indicated in Figure 2.7, most of the radiated microwave power heats up the center of tumorous tissue, into which the dielectric radiator section has been inserted. While the maximum SAR in the tumorous cell is 208 W/kg, the maximum power loss density is 6.668 MW/m³ under 15 W microwave power. The electric and magnetic energy densities are also computed in order to understand the field behavior of electromagnetic power in the near field region. Simulation results of electric and magnetic energy densities are shown in Figure 2.8.

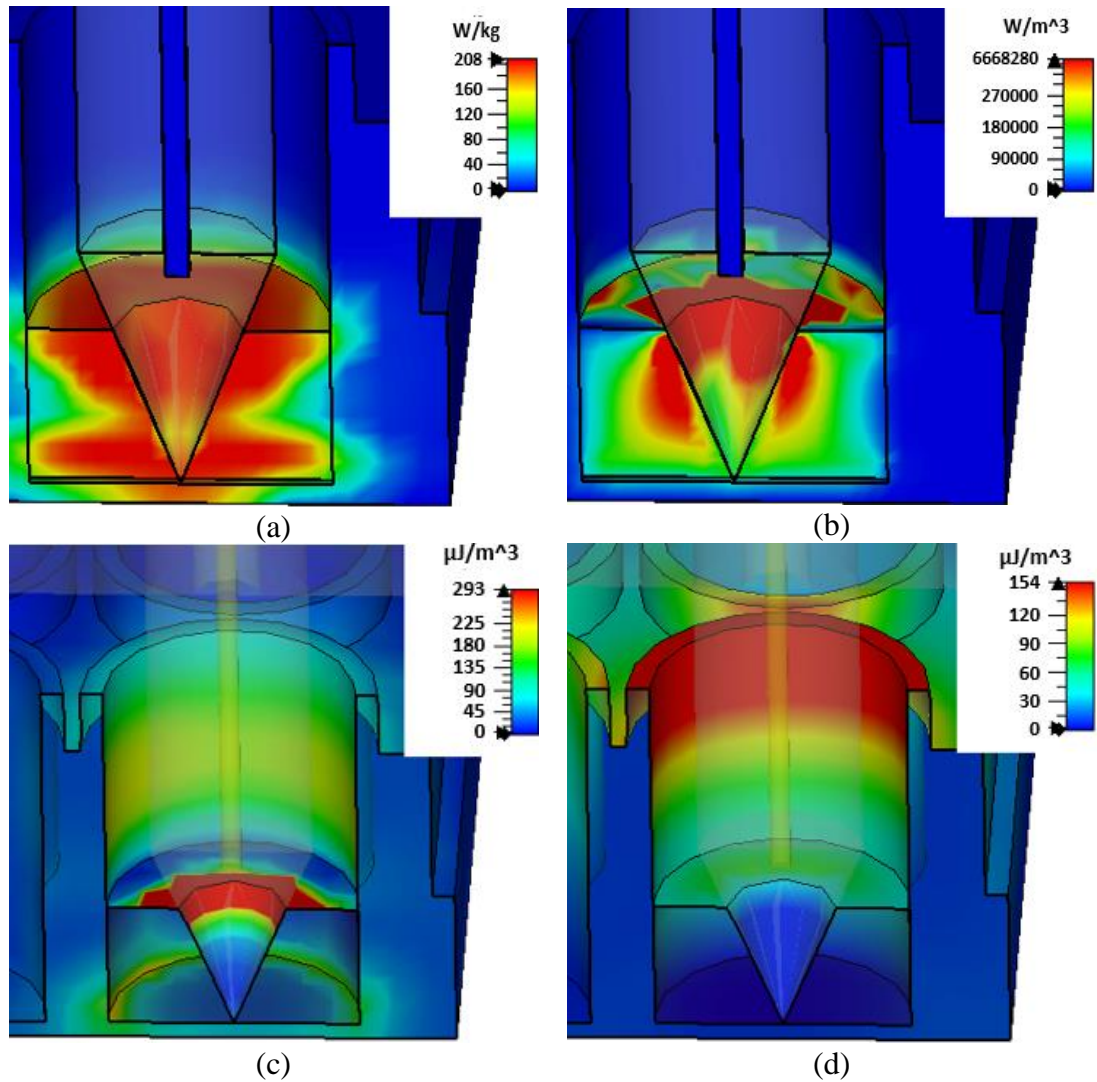


Figure 2.8: (a) SAR pattern, (b) PLD, (c) electric and (d) magnetic energy densities of 1.76 g tumorous cell which is exposed to microwave power emitted by reflector type microwave applicator in the presence of 15 W microwave power excitation.

In Figure 2.8(a) and Figure 2.8(b), the electric and magnetic energy densities have been computed to analyse the dominant mode of the penetrating electromagnetic wave in the near field region. As concluded from the statistical field analysis, the average electric energy density of $48.79 \mu\text{J}/\text{m}^3$ is higher than the average magnetic energy density of $27.79 \mu\text{J}/\text{m}^3$ in the tumorous tissue volume for 15 W microwave input power. While the electric energy density is higher than the magnetic energy density, TM mode is effective to obtain the high radiation power in the near field region penetrating through tumorous tissue for the microwave ablation process. The numerical calculation results obtained in Section 2.1 are given in Table 2.6.

During the numerical computation phase, when the input power of the microwave ablation system is set at 15 W, which aligns with the experimental input power level, significant results are obtained. In particular, a maximum SAR of 208 W/kg, a maximum PLD of 6.668 W/cm³, and an average electric field value of 449 V/m are achieved within a tumor sample weighing 1.76 g. These findings are presented in Table 2.6. Overall, the paragraph presents compelling evidence of the superior microwave ablation performance of the proposed microwave probe design.

Table 2.6: Optimized parameters of reflector type microwave applicator

Simulated Parameters	Results
Input Power (W)	15
Power Absorbed by Tumor (mW)	357
Reflection Coefficient (dB)	30.42
Average E field in Tumor (V/m)	449
Tumor Mass (g)	1.76
Max. SAR (W/kg)	208
Max. Power Loss Density (W/cm ³)	6.668
E Energy Density in Near Field (μJ/m ³)	48.79
H Energy Density in Near Field (μJ/m ³)	27.79

The proposed design of the microwave probe exhibits superior performance in terms of the S11 parameter, compared to alternative microwave probe designs found in the literature. This enhanced performance enables more effective microwave power transfer to the targeted area for ablation. Table 2.1 reveals that existing microwave probes in the literature are predominantly employed for biomedical applications with input power levels up to 100 W.

In the proposed microwave applicator, with an input power level of 15 W, a temperature rise of 68.3 °C is observed on the surface of the tumorous tissue to be ablated. Notably, even at a much higher microwave input power level of 42 W, resulting in a temperature rise of approximately 60 °C on the tumorous tissue, the proposed microwave applicator achieves a similar effect at the same operation frequency. Consequently, the proposed reflector-type microwave probe requires less input power due to the capacity to direct a greater amount of microwave power locally to the ablation zone, facilitated by the dielectric cylindrical radiator located at the probe's end section.

2.2 3DPMWAP Design and Optimization in In Vitro

Nowadays, 3D printed electromagnetic components come into prominence in academia and industry. Because 3D printed components offer to be more compact, lighter, cheaper and environmentally friendly with more complex geometric structures to be conveniently fabricated, it arises as an alternative manufacturing technique in the industry and research communities [120–121]. Researchers, who fabricate micro-strip patch antenna with the silver or aerosol inkjet printer, have discovered to provide convenience in producing new antennas compared to classical antenna production methods. These methods gave a competitive result in terms of flexibility and biocompatibility with the antennas produced by classical methods at frequencies up to 6 GHz [122–123]. Moreover, wearable sensors fabricated with 3D printed components are integrated in biomedical field [124]. Thanks to the fact that the operating frequency of the microwave probe produced for this study is not very high and the possibility of use in biomedical studies, production was carried out using 3D materials.

In this thesis, it is aimed to ablate the breast cancer in cell culture medium by designing a cost effective, easy to fabricate, 3D printed dielectric-loaded monopole antenna based coaxial probe operating at 2.45 GHz in ISM band. Thus, 3DPMWAP is proposed for the ablation systems operating between 2.39 GHz and 2.54 GHz covering the whole frequency range of ISM band with the numerical computation and experimental measurement results. The inner surface of 3D printed probe is coated with a copper spray having enough thickness not to change the dimensions of 3D printed applicator while sustaining the required electrical conductivity. *In vitro* experimental study is conducted where the microwave probe is kept directly over the upper surface of cell culture grown in the petri dishes without direct contact. However, while 3D printed applicator is designed to be used for the ablation of cancerous tissue with the direct penetration into the human breast, the numerical study is accomplished with the direct contact of the probe to the cell culture by locating the applicator inside the cancerous cell line as in the case of *in vivo* and *ex vivo* studies described in the literature.

In order to design a 3D printed microwave ablation probe, the optimized geometric parameters are determined by the numerical computations performed in 3D commercial electromagnetic field solver, CST Microwave Studio. The fabrication of

proposed microwave probe is realized by Zortrax M300 3D Printer. Thanks to the 3D printer capable of producing up to cubic volume with each side 30 cm, there has been no limitation in the production of the described applicator even in single piece. Thus, to improve the ease of final installation, 3D printed microwave ablation probe is modelled by two equal parts split longitudinally as shown in Figure 2.8(c). Each split parts are connected to each other with the railing mechanism in a surface mating form. Surfaces are formed in a way to be connected to each other tightly. By this means, the surface mating parts can be joined together and separated from each other in case any kind of structural design modification is required to be done. In addition, to satisfying the proper mechanical connection between the probe sections, it is also crucial to provide the electrical connection affecting the electromagnetic radiation performance of the proposed microwave probe. Since the connecting cable carrying high microwave power is stretched or elongated excessively during microwave ablation application, it can also result into the demounting of the connector screwed in from the microwave probe. Thus, it is necessary to ensure the mechanical strength between the fabricated probe and the connector to be mounted on. In order to have the proper connection, Sub-Miniature Version A (SMA) female connector with the 17 mm wide flange is connected to Acrylonitrile Butadiene Styrene (ABS) based feeding section by using 1.5 metric screw (M1.5) in a tight manner. \varnothing_o is set to be 17 mm so that match the flange width for proper screwing. Since it is expected that the microwave probe parts manufactured from ABS material, whose weights are much lower than the metal materials, do not cause a significant mechanical stress on the screw connection. The preferred screwing method in this study is confirmed to be a safe method for the mechanical stability in proposed 3D printed applicator design process. What is more, to the mechanical arrangement of 3D printed microwave ablation probe, it is necessary to prefer the heat resistant materials like ABS since the designed probe is under the effect of the produced high power microwave energy. ABS material is also preferred in order to form a cheaper design by using as a mould for copper spray instead of forming the whole volume of conductive parts to be metal, which cost more than ABS material. The dielectric section of 3D printed MWA probe, shown in Figure 2.9(a), is selected as the teflon material that is heat resistant and easily accessible in the market.

Numerical calculations have been performed to obtain the optimized geometric parameters of 3D printed microwave ablation probe resulting into return loss smaller

than -10 dB at 2.45 GHz. l_f and \varnothing_f are set to 32.5 mm and 4.2 mm, respectively due to the dimensions of SMA connector. In order to define the optimal probe geometry, parametric sweep analysis is applied in dimensions l_d and l_i that involved in radiation and l_s involved in transmission. Remaining parameters are defined based on the optimizer tool of CST Microwave Studio. The optimized parameters of 3D printed microwave ablation probe are shown in Table 2.7.

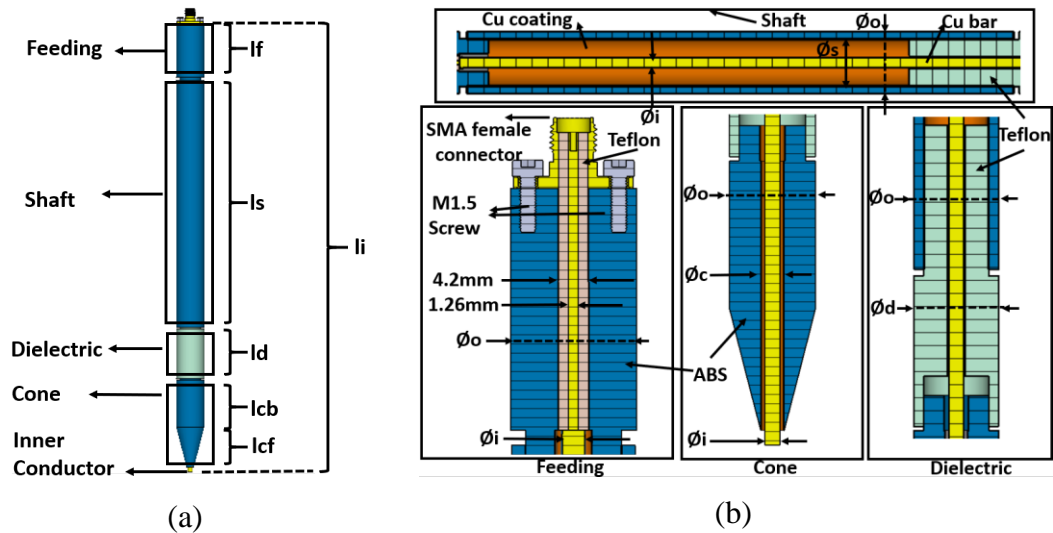


Figure 2.9: (a) Section and length information, (b) diameter and material information and (c) installation of fabricated 3D printed microwave ablation probe

Table 2.7: Proposed dimensions of the 3DPMWAP

Parameter	Length(mm)
Inner conductor diameter ($\text{\O}i$)	3
Inner conductor length (l_i)	220
Feeding length (l_f)	32.5
Feeding diameter ($\text{\O}f$)	4.2
Shaft length (l_s)	150
Shaft outer diameter ($\text{\O}o$)	17
Shaft inner diameter ($\text{\O}s$)	13
Dielectric length (l_d)	30
Dielectric diameter ($\text{\O}d$)	17
Back cone length (l_{cb})	29
Forward cone length (l_{cf})	24
Cone inner diameter ($\text{\O}c$)	4.5

The proposed structure of the microwave probe is primarily constructed using a circuit model based on coaxial waveguide and dielectric-loaded monopole antenna geometry. The theoretical models for this structure are illustrated in Figure 2.10. To facilitate the excitation of the dielectric-loaded monopole antenna, the feeding and shaft sections are represented as lumped element circuit models for the transmission line, connected in cascade. These sections serve the purpose of microwave power transmission.

Furthermore, the dielectric loading and cone sections, which contribute to impedance matching and electromagnetic radiation, are also expressed as part of the dielectric-loaded monopole antenna. The radiation of electromagnetic power in the surrounding air and its penetration through breast cancer mediums with distinct constitutive parameters are addressed by solving the Helmholtz Time Harmonic Wave Equation. This solution is carried out for the electric and magnetic field components in the near field region, considering the relevant boundary conditions. The complex nature of these formulations necessitates the use of numerical computation methods [125].

Additionally, the transmission of the TEM mode wave in the coaxial waveguide can be described using the lumped element circuit parameters, as outlined in Equation (2.7), Equation (2.8), Equation (2.9) and Equation (2.10) [113]. These equations provide a comprehensive understanding of the wave propagation characteristics within the coaxial waveguide.

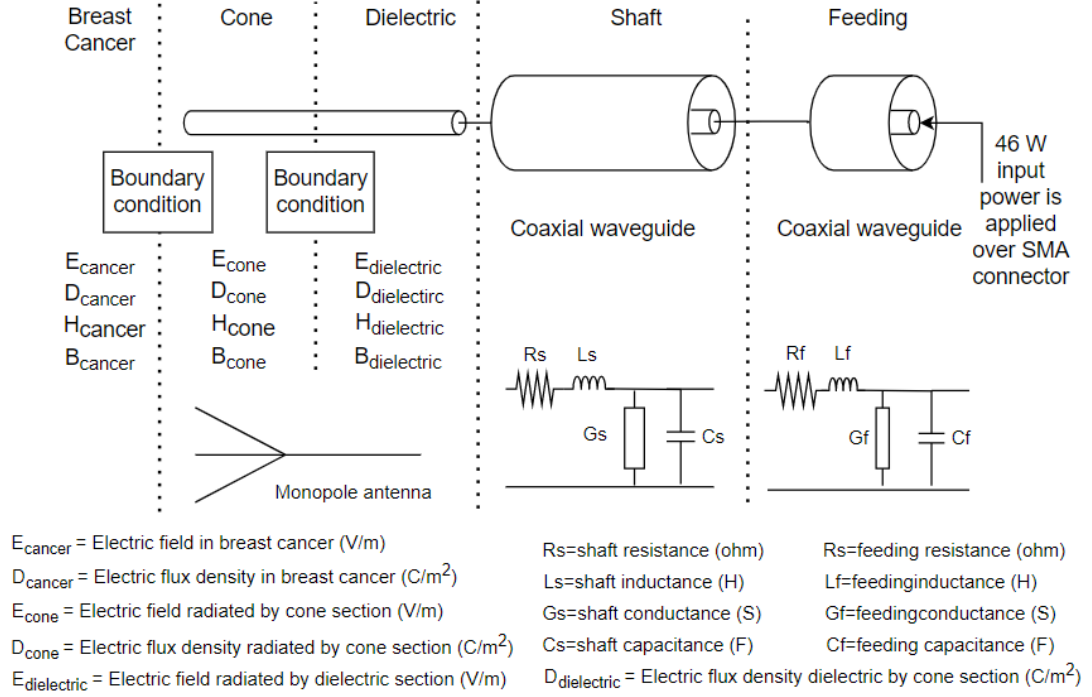


Figure 2.10: Proposed microwave applicator theoretical model.

$$L = \frac{\mu}{2\pi} \ln \frac{r_o}{r_i} \quad (2.7)$$

$$C = 2\pi\epsilon' \ln \frac{r_i}{r_o} \quad (2.8)$$

$$R = \frac{R_s}{2\pi} \left(\frac{1}{r_o} + \frac{1}{r_i} \right) \quad (2.9)$$

$$G = 2\pi\omega\epsilon'' \ln \frac{r_i}{r_o} \quad (2.10)$$

Where L and R are the per unit length series inductance and resistance, respectively while C and G are the per unit length shunt capacitance and conductance, respectively. Moreover, μ and ϵ are the permeability and permittivity of material between the inner conductor radius (r_i) and outer conductor radius (r_o) of each probe section in coaxial waveguide. ϵ' and ϵ'' are real and imaginary parts of complex dielectric constant at angular frequency ω (rad/s), R_s is the surface resistance of conductors inside the coaxial waveguide. The outer conductor is formed by coating commercially available silver-plated copper compound (RS 247-4251), whose electrical conductivity is included in the range 1.43–3.33 S/m and RF loss is equal to 75 dB/m.

For the numerical computation of proposed applicator, Finite Difference Time Domain (FDTD) based solver has been performed to determine the optimized geometric parameters of 3D printed probe by dividing in roughly 700 thousand mesh. The discretization of proposed applicator geometry and petri dishes contained MCF7 cells are performed by using centered finite difference (CFD) approximation technique, which yields derivatives of the scattering parameters over a frequency range of 2–3 GHz [126–127]. The most effective geometric parameter, impact on reflection coefficient S_{11} , is shaft length. The change of scattering parameters for different dielectric and inner conductor lengths creates only minor changes in S_{11} -parameters as indicated in Figure 2.11.

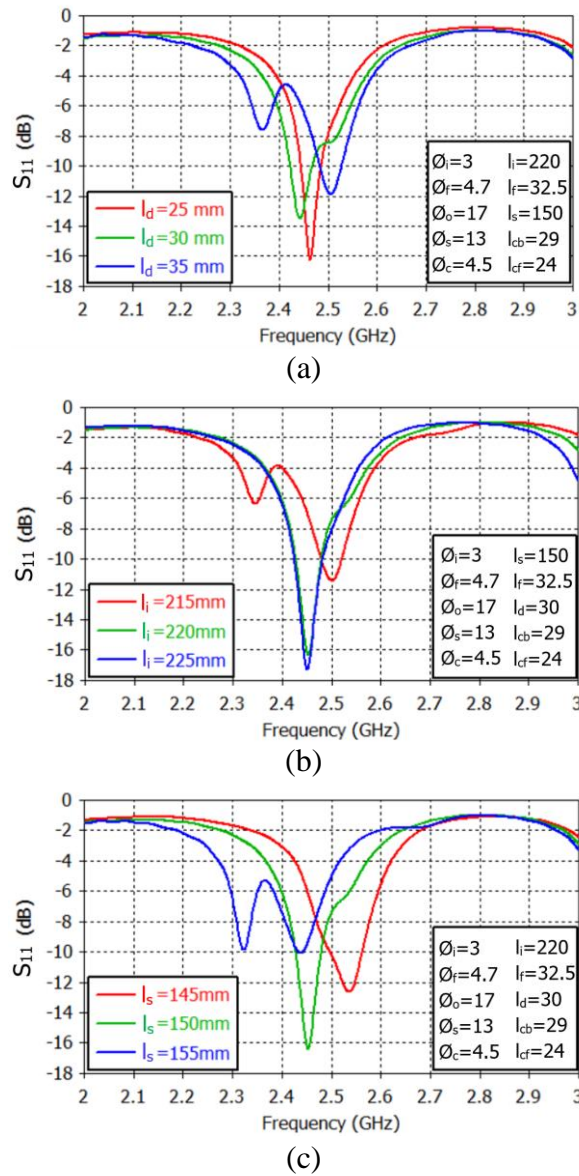


Figure 2.11: Simulated curves of reflection coefficient, S_{11} , of proposed microwave probe for different values of (a) l_d , (b) l_i and (c) l_s .

Numerical computations have been done in an attempt to obtain the minimum values of reflection coefficient of 3DPMWAP at the frequency of 2.45 GHz. Challenging task to design a MWA applicator is the requirement of S11 parameter of 3D printed microwave probe not to be affected by the cancerous cells during the surgical operations. Therefore, numerically calculated resonance frequency of 3DPMWAP with the tumor sample in petri dishes has to be 2.45 GHz even in the near field coupling to the tumor cells region.

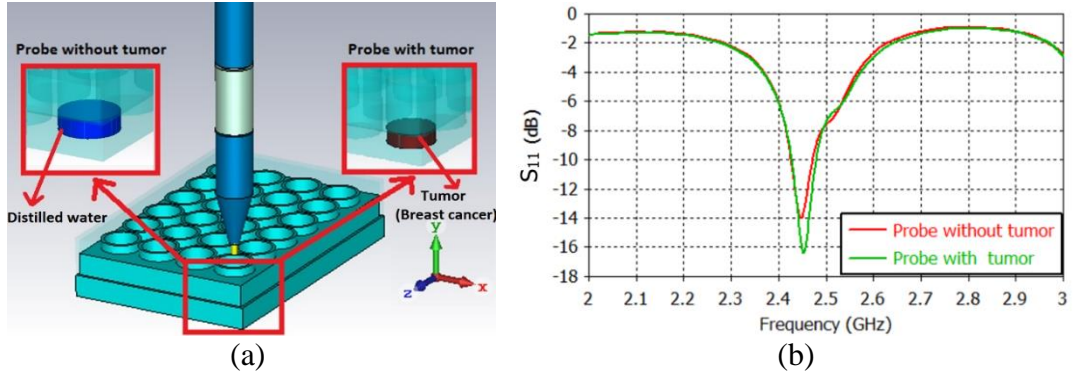
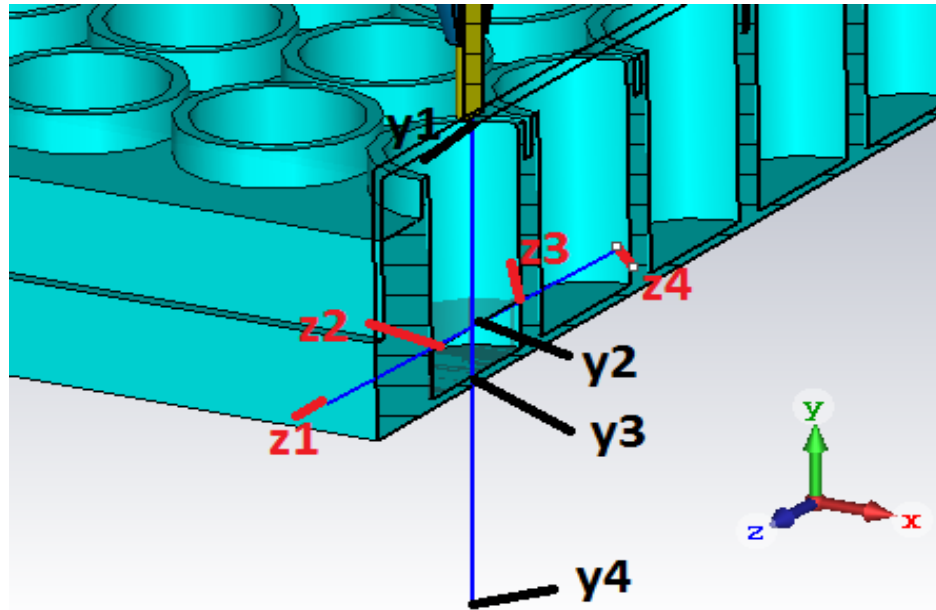


Figure 2.12: (a) Simulation model, and (b) reflection coefficient comparison of cases with/without tumor cells near the cone section of 3D printed MWA probe

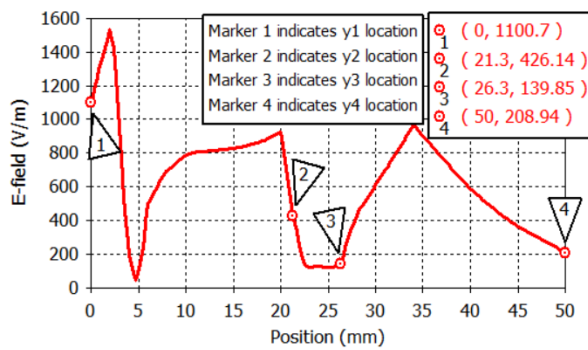
As indicated in Figure 2.12(b), that is the numerical return loss results for model presented in Figure 2.12(a), the existence or absence of tumor sample contained petri dishes placed near the cone section of 3DPMWAP causes only minor changes in S₁₁ parameter values. The reflection coefficient of the proposed applicator is in the acceptable range at 2.45 GHz with the numerically calculated bandwidth of 10 MHz to avoid the reflected power in both with and without tumor cases.

Next, the numerical computations have been performed specifying the EM radiation performances. Since the tumor cells are placed in the near field region of MWA probe, near field formulations have to be utilized as indicated in Equation (2.11) for the calculation of the EM radiation performances [128]. Therefore, the electric field distribution around the surface of the tumor sample under the ablation process with 46 W signal excitation at 2.45 GHz is indicated in Figure 2.13.

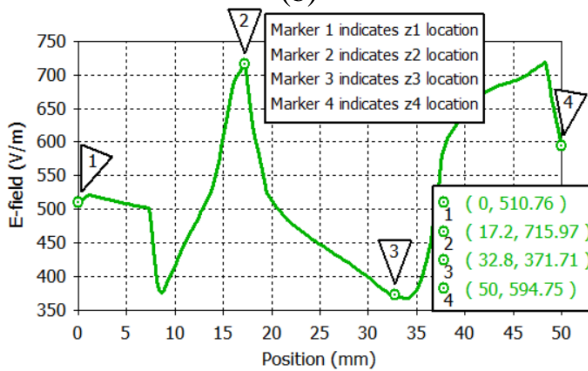
$$\nabla^2 \mathbf{E} = \omega^2 \left(\epsilon_r(T) - j \frac{\sigma(T)}{\omega} \right) \mathbf{E} \quad (2.11)$$



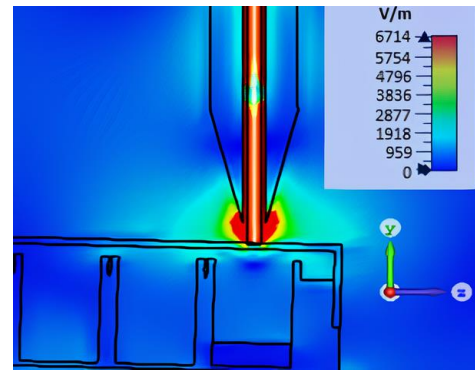
(a)



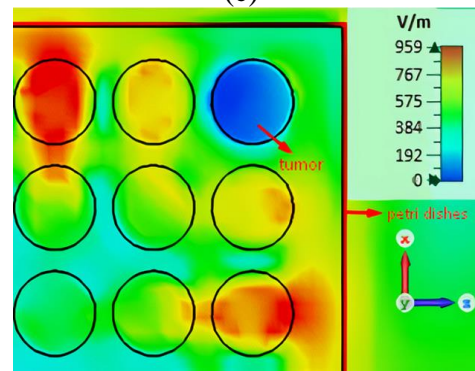
(b)



(d)



(c)



(e)

Figure 2.13: (a) Numerical computation model for the calculation of the electric field strength inside and on the surface of breast tumor cells. Electric field distributions are respectively along: (b) y-axis, and (d) z-axis. Electric field distributions on: (c) x plane, and (e) y plane.

In Equation (2.11), ϵ_r is the relative dielectric constant, σ (S/m) is the electrical conductivity and T ($^{\circ}\text{C}$) is the body temperature of cancerous cell under electromagnetic field exposure with vector of electric field strength shown as \mathbf{E} (V/m) and angular frequency ω (rad/s).

The electric field has been absorbed while penetrating into the tumor sample of mass 1.17 g as deduced in Figure 2.13(a). In Figure 2.13(b), the electric field strength around the cancerous cells decreases from 1535 V/m to 426 V/m as penetrating through the tumor sample along the horizontal and the vertical axis, respectively. In addition, to the investigation of electric field distribution, SAR pattern calculation of tumor is also shown in Figure 2.14 to decide the electric field absorbed by the tumor. The governing equation including SAR calculation and temperature changes inside tumor tissue due to the electromagnetic field exposure are given by Equation (2.12) and Equation (2.13) [129].

$$\text{SAR} = \frac{\sigma |\mathbf{E}|^2}{2\rho} \quad (2.12)$$

$$\rho c_p \frac{\partial T}{\partial t} = k_T \nabla^2 T + \rho \text{SAR} - Q_h \quad (2.13)$$

where SAR is the electromagnetic power absorbed by unit mass (W/kg), σ is the electrical conductivity (S/m), c_p (J/(kg·K)) heat capacity, k_T (W/(m·K)) thermal conductivity and ρ is the density (kg/m³) of breast cancer, and $|\mathbf{E}|$ is the magnitude of electric field intensity (V/m) inside the tumor tissue. Q_h represents the heat lost to blood perfusion or gained by tissue metabolic processes. However, it is neglected in this study because it is a small value compared to the high microwave power applied externally. The simulated electromagnetic radiation performances of 3DPMWAP are indicated in Table 2.8.

Table 2.8: Electromagnetic radiation performances of 3DPMWAP in electrical and thermal properties given breast cancer and distilled water [130-132]

	Breast Cancer	Distilled Water
ϵ_r	55+0.11T-0.003T ² , [132]	75.8+0.3T-0.01T ² , [132]
σ (S/m)	2.66+0.013T-0.0002T ² , [132]	1.88-0.004T+0.0002T ² , [132]
k_T (W/(m·K))	0.48, [131]	0.62, [130]
c_p (kJ/(kg·K))	3.9, [131]	4.18, [130]
ρ (kg/m ³)	1050, [131]	1000, [130]
S11 (dB)	-16.11	-14.02
$ \mathbf{E} $ (V/m)	157	129
SAR (W/kg)	12	8

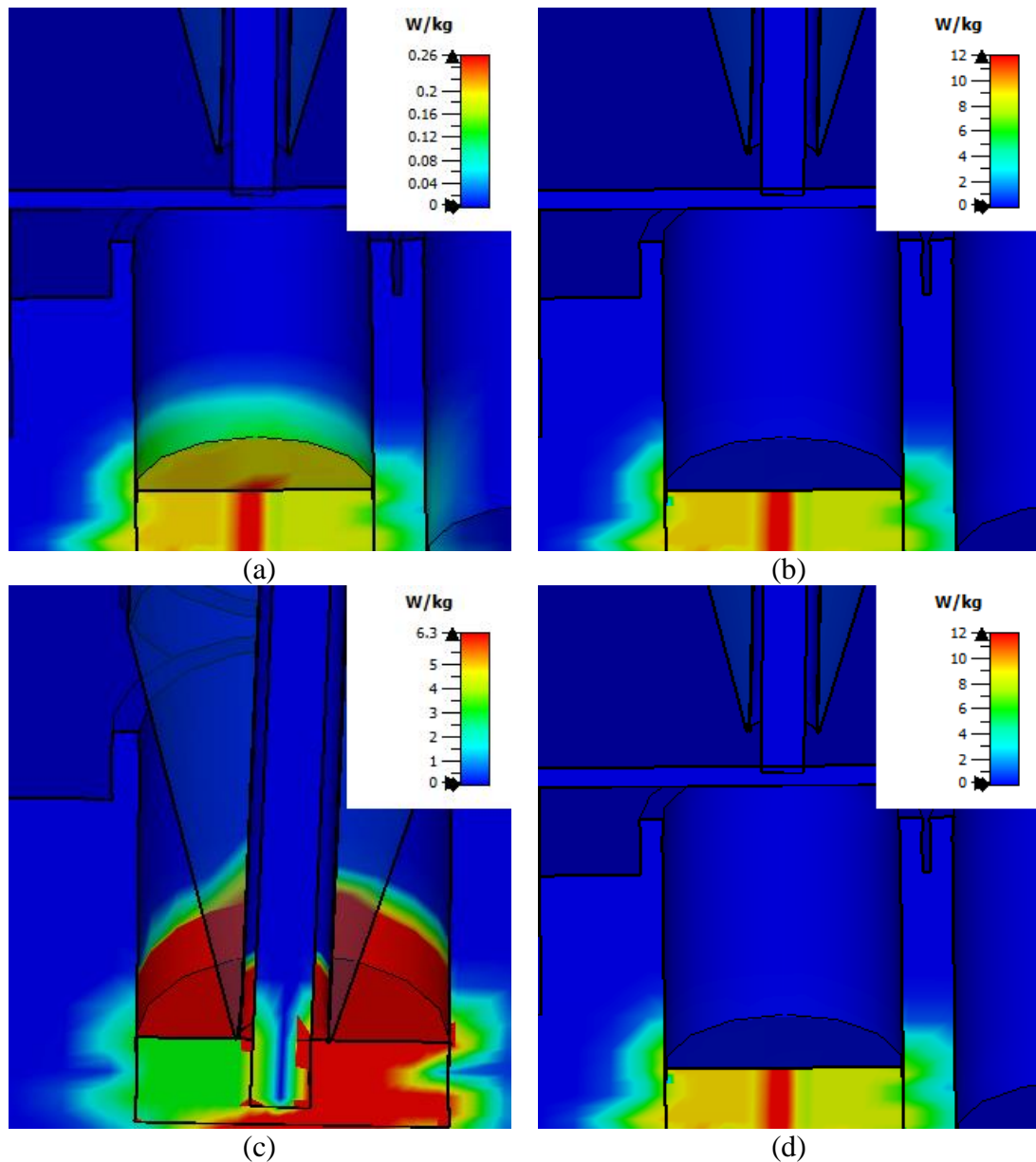


Figure 2.14: SAR value of tumor sample under (a) 1 W and (b) 46 W microwave input power of proposed probe placed on the petri dishes. SAR value of tumor sample under (a) 1 W and (b) 46 W microwave input power of proposed probe inserted in the petri dishes.

Although the SAR value of 12 W/kg is a small value for *ex vivo* microwave ablation applications, the SAR value can be enhanced due to the absorbed electric field when proposed 3DPMWAP is located closer to the cancerous cells. The enhancement in SAR value is attributed to the greater absorption of the electric field by the tumor cells. The numerical calculations demonstrate the variations in SAR value for different separation distances between the 3DPMWAP and breast tumor cells, as presented in Table 2.9.

Table 2.9: SAR values of 1.76 g breast cancer with changing distance between 3DPMWAP and tumorous cell

Distance between microwave applicator and breast tumor cell (mm)	SAR (W/kg) under 46 W input power excitation
21.3	12
16.3	16
11.3	21
6.3	28
1.3	102

The inversely proportional relationship between the probe-tumor distance and tissue SAR value can be understood due to the higher electric field in the tumor tissue closer to the MW probe having TM mode wave feature in the near field region. As it is expressed in Equation (2.12), the square of electric field intensity is directly proportional to the SAR value. As deduced from Table 2.9, so long as the separation distance between breast tumor cells and 3DPMWAP is reduced, the SAR value of the cancerous cells increases as theoretically expected.

For designing method, the characteristic impedance of microwave applicator feeding is purposed to be nearly 50Ω in order to avoid reflected power originated from the SMA connector and feeding part connection. Since the SMA female connector is a kind of coaxial waveguide, characteristic impedance is calculated from Equation (2.4), which is suitable for TEM mode wave propagation. In order to avoid the reflection between SMA connector and 3DPMWAP, the probe section must also be designed in the form of coaxial waveguide. In this regard, feeding outer diameter is arranged to be 4.2 mm when taking into consideration the inner conductor diameter of SMA connector to be approximately 1.25 mm with 4.2 mm teflon substrate. On the other hand, return loss is not affected from the shaft outer diameter. Nevertheless, ϕ_o is arranged to 17 mm due to screwing surface of SMA connector, which is 15 mm.

The verification is also done between the experimental and numerical computation results with the CST Thermal Transient Solver shown in Figure 2.15. The governing equation describing the temperature changes inside tumor tissue due to the electromagnetic field exposure is shown in Equation (2.14). This equation provides a mathematical representation of the thermal dynamics within the tumor tissue, allowing for a comprehensive understanding of the temperature variations induced by the electromagnetic field.

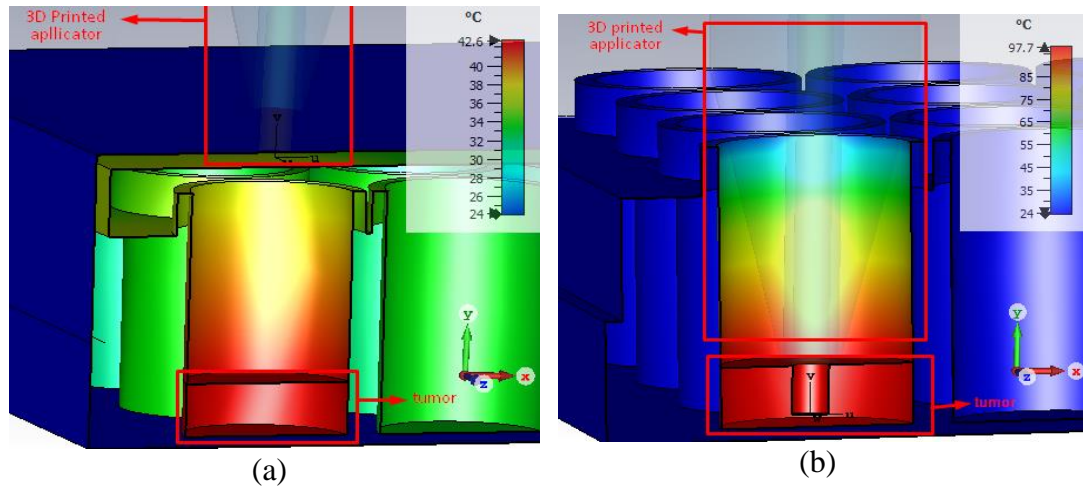


Figure 2.15: CST Thermal Transient Solver results of tumor after 20 min exposure emitted by 3DPMWAP (a) outside, and (b) inside the MCF7 cells culture.

As illustrated in Figure 2.15(a), the maximum temperature of tumor tissue is numerically computed as 42.6 °C, when the proposed microwave probe is located over the open petri dishes without direct contact to the cancerous tissue inside. Both the numerical and experimental temperature results of the *in vitro* applications covered in this study are in good agreement with each other. It is ensured that the 3DPMWAP has technical potential to provide the annihilation of tumorous cells successfully. Moreover, in Figure 2.15(b), the simulated temperature can increase to value of 97.7°C if the proposed microwave applicator is inserted in breast tumor tissue as in the *ex vivo* and the *in vivo* applications studied in literature. The effect of 3DPMWAP location inside malignant tissue under various penetration depths on operation frequency and reflection coefficient is investigated as well as the effect of probe location outside the tumorous tissue under different distances away from the MCF7 and shown in Figure 2.16.

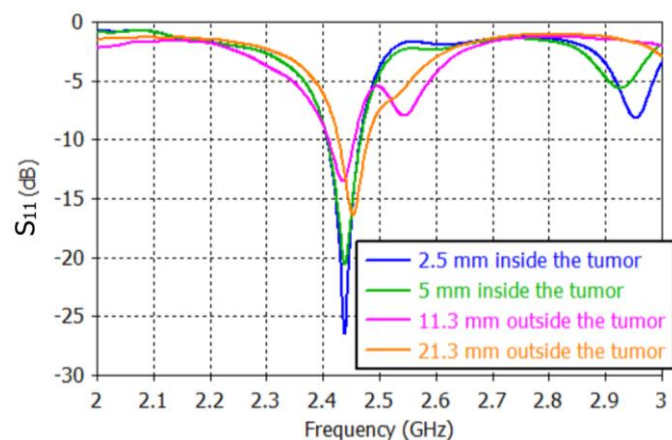


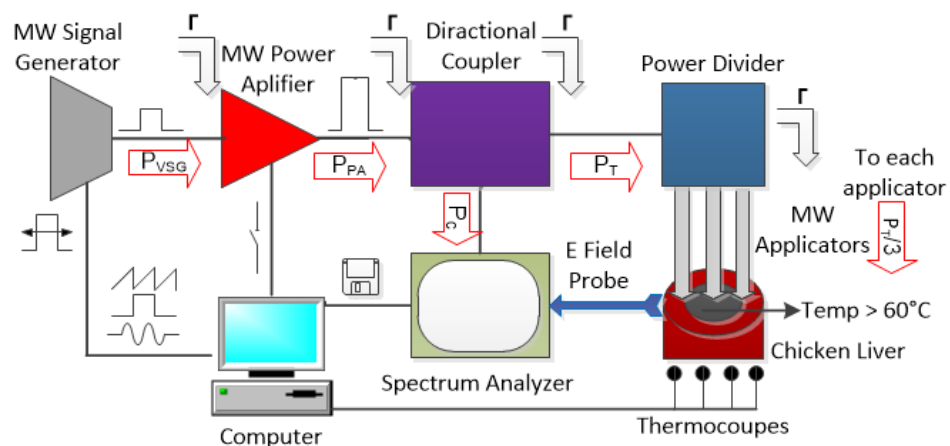
Figure 2.16: Numerically computed S11-distributions of proposed microwave probe inside / outside regions of the breast tumor tissue.

As shown in Figure 2.16, the operating frequency of the proposed applicator shifts only 20 MHz at maximum from the interior part to exterior region of tumor tissue, which indicates the proposed microwave probe is suitable for both in body and on body applications. Alternative microwave probe designs in the literature are listed in Table 2.1 to demonstrate the comparatively improved microwave performance of proposed 3D printed microwave ablation probe in compact size and light weight due to ABS based 3D printing methodology. As illustrated in Table 2.1, most of microwave probe designs in literature are experimentally studied in *ex vivo* applications, while the proposed 3DPMWAP is studied in *in vitro* applications. It must be noted that the biological sample under microwave power exposure is heated by both convectional heating and electromagnetic radiation in *ex vivo* applications. Contrary to *ex vivo* applications, heat transfer to biological sample is provided by only electromagnetic radiation during *in vitro* applications since the microwave applicator do not touch on biological sample to avoid cellular contamination. Since the main purpose of this thesis is to design more compact, lighter, cheaper and environmentally friendly microwave ablation applicator it is sufficient to provide as the ablation performance of microwave probe design in literature.

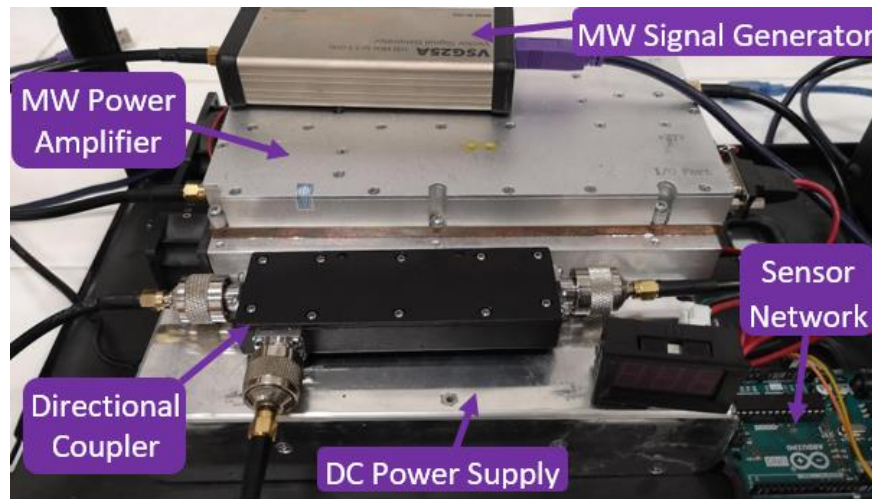
As shown in Table 2.1, due to having noncontact exposure of microwave power on the breast cancer cell cultures over the open petri dish, time interval more than 20 minutes is required for the annihilation of breast cancer cells under 46 W input power. In order to compete with the stated exposure times and temperature increments of the directly contacted microwave probes in the literature, the numerical study of the microwave probe, which is directly immersed into the cell culture is conducted to prove that high cancerous cell temperatures in short exposure time can be obtained. Accordingly, in comparison to SAR values described in literature, 0.26 W/kg provided by proposed microwave probe is satisfactory high value for microwave heating because the SAR value is dependent on electric component of electromagnetic field emitted by the microwave applicator. On the other hand, the physical structural size of the proposed microwave ablation probe can be conveniently reduced by the integration of high-power surface-mount devices (SMD) components to be inserted into the interior region of the coaxial feeding section. This flexible prototype manufacturing is to be successfully achieved due to the ease of fabrication of complex geometric structures by ABS based 3D printing technology.

2.3 MMWAP Design and Optimization in Ex Vivo

The microwave ablation system includes microwave components that all work at 2.45 GHz. Microwave components perform the function of high-power generation by gathering, monitoring, and analyzing data. The block diagram of the presented microwave ablation system is indicated in Figure 2.17(a), and the corresponding system components are in Figure 2.17(b).



a)



b)

Figure 2.17: (a) Microwave ablation system block diagram (b) system component

A controllable microwave signal generator generates power at 2.45 GHz with amplitude modulation to the microwave power amplifier to reach the high-power level. The user can also control the microwave power amplifier via a computer interface and display hardware parameters such as core temperature, VSWR, and output power. A wideband directional coupler gathers forward and reverse power data at the input port

of the power divider connected to the coaxial slot antenna array. Three identical coaxial slot antennas driven by a low-loss power divider create a large ablation zone at chicken liver with a high homogeneity rate. The Anritsu spectrum analyzer displays the instantaneous electric field in the near field region of chicken liver and information gathered from the directional coupler. Finally, for temperature analysis, the high-resolution temperature sensor placed inside the chicken liver measures the time dependence of temperature precisely.

In this section, the geometric structure of the microwave multiapplicator (MMWAP) is proposed. The ISM band MMWAP contains three identical slot antennas by utilizing a coaxial transmission line with a cancelling slot on the ground surface itself. Each identical slot antenna is conceived to radiate an electromagnetic wave in the lossy chicken liver medium, as indicated in Figure 2.18.

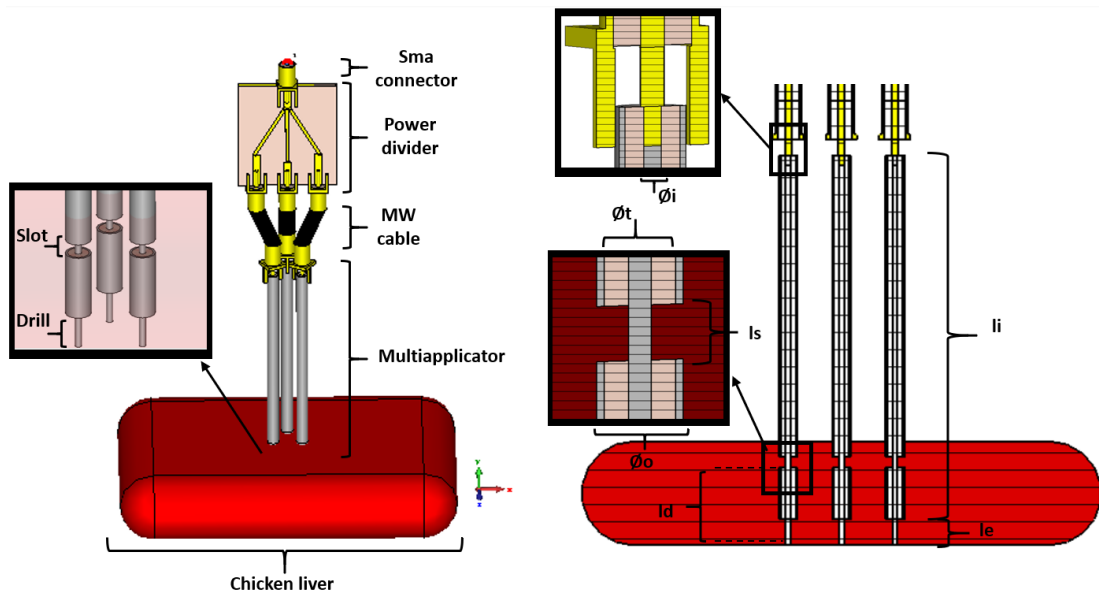


Figure 2.18: MMWAP structure inside the chicken liver model

The input port of each slot antenna is made of 180C female sma connector. It is modelled in a way that the inner conductor diameter of this part is 1.25 mm, the outer diameter of PTFE is 4.2 mm, and the outer conductor diameter is 4.5 mm. The 1:3 microstrip power divider is also designed to be compatible with each slot antenna by modelling the input and output ports 180C SMA connector and commercially available FR-4 substrate. The optimized MMWAP dimensions and material information microwave in ablation system components are shown in Table 2.10 and Table 2.11, respectively.

Table 2.10: Optimized dimensions of MMWAP

Parameter	Length(mm)
Inner conductor diameter (Ø_i)	0.94
Inner conductor length (l_i)	70
Length of slot space (l_s)	2
Outer diameter of each antenna (Ø_o)	3.58
Penetration depth inside liver (l_d)	10
Drilling edge length (l_e)	5
PTFE diameter in applicator (Ø_t)	2.95

The dimensions of the antenna given in Table 2.10 are critical to its performance, and the parameters that were selected in this design were chosen to optimize the ablation of liver tissue. The inner conductor diameter and PTFE diameter are selected to set the characteristic impedance of the transmission line to 50Ω , as per Equation 2.2. On the other hand the length of the inner conductor is selected to be equal to the wavelength of the signal generated by the antenna. In this design, l_i is selected to be 70 mm. This is because the wavelength of the teflon filled transmission line inside the MMWAP is 84 mm, which is close to the selected value. Moreover, the penetration depth inside the liver (l_d) is selected to be 10 mm, which is sufficient to ablate liver tissue. However, l_d could be arranged to alter the surgical orientation of ablation application. The drilling edge length (l_e) is selected to be 5 mm, which ensures that the signal generated by the antenna penetrates the liver tissue smoothly.

The values in Table 2.11 can be used to calculate the penetration depth of the signal into the liver tissue, as well as the amount of heat that is generated by the signal. These properties affect the way that the signal propagates through the tissue and how it is absorbed by the tissue.

Table 2.11: Material information of MWA components at 2.45 GHz. [133–136]

	Liver	PTFE	Copper	FR-4
ϵ_r	48.9	2.1	1	4.9
σ (S/m)	1.8	2.7×10^{-5}	5.96×10^7	0.04
k (W/(m \cdot °C))	0.57	0.2	401	0.03
c (kJ/(kg \cdot °C))	3.63	1	0.39	1.37
ρ (kg/m 3)	1050	2200	8930	1850
Dielectric Constant: ϵ_r ,			Electrical Conductivity: σ	
Thermal Conductivity: k ,	Specific Heat: c ,		Density: ρ	

2.3.1 Modeling Structure

In this section, 3D-aided computer simulations have been performed in CST Microwave Studio with a FDTD method by dividing 1223000 mesh cells. Firstly, optimized parameters given in Table 2.10 are determined for a single coaxial slot antenna in the light of S11 simulations. After the optimization to design a single applicator, three coaxial slot antennas with the same optimized parameters that constitute the MMWAP are numerically studied as in a single slot antenna. Numerical compilation results of single applicator and multiplier are compared in Subsections 2.3.1, 2.3.2, and 2.3.3.

2.3.2 Numerical Return Loss Computation

In order to design a 2.45 GHz MMWAP, it is necessary to minimize the return loss value by optimizing the antenna parameters. Since the MMWAP elements, slot antennas, consist of coaxial transmission lines, the characteristic impedances are calculated in Equation (2.14) [137] and corresponding return loss values are in Equation (2.15) [138] and Equation (2.16) [113] as follows.

$$Z_0 = \frac{\ln \frac{\varnothing_o}{\varnothing_i}}{2\pi} \sqrt{\frac{\mu}{\varepsilon}} \quad (2.14)$$

$$\Gamma = \frac{Z_L - Z_0}{Z_L + Z_0} \quad (2.15)$$

$$RL = -20\log|\Gamma|dB = -10\log \frac{P_{out}}{P_{in}} dB \quad (2.16)$$

Where Γ is the reflection coefficient and RL is the return loss of a single slot antenna, P_{out} is the power accepted by slot antenna and P_{in} is the input port of slot antenna Z_0 and Z_L are the characteristic impedances of transmission line and radiating impedances of slot section of each coaxial slot antennas respectively, μ and ε are the permeability and permittivity of chicken liver, respectively. The return loss value of each slot antenna and 1:3 power divider in the presence of MMWAP connection are shown in Figure 2.19.

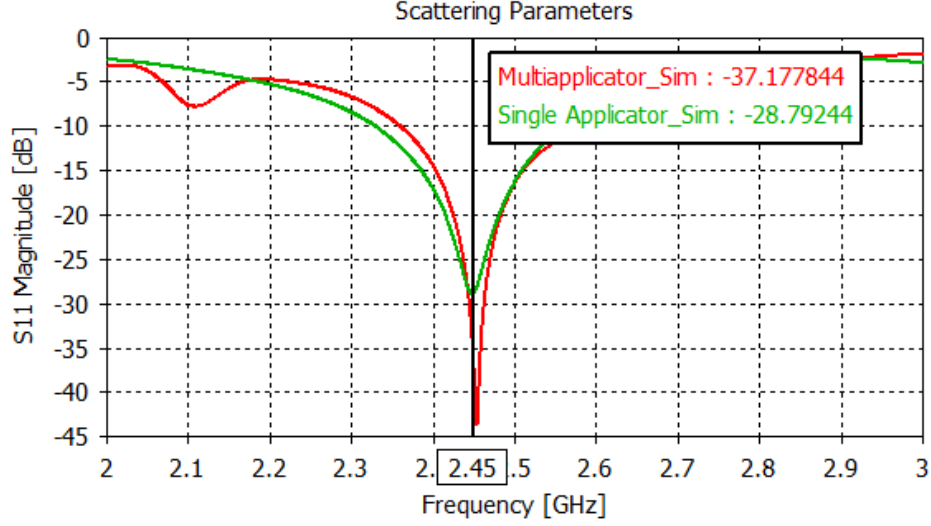


Figure 2.19: The return loss values of single coaxial slot antenna and 1:3 power divider in the presence of MMWAP connection inside the chicken liver model

As shown in Figure 2.19, a coaxial-based slot antenna can operate in a chicken liver with 99.86% power transfer, and 99.98% of the input power of the power divider transfers to the MMWAP at 2.45 GHz. Both applicator designs operate in the ISM band with low return loss and relatively high bandwidth, approximately 200 MHz.

2.3.3 Scattering Parameters Radiation Mechanism in Near Field Region

In MWA applicator design, the radiation mechanism is also significant as scattering parameter calculations. Since the proposed microwave applicators directly interact with ex vivo liver samples, temperature increases due to electromagnetic radiation in the near field region. Therefore, near field equations indicated in Equations (2.17.a), (2.17.b), (2.17.c) and (2.17.d) have to be used to express the radiation mechanism inside the biological tissue in spherical coordinate system [125].

$$E_r = \frac{I_0 \sin^2\left(\frac{\beta l_i}{2}\right) \cos\theta}{2\pi r \omega \epsilon} \left[j \left(\frac{1}{\beta r} + \frac{1}{\beta} \right) - 1 \right] e^{-j\beta r} \quad (2.17.a)$$

$$E_\theta = \frac{I_0 \sin^2\left(\frac{\beta l_i}{2}\right) \sin\theta}{2\pi r \omega \epsilon} \left[j \left(\frac{1}{\beta r} + \frac{2}{\beta r^2} - k \right) - \left(1 + \frac{2}{r} \right) \right] e^{-j\beta r} \quad (2.17.b)$$

$$H_{\Phi} = \frac{-I_0 \sin^2\left(\frac{\beta l_i}{2}\right) \sin\theta}{2\pi r} \left[\left(\frac{1}{\beta r} + \frac{1}{\beta} \right) + j \right] e^{-j\beta r} \quad (2.17.c)$$

$$H_r = H_{\theta} = E_{\Phi} = 0 \quad (2.17.d)$$

Where I_0 is the magnitude of electrical current of coaxial slot antenna, l_i is the antenna length, r is the distance from antenna slot to the observation point and β is the propagation constant. After generation of electric field by current source I_0 , the electric field radiation in lossy biological medium is expressed through Helmholtz harmonic wave equation as indicated in Equation (2.18) [139].

$$\nabla \times \mu_r^{-1} (\nabla \times E) - k_0^2 \left(\epsilon_r - \frac{j\sigma}{\omega \epsilon_r} \right) = 0 \quad (2.18)$$

Where ϵ_r is the relative dielectric constant of chicken liver, ϵ_0 is the relative dielectric constant of free space, σ is the relative dielectric constant of chicken liver (S/m), E is the Electric field intensity (V/m), μ_r is the relative permeability of chicken liver, k_0 is the wave number. The solution of the Helmholtz wave equation via CST Microwave Studio is given in Figure 2.20.

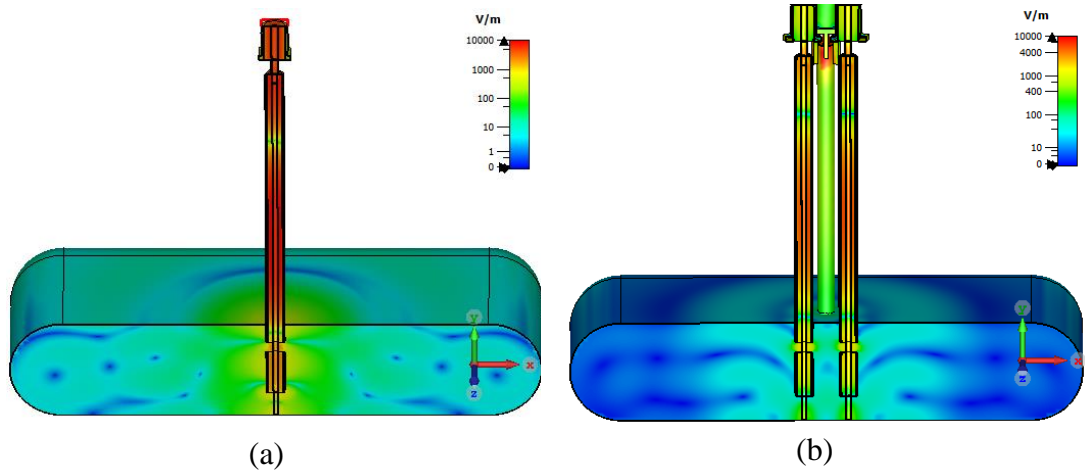


Figure 2.20: Electric field distributions in chicken liver under 0.5 W gaussian sine input power emitted by (a) coaxial slot antenna (b) MMWAP

Electrical field simulation has been performed under 0.5 W input power in gaussian sine form. The maximum E field magnitude in chicken liver emitted by a MMWAP is 419 V/m, while the single applicator emits 512 V/m. Although the maximum Electric field radiation is reduced in MMWAP, nonblue-tinged colour areas in a target tissue,

in which the Electric field magnitude is dramatically increased compared to nearby points, have been improved.

2.3.4 SAR Calculation in Biological Tissue

This section of the study aims to investigate the phenomenon of biological power absorption resulting from the emission of electromagnetic fields using CST Microwave Studio. The term SAR is valid to quantize the power absorption in biological tissues. The SAR, power absorption in unit mass, is mathematically defined in Equation (2.19) [140]

$$\text{SAR} = \frac{\sigma|E|^2}{2\rho} \quad (2.19)$$

Where SAR specific absorption rate (W/kg), σ is the electrical conductivity and ρ is the density (kg/m^3) of biological tissue under electromagnetic field exposure, E is the electric field intensity (V/m) radiated by microwave applicator. It is obviously interpreted that the SAR in any biological tissue is directly proportional to exposed Electric field intensity and electrical conductivity of biological tissue. The numerical SAR computations in chicken liver sample are indicated in Figure 2.21.

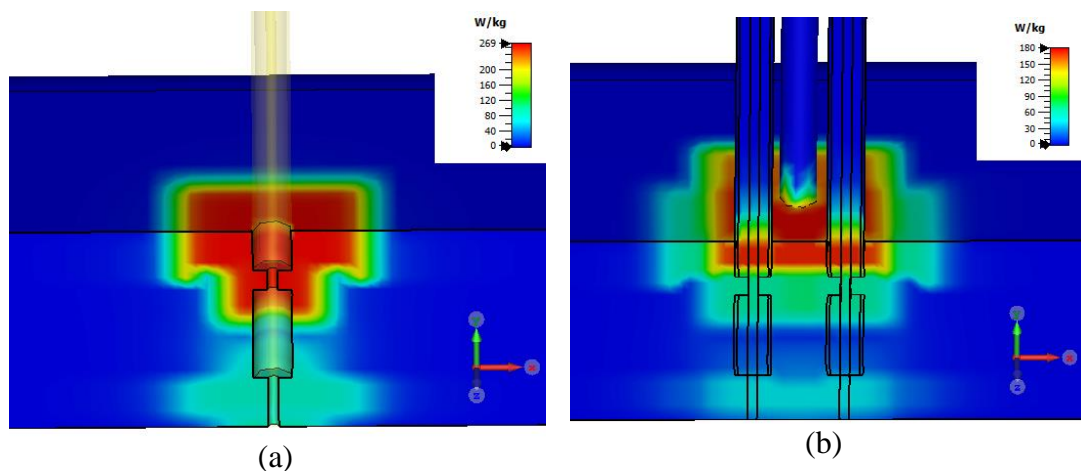


Figure 2.21: Numerical SAR distributions in 125 g chicken liver model with (a) coaxial slot antenna (b) MMWAP usage

In Figure 2.21 the numerical SAR distribution calculation in 125 g chicken live due to an electric field generated by a single coaxial slot antenna under 0.5 W input power is shown in Figure 2.21(a), while the MMWAP under 0.5 W input power is shown in

Figure 2.21(b). Numerical SAR calculations show that the maximum SAR value is reduced from 269 W/kg to 180 W/kg when the microwave slot antenna is replaced with a MMWAP. However, a more extensive hypothetical ablation area is achieved in MMWAP usage. If nonblue-tinged colors define as the hypothetical ablation area in order to be capable of making a comparison before the actual ablation zone measurement.

The numerical computations of the slot applicator and MMWAP included S11, E field and SAR values in 125 g chicken liver, hypothetical ablation area and ablation efficiency, which is calculated by dividing the power absorbed by the chicken liver by the input power, are gathered up in Table 2.12.

Table 2.12: Applicator performances table on 125 g chicken liver

	Slot Antenna			MMWAP		
	Max	Min	Avg	Max	Min	Avg
Input Power	0.5 W Gaussian			0.5 W Gaussian		
S11	−28.79 dB			−37.18 dB		
Ablation Region	4.2 cm ³			7.2 cm ³		
Absorbed Power	433 mW			348 mW		
Efficiency	86.6%			69.4%		
E Field (V/m)	512	20	58.1	419	13.5	52.2
SAR(W/kg)	269	0.04	3.45	180	0.02	2.78

According to Table 2.12, numerically calculated maximum, average and minimum Electric field and SAR values of chicken liver created by single slot antenna are bigger than MMWAP created under 0.5 W power excitation in gaussian sine form. However, the hypothetical ablation region that a single applicator create is nearly half of the region that a MMWAP creates.

Chapter 3

Non-Foster Circuit Implementation for Active Matching in MWA System

The synthesis of linear networks involves achieving specific properties at network terminals using idealized network elements. Passive networks utilize positive inductors, capacitors, resistors, and ideal transformers. The inclusion of active and non-reciprocal elements, such as negative resistors, capacitors, inductors, and gyrators, expands the range of synthesizable properties and engineering applications. However, not all of these basic network elements are separate entities in network theory. By having access to a restricted class of elements, other elements can be synthesized. For instance, by adding negative resistors to the usual set of lumped passive elements, networks with any linear relation between n -port voltages and currents prescribed in terms of real, rational functions of a complex-frequency variable can be synthesized, including negative capacitors and inductors. The synthesis of negative capacitors and inductors, as non-foster reactive elements, is particularly significant as they enable interesting engineering applications beyond lumped networks, including distributed networks and electromagnetic structures like antennas. This thesis focuses on enhancing the properties of electromagnetic structures by augmenting them with active lumped elements. Traditional implementation techniques and applications of non-Foster reactive elements are reviewed, and the challenging stability issues associated with these methods are highlighted. To overcome these stability issues, an alternative approach for implementing reactive non-foster elements is sought in this dissertation. Research is motivated by the desire to overcome performance limitations and investigate methods that outweigh these limitations. Overcoming Foster's reactance theorem provides a means to surmount the limitations of electronic support measures. The reactance theorem, presented almost a century ago, states that the variation of

lossless reactance with frequency must have a positive slope. This theorem applies to any lossless passive matching network. The objective of this research is to explore methods of achieving broadband small antennas for use in mobile devices or mobile cognitive radio (CR) nodes. Since these devices operate over a wide frequency range and CR nodes are frequency nomadic without the benefit of frequency planning, the matching networks need to operate over a wide frequency range with high frequency cut-off points while maintaining linearity. Linearity is crucial for CR nodes to operate adjacent to other signals without causing harmful interference and to be immune to other signals, making the linearity of matching networks important.

3.1 Theoretical Background of Non-Foster Reactance

The initial chapters of this study provided separate discussions on the properties of non-foster reactive elements and their relation to reactive networks. Building on this background, the current chapter establishes a significant connection between non-foster reactive elements and loss-compensated networks. It is demonstrated that any network configuration containing non-foster reactive elements operates as a reactive network. Additionally, the study shows that loss-compensated networks exhibit reactive behavior with non-foster characteristics. These findings highlight the intimate relationship between these properties, suggesting that reactive networks can be utilized to implement non-foster reactive elements such as negative capacitors and inductors. This work introduces a novel perspective for realizing non-Foster reactive elements, leading to well-behaved and predictable designs that offer improved stability and operation compared to traditional approaches. The proposed design technique, based on wave propagation theory and dispersion engineering, enables the synthesis of non-foster behavior using reactive networks, which can be entirely passive and stable. Furthermore, the study proposes passive non-foster elements with limited quality factors, where the minimum quality factor and the maximum achievable bandwidth are inversely related. These design principles allow for the realization of standalone non-foster reactive elements within a specific bandwidth. Experimental demonstrations of such non-Foster reactive elements and networks validate their stability and feasibility. The explanation of non-foster circuit in terms of impedance is indicated in Figure 3.1.

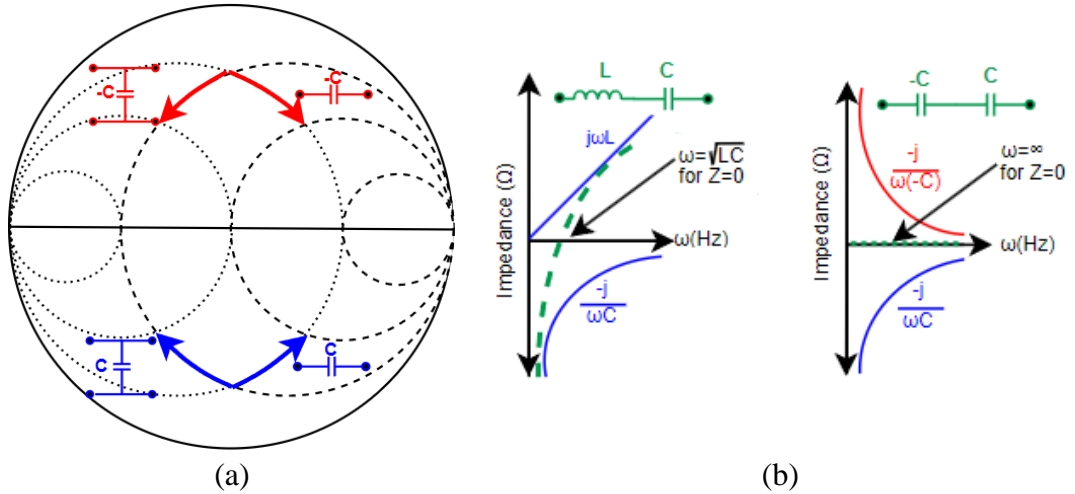


Figure 3.1: Negative capacitance principle from (a) S_{11} and (b) impedance

The impedance and admittance lines are depicted in Figure 3.1(a) using the Smith chart. It is well-known that operations involving series capacitor connections are performed on admittance lines, whereas parallel connections involve impedance lines. When a conventional capacitor is connected in series or parallel within a circuit, such as indicated by the blue arrow within the negative impedance region, the impedance magnitude decreases as the frequency increases, but it never reaches zero. Conversely, the negative capacitance, represented by the red arrow, is observed as a symmetrical curve on the S_{11} graph aligned with the impedance line on the Smith chart. In negative capacitance, the impedance magnitude decreases with frequency but does not reach zero, instead staying within the positive reactance range.

Examining the reactance graphs in Figure 3.1(b) from an impedance perspective, it becomes evident that neutralizing reactance using conventional coil and capacitor configurations is only achievable at the $\omega\sqrt{LC}$ frequency. However, by employing negative capacitance and the reactance elimination method, the frequency dependency is eliminated, theoretically enabling reactance elimination at every frequency. It should be noted that in practical implementations, reactance neutralization occurs within band gaps resulting from the parasitic effects of circuit elements.

To estimate negative impedance in a two-port non-foster circuit (NFC), Y-parameters are used. These terminals are series-connected with the network to incorporate non-foster behavior. In Figure 3.2, the floating NFC exhibits negative impedance Z_{NFC} , ideally equal to $-Z_L$ as discussed earlier. Applying network circuit theory, indicated in Equation (3.1) and Equation (3.2), yields the following analysis [141].

$$I_1 = -I_2 \quad (3.1)$$

$$V_1 - V_2 = I_1 Z_{\text{NFC}} \quad (3.2)$$

The simultaneous formulation of these equations as a Z-parameter model is not feasible due to the lack of a direct input-output voltage relationship. Consequently, the two-port Y-parameters matrix is provided in Equation (3.3).

$$\begin{bmatrix} I_1 \\ I_2 \end{bmatrix} = \begin{bmatrix} 1 & -1 \\ \frac{1}{Z_{\text{NFC}}} & \frac{1}{Z_{\text{NFC}}} \end{bmatrix} \begin{bmatrix} V_1 \\ V_2 \end{bmatrix} \quad (3.3)$$

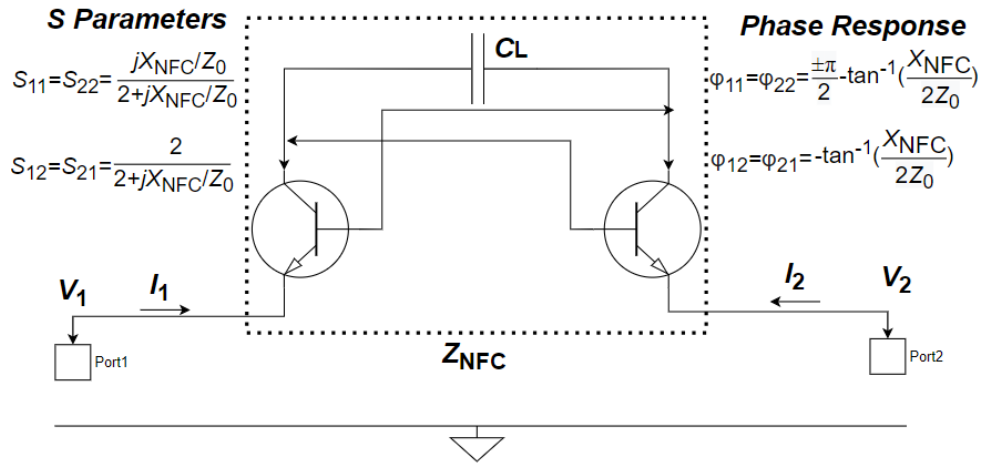


Figure 3.2: Linville based NFC equivalent model [141].

Due to the inherent limitations in representing the Z-parameter matrix for a two-port floating NFC the Y_{21} parameter becomes essential for estimating the overall impedance across the terminals. The expression for this estimation is provided in Equation (3.4).

$$Z_{\text{NFC}} = \frac{-1}{Y_{21}} \quad (3.4)$$

The analysis unequivocally demonstrates that employing Z_{21} for estimating Z_{NFC} in a floating two-port NFC series element (balanced) is an inappropriate approach, and instead, Y-parameters should be utilized. In the case of a grounded one-port NFC shunt element (unbalanced), both Z-parameters and Y-parameters, or a combination of both, are equally suitable. This analysis has played a pivotal role in extracting the negative capacitance phenomenon, which is further explored in subsequent chapters, encompassing the advancement of two-port NFC [141].

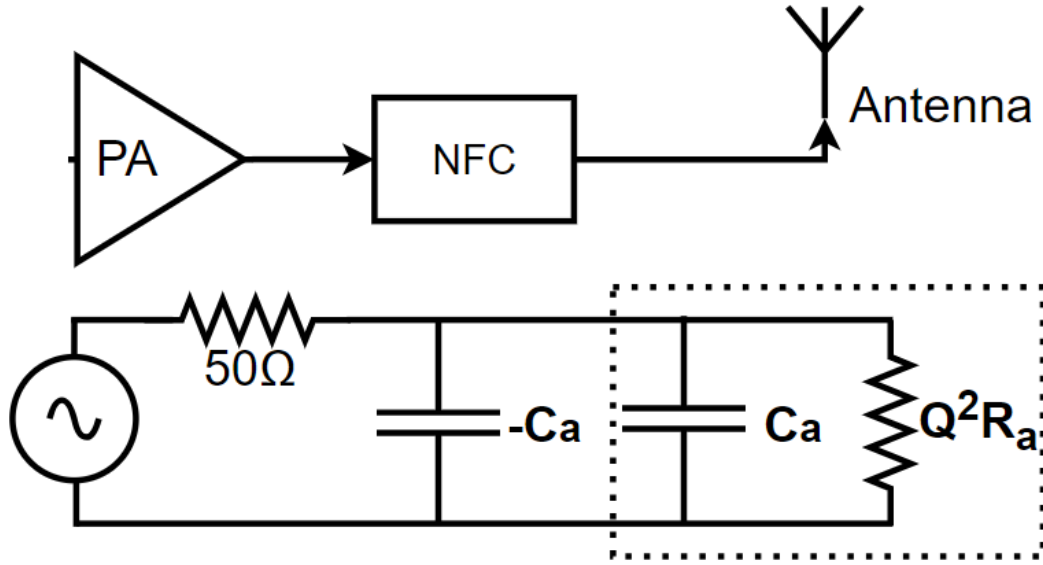


Figure 3.3: MWA system simplified model including NFC [142].

In Figure 3.3, efforts have been made to enhance the bandwidth performance of high-Q small antennas, with non-foster antennas being one solution. Subsequent works explored NFC matching for high-Q passive antennas using NFC elements. Practical limitations on small passive antennas led to the investigation of alternative approaches, such as broadband matching directly to the input impedance of a power amplifier (PA), which demonstrated advantages over traditional $50\ \Omega$ matching. The use of non-foster elements resulted in significant improvements in antenna bandwidth. NFC matching techniques employed bipolar junction transistors, CMOS circuitry, and resonant tunnel diode-based circuits. The concept of tunable matching networks was also explored. Antennas operating at low frequencies face challenges due to their size limitations, and passive matching may be difficult. The early works of A.D. Harris et al. observed gain enhancement using negative capacitors on whip antennas. Harris also discussed the non-linear effects of NFC impedance matched antennas. Conjugate reactive load elements and complex conjugate matching techniques were proposed to improve bandwidth in inductive dipole antennas. Op-amp-based NFC and negative capacitors were used for matching, but their implementation posed design and practical challenges. Sussman-Fort introduced floating series NFC impedance matching, achieving improved gain and signal-to-noise ratio (SNR) from 20 MHz to 120 MHz. Recent studies demonstrated the use of grounded shunt NFC to match capacitive antennas [142].

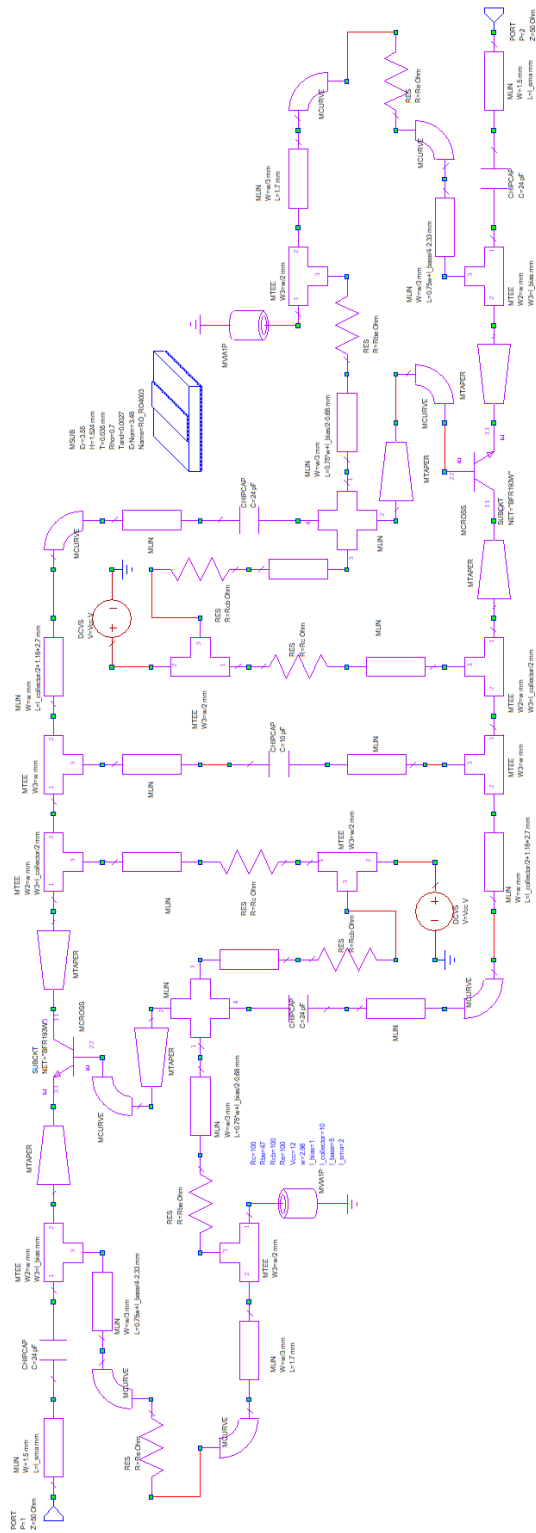
3.2 Simulation Results and Practical Application of NFC

The generation of both the schematic and layout of NFC plays a crucial role in achieving accurate impedance characteristics and ensuring efficient circuit performance. In this study, the schematic and layout were generated using AWR Microwave Office, a comprehensive design tool for microwave circuits. The primary objective was to design the NFC layout in such a way that the impedance closely resembled the target impedance profile illustrated in Figure 3.1. The generated layout aims to closely match the desired impedance characteristics of the NFC, as depicted in Figure 3.1. By leveraging the capabilities of AWR MWO the schematic and layout generation process facilitates the design and implementation of NFC circuit with precise impedance characteristics. Table 4.3 shows the optimized parameters of NFC whose schematic, layout and fabricated form demonstrated in Figure 3.4

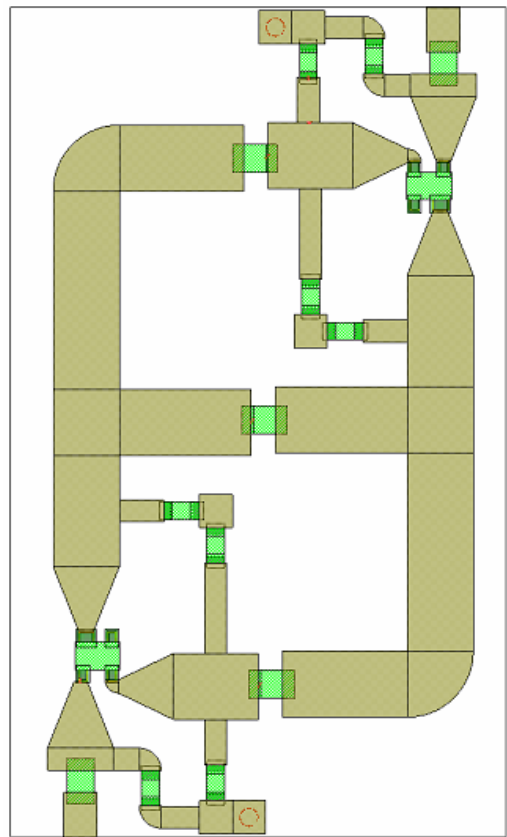
Table 3.1: Optimized parameters of Non Foster NIC

Parameter	Value
w (transmission line width)	2.96 mm
l_sma (length of sma connector mounting pad)	2 mm
l_bias (distance between bias capacitors and emitter)	1 mm
l_collector (collector line length)	10 mm
l_base (base line length)	5 mm
Rc (collector resistor)	100 Ω
Rbe (resistor between base and emitter)	47 Ω
Rcb (resistor between collector and base)	100 Ω
Re (emitter resistor)	100 Ω
Effective dielectric constant of Rogers RO 4003	3.55
Tangent Delta of Rogers RO 4003	0.0027
Substrate thickness of Rogers RO 4003	1.524 mm
Copper thickness of Rogers RO 4003	0.035 mm
Feeding Voltage (VCC)	(8-12) V

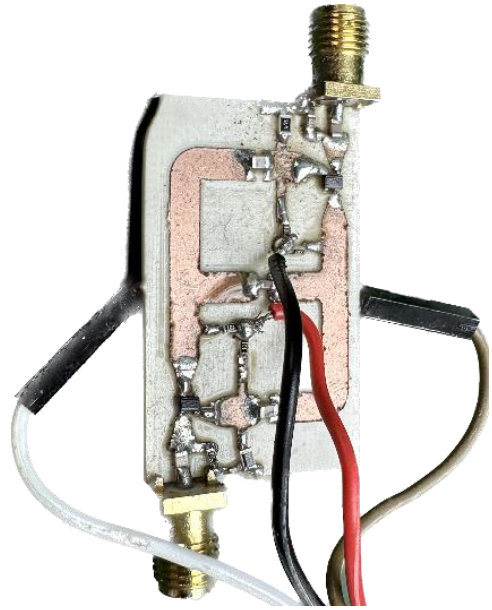
Within Table 3.1, the transmission line width, denoted as 'w,' is selected to be 2.96 mm, ensuring the establishment of a 50 Ω characteristic impedance at 2.45 GHz. Conversely, the width of the DC feeding lines is set to one-third of the transmission line width, enabling the reflection of microwave signals back to the 2.96 mm transmission line. This technique effectively prevents additional loss caused by the DC line, thereby optimizing the circuit's overall performance



(a)



(b)



(c)

Figure 3.4: (a) Schematic, (b) layout and (c) fabricated prototype of NFC

3.3 Empirical Measurement Results of NIC

The experimental measurement of a Negative Impedance Converter (NIC) entails the assessment of various parameters to get valuable insights into its performance. Among the available methods, employing a network analyzer emerges as the most effective and reliable approach. This sophisticated instrument facilitates precise and accurate measurements of the NIC's impedance characteristics.

As shown in Figure 3.5, by connecting the NIC to a network analyzer, the reflection coefficient (S_{11}) is measured, enabling a comprehensive evaluation of the circuit's impedance matching capability. The network analyzer permits the acquisition of S_{11} data over a specific frequency range, providing comprehensive information about the behavior of the NIC across various frequencies. Moreover, the network analyzer offers a direct means of measuring the circuit's capacitance. By analyzing the changes in the reflection coefficient during frequency sweeps, the capacitance effects within the NIC can be precisely determined. The network analyzer captures subtle impedance variations, ensuring precise readings and assisting in the estimation of capacitance values associated with the circuit. The utilization of a network analyzer in the experimental measurements of the NIC presents several notable advantages. It ensures meticulous and reliable data acquisition, thereby enabling a thorough investigation of the circuit's behavior. Through direct measurements of capacitance and reflection coefficients, the network analyzer furnishes crucial information for assessing the performance and tuning capabilities of the NIC.

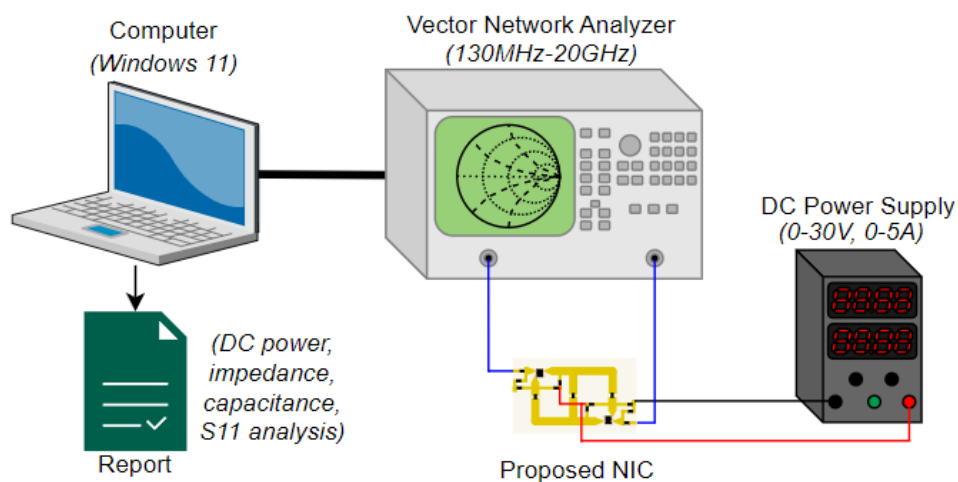


Figure 3.5: Block diagram illustrating the experimental measurement setup of NIC.

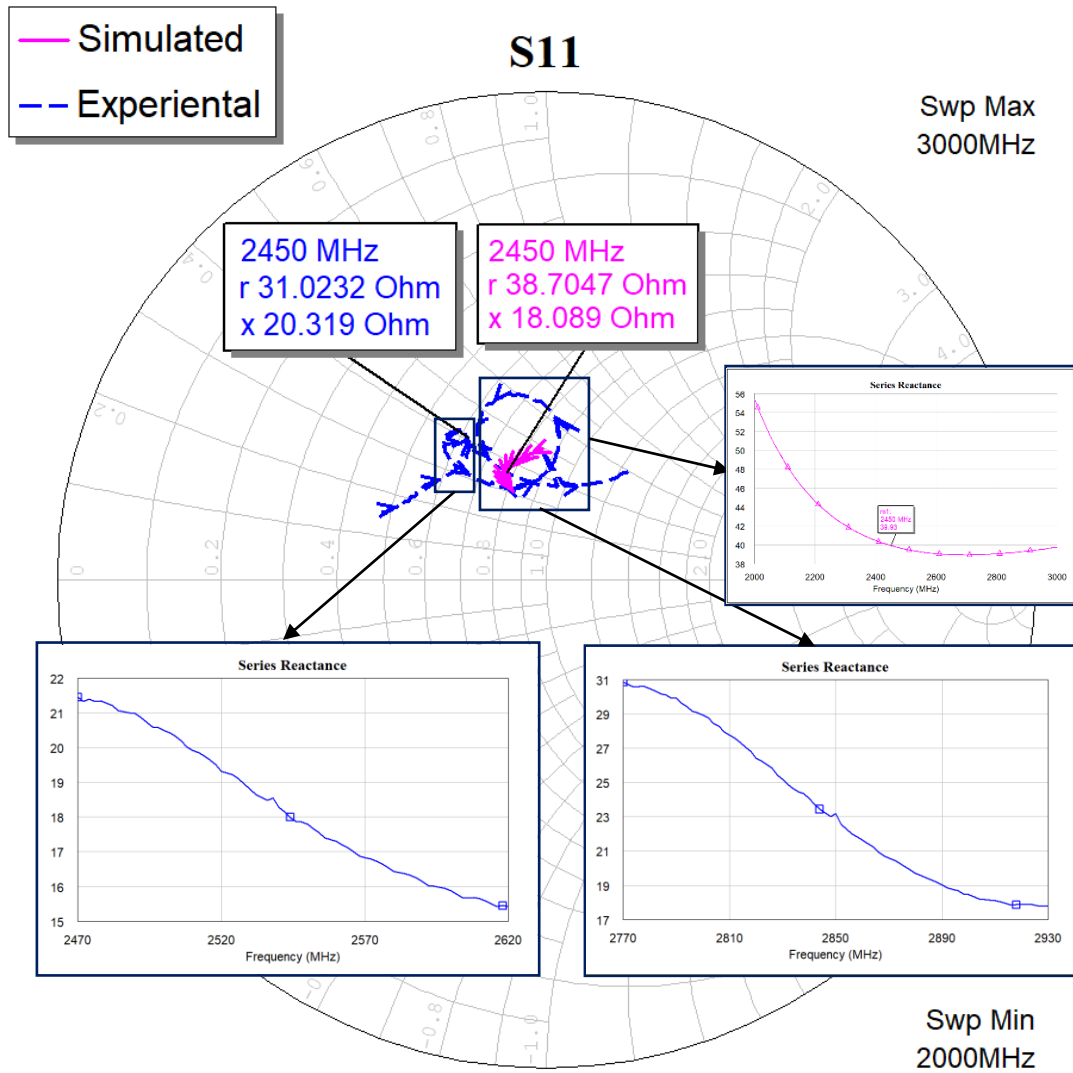


Figure 3.6: S11 and Series Reactance of Non Foster NIC, $V_{cc}=12V$

Figure 3.6 demonstrates a notable congruity between the Simulation and Experimental S11 results of the proposed NIC. Within the simulated results, the series reactance exhibits a decline as the frequency increases from 2 GHz to 3 GHz, indicating a capacitive effect between the input and output ports. Despite the series reactance of the capacitive component being assigned a negative value, the proposed circuit exhibits a positive reactance value. The alteration in sign of the reactance value coincides with the change in sign of the capacitance, which can be elucidated by the presence of negative capacitance. In accordance with the experimental measurements, negative capacitance is observed within the frequency ranges of 2.47-2.62 GHz and 2.77-2.93 GHz for the same underlying mechanism. Notably, real-world implementation introduces material variations due to fabrication and temperature factors, deviating from the simulated values. These variations manifest as parasitic

effects on the proposed circuit, resulting in the occurrence of negative capacitance in two distinct regions within the current frequency range. However, due to the circuit's adjustable supply voltage tune series capacitance as seen in Figure 3.7, it remains a suitable choice for impedance matching purposes.

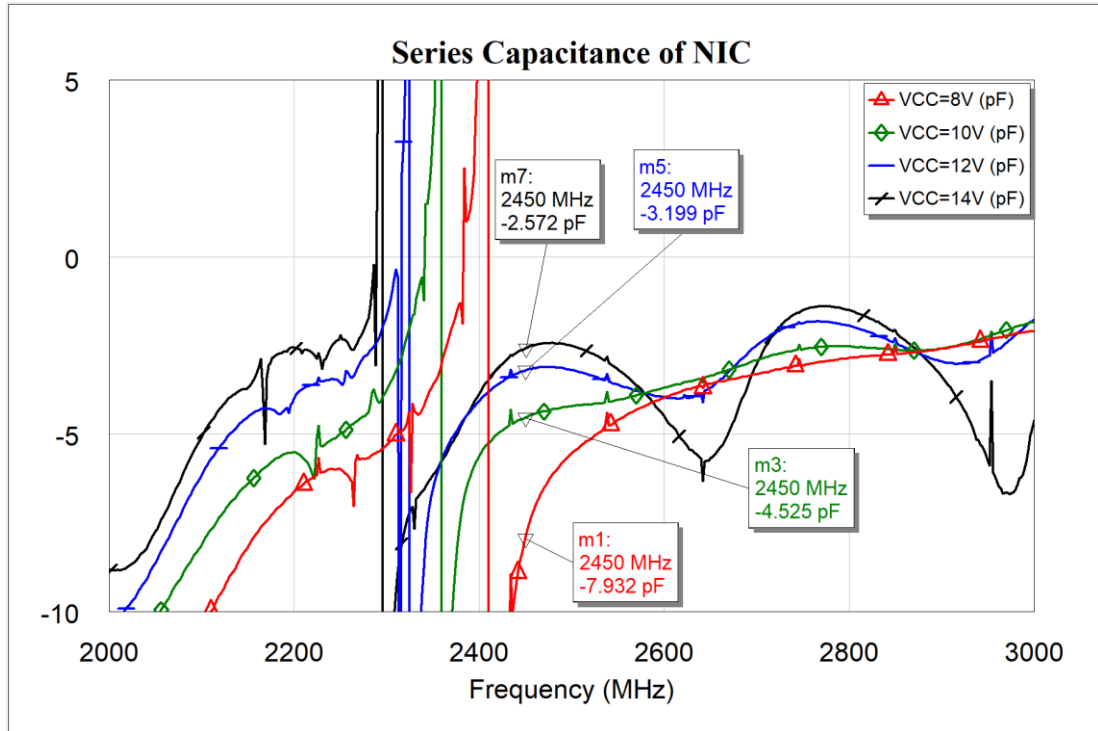


Figure 3.7: Series Capacitance of Non Foster NIC changing feeding voltage

Figure 3.7 illustrates the correlation between the voltage supply (VCC) and the corresponding capacitance values in the proposed negative capacitance circuit. At a frequency of 2.45 GHz, the measured capacitance values exhibit a dependency on VCC. Specifically, when VCC is set to 8V, the capacitance is recorded as -7.93 pF. As the VCC is incremented to 10V, the capacitance diminishes to -4.53 pF. Similarly, for VCC values of 12V and 14V, the capacitance further decreases to -3.2 pF and -2.57 pF, respectively.

These observations indicate an inverse relationship between the voltage supply and the magnitude of negative capacitance. Increasing the feeding voltage leads to a reduction in the effective capacitance demonstrated by the circuit. This behavior underscores the tunability of the proposed circuit, as adjusting the VCC enables the attainment of desired capacitance values for impedance matching objectives.

Furthermore, it is notable that negative capacitance manifests within specific frequency ranges. Deviations of 5 pF are observed in the capacitance within the 2.46-2.62 GHz and 2.62-2.93 GHz frequency intervals where the negative capacitance effect occurs. In these frequency ranges, the measured capacitance values of -7.93 pF, -4.53 pF, -3.2 pF, and -2.57 pF, corresponding to VCC values of 8V, 10V, 12V, and 14V respectively, indicate the presence and extent of the negative capacitance phenomenon. These findings emphasize the significance of considering the frequency-dependent characteristics when analyzing the proposed negative capacitance circuit. The pronounced manifestation of negative capacitance within the specified frequency ranges underscores its importance and impact on circuit behavior, particularly in the context of impedance matching applications.

In additional analysis, the steady state temperature distribution of the NIC was examined using a Testo 882 thermal imager, while varying the DC feeding voltage for 30 s. Figure 3.8 presents the spatially resolved temperature measurements of the NIC circuit across a range of feeding voltages from 6V to 12V.

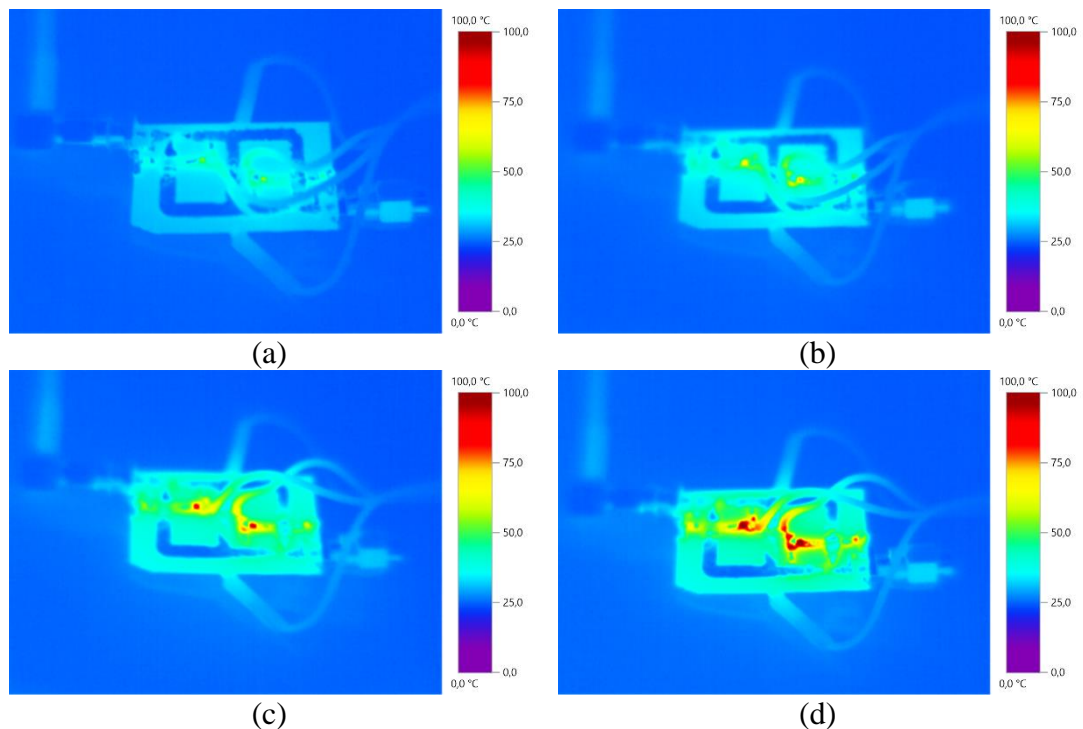


Figure 3.8: Steady state temperature distribution measurement of the NIC circuit under various feeding voltages: (a) 6 V, (b) 8 V, (c) 10 V, and (d) 12 V for 30 s.

For an input power excitation of 0 dBm, the substrate of the proposed Negative Impedance Converter (NIC) circuit exhibits minimal changes. This can be attributed

to the small RF loss tangent value of RO 4003, which prevents excessive heating at the 0 dBm power level. However, significant variations in transistor temperatures are observed with varying DC feeding voltages. The temperature rise in each transistor within the NIC circuit reaches 56 °C, 74.4 °C, and 97.4 °C for DC feeding voltages of 6V, 8V, and 10V, respectively. Considering that the BRF193W transistor can withstand temperatures up to 150 °C, it can be concluded that the NIC circuit operates safely in terms of the absolute maximum temperature. Moreover, when the feeding voltage is increased to 12V, the temperature of each transistor reaches 141.8 °C. Therefore, the 12V feeding voltage is regarded as the limit value to remain within the temperature safe region. It is crucial to note that operating the transistors within their specified temperature limits ensures their reliability and prevents potential damage. Hence, by maintaining the transistor temperatures below the specified maximum value, the NIC circuit demonstrates safe operation in terms of temperature. In Figure 3.9, transient temperature graph of the NIC is indicated.

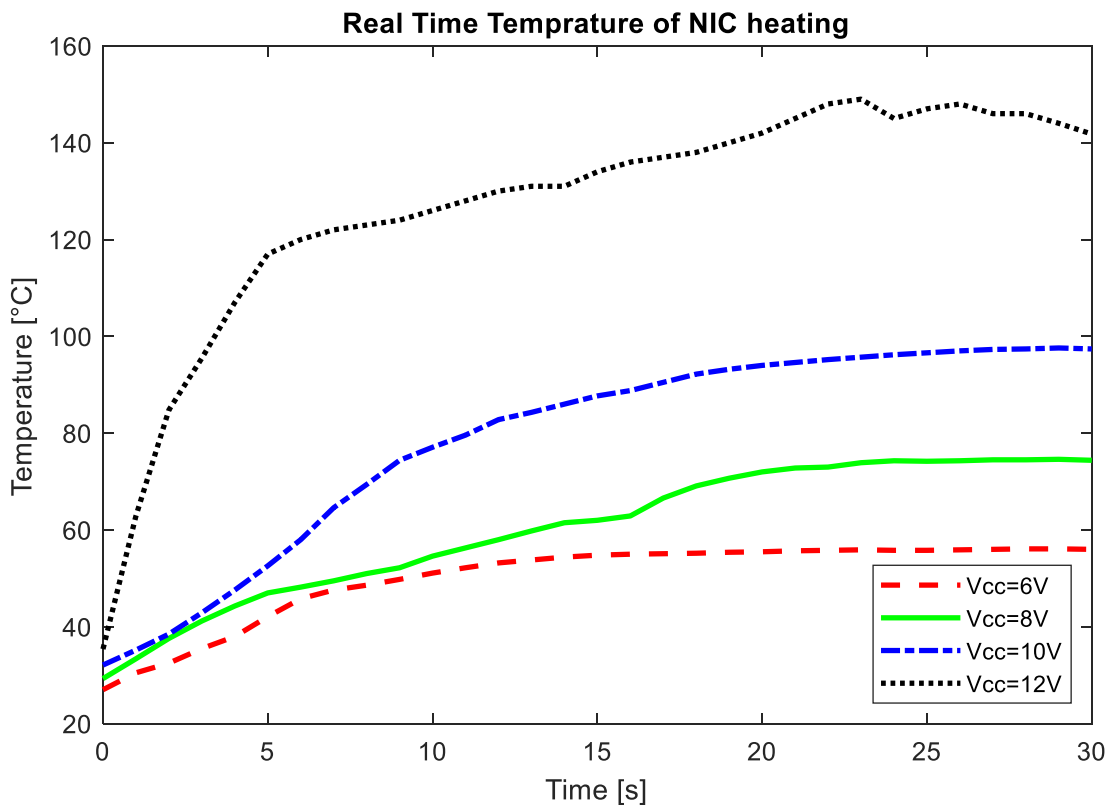


Figure 3.9: Transient temperature graph of the NIC circuit under various feeding voltages: (a) 6 V, (b) 8 V, (c) 10 V, and (d) 12 V for 30 s.

Figure 3.9 demonstrates that the application of varying supply voltages results in consistent heating behavior. Specifically, the temperature exhibits an exponential

increase during the initial 10 s, followed by an exponential decrease until approximately 15-20 s. Subsequently, a steady-state temperature is attained within the 15-30 s timeframe. The performance table of NIC including feeding current, collector current, base current, power from source, transistor power transistor temperature and capacitance; under 0 dBm microwave power at 2.45 GHz summarized in Table 3.2

Table 3.2: Performance table of NIC at 2.45 GHz

Feeding Voltage (V)	8	9	10	11	12	13	14
Feeding Current (mA)	140	161	178	196	215	230	258
Collector Current (mA)	17.3	20.6	23.6	26.7	29.8	32.9	36.1
Base Current (mA)	0.18	0.21	0.24	0.27	0.3	0.33	0.36
Power from Source (W)	1.11	1.44	1.79	2.16	2.58	2.99	3.60
Transistor Power (mW)	77.5	103.8	132.1	164.4	200.2	239.5	283
Transistor Temperature (°C)	74.4	92.5	97.4	123.1	141.8	165.2	189.3
Capacitance (pF)	-7.93	-5.71	-4.53	-3.75	-3.2	-2.9	-2.57

The table provides several noteworthy observations based on the distribution of values. The feeding current shows a consistent increase, but there is a significant jump to 258 mA at the highest feeding voltage. Similarly, the power consumption gradually rises, but there is a notable increase to 3.6 W for the last data point.

The measured transistor power values show a steady increase, reaching a maximum value of 283 mW at the highest feeding voltage. This value is below the absolute maximum power dissipation specified for the BFR193W transistor, which is 700 mW. Therefore, based on the provided data, the transistor operates within its maximum power dissipation limits.

Regarding the transistor temperature, the values range from 74.4°C to 189.3°C. It's important to note that these temperatures represent the measured temperatures, and the actual junction temperature of the transistor may be higher due to thermal resistance and other factors. However, all the measured temperatures are below the transistor's absolute maximum temperature of 150 °C. Therefore, based on the provided data, the transistor operates within its specified temperature limits. Additionally, the capacitance values demonstrate a decreasing trend, particularly with a significant decrease from -3.2 pF to -2.9 pF. These remarkable values indicate potential shifts in system behavior, suggesting the need for further investigation and consideration in the overall circuit analysis.

3.4 Active Impedance Matching Techniques Utilizing Non-Foster NIC

The AC and DC characteristics of the NIC circuit is examined using a 50 Ω termination. This section aims to utilize the Non-Foster matching (NFC) circuit to enhance the performance of the impedance matching circuit developed for the Marble-Filled Microwave Ablation Probe (MFMWAP). Figure 3.10(a) illustrates the design of an open stub matching configuration, employed to connect the input port of the NFC, powered by a 3V source, to achieve impedance matching between the MFMWAP and a 50 Ω load at a frequency of 2.45 GHz. Simulation results, comparing the performance with and without the inclusion of NFC, are presented in Figure 3.10(b). Additionally, the corresponding experimental setup and measurement outcomes are depicted in Figure 3.10(c) and Figure 3.10(d), respectively, conducted under varying feeding voltages of the NFC ranging from 3 V to 6 V.

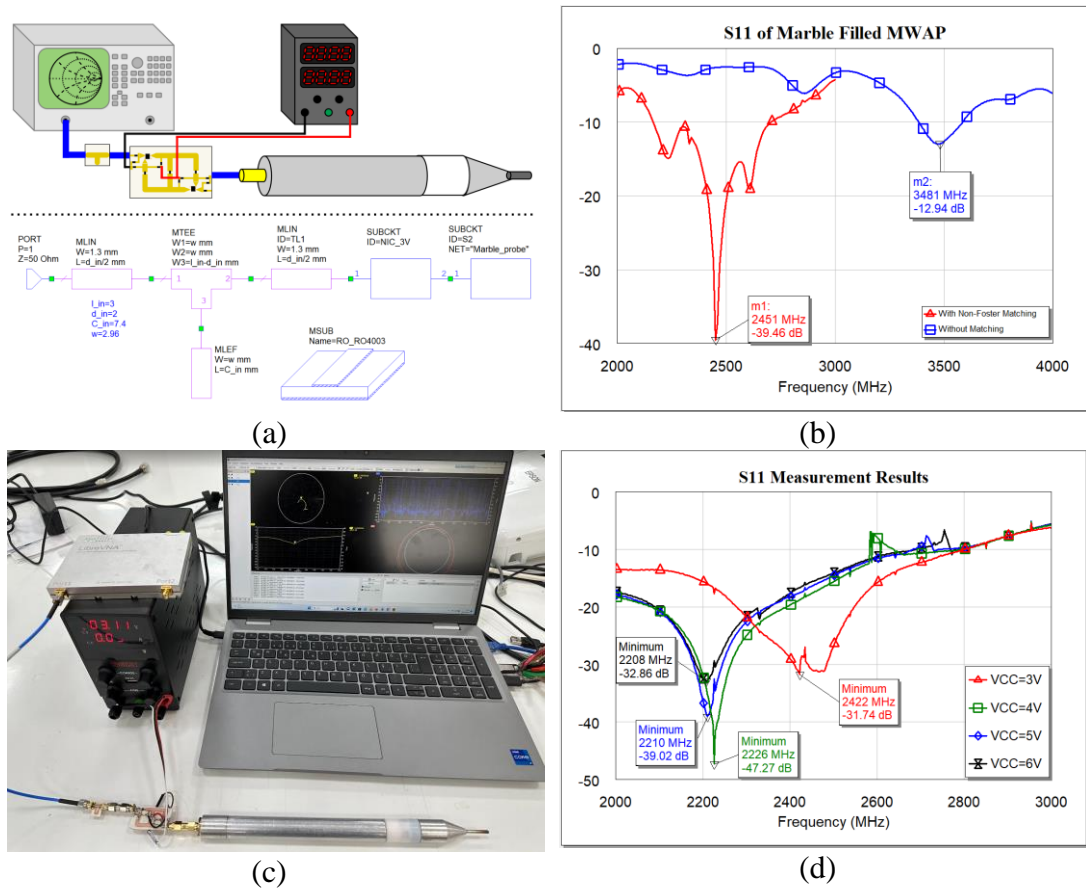


Figure 3.10: (a) Schematic, (b) simulated S11 with/without NFM, (c) experimental setup, (d) experimental S11 with NFM varying feeding voltage using MFMWAP

In Figure 3.10(b), the experimentally measured reflection coefficient of MFMWAP without impedance matching circuitry is -12.94 dB at its resonant frequency of 3.48 GHz. However, through the utilization of the impedance matching circuit, comprised of open stub matching and the NIC shown in Figure 3.10(a), the resonant frequency is shifted to 2.45 GHz in the simulation environment. At this frequency, the reflection coefficient is significantly improved, measuring -39.46 dB, which demonstrates excellent power transfer capabilities. In addition to reflection coefficient, operation bandwidth is also improved from 200 MHz to 540 MHz when the non foster NIC matching is used.

In the experimental measurement setup depicted in Figure 3.10(c), the application of a 3V supply voltage from the DC power source to the NIC circuit resulted in the successful impedance matching of the MFMWAP with an S11 value of -31.74 dB and wider than 800 MHz bandwidth at the frequency of 2.45 GHz. However, upon increasing the supply voltage to 4V, a significant shift in the resonant frequency was observed, now occurring at 2.23 GHz. Subsequently, as the supply voltage was further increased to 5V and 6V, the resonance frequency exhibited slight variations within a few MHz steps, leading to corresponding small changes in the reflection coefficient values. As a result of achieving broadband impedance matching with these processes, the experimental measurement setup in Figure 3.11 was created and the input-output power analysis in the proposed system was performed. The power measurement results when the pancreas recipe is placed on the applicator tip are given in Figure 3.12, and the measured power values in the no-load condition are given in Figure 3.13.

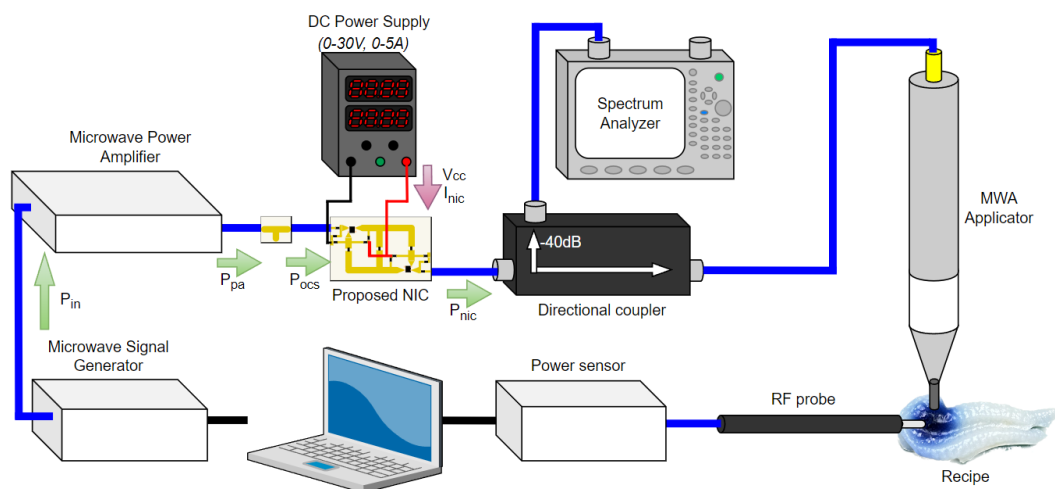


Figure 3.11: High power measurement setup using MFMWAP with NFC matching.

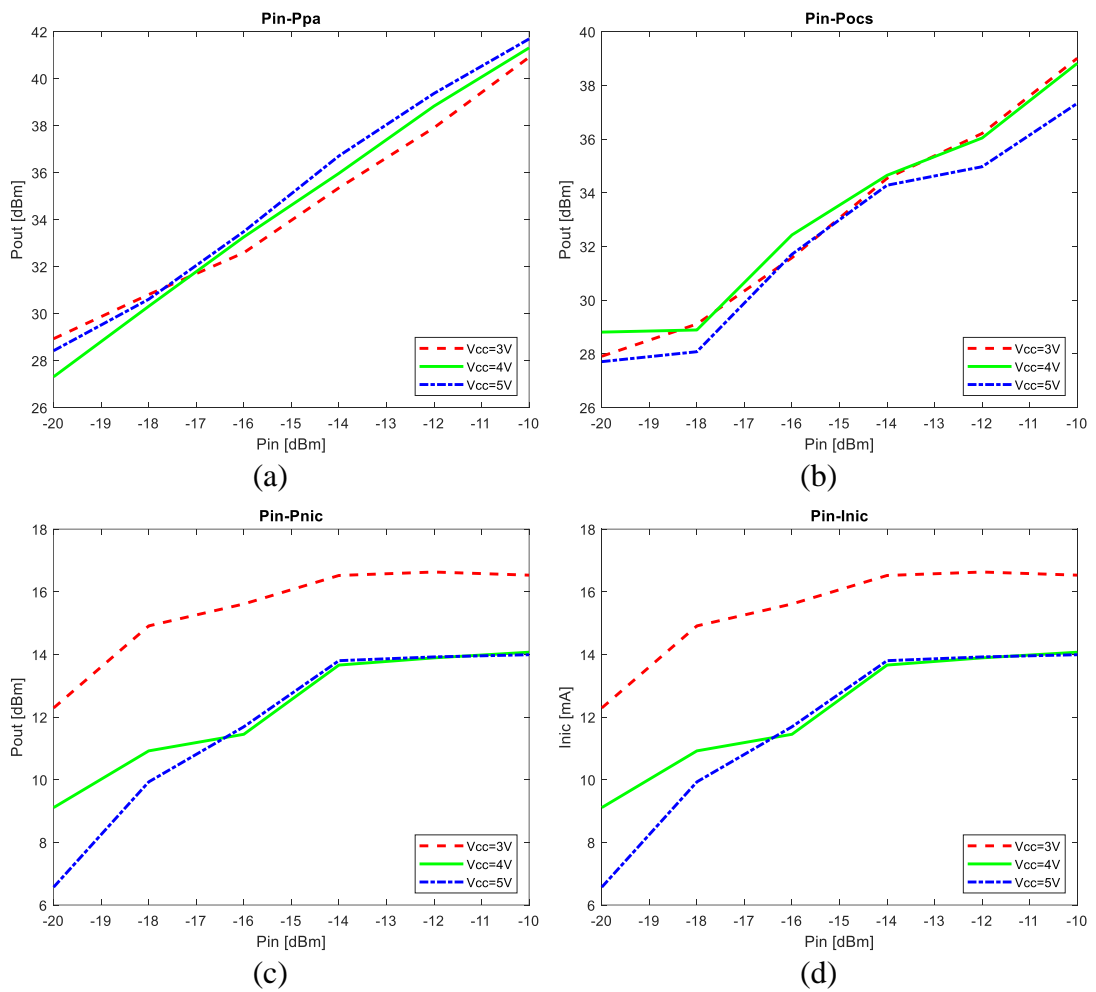


Figure 3.12: Input power versus output powers of (a) PA, (b) OCS (c) NIC and (d) feeding current when $V_{cc}=3\text{ V}$, $V_{cc}=4\text{ V}$ and $V_{cc}=5\text{ V}$.

The non-Foster impedance matching system in Figure 3.11 utilized the electrical equivalent model of the pancreas as the dielectric charge for impedance power measurement. In Figure 3.12(a), the NIC circuit operated with a 3 V supply voltage, achieving adaptation of the microwave power amplifier's output impedance at 2.45 GHz. When input power varied from -20 dBm to -18 dBm, the power transfer exhibited better performance compared to the results obtained at 4 V and 5 V supply voltages. However, as depicted in Figure 3.12(c), applying input power greater than -18 dBm resulted in current saturation within the NIC circuit, leading to a gradual decrease in impedance matching advantage. Additionally, the input power increased in proportion to the supply voltages and transistor currents, resulting in higher output power at 5 V supply. Figure 3.12(b) indicated that the OCS circuit, when considered individually, exhibited lower reflection loss at a 4 V supply voltage. The measurement of power levels 1-2 dB lower than the power level at the power amplifier output suggested that

the microwave power consumed in the OCS circuit ranged from 1-10 mW. Conversely, when analyzing the power levels measured from the output of the NIC circuit in Figure 3.12(c), it was observed that approximately 1 W of microwave power was consumed in the NIC circuit. However, in applications where the advantage of creating an adjustable negative capacitance outweighs the microwave power consumed, this power loss may be disregarded.

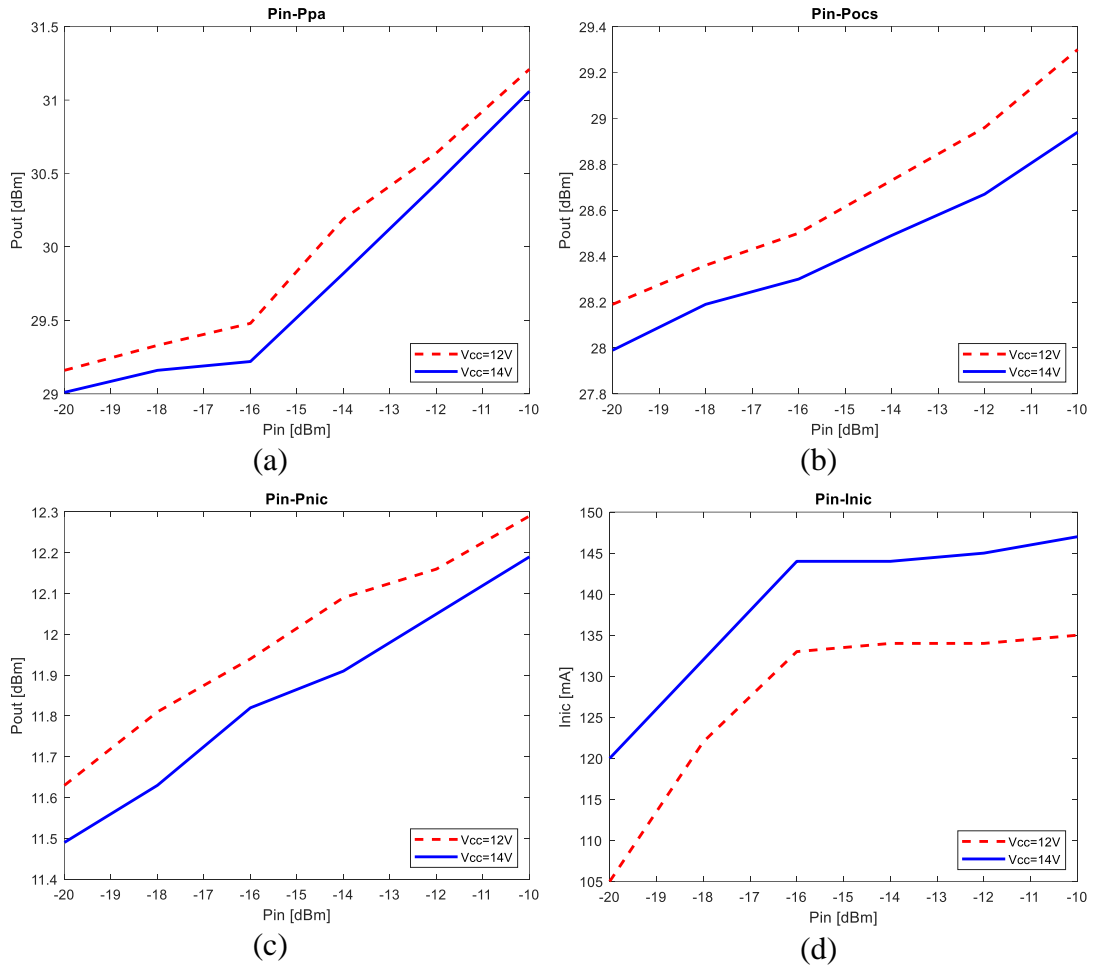


Figure 3.13: Input power versus output powers of (a) PA, (b) OCS (c) NIC and (d) feeding current when Vcc= 12 V, and Vcc=14 V.

The impedance power measurement of the non-foster impedance matching system is conducted in air. Upon applying a supply voltage of 12 V to the NIC circuit, the microwave power amplifier adjusts its output impedance at the frequency of 2.45 GHz. Notably, when input power ranging from -20 dBm to -16 dBm is applied, the power transfer surpasses the performance achieved with 14 V supply voltage. However, Figure 3.13(c) reveals that as the input power exceeds -16 dBm, the NIC circuit experiences current saturation, resulting in a gradual reduction of the impedance

matching advantage. In this scenario, the input power amplifies proportionally with the supply voltages and transistor currents, leading to higher output power with 14 V supply. Conversely, Figure 3.13(b) highlights that the OCS circuit exhibits lower reflection loss at 14 V supply voltage. The power measurements demonstrate a discrepancy of 1-2 dB compared to the output power level of the power amplifier, indicating a microwave power consumption of 1-10 mW in the OCS circuit. Conversely, the power levels measured at the output of the NIC circuit in Figure 3.13(c) indicate a microwave power consumption of approximately 1-5 W. However, it is important to note that in applications where the advantage of creating an adjustable negative capacitance outweighs the microwave power consumed in the circuit, this power loss may not be a significant concern.

Chapter 4

MWA System Design

4.1 Microwave Power Amplifier Design Utilizing a 400 W HEMT

Microwave power amplifiers (MWPAs) are electronic circuits that are used to amplify high-frequency signals, typically in the microwave frequency range of 1 GHz to 100 GHz. These amplifiers are used in a wide range of applications, such as in telecommunications, radar systems, satellite communication, and medical imaging equipment.

The design of microwave power amplifiers for microwave ablation is a complex and multi-disciplinary process that requires careful consideration of various factors such as technology, frequency range, power output, linearity, efficiency, noise, and stability. The choice of technology and the design of the amplifier circuit, as well as other supporting components, must be optimized to achieve the desired performance characteristics for the specific application and the patient's safety.

Microwave ablation is a medical procedure that uses high-frequency electromagnetic waves to destroy cancerous cells. To design a microwave power amplifier for microwave ablation, it is crucial to consider several factors such as the desired 900-2450 MHz frequency range, sufficient output power to heat the targeted tissue, providing adequate gain to compensate for transmission losses, impedance matching, maintaining stability, thermal management, and meeting the required safety standards for medical devices. These factors ensure that the power amplifier operates within the desired range with high efficiency and minimal distortion while preventing damage to the tissue and components and maintaining patient safety. Effective heat dissipation is another crucial consideration as the amplifier generates heat during operation. Proper

thermal management helps prevent overheating and damage to the components. Finally, the amplifier should meet the required safety standards for medical devices to ensure that the patient is not exposed to excessive radiation.

4.2 Overview on Microwave Power Amplifier Design

Microwave power amplifiers have been developed over several decades for various applications such as military radar, telecommunications, satellite communications, and wireless networks. The first microwave power amplifiers were developed during World War II for military radar applications. These early amplifiers were based on vacuum tube technology and were bulky, inefficient, and had limited output power. In the 1950s and 1960s, the development of solid-state electronics led to the creation of the first microwave power amplifiers based on transistors. These amplifiers were smaller, lighter, and more efficient than their vacuum tube predecessors, and they allowed for the creation of compact, high-performance microwave systems. In the 1970s and 1980s, the development of GaAs (gallium arsenide) semiconductor technology enabled the creation of high-power, high-frequency microwave amplifiers with improved performance and efficiency. In the 1990s, the development of MMIC (monolithic microwave integrated circuit) technology further improved the performance of microwave power amplifiers by allowing for the integration of multiple amplifiers on a single chip. Today, microwave power amplifiers are used in a wide range of applications, including radar systems, satellite communications, cellular networks, and wireless internet. Ongoing research and development in this field continue to improve the performance, efficiency, and reliability of MWPA

Over the course of the past decade and a half, there has been a notable surge in research and development endeavours with regard to the design of microwave power amplifiers (MWPA). One of the primary focal points of these efforts has been centered on enhancing the efficiency and linearity of power amplifiers. This has been accomplished by leveraging innovative circuit topologies, materials, and device technologies. Researchers have dedicated significant attention to exploring various circuit topologies, such as Doherty amplifiers, envelope tracking, and out phasing amplifiers, among others, with the goal of optimizing amplifier efficiency through the minimization of power dissipation and the maximization of power-added efficiency. Additionally, researchers have investigated new materials, including gallium nitride

(GaN) and silicon carbide (SiC), as well as novel device technologies, to further augment power amplifier performance. A comprehensive overview of MWPA designs studied over the past 15 years can be found in Table 4.1.

Table 4.1: MWPA designs studied in last 15 years.

Ref. No.	Year	Freq. (MHz)	BW (MHz)	Pout (dBm)	PAE (%)	Gain (dB)	Class	Stage
[143]	2008	1.95	160	33	53	11	B	3
[144]	2008	0.02-0.1	80	51.76	43	35	B	2
[145]	2005	2.12	50	44.5	47	30	AB	1
[146]	2005	2.14	-	33	40	16	AB	2
[147]	2022	0.041	-	61.76	89	-	E	6
[148]	2008	0.002	1	32.5	64.7	32	F	1
[149]	2000	39	14000	30	32.5	24.5	A	1
[150]	2009	2.4	-	31	33	24	AB	1
[151]	2010	1.95	60	28	47	-	-	-
[152]	2019	140	35000	21.76	9.8	17.5	-	2
[153]	2020	2.14	900	43.9	49	11	-	3
[154]	2021	0.9	-	24	38.4	20.8	AB	1
[155]	2016	0.6	90	21	45	-	D	2
[156]	2017	66	-	23.4	24	23.8	-	1
[157]	2021	35	10000	22.8	27	25.3	-	1
[158]	2017	190	24000	11.3	9.6	19.2		4
[159]	2019	83	23000	15.3	30.7	15.3	AB	4
[160]	2022	26.6	8000	30.8	26.7	13.9	AB	4
[161]	2020	1.875	-	43	62	-	B	2
[162]	2021	28	20000	18.6	42.1	23	AB	1
This work	2023	2.45	300	55.55	58.6	19.3	A	1

Comparative analysis of the performance characteristics of recently published MWPA designs indicates that the present study outperforms other studies in terms of power output, power added efficiency, and gain. In comparison to the MWPA design given in Table 4.1, this work exhibits remarkable characteristics in terms of its high output power (Pout) and power added efficiency (PAE). Firstly, this work achieves a significantly higher power output of 55.55 dBm while maintaining a high power-added efficiency of 58.6%. This performance exceeds that of the closest comparable studies in the table, which have power output ranging from 11.3 dBm to 43.9 dBm and PAE ranging from 9.6% to 62%. Secondly, proposed work operates at a frequency of 2.45

GHz with a bandwidth of 300 MHz, which is a widely used frequency band in various medical systems. In comparison, several studies in the table operate at frequencies ranging from 0.002 MHz to 140 MHz, with a limited bandwidth. This work thus presents a significant advancement in the suitability of the proposed design for practical applications.

When the amplifier classes are examined, the majority of the amplifiers are in Class A or AB, with a few in Class B and E. This work employs Class A amplification, which offers a linear response and low distortion. In contrast, several studies in the table employ AB or B classes, which can introduce non-linearities and higher distortion. This work has a higher P_{out} and PAE than the other Class A amplifiers listed in the table, indicating that it offers higher efficiency and output power while maintaining good linearity. However, it should be noted that different classes of amplifiers are designed for different applications, and the choice of amplifier class depends on the specific requirements of the application. The table highlights that the newly proposed work exhibits a gain of 19.3 dB, which is analogous with the gains demonstrated by Class A and AB power amplifiers in the table. Notably, Class B, C, D, and F power amplifiers usually feature higher gains, but their comparison is hindered by their distinct operating modes, bias conditions and the necessity of using more than one transistor.

Finally, this demonstrates a single-stage amplification design, which offers simplicity, low cost, and ease of integration. This is in contrast to several studies in the table that utilize multi-stage amplification designs, which can be complex and costly to implement. The comparative analysis of recently published MWPA designs shows that the present study outperforms others in terms of power output, power added efficiency, and gain. This work exhibits higher power output and power added efficiency compared to comparable studies in the table. It operates at a widely used frequency band and employs Class A amplification, providing a linear response and low distortion. The proposed design offers improved efficiency and output power while maintaining good linearity. The gain of this work is comparable to Class A and AB amplifiers in the table, while other amplifier classes have distinct operating modes and may require multiple transistors.

4.3 QORVO 400W HEMT Nonlinear Model Evaluation

The Qorvo QPD2795 is a 2-lead NI400 package containing a discrete 400W (P3dB) GaN on SiC HEMT, utilizing Qorvo's QGAN25 process. A non-linear model, the HMT-QOR-QPD2795-001, has been developed based on a customized Angelov non-linear model as shown in Figure 4.1. This model has been verified through analysis of Qorvo's Current-Voltage measurement and large signal load pull data in the 2.5-2.7 GHz frequency range. The model has been tested under both class AB operation for Doherty architecture designs.

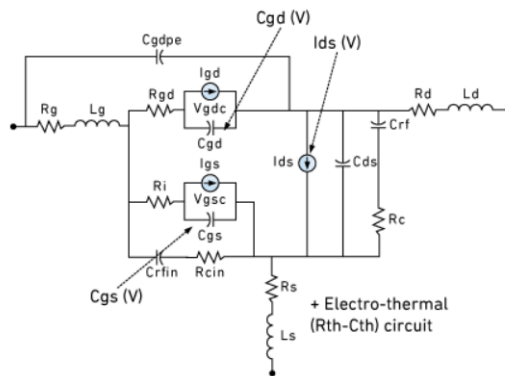


Figure 4.1: Angelov model for QORVO GAN technology

The Angelov model is a mathematical model used to describe the behavior of GaN transistors, which are used in the Qorvo QPD2795 amplifier. The Angelov model includes parameters such as gate leakage, gate resistance, and parasitic capacitances, which can affect the performance of the transistor. By using the Angelov model, designers can simulate the behavior of the transistor under various operating conditions and optimize the circuit design for optimal performance. This can help to ensure that the Qorvo QPD2795 amplifier operates reliably and efficiently in high-frequency applications.

To incorporate the large-signal elements into the extrinsic parameters modeled earlier, a final optimization of the nonlinear current and capacitance model parameters was carried out using the CAD software AWR Microwave Office. This was necessary to prevent the extrinsic resistances from being accounted for twice in the IV characteristics of the HEMT and to avoid a similar situation with the extrinsic capacitances.

4.3.1 Current-Voltage Simulation of Nonlinear HEMT Model

The current-voltage (IV) curve of a microwave power amplifier describes the relationship between the input current and output voltage of the amplifier. The IV curve is important because it helps to characterize the performance of the amplifier, particularly in terms of its linearity, efficiency, and saturation power.

The circuit schematic indicated in Figure 4.2, which work to generate the IV curve of QPD2795 is built by sweeping the drain and gate current of transistor. Amperemeter and voltmeter are measure the current and voltage to which obtain the axis of IV curve. Figure 4.2 output provide valuable information about its behavior and can be used to optimize its performance for specific applications. It is important to note that the range of allowable drain and gate voltages for a given transistor is limited by its specifications and exceeding these limits can cause damage to the device.

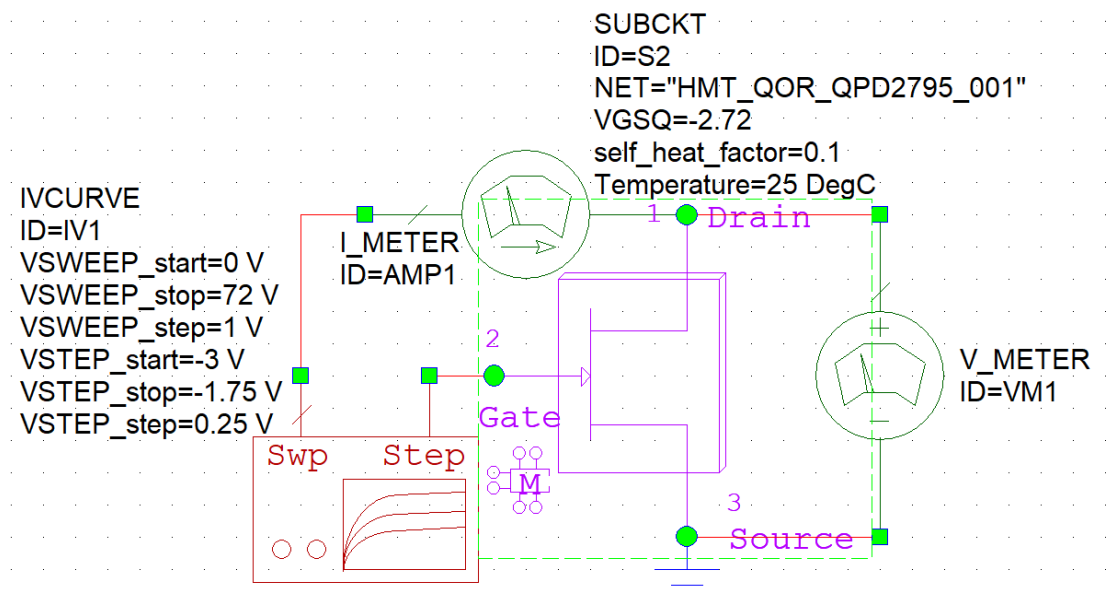


Figure 4.2: Simulation setup generating drain current versus drain voltage curve

Since the gate operation voltage is given as -2.72 V in the datasheet of the QPD2795, voltages from -1.75 V to -3 V are applied to the gate terminal of the transistor in -0.25 V steps as shown in Figure 4.3. With a similar logic, the horizontal axis of the IV curve is applied from 0 V to 72 V with 1 volt sweeping, to include 48 V operating drain voltage given in the datasheet of the QPD2795.

In Figure 4.3, The IV curve of QPD2795 is divided into three regions: the linear region, the saturation region, and the breakdown region. In the linear region, the output voltage of the amplifier is directly proportional to the input current, and the amplifier behaves like a linear device. The slope of the IV curve in this region is the small-signal transconductance of the amplifier, which is a measure of its ability to amplify small signals. In the saturation region, the output voltage of the amplifier increases more slowly as the input current increases, and the amplifier begins to exhibit nonlinear behavior. The saturation point is the point at which the output voltage no longer increases with an increase in input current. In the breakdown region, the output voltage of the amplifier starts to decrease as the input current increases, and the amplifier can be damaged if operated beyond this point.

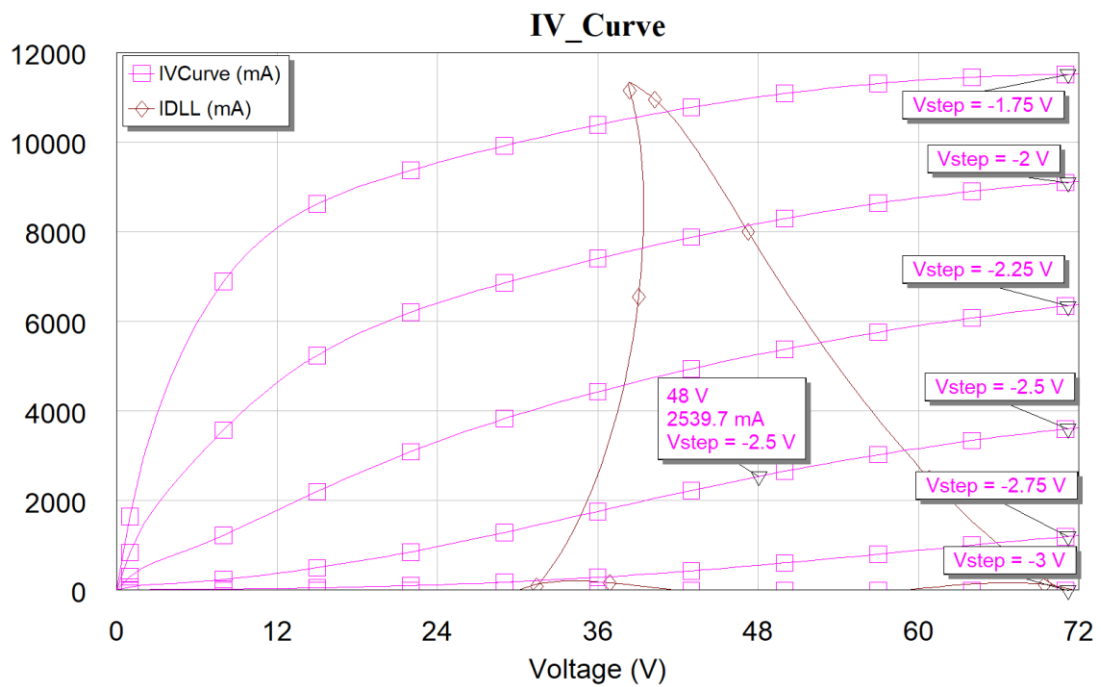


Figure 4.3: Drain current versus drain voltage curve of QPD2795

From Figure 4.3, As the gate voltage increases, the linear curves observed in the graph are replaced by decreasing exponential curves. Moving away from the linear region causes a decrease in amplifier gain, and the heat generated by the lost gain in the transistor is an undesirable situation. Therefore, during the optimization phase of the PA design, the gate voltage was applied within the range of -2.5 to -3 V, and the drain voltage within the range of -36 to -50 V. These selected voltage ranges also stay within the dynamic load line, ensuring that the designed amplifier is suitable for variable loads.

4.3.2 Assessing Nonlinear HEMT Model via Load Pull Analysis

Load pull is a technique used in radio frequency and microwave engineering to optimize the performance of a power amplifier. The goal of load pull is to determine the optimal impedance at the output of the power amplifier for a given frequency and power level. By optimizing the load impedance, the power amplifier can operate more efficiently and produce less distortion, leading to better signal quality and longer battery life in mobile devices.

In load pull, the power amplifier is connected to a variable impedance load, typically a tuner or an impedance matching network as shown in Figure 4.4. The load impedance is then adjusted to different values while the amplifier is driven at a fixed power level and frequency. The amplifier's output power and efficiency are measured for each impedance setting, and the optimal impedance for the desired performance criteria is determined.

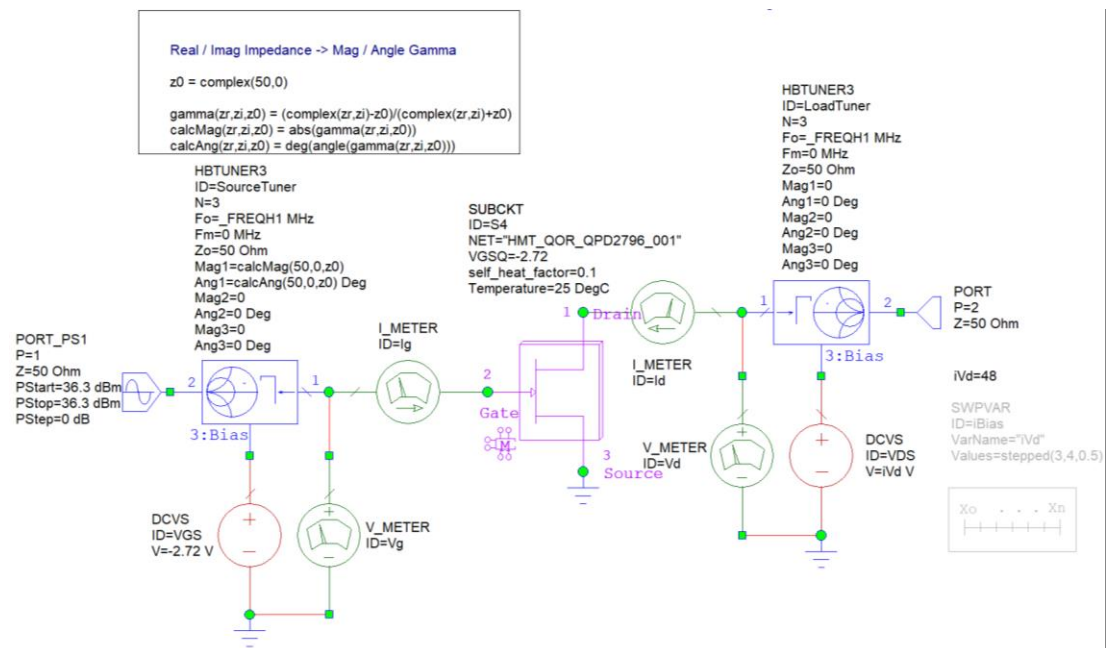


Figure 4.4: Circuit schematic for generating load pull output of QPD2795

The load pull calculation is performed by varying the impedance seen by the power amplifier output using the tuner. The output power and efficiency of the power amplifier are measured at different impedance values using the power meter. The numerically calculated results are plotted on a Smith chart that is shown in Figure 4.5.

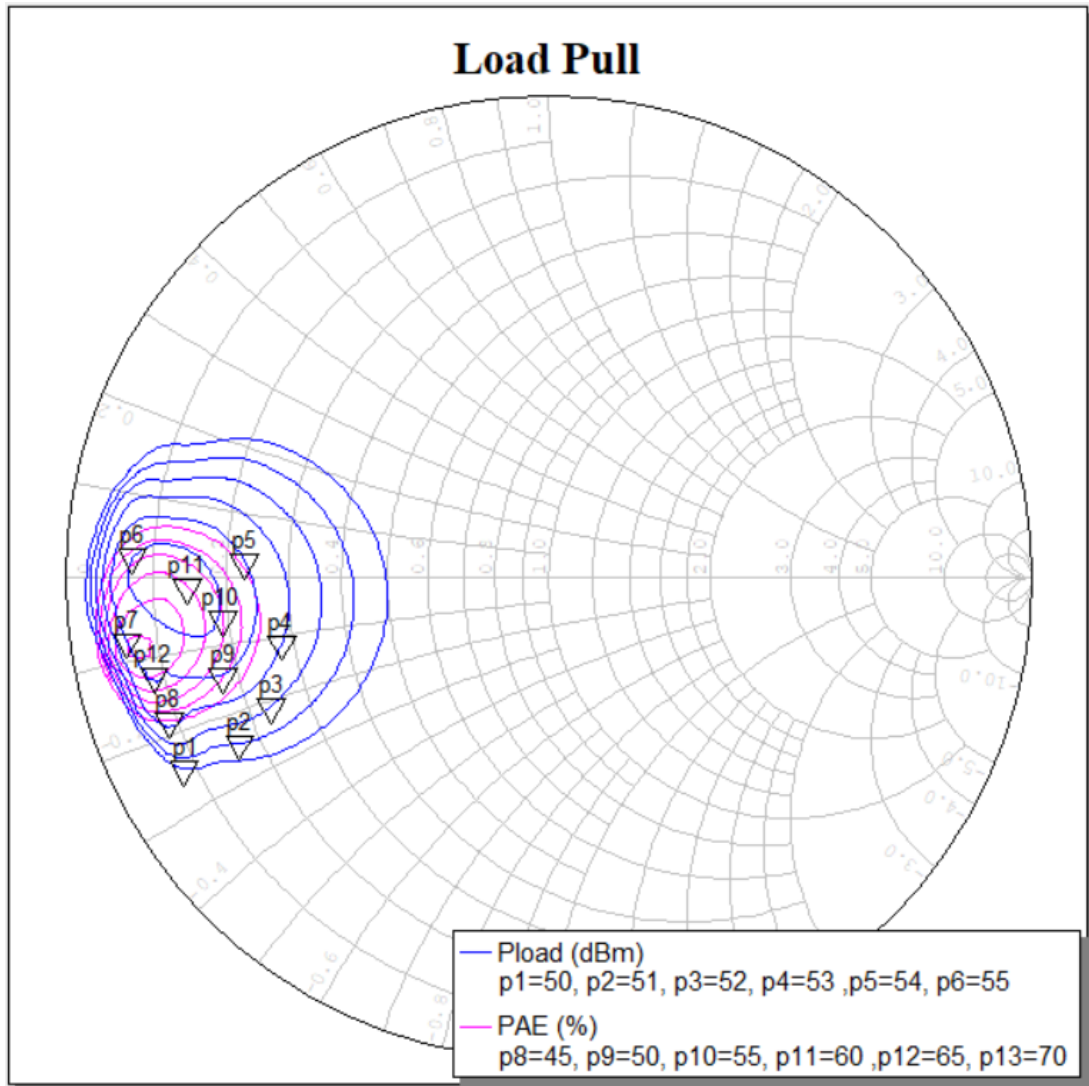


Figure 4.5: Load pull contour of QPD2795 at 2.4 GHz fundamental frequency.

In smith chart shown in Figure 4.5, output power contour from 50 dBm to 55 dBm and PAE contours from % 45 to %70 is given together. In order to create the targeted output power of 55.55 dBm between the Pload limits in this graph, it is necessary to create an impedance between the drain and source terminals of the QPD2795 to be within the p6 numbered contour. In addition, after the target output power is established, a contour should be selected in p6 that will give as high power as possible. PAE contours numbered p10, p11 and p12 are available to ensure highest output power and PAE. In optimization process output matching network system is generated to match the conjugate impedance of load pull data and 50Ω . Thus, the proposed 350 MWPA (QPD350) output is compatible with the standard 50Ω impedance of many microwave device.

4.4 Design Technique for Optimization of QPD350

The process of optimizing a QPD350 through the utilization of AWR Microwave Office involves a sequence of interdependent stages to guarantee the optimal performance of the amplifier. The foremost stage entails designing the amplifier circuit while considering the desired frequency range and power output specifications. This design phase comprises the selection of appropriate electronic components such as inductors, capacitors, resistors, and transistors, which must satisfy specific criteria such as high-power handling capability and low noise performance. Subsequently, the simulation stage utilizing AWR MWO's simulation tools is conducted, where the designed amplifier circuit undergoes analysis and evaluation of various parameters, such as gain, efficiency, and stability. This stage enables the identification and resolution of potential design flaws, and the optimization of the circuit design to enhance its performance. The performance evaluation process allows for the selection of the optimal biasing conditions, which can further enhance the amplifier's performance. The final stage of the optimization process entails the prototyping and testing of the amplifier to validate its performance and ensure it satisfies the desired specifications.

At the outset of optimizing a QPD350, it is imperative to decide regarding the flow of AC and DC signals within the circuit. The DC signal is responsible for driving the transistor into the active region to amplify the desired output power level of the AC signal. In the proposed QPD350 employing the common source amplifier type, both the DC and AC signals traverse the same route on the gate and drain terminals. However, it is crucial that these routes be separated at the DC power supply and input-output port connection points. In the event that the DC signal flows through the input-output ports of the amplifier, there is a risk of high DC power causing damage to these ports, while the transmission line effect of the AC signal and DC power supply connection can lead to unpredictable circuit impedance. To circumvent this undesirable scenario, lumped elements can be placed at critical points. Bias capacitors enable the flow of AC signals while preventing DC signal excitation at the input and output ports. To determine the appropriate bias capacitors, simulations of the capacitance of ceramic capacitors versus frequency were conducted on AWR MWO, as depicted in Figure 4.6.

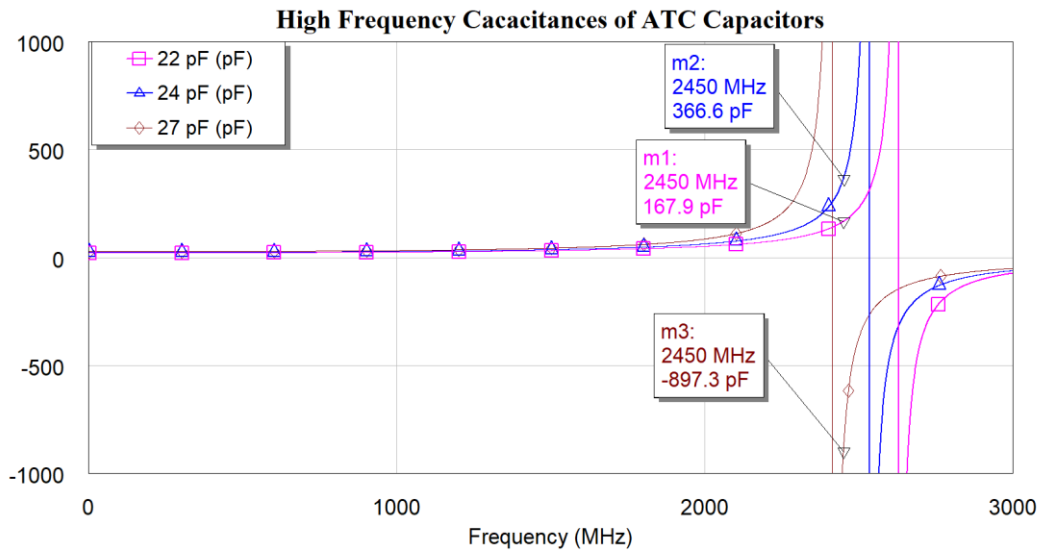


Figure 4.6: Capacitance simulations of ATC capacitors from DC to 3 GHz

To further elaborate on the selection of the 24pF ATC capacitor in the design of the microwave power amplifier, it is worth noting the capacitance values of other capacitors at the same operating frequency. The capacitance of the 22pF ATC capacitor is 168 pF at 2.45 GHz, while the capacitance of the 27pF ATC capacitor is -892 pF at the same frequency. In selecting a bias capacitor for the MWPA design, it is crucial to consider its capacitance value at the operating frequency to ensure optimal AC signal flow and DC signal blocking at the input and output ports. In this context, the negative capacitance value of -892 pF for the 27 pF ATC capacitor at 2.45 GHz means that it would behave as an inductor, which is not suitable for biasing purposes in the MWPA design. Therefore, it was not selected as a bias capacitor. Capacitance values shown in Figure 4.6 indicate that the 24 pF ATC capacitor offers the most desirable capacitance at the specified operating frequency, as it provides a capacitance of 365 pF. Therefore, the use of this capacitor in the MWPA design is expected to result in the desired performance characteristics, as it effectively biases the amplifier for optimal AC signal flow while preventing DC signal excitation at the input and output ports.

In the context of blocking AC signals on the DC feeding points of QPD350, inductors are commonly used in series with the DC feeding transmission line to achieve this objective. However, due to their comparatively lower power handling capacity in comparison to capacitors, inductors are generally not preferred in high power applications. To overcome this limitation, a low pass filter configuration can be used

instead by placing a capacitor in parallel with the DC feeding transmission line. This configuration effectively blocks high frequency signals from passing through the DC power supply while allowing low frequency signals to pass through to the load. Thus, this configuration can be a more suitable alternative to the use of inductors in high power applications where the power handling capacity of components is a critical consideration.

Capacitors with a large capacitance of $4.7 \mu\text{F}$ and $47 \mu\text{F}$ a resonant frequency greater than the operating frequency of 2.45 GHz would theoretically provide a short circuit to all frequencies from DC. However, in the bias circuit, multiple shunt decoupling capacitors have been used in increasing order of capacitances from the gate and drain terminals to DC feeding points. This approach is adopted because the resonant frequencies of capacitors decrease with an increase in their capacitances. For the first shunt capacitor towards the gate and drain terminal has a value of 24 pF filter the operating frequency of 2.45 GHz, whereas the second capacitors CL31B102KBCNNN, 1000pF Samsung Multilayer Ceramic Capacitor, filter possible intermodulation product of proposed QPD350 in two tone signal excitations. This technique also contributes towards providing stability to the amplifier due to minimal resonance between the body inductance of the amplifier circuitry and shunt decoupling capacitors in the bias circuitry. Table 4.2 shows the bias and decoupling list of QPD350.

Table 4.2: Lumped elements used in QPD350

Component	Value
Input port	24 pF, ATC600F240JV250T
Output port	24 pF, ATC600F240JV250T
1 st Capacitors from gate to DC feeding	24 pF, ATC600F240JV250T
1 st Capacitors from drain to DC feeding	24 pF, ATC600F240JV250T
2 nd Capacitors from gate to DC feeding	1000pF, CL31B102KBCNNN
2 nd Capacitors from drain to DC feeding	1000pF, CL31B102KBCNNN
3 rd Capacitors from gate to DC feeding	$4.7 \mu\text{F}$, TAJB475K010R
3 rd Capacitors from drain to DC feeding	$47 \mu\text{F}$, UUX2A470MNL1GS

The design of matching networks and bias circuits involves the use of lumped and distributed elements, each with their own benefits and drawbacks based on the operating frequency, application area, parasites, and dimensions. Low-frequency

applications generally benefit from lumped components, but high Q -factor resonators and filters operating in microwave frequencies require inductance values that are too small to be practically realized with lumped components. The parasites associated with lumped components are difficult to model accurately at higher frequencies, as even capacitors can exhibit resistance and inductance at C-band frequencies, resembling RLC circuits that can cause resonance or gain roll off. As a result, special care must be taken when incorporating lumped components into microwave-frequency circuits. To model and simulate the performance of DC block and decoupling capacitors, device models provided by manufacturers have been utilized, while distributed elements have been used to handle electromagnetic modeling and optimization at step discontinuities, bend junctions, and where parasitic behavior could arise. Furthermore, in Figure 4.7, multi-section impedance matching networks with stepped transmission lines have been used in amplifiers to ensure matching across a wider frequency range, making them less susceptible to performance degradation.

As depicted in Figure 4.7, stepped transmission lines and open circuit stubs are favored in the input matching section, while output matching is only stepped transmission lines. The matching parameters are optimized to achieve maximum output power, PAE, and gain. Figure 4.7 illustrates the optimized circuit for the QPD350, and Table 4.3 indicates proper parameters.

Table 4.3: Optimized parameters of proposed MWPA

Parameter	Length [mm]	Width [mm]
TL41 (Input Matching Line)	$l_{in2}=19.8$	$w_{in1}=5.9$
TL14 (Input Matching Line)	$l_{in3}=10.8$	$w_{in3}=10$
TL19 (Output Matching Line)	$l_{in2}=24.8$	$w_{out1}=6.9$
TL15 (Output Matching Line)	$l_{in3}=21.4$	$w_{out3}=10$
TL13, TL9, TL16, TL22 (bias lines)	10	3
TL6, TL7 (DC lines)	16	3
TL24, TL31, TL37, TL38, TL39, TL40 (DC lines)	10	3
TL26, TL34 (DC lines)	15	3
TL10, TL2 (DC lines)	18	3
TL18 (Open Stub Matching)	17.3	3
TL12 (Open Stub Matching)	14.2	3
TL28 (Open Stub Matching)	9.5	2.6
TL42 (Open Stub Matching)	2.9	2.1
Substrate	ROGERS RO4003	

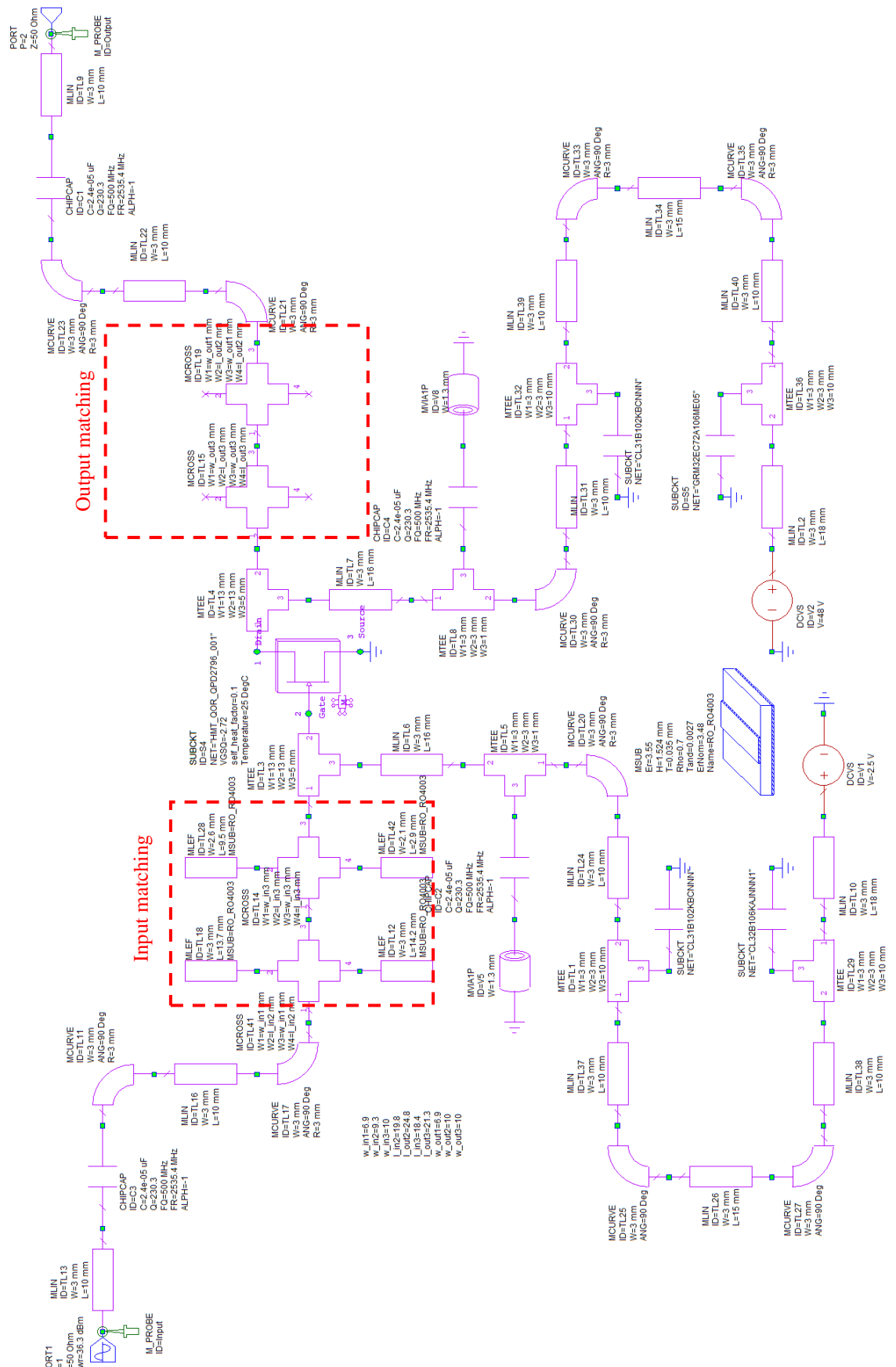


Figure 4.7: Proposed QPD350 in schematic view

4.5 Simulation-Based Analysis of QPD350 Design

In this subsection, proposed QPD350 has been numerically studied with the optimized parameters. Following subsections indicate that the Large Signal Scattering Parameters, Output Power (P_{out}), Power Added Efficiency (PAE), Gain, 1dB Compression Point, Output Spectrum of Harmonics, Current and Voltage Amplification Analysis of designed PA.

The large signal S-parameters for a power amplifier are typically denoted as S11, S21, S12, and S22, just like for any other microwave circuit. However, the interpretation and meaning of these parameters are different for a power amplifier, as they are characterized by their nonlinear behavior. S11, Input reflection coefficient, describes how much power is reflected to the input of the amplifier under large signal conditions, and how these changes as the input power are increased. A high value of S11 can cause instability, while a low value is desired for good matching. S21, gain under large signal conditions, describes the change in output power as a function of input power. It is an important metric for power amplifiers, as the gain must remain relatively constant over a wide range of input powers to ensure good performance. S12 and S22 are the same type of parameter under the reverse signal excitation to the MWPA. Since the input signal is not going to be applied from the output port for proposed PA, the numerical calculations of S12 and S22 does not included in this study. Reflection and transmission coefficients of QPD350 are indicated, in Figure 4.8.

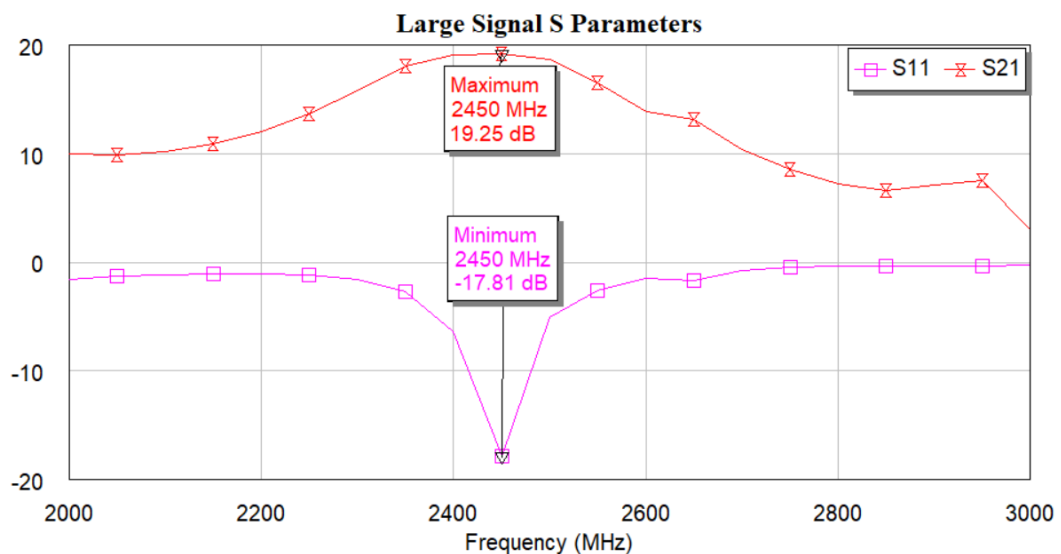


Figure 4.8: Reflection and transmission coefficients of QPD350 at 2.45 GHz.

A large signal S11 parameter of -17.81 dB for proposed PA. It is desirable for good matching between the input signal and the amplifier, as this implies that less power is being reflected towards the source. Concordantly, only 71 mW reflected power converted to heat in input SMA connector when 4.3 W input power is applied to designed PA under that S11 value. Since this heat generated in the SMA connector is at a very low level, it does not damage either the input port of the power amplifier or the output port of the preamplifier connected to it. In addition, the reflected microwave power in the order of milliwatts is much lower than the withstand power of many circuit elements. Thus, the preamplifier stage maintains its function without being damaged by the reflected power.

Creating a high gain value is very important for this study because a high level of input power and therefore high gain is needed to create the targeted output power of 350 W. Large signal S21 parameter of 19.25 dB means that the output power of the amplifier is 19.25 dB higher than the input power at 2.45 GHz. This level of gain is considered relatively high for a power amplifier, and suitable for some high-power applications like microwave thermal ablation that require a significant increase in signal strength. The value of 19.26 dB large signal S21 keeps the input power requirement to 4.3 W, which most of the power amplifier can provide that power.

The output power of a QPD350 is the power delivered to the load or antenna. The output power is determined by the input power and the gain of the amplifier. The power-added efficiency (PAE) of a microwave power amplifier is the ratio of the output power to the input power without the DC power consumption. It is expressed as a percentage. PAE is a measure of how efficiently the amplifier converts DC power into RF power. A higher PAE means that the amplifier is more efficient and wastes less power as heat. The gain of a microwave power amplifier is the ratio of the output power to the input power. It is usually expressed in decibels (dB) or as a linear ratio. Gain is a measure of how much the amplifier amplifies the input signal. The output power, PAE, and gain are all important parameters that describe the performance of a microwave power amplifier. The output power is the power delivered to the load or antenna, PAE is a measure of efficiency, and gain is a measure of amplification.

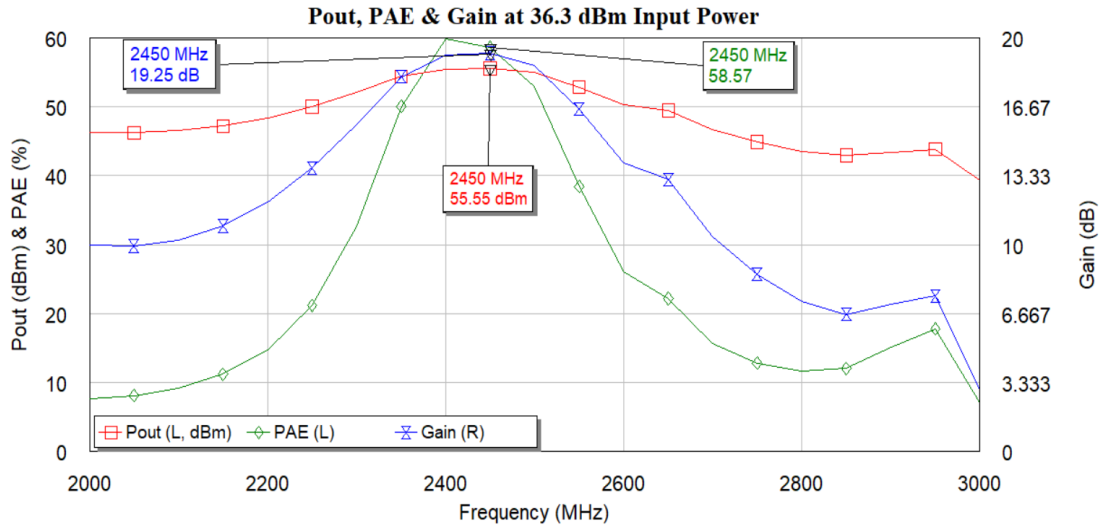


Figure 4.9: Output power, PAE and Gain of proposed PA.

In Figure 4.9, the gain of proposed PA is 19.25 dB at 2.45 GHz to be the same with large signal S21 value of it, As stated in subsection 4.4.1. When 36.3 dBm input power is applied to input port of the QPD350, it amplifies to 55.55 dBm microwave power level at 2.45 GHz. It means that the output microwave power is 350 W in linear scale higher than the solid-state microwave power amplifier design studied in literature. Providing high microwave output power is predicted to produce a rapid temperature increase in the target tissue for microwave ablation applications. In this way, ablation temperatures can be reached in a short time and the patient can be treated in a way that feels less pain.

The 3 dB bandwidth is also an important performance parameter for QPD350, as it determines the range of frequencies over which the amplifier can operate effectively. The 3 dB bandwidth is the frequency range over which the output power level is within 3 dB of the maximum output power level. Since the 3 dB bandwidth of designed PA is 300 MHz, it can handle a larger range of frequencies and are more versatile.

In addition, the PAE value is also higher than many PA designs in the literature. Although there is % 50 PAE theoretically in A class PA topology, this value has been exceeded thanks to the QPD2795 HEMT, whose design has been optimized to create a maximum of % 72 PAE during the fabrication phase. As shown in Figure 4.9, the PAE value of proposed MWPA is % 58.57. Although high PAE is compromised in PA designs with high gain value, the optimization work in section 4.3 also resulted in an acceptably high PAE.

The 1 dB compression point of an amplifier is a measure of its nonlinearity and is defined as the input power level at which the output power of the amplifier is reduced by 1 dB (decibel) from its linear gain value. At the 1 dB compression point, the amplifier's output power is compressed, and further increases in input power will result in less than proportional increases in output power. The 1 dB compression point is an important performance parameter of an amplifier, particularly in applications where the amplifier is required to deliver a high level of output power while maintaining good linearity. In such cases, it is desirable to have an amplifier with a high 1 dB compression point, which means that it can operate at higher input power levels before the output power is compressed. The 1 dB compression point of QPD350 is given in Figure 4.10.

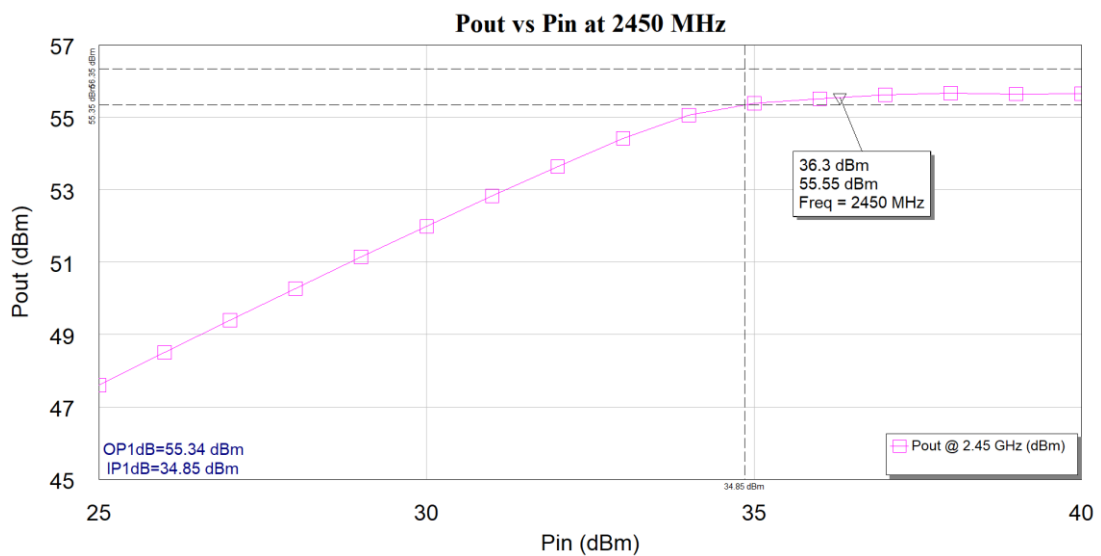


Figure 4.10: Output power versus input power graph of proposed PA.

Based on the values provided in Figure 4.10, proposed microwave PA has an IP1dB (input power at 1 dB compression point) of 34.85 dBm and an OP1dB (output power at 1 dB compression point) of 55.34 dBm. This indicates proposed amplifier has a high level of output power, as the OP1dB value is significantly higher than the IP1dB value. This suggests that the amplifier can deliver a large amount of power to the load before its output power starts to compress. It is important to ensure that the proposed QPD350 is used within its specified operating conditions and that any load or impedance mismatches are avoided to prevent damage to the amplifier and to ensure optimal performance.

The power spectrum of harmonics refers to the distribution of power across different frequencies in a signal that is composed of harmonics. Harmonics are integer multiples of a fundamental frequency, and they have amplitudes and phases that depend on the specific signal being analyzed. The power value returned by an analysis of a periodic waveform may be expressed as the sum of the RMS power components at each harmonic of the fundamental frequency as shown in Figure 4.11.

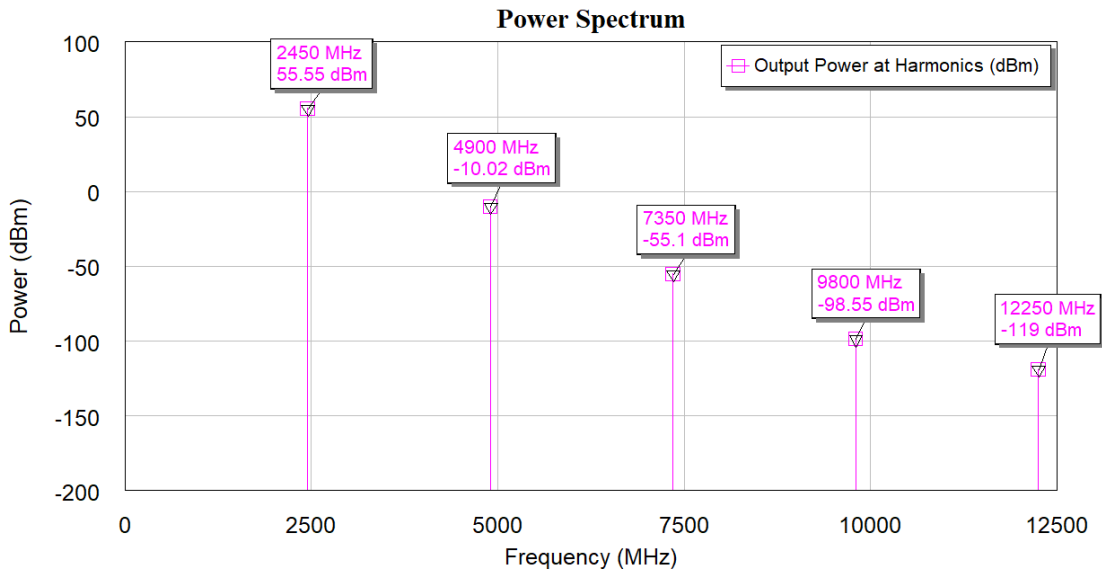


Figure 4.11: Power spectrum of harmonics graph of proposed PA

In the proposed QPD350, it is important to minimize the level of harmonic distortion in the output signal. Harmonic distortion can occur due to nonlinearities in the amplifier, which can generate unwanted harmonics of the input signal. From Figure 4.11, the first harmonic has a power level of 55.55 dBm. This is the desired output power of the amplifier at the fundamental frequency. The 2nd harmonic has a power level of -10.15 dBm, which is 65.57 dB below the first harmonic. This power difference also gives a harmonic distortion value. For the 3rd harmonic, the harmonic distortion is 110.6 dB lower than the fundamental frequency at a power level of -54.74 dBm. In this way the, as the harmonic increases, the harmonic distortion decreases, and the harmonic distortions of the 4th and 5th harmonics, which are -97.47 dBm and -116.6 dBm, respectively, are 154.1 dB and 174.7 dB, respectively. Since the power levels of the second, third, fourth, and fifth harmonics are all significantly lower than the desired output power, indicating that the amplifier is operating with low levels of harmonic distortion.

Proposed PA is designed to amplify high-frequency signals, in the microwave frequency range. The amplification of these signals is often measured in terms of both current and voltage amplification. Current amplification, also known as gain, is a measure of how much the input current is increased by the amplifier while voltage amplification, also known as voltage gain, is a measure of how much the input voltage is increased by the amplifier. The current and voltage gain of a microwave power amplifier depends on the design of the amplifier and the operating frequency. The instantaneous voltage and current amplification graphs of proposed QPD350 with optimum design at 2.45 GHz operating frequency is indicated in Figure 4.12.

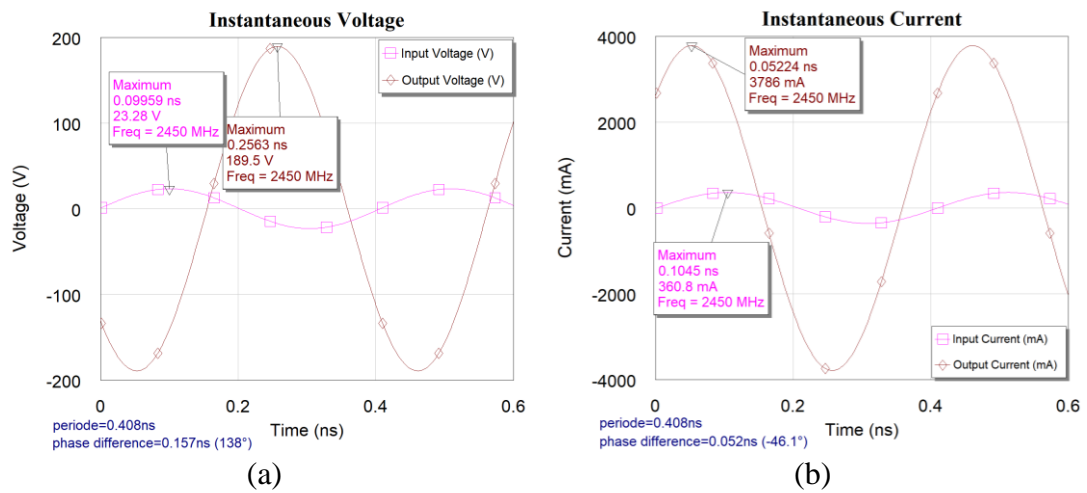


Figure 4.12: Input versus output (a) voltage and (b) current of QPD350

The current and voltage amplification of a microwave power amplifier are related by the input and output impedance of the amplifier. In general, a higher current gain is achieved by a lower output impedance and a higher voltage gain is achieved by a higher output impedance. As seen in Figure 4.12, the input current is amplified from 360.8 mA to 3786 mA and input voltage from 23.28 V to 189.5 V at 2.45 GHz by using QPD350. As the current gain is 10.49 and the voltage gain is 8.14, 85 times power gain occurs in proposed PA. This value is also the linear scale expression of 19.25 dB gain value calculated in Section 4.4.1 and Section 4.4.2. This high current and voltage amplification can result in lower power dissipation and heat generation, which can be beneficial for prolonging the lifetime of the device and reducing cooling requirements. In addition to the current and voltage gains, there are also changes in the phase of the PA output signal. The output current of an MWPA is lagging behind the input current by 46.1° while the output voltage of this is leading the input voltage by 138°.

4.6 Manufacturing Process of the Proposed QPD350

The fabrication of high-power microwave amplifiers is a complex and challenging process that requires expertise in various areas such as electromagnetics, microwave engineering, solid-state physics, and device fabrication. These amplifiers are used in a variety of applications that require the amplification of electromagnetic waves within the microwave frequency range.

The design of a high-power microwave amplifier involves the selection of the appropriate materials and components, such as transistors, capacitors, and inductors, which must be capable of withstanding high-power levels and operating within the desired frequency range. The design must also take into account factors such as thermal management and electromagnetic interference.

High-power transistors are a critical component of a high-power microwave amplifier. They must be capable of handling the high-power levels and operate at the desired frequency range. Gallium nitride (GaN) transistors are commonly used in high-power microwave amplifiers due to their high-power handling capabilities and low on-resistance.

Capacitors are used to store and discharge electrical energy in the amplifier. High-power capacitors must be able to handle the high voltages and currents present in the amplifier. For example, high-voltage ceramic capacitors with low ESR and ESL (Equivalent Series Resistance and Inductance) are often used in high-power microwave amplifiers. In this study ATC brand capacitors are preferred due to low ESR, ESL and high voltage capabilities. Whereas any inductor does not used in the proposed QPD350. Capacitors are generally preferred to inductors in high power microwave amplifiers because they have several advantages over inductors such as efficiency, compact size, and high frequency response are critical factors. Capacitors are smaller in size than inductors, making them more practical for high power microwave applications where space is often at a premium. Another advantage is that capacitors have a faster response time than inductors, making them better suited for high frequency applications. They also typically have lower losses than inductors, which means they are able to transfer more energy with less power loss. In addition to that they can handle higher voltages than inductors, making them suitable for use in

high power microwave amplifiers. Moreover, that can be easily fabricated using a variety of materials and processes, whereas inductors are often more difficult and expensive to manufacture.

High-power microwave amplifiers generate a significant amount of heat, which must be dissipated to prevent damage to the components and ensure reliable operation. Effective thermal management techniques such as heat sinks, fans, and liquid cooling systems must be incorporated into the design to keep the temperature within safe limits. As indicated in Figure 4.13(b), aluminum heat sink is connected to back side of QPD350 board via thermal paste in order to expand the heat due to the high-power generation.

High-power microwave amplifiers can generate significant electromagnetic interference (EMI) that can interfere with other electronic devices. The design must take into account measures such as shielding, filtering, and grounding to minimize EMI. Lots of vias is used, as shown in Figure 4.13(a) and Figure 4.13(b), to avoid high order electromagnetic power interference.

Successful fabrication of high-power microwave amplifiers requires advanced knowledge of microwave circuit design principles and materials science, as well as the ability to develop and use sophisticated testing equipment and techniques to ensure optimal performance. Microwave circuit design principles involve designing circuits that can amplify high-frequency signals while minimizing losses and maintaining stability. Materials science knowledge is crucial in selecting materials with the appropriate properties for the specific application, such as low-loss dielectric materials and high thermal conductivity materials. Properties of commonly used materials in QPD350 design is indicated in Table 4.4.

Table 4.4: Properties of commonly used materials in QPD350 design

Material	Electron Mobility	Breakdown Voltage	Thermal Conductivity	Cost
GaAs	High	Moderate	Low	High
Si	Low	Low	Moderate	Low
InP	High	High	Moderate	High
SiC	High	High	High	High
GaN	High	High	Moderate	High

The table provides information on five materials (GaAs, Si, InP, SiC, and GaN) based on their electron mobility, breakdown voltage, thermal conductivity, and cost. GaAs, InP, SiC, and GaN have high electron mobility, making them well-suited for high-speed electronic applications, while Si has low electron mobility. Si, SiC, and GaN exhibit high breakdown voltage, indicating their ability to withstand high voltages. SiC and GaN have high thermal conductivity, making them good candidates for applications requiring efficient heat dissipation. Although Si is the cheapest materials in table it is not preferred because the price is the less priority in high power microwave application. To achieve the desired performance, high power microwave amplifiers require specialized materials such as GaN and InP. GaN has a high electron mobility and high breakdown voltage, which allows it to operate at high frequencies and handle high power levels while InP, low noise characteristics, which make it ideal for low-noise amplifier applications. In this study GaN based HEMT is preferred to achieve high microwave power.

The choice of substrate is critical in high power microwave amplifier design because it can have a significant impact on the amplifier's performance, reliability, and cost. Selecting the appropriate substrate that meets the required performance specifications and can withstand the high power and temperature conditions is crucial for designing an efficient and reliable high power microwave amplifier. Substrate electrical, thermal and mechanic properties of commercially available Rogers substrates are shown in, Table 4.5.

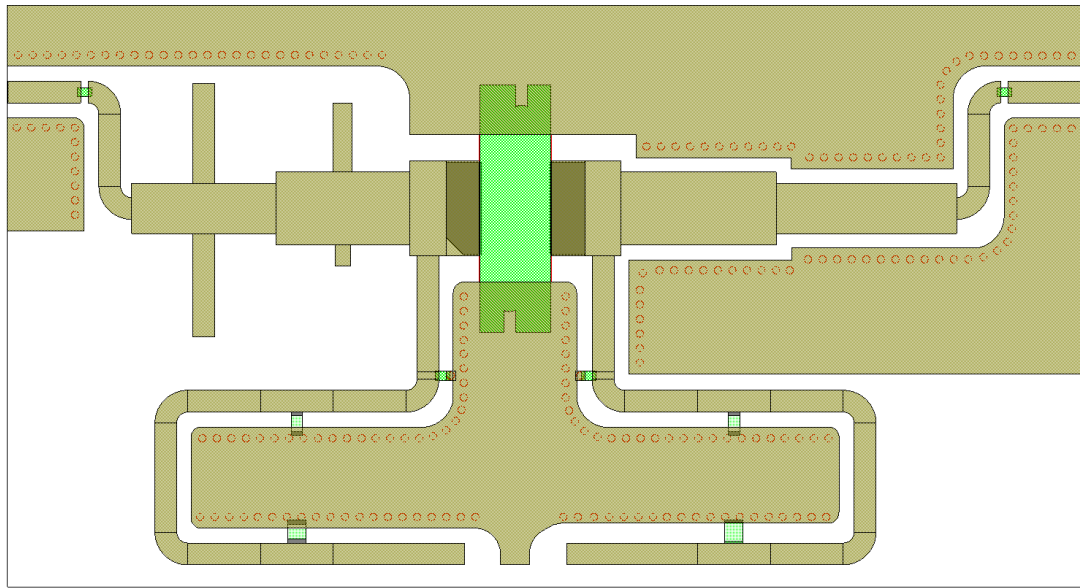
Table 4.5: Substrate properties of commercially available Rogers substrates.

Property	RO4003C	RO4350B	RO4360G2	RO4835	RO5880
Dielectric constant	3.38	3.48	6.15	3.5	2.25
Loss tangent	0.0027	0.0037	0.0025	0.003	0.0009
Thermal conductivity W/(m·K)	0.69	0.44	0.43	0.38	0.27
Coefficient of thermal expansion (ppm/°C)	17	14	12	15	12 - 13
Decomposition temperature (°C)	> 500	> 500	> 500	> 400	> 500
Surface resistivity (MΩ/sq)	> 10	> 10	> 10	> 10	> 100
Dielectric breakdown voltage (kV)	> 60	> 40	> 35	> 35	> 45

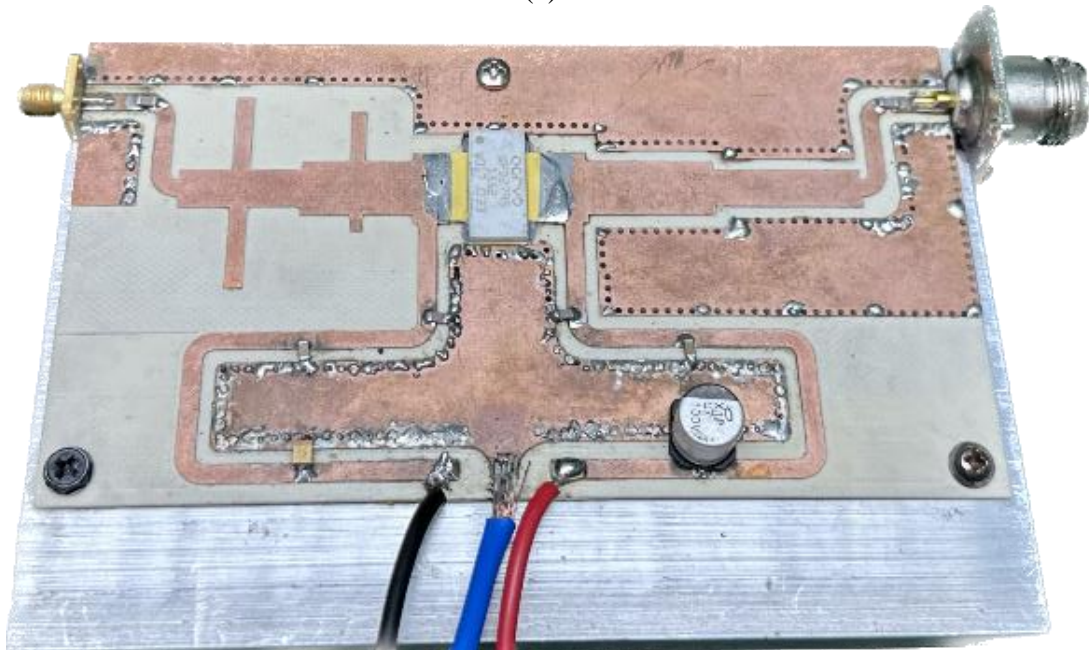
Based on the properties listed in Table 4.5, the Rogers 4003C appears to be a better choice for high power microwave amplifier design compared to the other materials listed. The RO4003C has a relatively low dielectric constant of 3.38, which makes it a suitable material for microwave circuits with high-frequency applications. Its low loss tangent of 0.0027 indicates that it has a low level of dissipation, making it ideal for high-power microwave amplifier design. Additionally, the RO4003C has the highest thermal conductivity of all the materials listed, which indicates that it can effectively dissipate heat generated during high power applications. The RO4003C also has a high dielectric breakdown voltage and a high decomposition temperature, indicating that it can withstand high temperatures and high voltage conditions. Overall, the Rogers 4003C is a preferred material for high power microwave amplifier design due to its low loss tangent, high thermal conductivity, and ability to withstand high temperatures and voltages.

Microwave power amplifier (PA) fabrication is a complex process involving multiple stages from layout design to PCB assembly. This process begins with the creation of a layout using specialized software tools, which is then converted into masks for patterning the device layers. The wafer processing stage follows, where thin films of materials such as silicon, metal, and dielectric are deposited and etched to create the device. After testing to ensure the device meets required specifications, it is packaged in a housing and mounted on a PCB with other components. Quality control is crucial throughout the entire process to achieve optimal device performance.

QPD350 fabrication involves several stages, including layout, Gerber file generation, packaging, and printed circuit board (PCB) assembly. The design of the PA is created using AWR Microwave Office. The layout in Figure 4.13(a), includes the physical dimensions of the device, the placement and interconnection of the various components, and the routing of the transmission lines. The layout is then converted to Gerber file, which are used to pattern the layers of the device. The Gerber file is used to pattern the layers of the device on a PCB. After the devices have been fabricated, they are packaged in a suitable housing. As indicated in Figure 4.13(b), the packaged devices are mounted on a printed circuit board (PCB) along with other components, such as bias networks, filters, and matching circuits. The PCB layout is designed to minimize parasitic effects that can degrade the performance of the PA.



(a)



(b)

Figure 4.13: (a) Layout and (b) fabricated prototype of proposed QPD350

In Figure 4.13, it is considered a recommended practice to incorporate a solid ground plane. This can aid in reducing noise and interference in the circuit by means of utilizing ground vias to interconnect the top and bottom ground planes. In this scenario, it is crucial to ensure that the ground vias are arranged to encompass the maximum available area, while being positioned in proximity to the respective components to maintain the same ground reference as the QPD2795 decoupling capacitors. The implementation of an RO4003 board and an aluminum block affixed with an M4 screw to secure QPD2795 can also provide effective heat dissipation. This is of utmost

importance, as amplifiers can generate heat, and overheating can have detrimental effects on the amplifier's performance and may even cause damage to the electronic components.

The successful soldering of high-power microwave transistors demands meticulous attention to detail and the utilization of appropriate tools and techniques to prevent any potential damage to the device. Adhering to established guidelines is imperative to ensure a successful soldering process and to attain optimal performance of the transistor in the amplifier. The soldering process for high-power transistors necessitates the use of a high-temperature soldering iron capable of withstanding the elevated temperatures produced during operation. It is typically recommended that a soldering iron with a temperature range of 350 °C to 400 °C be employed. To safeguard the transistor from overheating and damage, it is essential to use a heat sink, which is placed on the transistor's backside to absorb heat generated by the device. Additionally, a small amount of solder paste may be applied to the terminals of the transistor to facilitate the creation of a robust bond. Prior to connecting the component, the soldering iron is applied to the connection surfaces individually. Then, the individually soldered surfaces are brought together using indirect heating to prevent the transistor from directly heating. After completing the soldering process, a thorough inspection of cold solder joints must be conducted. Cold solder joints are characterized by incorrect solder flow, resulting in a weak bond. Cold solder joints may cause signal distortion and result in diminished amplifier performance. Upon completion of the soldering process, cleaning the transistor surface with isopropyl alcohol is crucial to remove any residual flux that may have been left behind.

In the Subsection 4.7, "Evaluating MWPA Performance in MWA Study", the performance of the proposed QPD350 is thoroughly assessed. The focus is on evaluating key parameters such as power output, power-added efficiency, gain, time dependent temperature and stability. The results are compared to existing studies to highlight the superiority of the proposed design. Additionally, considerations for heat dissipation and soldering techniques are discussed to ensure optimal performance and component protection. The section provides valuable insights into the performance evaluation and practical implementation of the QPD350 in the context of the MWA study.

4.7 Evaluating QPD350 Performance in MWA Study

Microwave power amplifiers have gained widespread use in various application domains, highlighting the need for accurate testing procedures for these devices. This thesis subsection endeavors to provide an account of the outcomes of studies conducted on the testing of microwave power amplifiers. Figure 4.14 shows the experimental measurement setup of QPD350.

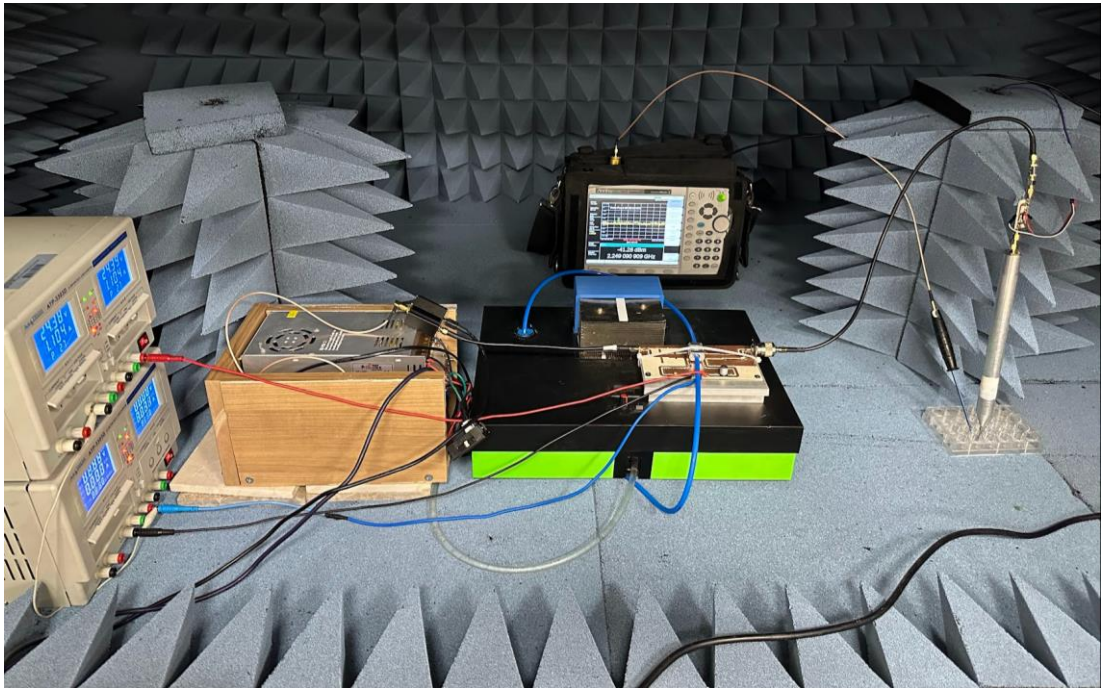


Figure 4.14: Experimental measurement setup including the microwave ablation of in vitro prostate cancer using QPD350.

In the depicted circuit illustrated in Figure 4.14, the MFMWAP was interconnected with the proposed amplifier's output. Various analyses were performed using a thermal camera, an electric field analyzer, and an RF probe. The MFMWAP serves to amplify the microwave signal originating from the broadband low-power amplifier signal generator, yielding a microwave power range of 14-19 dBm at the input of the QPD350. Measurements of the output power using the RF probe enable the determination of input-output power (P_{in} - P_{out}) and input power-gain (P_{in} -Gain). Moreover, by applying a direct current (DC) power supply capable of delivering up to 48 volts and 3 amps, the input-power added efficiency (P_{in} -PAE) is assessed. Figure 4.15 presents the measured current-voltage characteristic of the QPD350 solely under DC power, accompanied by the associated transistor temperature.

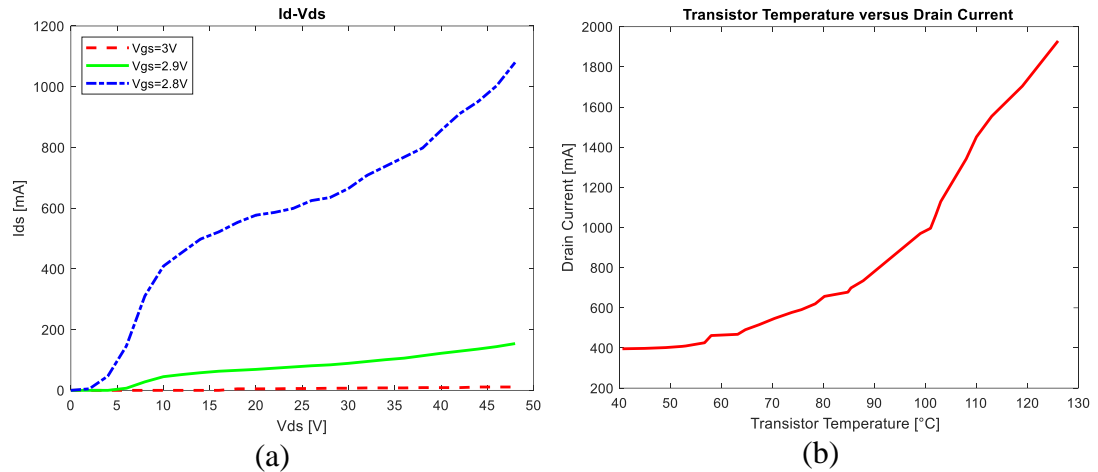


Figure 4.15: (a) Drain current versus drain-source voltage graph and (b) drain current versus transistor temperature graph of proposed MWPA.

In Figure 4.15(a), a graph is presented depicting the application of DC supply voltages ranging from 0 V to 48 V between the drain-source terminals and -3 V, -2.9 V, and -2.8 V between the gate-source terminals. The resulting drain current is measured. At a gate voltage of -3 V, the QPD2795 transistor operates in the initial conduction state, yielding a drain current of less than 10 mA. However, with a gate voltage of -2.9 V, the drain current exhibits nearly linear growth, reaching up to 154 mA. Subsequently, when the gate voltage is set to -2.8 V, a significant increase in drain current is observed, accompanied by a non-linear rise in drain voltage exceeding 1 A due to the high output power. These measured currents cause the transistor's temperature to gradually increase over time, as depicted in Figure 4.15(b). Considering the QPD2795 transistor's tolerance of 6 minutes at 250 °C, it can be utilized without causing damage, even when it reaches a surface temperature of 125 °C during the occurrence of a 2 A drain voltage. However, since the use of the transistor at higher temperatures will cause noise, it was found appropriate to reduce the temperature with liquid cooling.

It is important to consider that the stability of an amplifier circuit is often dependent on the frequency due to the influence of input and output matching networks, which typically vary with frequency. This means that an amplifier can exhibit stability at its intended design frequency but may become unstable at other frequencies. When designing an amplifier, careful attention should be given to account for this possibility. Furthermore, it is worth noting that the discussion regarding stability in this context is specific to two-port amplifier circuits, particularly those involving negative impedance converters, where the scattering parameters of the active device can be measured

without encountering oscillations within the frequency range of interest. For a comprehensive and rigorous treatment of stability, it is necessary to ensure that the network scattering parameters (or other relevant network parameters) do not possess poles in the right-half complex frequency plane. Additionally, satisfying the conditions $|\Gamma_{in}| = 1$ and $|\Gamma_{out}| = 1$ is crucial in evaluating stability.

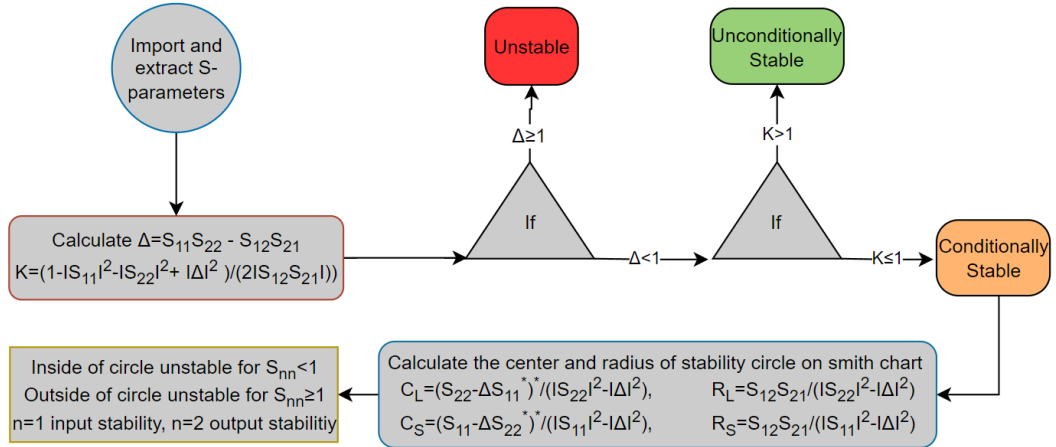


Figure 4.16: The algorithm for determining stability, including the K- Δ test.

As depicted in the algorithm presented in Figure 4.16, the S-parameters of the QPD350 circuit are imported into the MATLAB program, and both the frequency and S-parameters are stored in an array. Subsequently, the stability factor (Δ) is calculated, and its absolute value is examined to determine if it exceeds 1. This evaluation is crucial in assessing the stability of the QPD350.

If the stability factor (Δ) is found to be greater than 1, it indicates that the amplifier circuit is unstable. In this case, the amplifier may exhibit oscillations or instability issues that can lead to undesirable performance, such as distortion or even damage to the circuit components. It is essential to address the stability concerns by redesigning the circuit or implementing stability-enhancing techniques to ensure reliable and proper operation of the amplifier. If the stability factor (Δ) is found to be less than 1, further analysis is performed using the K-factor. The K-factor is calculated and if its value is greater than 1, it indicates that the QPD350 circuit is unconditionally stable. This means that the amplifier circuit is inherently stable and will maintain its stability regardless of variations in operating conditions or external factors. The K-factor serves as an additional criterion to ensure the robustness and reliable performance of the amplifier circuit.

If the K-factor is found to be less than 1 it indicates that the circuit is conditionally stable, which implies that certain operating conditions or external factors may lead to instability. To determine the range of stability for the conditionally stable condition based on the μ -factor test, it is essential to identify the region in which the circuit remains stable. To achieve this, the equations involving $|\Gamma_{in}| = 1$ and $|\Gamma_{out}| = 1$ are solved in conjunction with the S parameters, leading to the formulation of circle expressions. In instances where the magnitudes of $|S_{11}| < 1$ and $|S_{22}| < 1$ are small, the interior regions of the input and output circles respectively indicate an unstable situation. Conversely, if $|S_{11}| \geq 1$ and $|S_{22}| \geq 1$, the outer region of the circle is deemed unstable.

Where C_L and C_S are center; R_L and R_S are radius of input and output stability circle, respectively. Based on the computations performed in the MATLAB utilizing the stability test algorithm, the frequency-dependent K- Δ parameters presented in Figure 4.17 were derived, and subsequently, the stability status was interpreted.

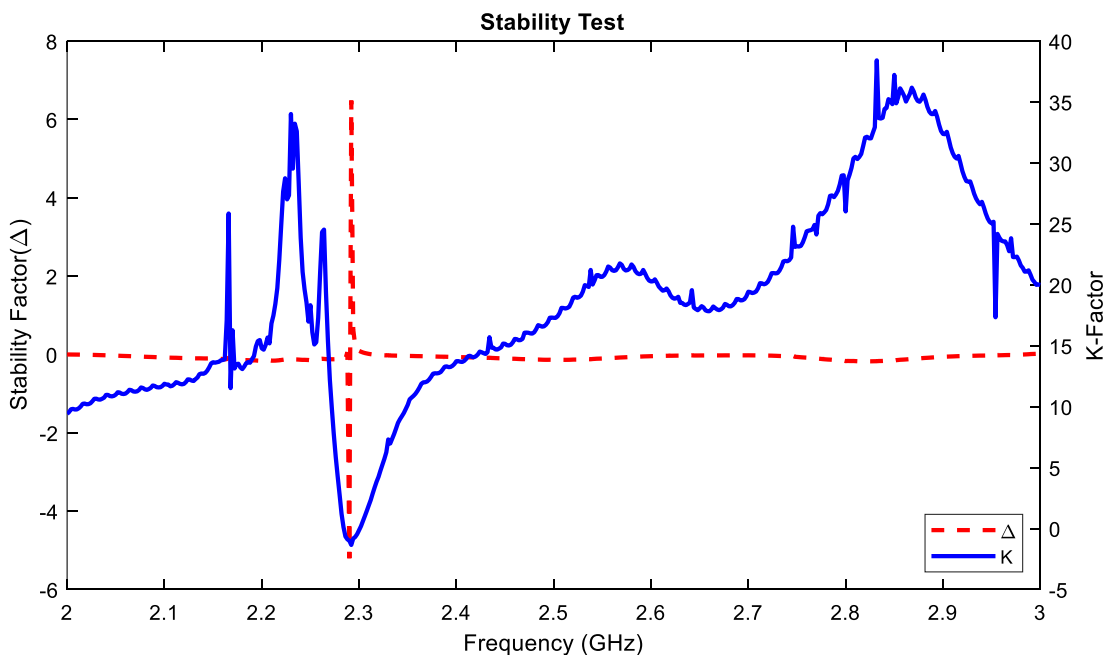


Figure 4.17: Stability determination graph via K- Δ test

The information in Figure 4.17 provided pertains to the stability analysis of an NIC across different frequencies. According to the given K- Δ test graph, the QPD350 is declared to be “unconditionally stable” at specific frequencies from 2 GHz to 2.32 and from 2.46 GHz to 3 GHz. This assertion signifies that the amplifier inherently maintains stability at these frequencies, regardless of the operational conditions or

external influences. It implies that the amplifier consistently delivers reliable and predictable performance without any concerns related to stability. However, at certain frequencies, the stability of the amplifier becomes “conditionally stable.” For proposed NIC, in the frequency range from 2.322 GHz to 2.33 GHz, the stability of the amplifier is dependent on specific operational conditions or the presence of external factors. These conditions, also known stability circles, are illustrated in Figure 4.8. Consequently, it suggests that additional measures or adjustments may be necessary to ensure stable operation at these frequencies. Lastly, at 2.336 GHz and 2.338 GHz, the amplifier is deemed “unstable.” This indicates that the amplifier fails to exhibit the desired performance characteristics at these frequencies, thereby manifesting oscillatory behavior or other forms of instability as shown in Figure 4.18.

Input and Output Stability at 2328 MHz

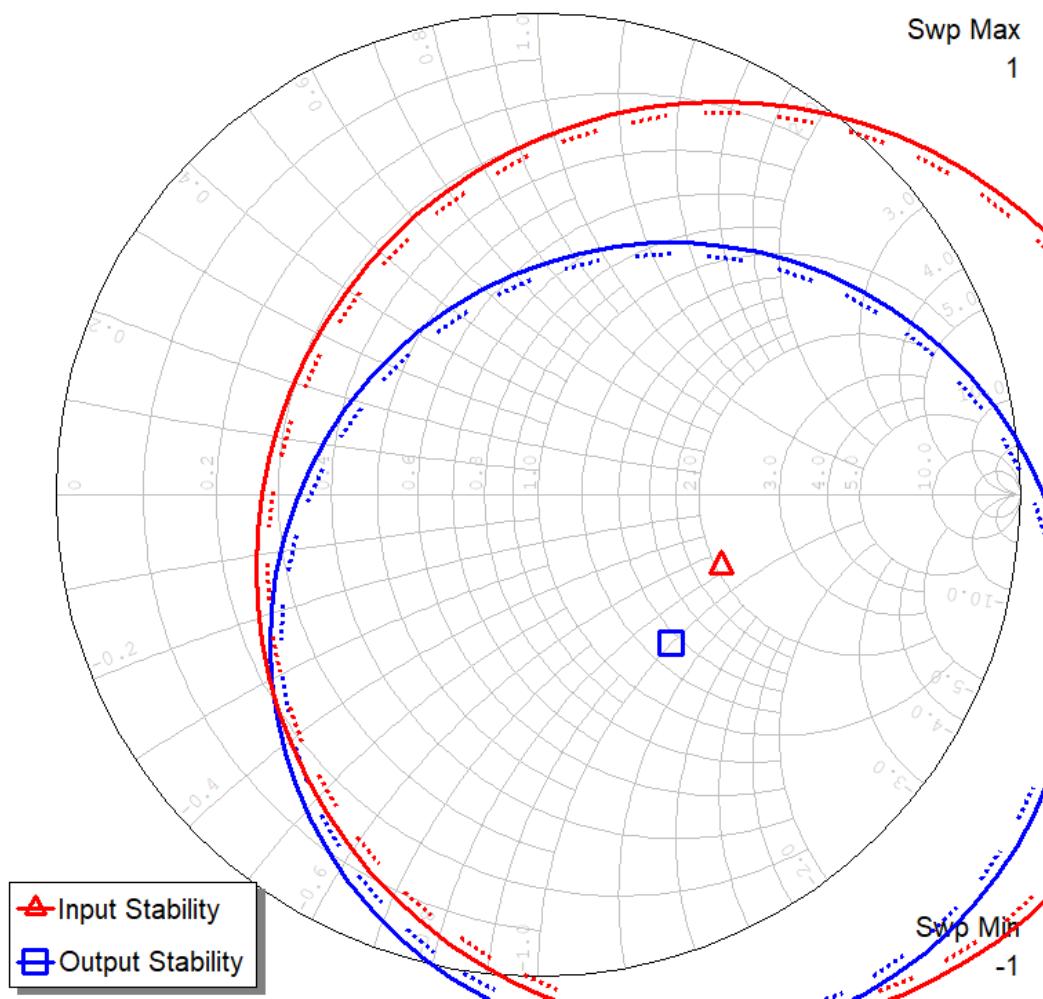


Figure 4.18: Input and output stability circles of NIC, $V_{cc}=12$ V.

The regions within the stability circles are considered unstable as they satisfy the condition $|S_{11}| < 1$ and $|S_{22}| < 1$. In Figure 4.18, it is observed that the input of QPD350 remains stable for every load at a frequency of 2320 MHz. As the frequency increases from 2320 MHz to 2336 MHz, the range of source impedance leading to instability expands until the stability circles vanish on the Smith chart. Above 2336 MHz, an unconditionally stable situation is established for the input of QPD350.

The output stability circles reveal that the load impedance causing instability remains outside the Smith chart below 2320 MHz, like the input stability circle. Conversely, when the load impedance is 50Ω or close to that value, the system becomes unstable within the frequency range of 2320 MHz to 2344 MHz. Due to the narrow range of stable load operation within this frequency range, it is advisable to utilize the proposed QPD350 circuit within the unconditionally stable frequency range. In addition to stability, S_{21} of the QPD350 under -2.9 V gate voltage was measured to design impedance matching circuit that will increase the power transfer in Figure 4.19.

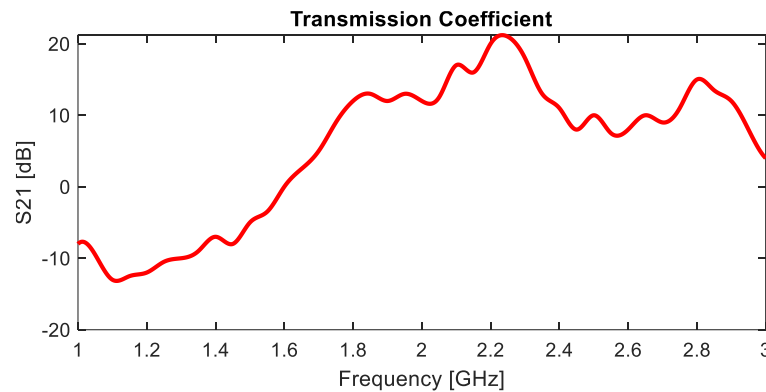


Figure 4.19: S_{21} measurement result of QPD350, $V_{GS}=-2.9 \text{ V}$

In Figure 4.19, the frequency at which the transmission coefficient of the QPD350 is the highest with 20 dB is 2.25 GHz. Once the DC characteristics of the amplifier were determined, microwave signals ranging from 13-20 dBm were applied, and the resulting output power, gain, and PAE were subjected to analysis. The outcomes of these analyses are presented in Figure 4.20(b), Figure 4.20(c) and Figure 4.20(c) illustrates the results obtained by employing an open circuit stub matching (OCSM) technique. This matching approach was specifically devised to establish compatibility between the QPD350 and MFMWAP at a frequency of 2.45 GHz. On the other hand, Figure 4.20 showcases the outcomes obtained by integrating NFC-based NIC matching, as designed in the preceding section, into the same system.

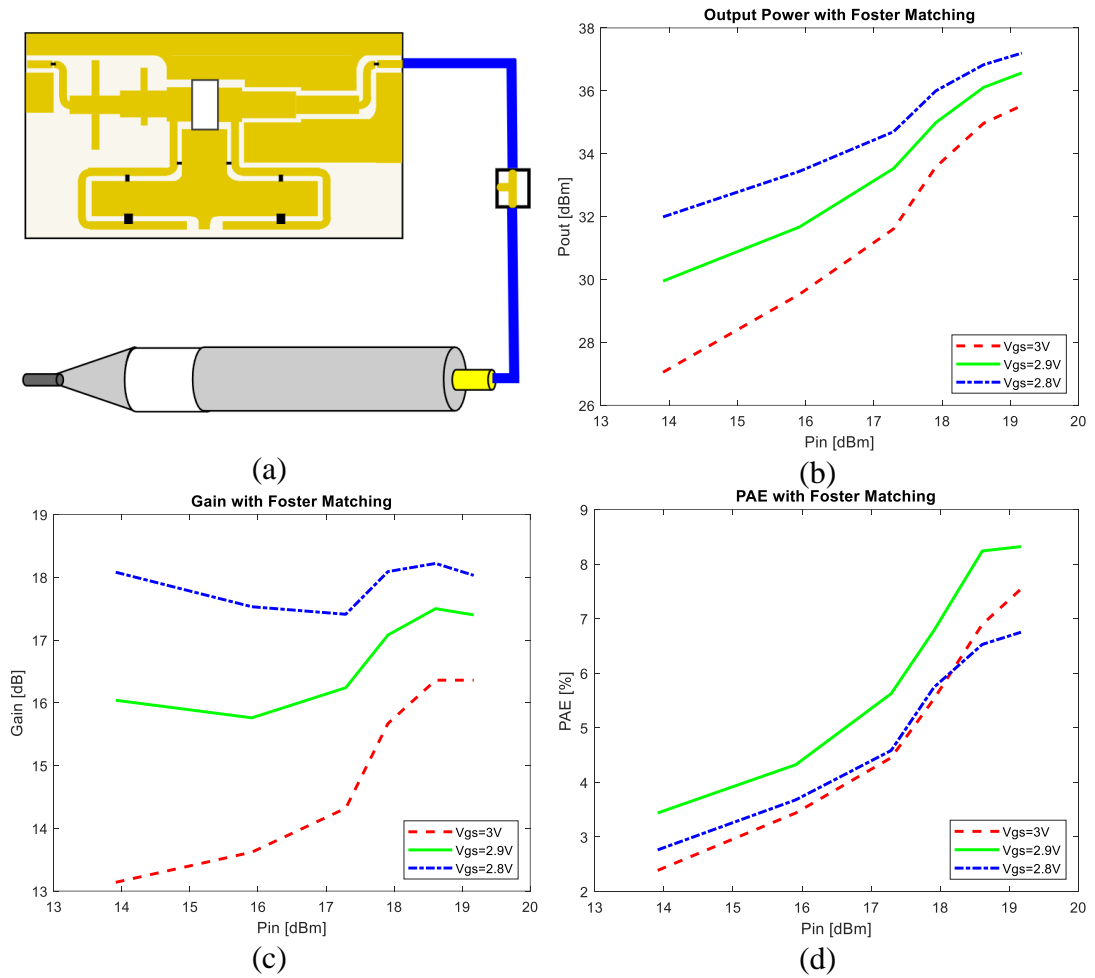


Figure 4.20: (a) Block diagram, (b) output power, (c) gain and (d) PAE of QPD350 with Foster Matching

The block diagram in Figure 4.20(a) illustrates the connection of OCSM between the proposed PA and MFDWAP. Their performance is evaluated at a microwave input power range of 14-19 dBm and a frequency of 2.25 GHz. Figure 4.20(b) displays the output power characteristics. At an input power of 13 dBm, the obtained output powers are 27.05 dBm, 29.53 dBm, and 31.99 dBm when gate voltages of -3 V, -2.9 V, and -2.8 V are applied, respectively. As the input power increases up to 17 dBm, a nearly linear relationship is observed with a decrease in the factor between the gate supplies. Upon further increase in the input power, the graph exhibits a decreasing exponential trend, resulting in output power levels of 37.2 dBm for each gate voltage.

The gain characteristics depicted in Figure 4.20(c) exhibit a direct relationship between the gain values and the gate supply. Specifically, at a gate supply of -3 V, the gain increases within the range of 14-17 dBm. Conversely, when a gate supply of -2.8 V is applied, a decreasing trend is observed within the same range. The gain values, while

being supplied with -2.9 V at the gate, exhibit a nonlinear behavior. They decrease within the range of $14\text{-}16\text{ dBm}$ and then increase within the range of $16\text{-}17\text{ dBm}$. This behavior is attributed to the unique nonlinear characteristics of the proposed PA. Despite the fact that the input power of up to 17 dBm falls below the dynamic region for the QPD350, the observed increase in gain across all three gate supplies for signals above this threshold suggests a more suitable operating range.

As observed in Figure 4.20(d), the -2.9 V gate voltage exhibits a higher PAE, compared to the other voltages. Additionally, the -3V gate voltage yields a higher PAE than the -2.8 V gate supply up to an input power of 18 dBm . However, this relationship reverses as the input power is further increased. Across all three gate supplies, the PAE demonstrates a direct proportionality with the input power. Nevertheless, for input signals exceeding 18 dBm , a sharp decrease in the gate voltage ratio is observed, primarily due to transistor heating rather than an increase in efficiency.

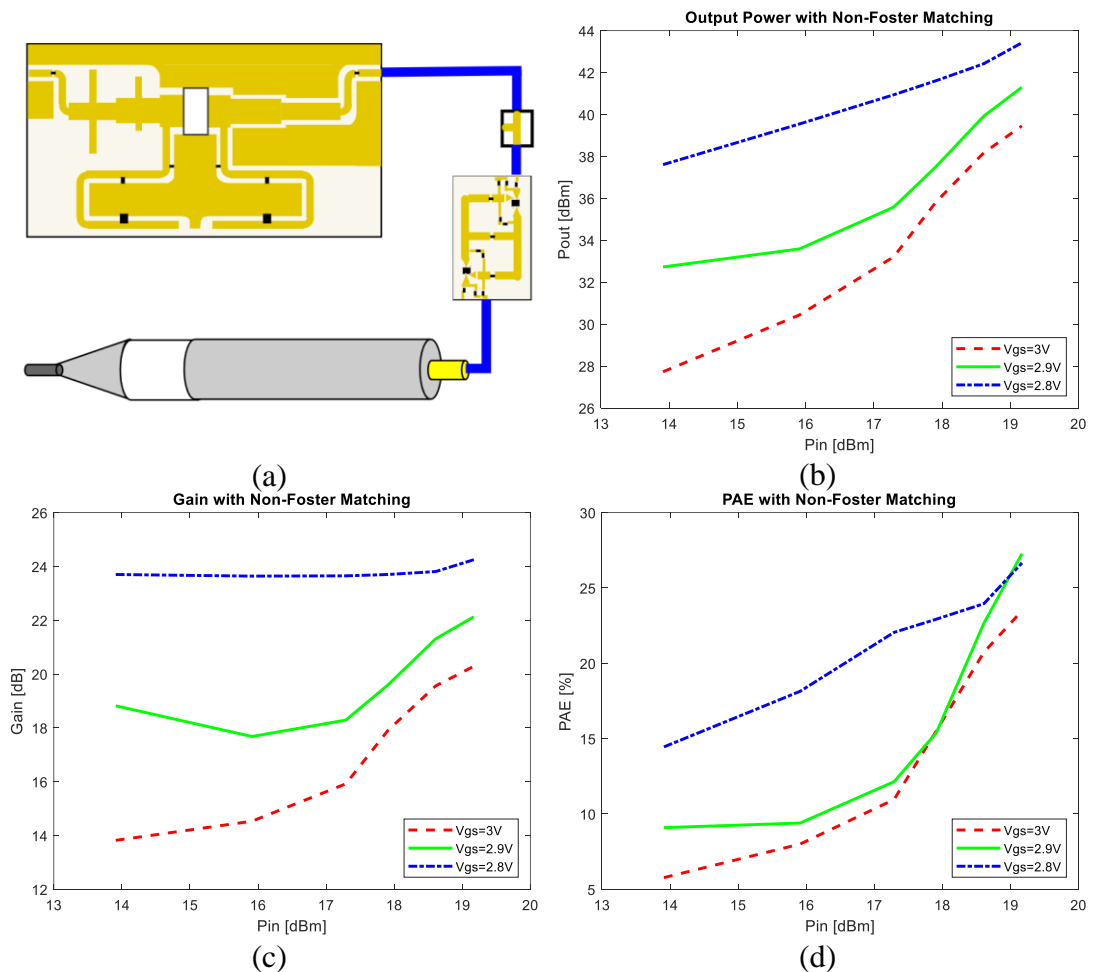


Figure 4.21: (a) Block diagram, (b) output power, (c) gain and (d) PAE of QPD350 with Non-Foster Matching

Figure 4.21(a) depicts the block diagram illustrating the interconnection of OCSM and Non Foster NIC between the proposed QPD350 and MFDWAP. Their performance evaluation focuses on a microwave input power range of 14-19 dBm at a frequency of 2.25 GHz. In Figure 4.21(b), the graph presents the characteristics of the output power. At an input power of 13 dBm, the respective output powers are 27.73 dBm, 32.73 dBm, and 37.61 dBm for gate voltages of -3 V, -2.9 V, and -2.8 V. A nearly linear relationship is observed as the input power increases up to 17 dBm, coinciding with a reduction in the gate supply factor. Subsequently, with further increments in the input power, the graph exhibits a decreasing exponential trend for each gate voltage. Additionally, Output power levels of 39.46 dBm, 41.3 dBm and 43.42 dBm for gate voltages of -3 V, -2.9 V and -2.8 V, respectively.

The gain characteristics illustrated in Figure 4.21(c) exhibit a clear association between the gain values and the gate voltage. Specifically, the application of a -3 V gate supply leads to an increase in gain up to 20 dB at an input power of 19 dBm. With a gate voltage of -2.9 V, a decreasing trend in gain is observed from 13 dBm to 16 dBm, followed by an increasing trend from 16 dBm to 19 dBm, resulting in a gain value of 22 dB. Furthermore, when a -2.8 V gate voltage is applied, a nearly constant gain of 24 dB is achieved. This distinctive behavior is attributed to the nonlinear characteristics of the proposed QPD350.

Figure 4.21(d) presents a noteworthy observation concerning the PAE in relation to various gate voltages. The analysis reveals that the -2.8 V gate voltage exhibits superior PAE compared to the other voltage settings. Likewise, the -3 V gate voltage outperforms the -2.9 V gate supply in terms of PAE for all input power levels except 18 dBm. At 18 dBm input power, the PAE results for these two gate voltage configurations are equivalent. Across all three gate supplies, the PAE demonstrates a direct proportionality with the input power. However, it is noteworthy that as the input signals exceed 18 dBm, a notable decrease in the gate voltage ratio is observed, primarily attributed to transistor heating rather than an increase in overall efficiency.

Figures 4.20 and 4.21 demonstrate notable observations regarding the performance metrics of the system. The maximum values of output power exhibit a significant increase, rising from 37.2 dBm to 43.42 dBm. Similarly, the gain experiences a notable improvement, escalating from 18.12 dB to 24.06 dB. Additionally, the PAE displays

remarkable enhancement, surging from 8.37 % to 27.2 % at the operating frequency of 2.25 GHz. These findings highlight the substantial improvements achieved in the system's output power, gain, and PAE, showcasing the effectiveness of the proposed approach. It concluded that non foster matching improve the AC output characteristic of proposed amplifier design.

4.8 MWA System Interface and Embedded Design

In the context of MWA system design, an embedded system refers to a computer hardware system based on microprocessors or microcontrollers that is specifically designed to perform the function of MWA. This embedded system can operate as a standalone unit or be integrated as a component within a larger system.

The core of the embedded system responsible for executing the MWA task consists of microprocessors or microcontrollers. Microprocessors are integrated on a single semiconductor and serve as the central processing unit (CPU). They are digital electronic components capable of being programmed to meet the desired functionality through integration with an integrated circuit (IC).

On the other hand, microcontrollers are chipsets that encompass a microprocessor, memory, digital inputs and outputs (I/O), and other essential peripherals such as timers, counters, breakers, and analog-to-digital converters. These microcomputers are designed to combine these components and form a cohesive unit within the embedded system for MWA.

Embedded software is a type of software that runs within electronic devices and controls the functions of these devices. Embedded software is tightly integrated with the hardware of a particular device and is often optimized to perform a specific task or control a function. Embedded software has an important place in this project. Observing the data coming from the sensors and controlling the system are realized in this way. STM32F756ZG microcontroller is used in our system. MicroC programming language was used as the software language. The development environment is STM32CubeIDE. First, the clock configuration was performed. The system clock is set to 216 MHz as indicated in Figure 4.22.

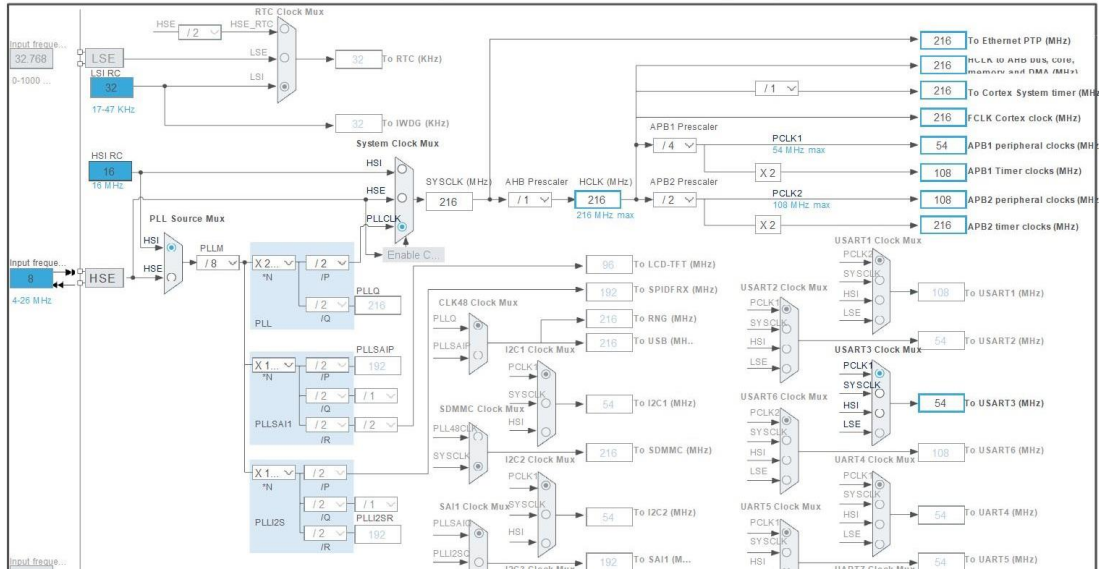


Figure 4.22: Clock configuration of embedded design

Following the system clock configuration depicted in Figure 4.22, the peripherals within the embedded system were automatically adjusted. Initially, a temperature sensor was utilized to measure both the coil and ambient temperature in the system. In this context, no specific peripheral was employed to receive data from the sensor. To enable this functionality, Timer6 was activated. It is worth noting that the APB1 Timer clock line holds significance as the sensor operates in synchronization with the clock signal. The Timer6 value was established as the negation of the frequency value on the APB1 line to facilitate data retrieval from the sensor. Subsequently, the clock settings of the microcontroller were configured to utilize a crystal resonator, as specified within the RCC tab.

Subsequently, configuration settings were implemented for the magnetic field sensor within our system. The ADC1 peripheral utilized the channel 0 line to interface with the magnetic field sensor. To enhance the conversion accuracy from analog to digital values, a 12-bit resolution was employed. This resolution provided a range of 4096 distinct digital values, allowing for precise conversion of the analog signal. By activating the continuous conversion mode, a continuous stream of data was obtained from the sensor. Similarly, the ECG sensor, which also produced analog signals, underwent the conversion process to digital data. The ADC2 peripheral was utilized, specifically the channel 3 line, to interface with the ECG sensor. A 12-bit resolution was applied for accurate analog-to-digital conversion. Similar to the magnetic field sensor, the continuous conversion feature was enabled to ensure a continuous flow of

converted digital data from the ECG sensor. Then, the ADC3 peripheral was activated and the channel 5 line was used to monitor the heart rate sensor. Likewise, 12-bit resolution and continuous loop mode have been activated. Thanks to the configurations made, data can be obtained from the sensors, but these data must be transferred to the originally created interface. For this, serial communication protocols are used. Therefore, the data from the sensors are transferred to the interface using the USART serial communication protocol. It was set as asynchronous in the configuration part and the baudrate part, which is the data communication rate, was set to 9600. Then the data transmission length was set to 8 bits, and the data transmission was set to both receiver and transmitter. Interrupts have been enabled to facilitate immediate intervention in the coils through the interface within the embedded system of the MWA. The hardware architecture and component configuration of the MWA embedded system are depicted in Figure 4.23(a), while Figure 4.23(b) illustrates the pin configuration employed in the system.

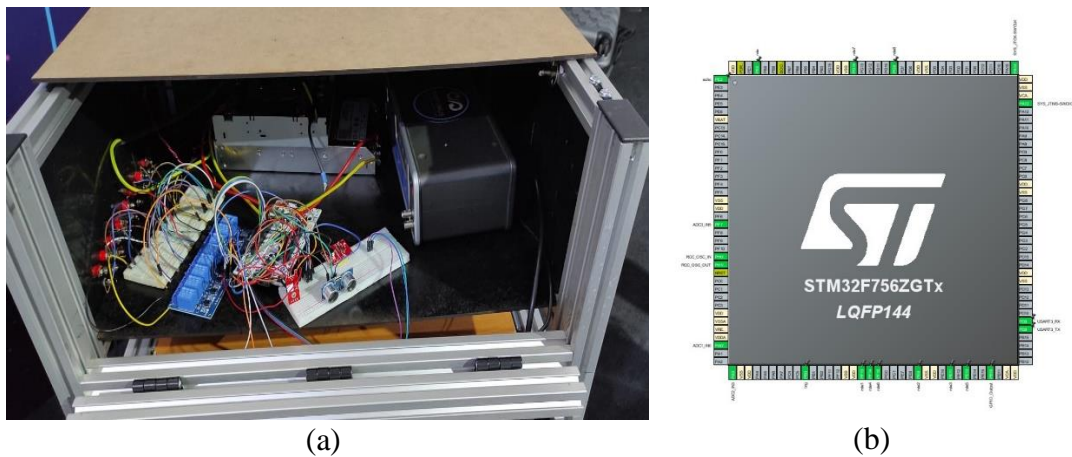


Figure 4.23: (a) Hardware architecture and (b) pin configuration of the embedded system design for MWA

The development environment of STM32CubeIDE proved instrumental in configuring the utilized sensors within the embedded system. This facilitated the setup of the microcontroller's pin settings. Initially, specific libraries were integrated into the project to provide essential functionalities. Subsequently, code was implemented to retrieve data from the temperature sensor. A delay function was created to introduce a time delay, followed by the definition of input and output pins specific to the sensor. The temperature sensor was connected to the 10th pin of port B, and this pin assignment was accomplished using the define macro.

To accommodate the sensor data, variables were declared with different data lengths of 8, 16, and 32 bits. Sequence definitions were established to handle future data for serial communication. Furthermore, a function was developed to read data from the temperature sensor, which returned a value relevant to the sensor's data.

The UART function was then configured to enable serial communication between the microcontroller and the interface. Interrupts were employed to swiftly execute commands received from the interface. By utilizing interrupts, the program could branch to the interrupt function without waiting in the main function. After executing the operations within the interrupt function, it returned to the main function and continued from the point it left off. The UART Interrupt function played a key role in this functionality. The strcmp function was employed to compare the data received in the ReceiveMessage array with the desired data. If the comparison resulted in a value of 0, the corresponding command was executed.

To understand the code logic, the first if structure of the Interrupt function was examined. The data transmitted from the interface was assigned to the ReceiveMessage array, defined as a character array. The received data was then compared with the character variable "1". The strcmp function returns a zero value when all characters in both strings are identical, and a non-zero value otherwise. Consequently, if the received data matched "1", relay 1 was activated. These operations were performed for all 8 coils. If the variable "0" was received from the interface, all relays were deactivated.

After enabling the Timer and UART Interrupt functions, the sensor data was continuously read within the while(1) loop to ensure a continuous flow of data from the sensors. The pin settings and variables were defined outside the loop since it was sufficient to define them only once. The initial step involved reading data from the temperature sensor. The status variable was assigned the value returned by the function responsible for reading data from the sensor. If the status variable differed from 0, the read operation was performed, and the acquired data was assigned to the respective variables. Next, ADC1 conversion was initiated for the magnetic field sensor. The resulting conversion value was assigned to the adcValue variable. Subsequently, the magnetic field data was obtained by converting the adcValue variable to a float type

and assigning the value to a separate variable. Similarly, ADC2 conversion was triggered for the ECG sensor. The process solely involved converting the analog data to digital format. The resultant value was assigned to the ad8232data variable.

Finally, the ADC3 conversion was performed for the pulse sensor, which observed the patient's pulse variation under the influence of the magnetic field in cancer treatment. The resulting value was assigned to the ritim variable. Further manipulations were executed to derive the patient's pulse value from the obtained data. The final calculated value was assigned to the yeniritim variable.

Subsequently, as data was collected from all the sensors, it needed to be transmitted to the interface. The sprintf function was employed for this purpose. The incoming data was written into the 'message' array variable, which had been defined as an array from the beginning. The data was formatted as an integer using the %d command. To avoid confusion arising from mixed incoming data, the values were separated using dots as delimiters. Finally, the variables containing the sensor data were sequentially inserted into the sprintf function. The sensor data stored in the 'message' string variable was then transmitted to the interface using the UART Transmit function, adhering to the serial communication protocol. These transmitted data were repeated every 600 ms.

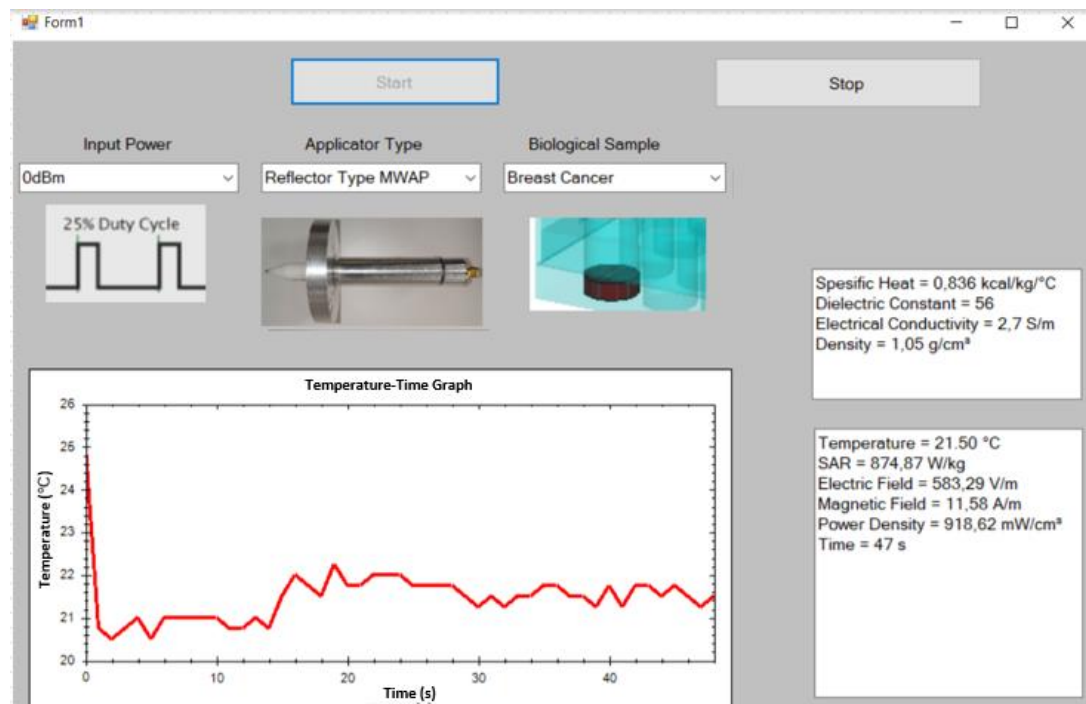


Figure 4.24: MWA system interface

In input parameter selection part shown in Figure 4.24, the signal type and power level to be generated in the signal generator is selected via the interface. Select the applicator type to be used from the menu next to the input power selection. As the applicator is selected, its picture changes and its properties are retrieved from the library. Similarly, the type of cancer to be ablated is selected from the "biological sample" menu. After the selection of the input parameters, the temperature time graph is plotted instantaneously by means of temperature sensors. Then the electric and magnetic fields on the biological tissue are measured with EMC near field probes. SAR and power density are calculated using the measured fields and the characteristics of the biological sample defined as input to the system. In this way, the MWA process can be followed in detail on a single screen.

Once the interface and the corresponding embedded system of the MWA system were developed, a prototype was constructed. Figure 4.25 provides a visual representation of the various stages involved in the prototype production and showcases the final version of the prototype. The chassis design comprises four distinct compartments, each serving a specific function within the system. These compartments consist of a microwave signal generator, a microwave power amplifier, a DC power supply, and a Lattepanda board, which facilitates system control through the interface. The internal components are interconnected with the screen located on the upper side through the utilization of a centrally positioned conduit, enabling the connection of cables.

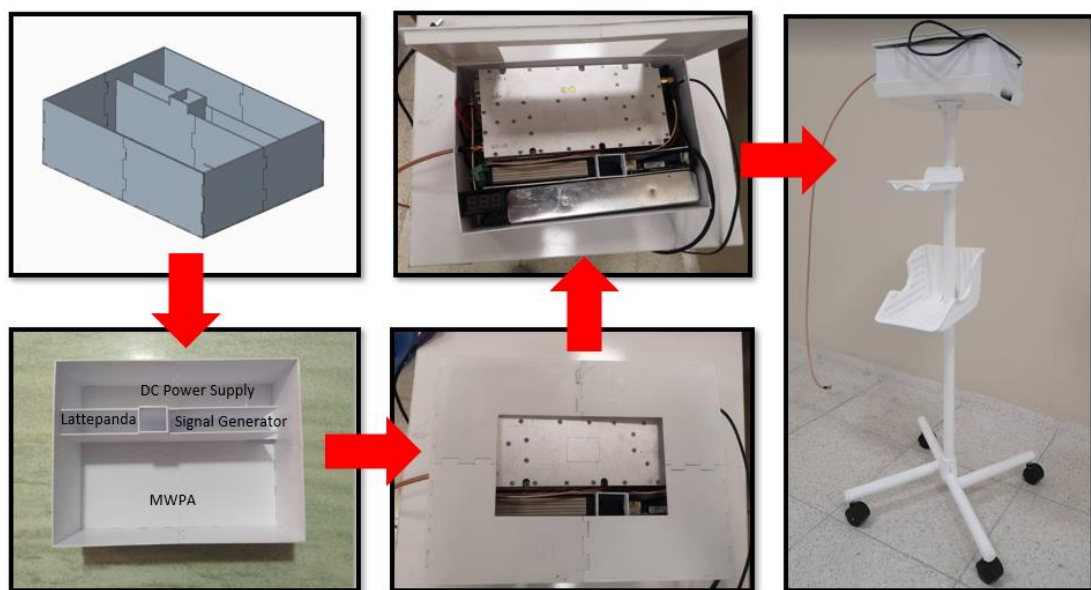


Figure 4.25: MWA system prototype

Chapter 5

Ablation Zone Analysis on 3D Phantom Model

Investigating the ablation zone is of paramount importance in microwave ablation studies. Although initial experiments using breast cancer pre-phantom fluid yielded promising electrical results similar to real biological samples, it became evident that the fluid lacked the necessary physical properties required for practical use, such as structural stability and resistance to temperature-induced deformations. To address this limitation, a three-dimensional breast cancer phantom model was developed to provide more realistic outcomes. The accurate assessment of the ablation zone is crucial for treatment benefit and patient safety. Additionally, incorporating magnetic nanoparticles (MNP) in microwave ablation has shown potential benefits, including improved tumor ablation by expanding the ablation area, faster temperature rise for shorter exposure times, and enhanced differentiation between cancerous and healthy tissue by modifying the electrical properties of the target region. Understanding the ablation zone and its characteristics contributes to optimizing treatment effectiveness. Exploring the electromagnetic energy transfer principle and the use of biocompatible particles with ionic properties in iron oxide nanoparticles (IONP) can further enhance the ablation zone and increase treatment efficiency. By investigating the ablation zone, researchers can advance the understanding and techniques of microwave ablation, ultimately improving patient outcomes.

This section explores various studies in the field of MWA, including investigations on 3D kidney, breast cancer, pancreas, lungs, and liver phantoms, utilization of iron oxide nanoparticles, as indicated in Figure 5.1. These studies provide valuable insights into the application and performance of MWA techniques.

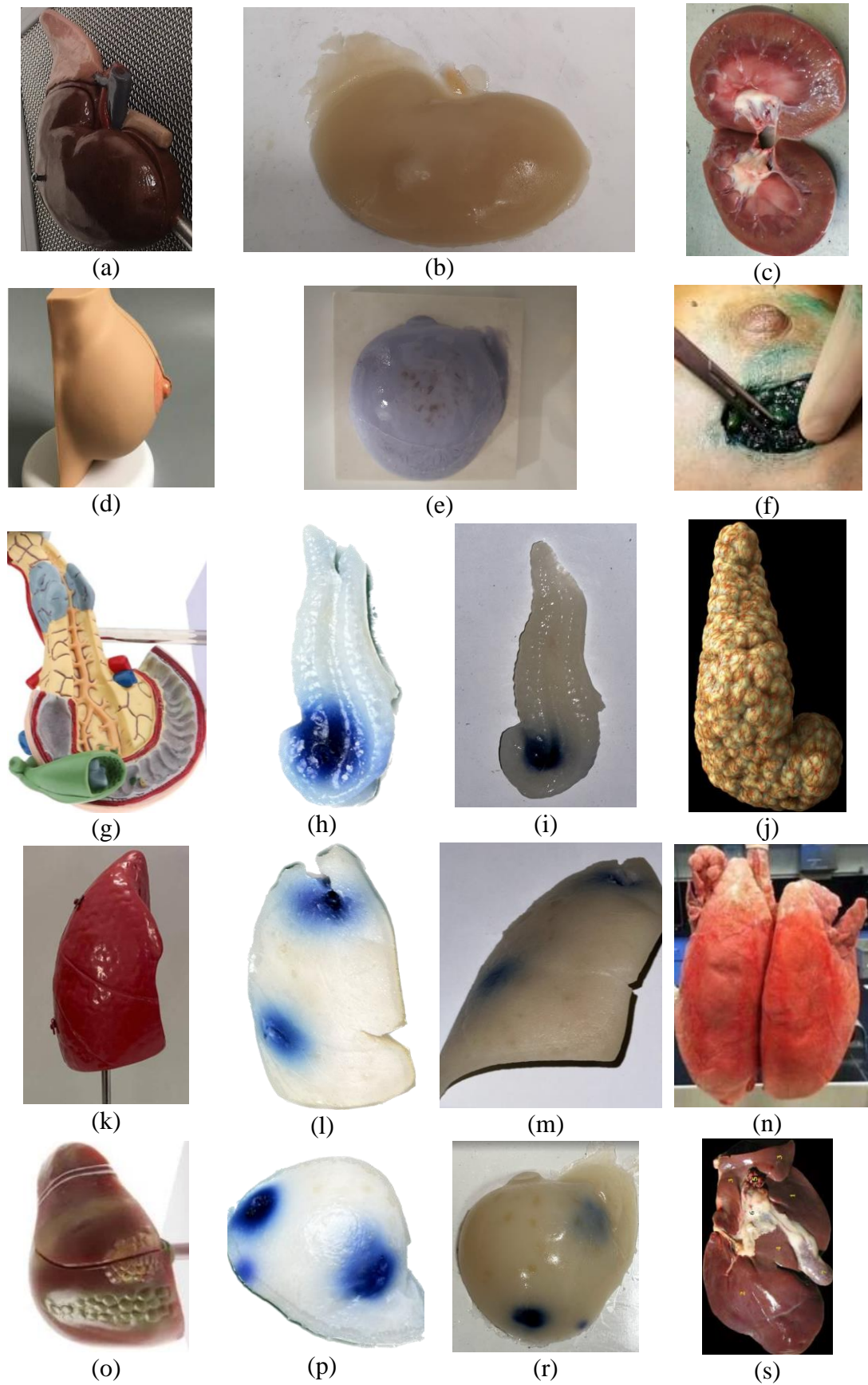


Figure 5.1: Anatomic model (a), (d), (g), (k), (o); 3D electrical equivalent model (b), (e), (h)-(i), (l)-(m), (p)-(n) and real organ view of kidney, breast, pancreas, lung and liver, respectively

The dielectric and thermal properties of kidney, breast, pancreas, lung and liver at 2.45 GHz, which are given in Figure 5.1 in anatomical model, 3D electrical equivalent model and real organ form, are given in Table 5.1.

Table 5.1: Dielectric and thermal properties of kidney, breast, pancreas, lung and liver at 2.45 GHz

Tissue	Relative Permittivity	Electrical Conductivity (S/m)	Thermal Conductivity (W/m·K)	Heat Capacity (J/kg·K)	Density (kg/m ³)
Kidney	52.7 [132]	2.43 [132]	0.12 [165]	3890 [165]	1050 [165]
Breast	5.1 [132]	0.12 [132]	0.42 [164]	1900 [163]	1020 [163]
Pancreas	41.7 [132]	1.58 [132]	0.34 [165]	3800 [165]	1040 [165]
Lung	48.4 [132]	1.68 [132]	0.3 [165]	2500 [165]	260 [165]
Liver	43 [132]	1.69 [132]	0.56 [165]	3600 [165]	1050 [165]

The dielectric and thermal properties in Table 5.1 are vital for microwave ablation (MWA). They reveal how tissues interact with 2.45 GHz microwave energy, aiding MWA optimization. Kidney exhibits a high relative permittivity (52.7), indicating strong electric field retention, while breast has a lower value (5.1), implying weaker electromagnetic field interaction. Varied relative permittivity affects microwave energy distribution within tissues during MWA. Tissues with higher electrical conductivity (kidney: 2.43, pancreas: 1.58, lung: 1.68, liver: 1.69) conduct electric currents more effectively, enhancing heating and energy transfer for thermal ablation. Thermal conductivity differentials influence heat dissipation; breast's higher thermal conductivity (0.42 W/m·K) facilitates heat dissipation, while lung experiences slower dissipation due to its lower value (0.3 W/m·K). Heat capacity and density values impact energy absorption and storage. Kidney's higher heat capacity (3890 J/kg·K) allows greater energy absorption before significant temperature rise, while lung's lower capacity (2500 J/kg·K) leads to faster temperature changes. Density influences energy transfer efficiency and heating distribution during MWA. Understanding these property variations is crucial for optimizing MWA, affecting tissue heating, thermal coagulation, and treatment advantage. Tailoring MWA parameters based on specific properties enables desired outcomes while minimizing damage to healthy tissues. The dielectric and thermal properties in Table 5.1 aid parameter selection and MWA optimization, determining energy absorption, distribution, and thermal response for effective treatment of various conditions.

5.1 Studies on 3D Kidney Phantom

Microwave ablation studies have employed tissue phantom models to anticipate physical alterations in tissue and to achieve outcomes closely resembling electrical properties of actual tissue. Nevertheless, it is anticipated that modeling electrically generated tissues, which represent organ shapes closer to real-life scenarios, will yield a wealth of information for pre-surgical assessments. The modeling process depicted in Figure 5.2 involved extraction of the mold from a 3D kidney model and its subsequent replacement with skin phantom fluid.

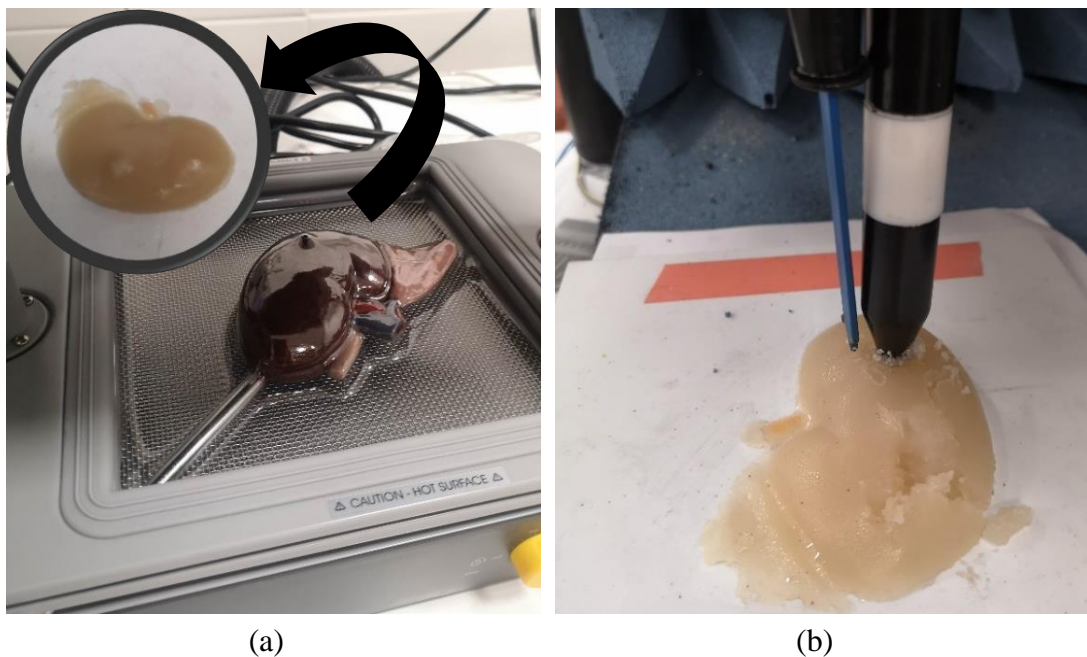


Figure 5.2: (a) Preparing 3D kidney phantom (b) and experimental setup

The Mayku Formbox shown in Figure 5.2(a) is used to heat glycol-modified Polyethylene Terephthalate (PETG) material to a temperature of approximately 150 °C, which makes it flexible and enables it to be molded into the shape of a kidney model obtained from the İKÇÜ Anatomy Laboratory. To create the molded kidney model depicted in Figure 5.2(b), skin phantom liquid was prepared and poured into the molded kidney model, then left to cool for 60 minutes at a temperature of 0°C. Subsequently, the 3D kidney phantom model was kept at room temperature for 90 minutes, allowing it to reach a temperature of approximately 18°C, which served as the initial temperature for the experiment. The molded skin phantom liquid solidified into its final form, as shown in Figure 5.2(b).

The prepared kidney phantom was then exposed to microwave power levels of 10 W, 25 W, 50 W, and 80 W for a duration of 6 minutes, using the experimental setup depicted in Figure 5.2(b), and its temperature was measured with a testo 882 thermal imager. The temperature data obtained from this experiment is presented in Figure 5.3.

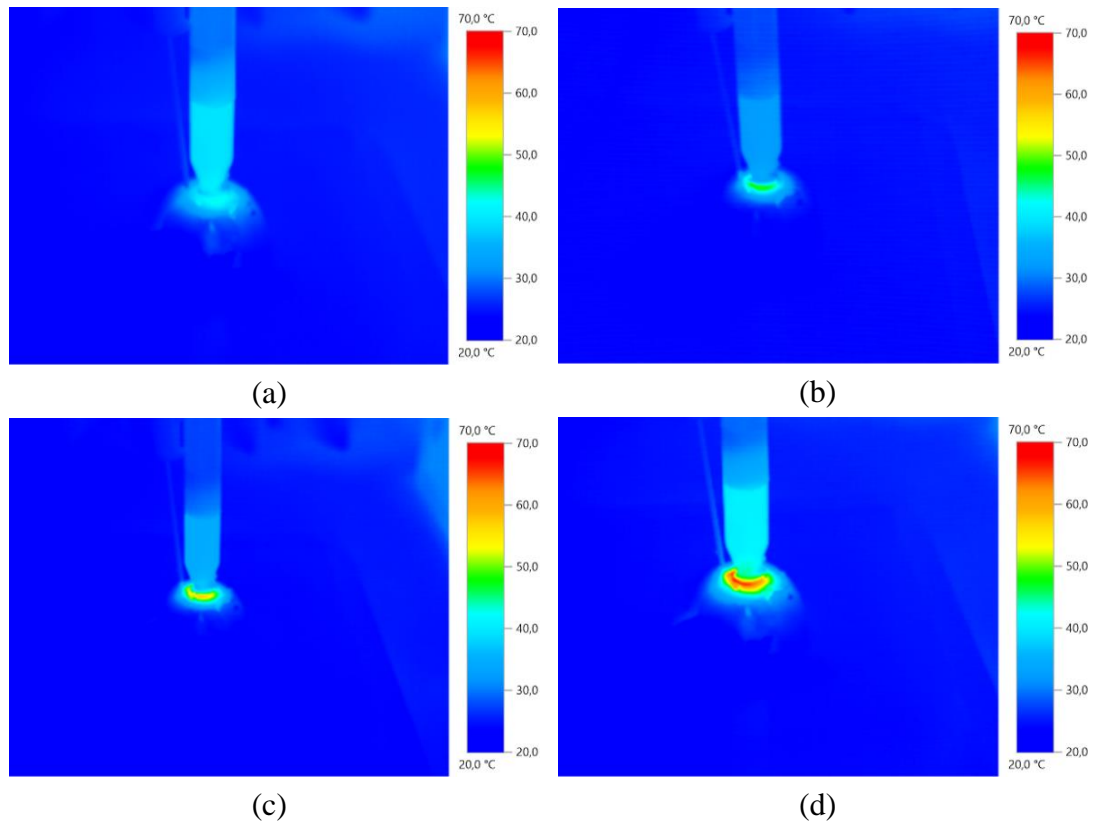


Figure 5.3: Temperature distribution resulting from the application of (a) 10 W, (b) 25 W, (c) 50 W and (d) 80 W microwave power to the 3D kidney phantom model for 6 minutes.

When the temperature measurement results from Figure 5.3(a) to Figure 5.3(d) are examined, it is seen that when 10 W, 25 W, 50 W and 80 W microwave powers are applied for 6 minutes via MTAP, the maximum temperature levels reached in the kidney phantom model are 42.9 °C, 48.9 °C, 57.3 °C and 66.2 °C, respectively. In addition to the measurement of the temperature distribution over the area with the thermal camera, the time-dependent temperature measurement was made and given in Figure 5.4 as the duration of the phantom model under microwave energy at the target ablation temperature of 50-60 °C affects the amount of destruction in the tissue.

Upon examination of the temperature-time graph in Figure 5.4, it can be observed that increasing the input power from 10 W to 80 W leads to a loss of linearity in temperature increase, as the increased microwave energy transferred to the phantom model creates

more distortions in its material structure. Following the application, water was introduced into the distortions that occurred in the 3D kidney phantom model, and the water that took the shape of the deteriorated areas was transferred to a graduated cylinder using a syringe to determine the ablation volume. Ablation volumes of 0.865 cm^3 and 1.180 cm^3 were achieved when input powers of 10 W and 25 W were used, respectively. Given that sustained temperatures above 50°C can rapidly destroy tissue, the 50 W and 80 W input powers led to the target temperature being reached after 210 s and 250 s, respectively. Consequently, ablation volumes of 1.655 cm^3 and 2.065 cm^3 were obtained in the phantom model for input powers of 50 W and 80 W, respectively.

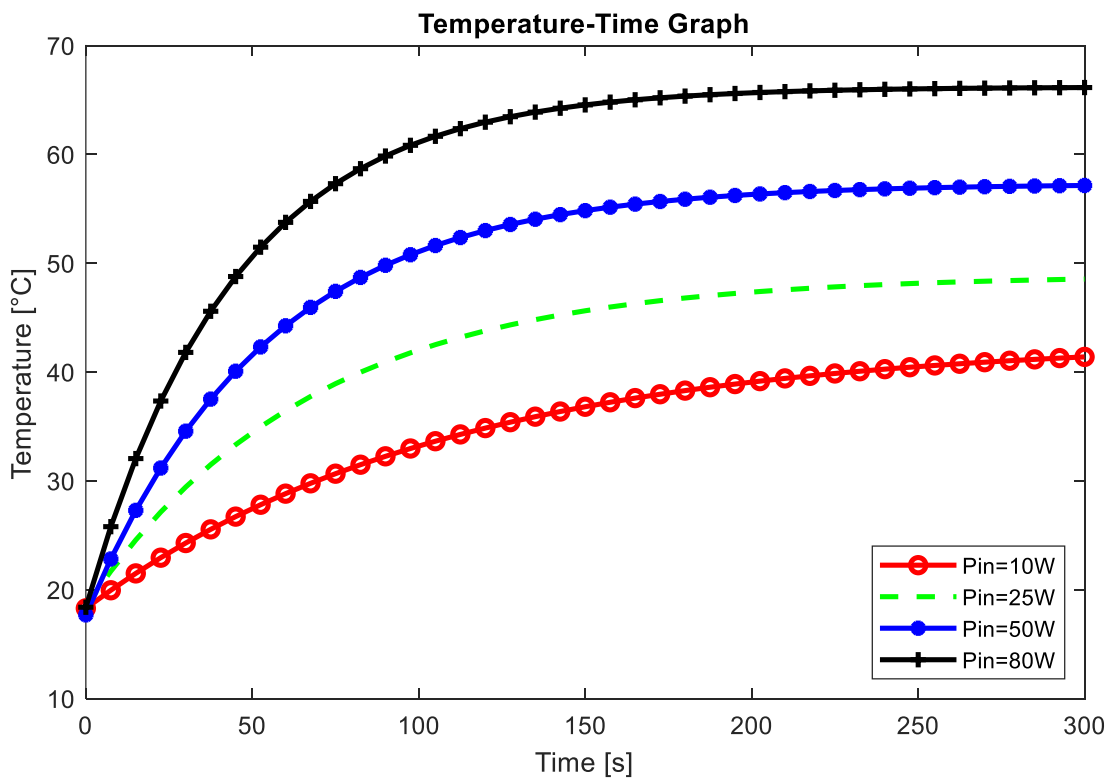


Figure 5.4: Time-dependent temperature measurement results of the kidney recipe

Table 5.2 presents the experimental measurement results obtained from the kidney recipe. The results show that the electric field magnitude is the main component responsible for the destruction of the phantom model structure by microwave power. To ensure accurate measurement, the electric field probe, which is shown in Figure 5.2(b) and is blue in color, was positioned parallel to the electric field radiation vector of the microwave applicator. Electric field magnitudes of 865 V/m, 1437 V/m, 1936 V/m, and 2239 V/m were measured in the center of the ablation zone when the input power is 10 W, 25 W, 50 W, and 80 W, respectively. The power levels over an area of

1 cm² in the ablation center were calculated using power density formulas based on the measured electric field magnitudes. The calculated power levels for 10 W, 25 W, 50 W, and 80 W were found to be 32 mW, 88 mW, 159 mW, and 213 mW, respectively. The results showed a linear relationship between the measured input power levels and the power levels calculated over the electric field measurement, considering the experimental measurement errors. Since the biological sample subjected to ablation does not contain an active element that reflects or generates microwave energy in the system, this linear relationship was experimentally established. The temperature distribution over volume shown in Figure 5.5, too. The volume exceeding 60 degrees is defined as the ablation zone and shown in Table 5.2.

Table 5.2: Experimental measurement results on a 3D kidney phantom model

Input Power [W]	E Field [V/m]	Power Density [mW/cm ²]	Exposure Time [s]	Maximum Temperature [°C]	Ablation Zone [cm ³]
10	865	32	300	42.9	0.865
25	1437	88		48.9	1.180
50	1936	159		57.3	1.655
80	2239	213		66.2	2.065

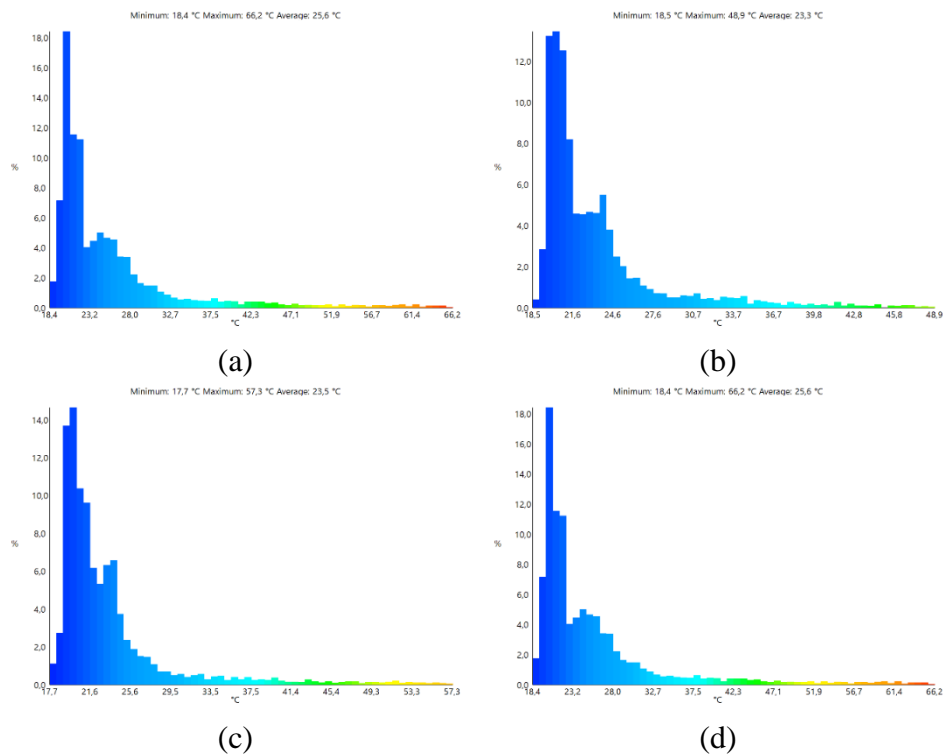


Figure 5.5: Temperature distribution as a result of applying (a) 10 W, (b) 25 W, (c) 50 W and (d) 80 W microwave power to the 3D kidney recipe for 6 minutes.

5.2 Ablation Zone Analysis on 3D Breast Phantom

Although the microwave ablation experiments with breast cancer pre-phantom fluid gave results similar to those used as if a real biological sample were used in electrical terms, it was seen that it was not suitable for use in terms of having a physically fluid structure, deforming with temperature and not collapsing the materials it contained in over time, being together for a long time and not losing its mixing feature. Therefore, the 3D breast cancer phantom model seen in Figure 5.6(a) and Figure 5.6(b) was used to obtain results closer to reality. Before starting the electric field and temperature measurements, which provide an interpretation of the actual performance of the microwave applicator used; To ensure that the MMWAP and CA20L1 microwave ablation probes operate in the 2.45 GHz ISM band, the S11 measurements shown in Figure 5.7 are shown.

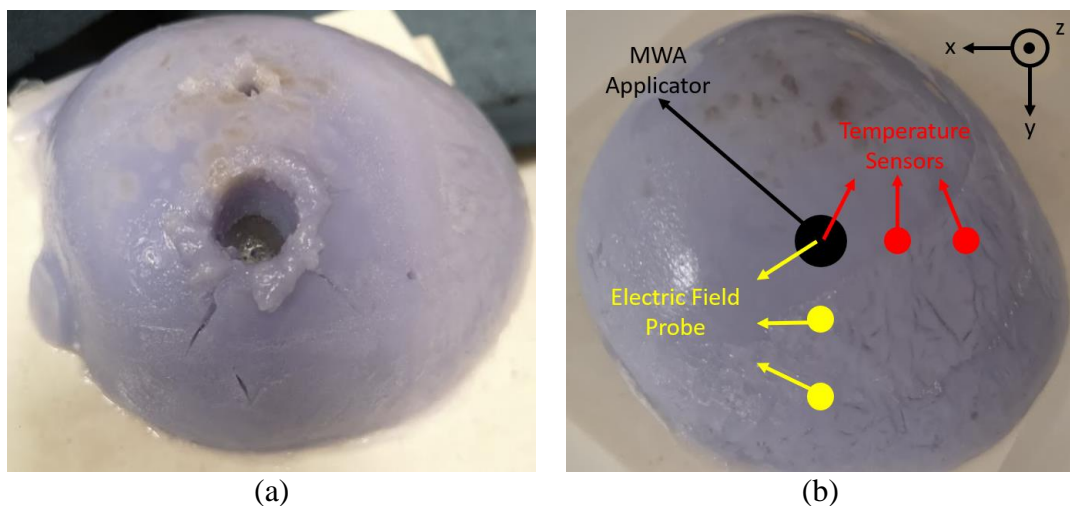


Figure 5.6: (a) 3D breast cancer phantom model (b) experimental measurement setup

Experiments were performed on the breast cancer phantom model shown in Figure 5.6(a) with the same ambient conditions and inputs with two different probes. An industrial microwave ablation probe called CA20L1, which is actively used in clinical applications, and the MMWAP structure preferred for this experiment are the preferred multiapplicator structures because they have more advantages than the microwave ablation probes designed during the project period. In order to obtain the S11 graph in Figure 5.7, all of the introduced probes within the project were obtained in the file format with the extension .csv and S11 measurements were obtained in file format

with the extension "USB-SA124B" used in S parameter measurements and plotted in CST Microwave Studio program.

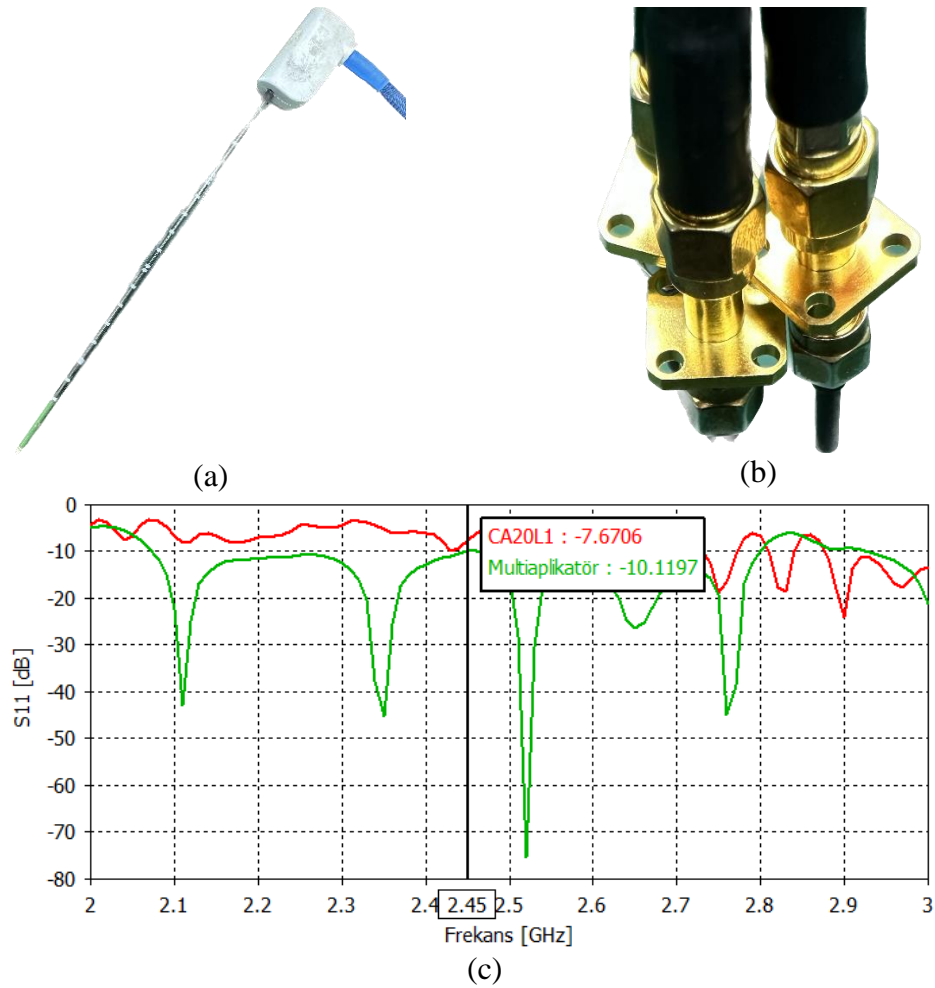


Figure 5.7: (a) CA20L1, (b) MMWAP and (c) S11 experimental measurement results when these two applicator were immersed in a breast cancer phantom model.

The S11 results shown in Figure 5.7 show that CA20L1 and its MMWAP structures have high return losses when in the breast cancer phantom model. S11 values were measured as -7.67 dB and -10.12 dB for CA20L1 and MMWAP at a frequency of 2.45 GHz, respectively. Despite the possible power losses in the power transfer transmitted to the applicators used in the experiment due to the high return loss, experiments have been conducted to examine the effect of different input signals on microwave ablation. Since the losses in power transfer apply to each of the different input signals applied to the probes, there will be no problem in the comparison of the test results. However, in experiments where high power transfer is required, it is possible to use the electronically controlled impedance adjustment circuit to eliminate the return losses in the existing system.

As shown in Figure 5.6(b), position-dependent temperature and electric field measurements were made with temperature sensors arranged on the x and y axes at intervals of one centimeter and away from the center and electric field measurement probes placed in the direction of the z axis. The measurements were made at room temperature and in an isolated environment from external electromagnetic field sources; The input power is made by adjusting the waveform and modulation frequencies of the input signal. The electric field results are given in Table 5.3.

Table 5.3: Electric field measurement results with the MMWAP and CA20L1

Wave Form	P _{gen} (mW)	P _{apl} (W)	P _{ref} (mW)	Electric Field (V/m)					
				r = 0 cm		r = 1 cm		r = 2 cm	
				CA20L1	Multi.	CA20L1	Multi.	CA20L1	Multi.
Cont.	0.1	11.51	0.4	664	491	51	120	39	77
	0.32	35.16	2.07	1012	724	69	196	51	96
	1	73.45	4.49	1390	1104	97	294	57	119
Sine MF:1kHz	0.1	6.98	0.37	689	509	50	99	106	89
	0.32	26.67	2.23	1093	711	93	189	78	107
	1	42.17	4.75	1219	924	128	217	41	112
Triangle MF:1kHz	0.1	6.98	0.38	718	425	86	152	45	88
	0.32	38.19	2.31	1057	558	119	243	61	131
	1	5.29	3.4	1213	906	128	234	78	157
Square MF:1kHz	0.1	10.33	0.39	1051	408	67	156	34	88
	0.32	29.17	1.82	1176	685	133	237	49	124
	1	51.88	3.3	1372	887	147	247	69	102
Pulse MF:1kHz D.C:25%	0.1	10.64	0.4	831	400	72	172	39	73
	0.32	30.27	1.73	1144	575	95	221	68	107
	1	55.34	3.35	1326	875	105	247	70	113
Square MF:10kHz	0.1	11.22	0.35	729	406	52	215	29	113
	0.32	32.51	1.92	1355	854	81	297	38	161
	1	65.92	4.09	1447	1060	106	378	55	186

When Table 5.3 is examined, the signal levels amplified by the microwave amplifier of each applicator for the same input power levels are; it changes slightly as the waveform changes. The fact that the input signals applied in continuous form and as amplitude modules differ when the type and position of the applicator are the same, is related to the formation of harmonics that are excessively in direct proportion to the modulation frequency in the operating frequency band range of the microwave amplifier used in the system. Therefore, the input signal and modulation frequency used in my system should be selected at appropriate levels. The modulation frequency of the input signal used in the experiment given in Table 5.3 is up to 10 kHz and

continuous, sine, triangle, square, pulse forms are used as the waveforms, resulting in a change of approximately 4.5% in the maximum output power of the 100 W microwave amplifier.

After inferring that the input signal waveforms caused changes in the signal levels applied to the applicators, it was observed that the electric field distributions created in the ablation regions were approximately proportional to the square roots of these power levels. Electric field levels in applicator centers It was seen that the use of CA20L1 was in the range of 1.5-2 times compared to the use of MMWAP, but when moving away from the applicator center, the electric field levels were higher in the use of MMWAP. According to the SAR formula, it is known that as the magnitude of the electric field increases, the power absorbed by the ablation zone and the maximum temperature reached increase accordingly. The maximum temperatures of the ablation zone electric field distributions shown in Table 5.4 by applying 150 seconds to the breast cancer phantom model are given in Table 5.4.

Table 5.4: Temperature measurement results of the MMWAP and CA20L1 at the end of 150 s

Wave Form	P_{gen} (mW)	P_{apl} (W)	P_{ref} (mW)	Target Zone Temperature After 150 Seconds (°C)					
				r = 0 cm		r = 1 cm		r = 2cm	
				CA20L1	Multi.	CA20L1	Multi.	CA20L1	Multi.
Cont.	0.1	11.51	0.4	58.8	46.9	29.2	37.3	20.3	21
	0.32	35.16	2.07	79.1	59.7	32.4	48.2	20.4	21.5
	1	73.45	4.49	101.2	80.5	37.4	62.3	20.5	22.3
Sine MF:1kHz	0.1	6.98	0.37	60.2	47.9	27.8	32.3	20.9	21.3
	0.32	26.67	2.23	83.8	62.1	31.7	43.6	21	21.9
	1	42.17	4.75	91.2	74.7	36	47.1	21.3	22.1
Triangle MF:1kHz	0.1	6.98	0.38	61.9	46.4	25.4	34.2	20.3	21.3
	0.32	38.19	2.31	81.7	54.6	31.4	38.2	20.6	22.8
	1	5.29	3.4	90.9	76.2	36.8	49.2	21	24.1
Square MF:1kHz	0.1	10.33	0.39	81.4	44.5	32	39.5	20.2	21.3
	0.32	29.17	1.82	88.7	61.2	35.9	45.3	20.4	22.5
	1	51.88	3.3	100.1	73.3	37.9	50.8	20.8	21.7
Pulse MF:1kHz D.C:25%	0.1	10.64	0.4	68.5	44.4	32.9	32.9	20.3	20.9
	0.32	30.27	1.73	86.8	55.1	37.1	36.6	20.8	21.9
	1	55.34	3.35	97.5	73.4	38.9	50.8	20.8	22.1
Square MF:10kHz	0.1	11.22	0.35	62.6	42.3	29.3	33.4	20.1	22.1
	0.32	32.51	1.92	99.1	66.8	34.5	40.2	20.2	24.3
	1	65.92	4.09	104.5	78.1	39	60.4	20.5	25.7

In parallel with the electric field magnitudes in Table 5.3, the temperature values in Table 5.4 are also higher than CA20L1 in the applicator center, but the maximum temperature values of the MMWAP reached at the end of 150 seconds as you move away from the center are much higher than CA20L1. The input signal to which the 10 kHz modulation frequency is applied with the square waveform to the temperature value applied with the carrier frequency of 2.45 GHz was applied to the CA20L1 applicator and the highest temperature value of 104.5 °C was reached in the target region. However, the microwave ablation target temperature of 60 °C was reached in all cases where a 1mW input signal was applied. In addition, with the MMWAP structure designed with the aim of creating a wider ablation zone, the ablation target temperature was reached up to approximately 10 mm away from the applicator center. In addition, as the applied signal waveform changed, it was observed that there were no significant differences between the ablation patterns created in the target region. When Table 5.3 and Table 5.4 are summarized, the carrier frequency of 2.45 GHz, the modulation frequency of 10 kHz and the microwave input signal in which the signal waveform is applied at a power level of 1mW in the form of pulse or square provide the most output of the 100 W microwave power amplifier used in the system, thus causing the fastest temperature increase in the breast cancer model for both applicators and creating a high temperature up to a width of 10 mm in diameter with the use of a MMWAP provided.

The summarized findings from Tables 5.3 and 5.4 underscore the significance of employing specific parameters, such as a carrier frequency of 2.45 GHz, a modulation frequency of 10 kHz, and a microwave input signal with a power level of 1mW in pulse or square waveform, for achieving effective and precise microwave ablation in breast cancer treatment. These parameters not only resulted in the fastest temperature increase but also facilitated the attainment of the desired target temperature of 60 °C within the breast cancer model. Moreover, the MMWAP design exhibited a wider ablation zone, reaching temperatures up to approximately 10 mm away from the applicator center. These findings highlight the potential impact of parameter optimization and innovative applicator designs in enhancing the efficiency and advantage of microwave ablation techniques for breast cancer therapy. These advancements hold great promise in improving the overall outcomes and success rates of microwave ablation as a treatment modality for breast cancer patients.

5.3 MWA Studies on 3D Pancreas Electrical Model

The pancreas is an organ that is difficult to surgically intervene because it is in a protected area in the body and is relatively smaller than other organs. In order to treat this organ with microwave ablation, a thin applicator that can change form, when necessary, should be used. For this reason, a three-dimensional pancreas model was produced and used in microwave ablation study by means of a HTIMWAP. The block diagram in Figure 5.8 shows the experimental measurement system. Here, microwave signals with a frequency of 2.45 GHz and an input power of -20 dBm are produced in a microwave signal generator and amplified with a 40 dB LNA. Signals amplified to the 15-20 dBm range are transmitted to the 350W PA introduced in Chapter 4. The directional coupler with 40dB coupling factor connected to the output of the MWPA measures the power transmitted to the HTIMWAP connected to the through port with a spectrum analyzer. Using high-power microwave energy, electric field and RF power probe transferred to the 3D pancreas model, the electric field value is measured over the spectrum analyzer and the radiant power is measured through the power sensor, respectively. Finally, the results obtained using the testo 882 thermal camera to measure and analyze the temperature data generated in the 3D pancreas model as a result of ablation are given in Figure 5.9.

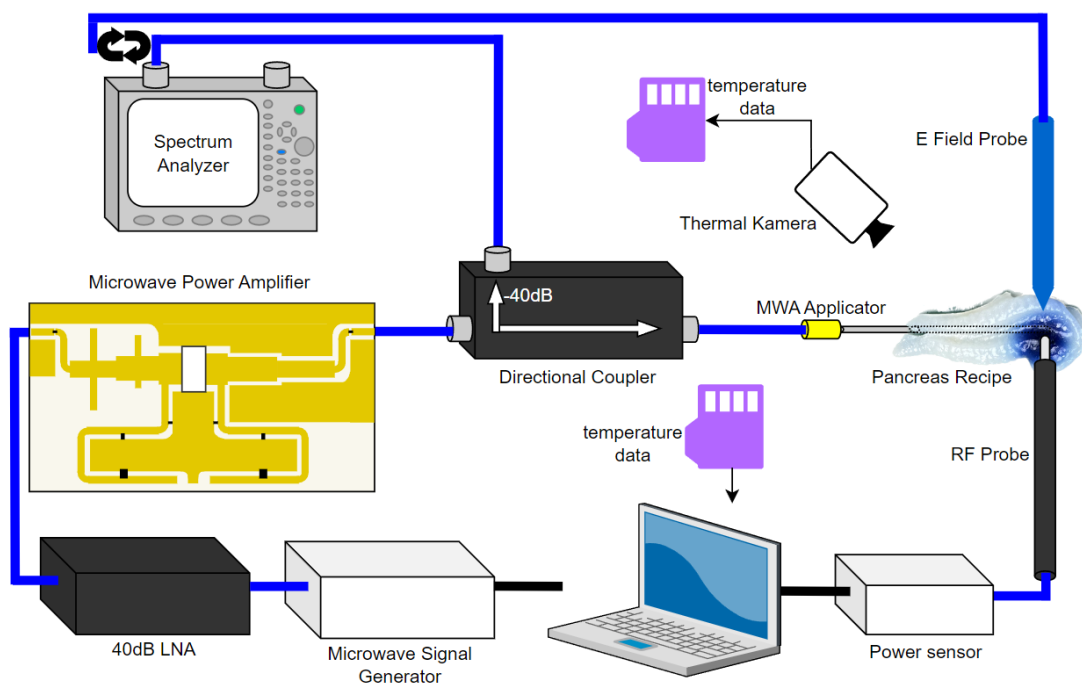


Figure 5.8: Experimental measurement setup ablation of pancreas recipe under microwave power exposure

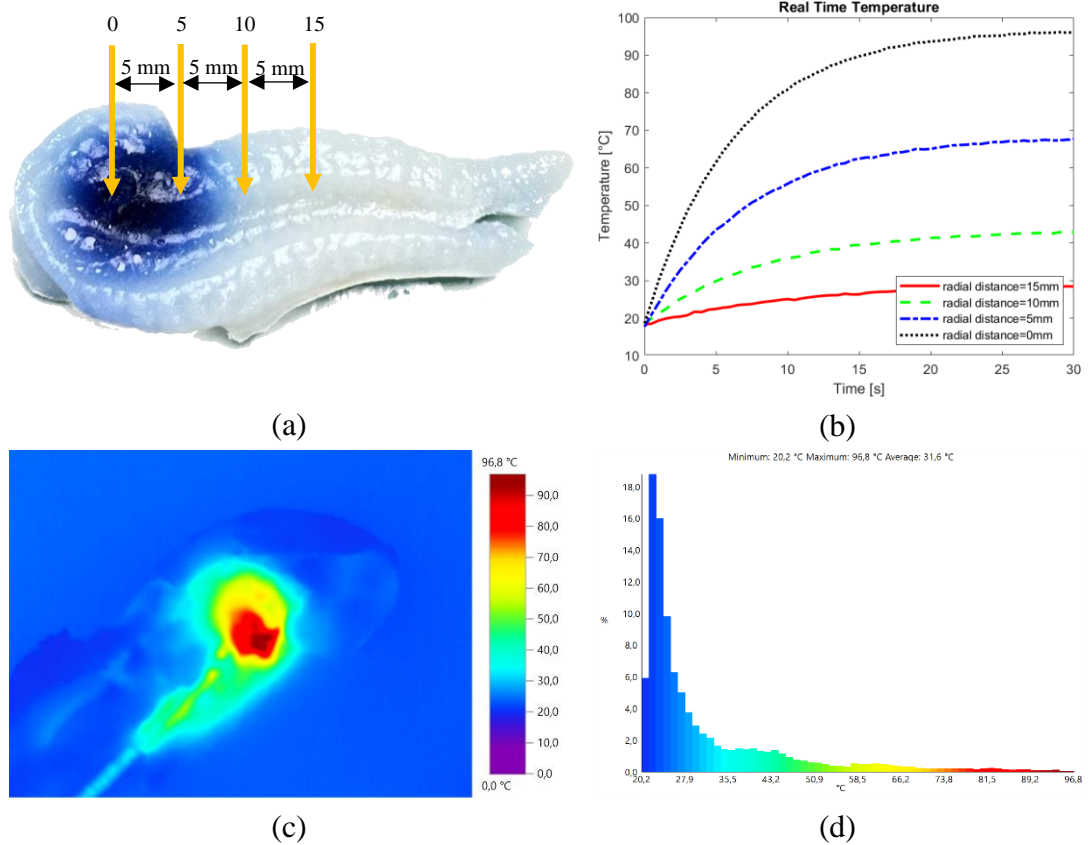


Figure 5.9: (a) Pancreas recipe with the measurement including (b) temperature distribution after 30 s microwave exposure, (c) Time-dependent temperature measurement results of the 3D pancreas phantom model (d) temperature histogram.

The points shown on the pancreas recipe given in Figure 5.9(a) represent the regions where the probes that measure the electric field, radiated power and real-time temperature. It should be noted that the 0 point is where the tumor is located and is also the center of the irradiation zone of the MWA applicator. The temperature-time measurement results of these measurement probes recorded for 30 s are shown in Figure 5.9(b). Although the graph preserves the temperature increase in the exponential form, which decreases as it moves away from the center of microwave energy, it is observed that this form gradually leaves its place to a linear graph. After 30 s microwave exposure, the temperature gradually decreases from 96.8 °C to 68.4 °C, 43.5 °C and 28.9 °C as it moves away from the center at 5 mm intervals consistent with the results in the temperature-time graph. As a result of the proportional temperature percentage within the pancreas recipe in Figure 5.9(d), the ablation temperature of 60 °C and above in 30 s is reached by 22%. The electric field and the radiant power that causes these temperature profile results are given in Figure 5.9 by recording at 1 s intervals and taken for 30 s.

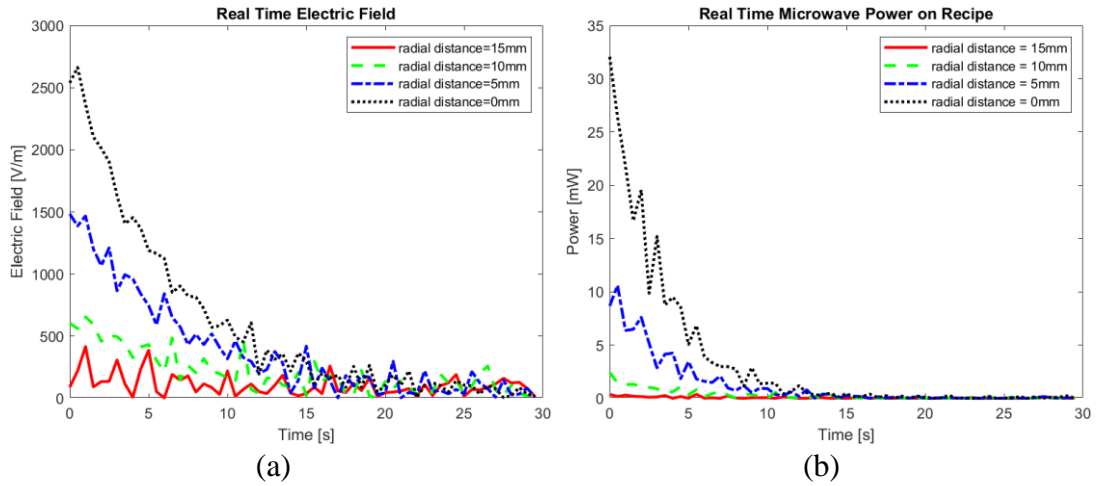


Figure 5.10: Time-dependent measurement results of the electric field (a) and radiated microwave power (b) at different distances from the pancreas recipe.

On the 0 mm axial distance, while the electric field was 2620 V/m at the beginning, it decreased to around 100 V/m at the end of 30 s. The electric field level decreased from 1506 V/m, 645 V/m and 150 V/m to 100 V/m, respectively, as it moved away from the center by 5 mm, 10 mm and 15 mm. The fact that the temperature rise form in Figure 5.9(b) is symmetrical with respect to the time axis proves that the measurement results have a mathematical relationship with each other. The time-dependent radiated power results given in Figure 5.10(b) are also seen in the same form as the decreases in the electric field graph, due to the same reason. Radiated power detected by the 1 mm² RF probe tip at 0 mm, 5 mm, 10 mm and 15 mm distances from the center decreased from 27 mW, 9 mW, 2 mW and 30μW levels to nW power levels, respectively, at the start. The change in the performance of the MWA applicator, which was used due to the deterioration of the dielectric structure because of the destruction of the tissue in the MWA process, caused the temperature, electric field and microwave radiation power in the pancreas recipe to change, although the input power applied to the system did not change. The damage to the tissue of the pancreas recipe is given in Table 5.5.

Table 5.5: Experimental measurement results on a 3D pancreas recipe

Input Power [W]	Distance [mm]	E Field [V/m]	Power Density [mW/mm ²]	Temperature [°C]	Ablation Zone [cm ³]
15	0	2620	27	96.8	5.4
	5	1506	9	68.4	1.8
	10	645	2	43.5	0.5
	15	150	0.03	28.9	0.3

5.4 MWA Studies on 3D Lung Electrical Model

The delicate nature of the liver, which contains air ducts, necessitates careful consideration during surgical interventions. Utilization of a flexible and adaptable thin applicator is suitable preference for microwave ablation of liver, specifically the helix-tipped thin MWAP. This MWAP is specifically designed to enable microwave ablation of the liver, addressing the unique challenges associated with this sensitive organ. To facilitate the study of microwave ablation in the lung, a three-dimensional lung model was developed, alongside a helix-tipped thin MWAP. Figure 5.11 presents the experimental measurement system employed in this study. Microwave signals with a frequency of 2.45 GHz and an input power of -20 dBm are generated by a microwave signal generator, amplified through a 40 dB LNA, and then transmitted to the previously discussed 350W MWPA in Chapter 4. The power transmitted to the helix-tipped MWAP, connected to the through port, is measured using a directional coupler with a 40 dB coupling factor, in conjunction with a spectrum analyzer. The electric field values within the three-dimensional lung model are measured by the spectrum analyzer, while the radiant power is measured using a power sensor. Furthermore, the temperature data generated during the ablation process in the 3D lung model is captured and analyzed using a thermal camera. Figure 5.12 presents the results obtained from these temperature measurements and analyses.

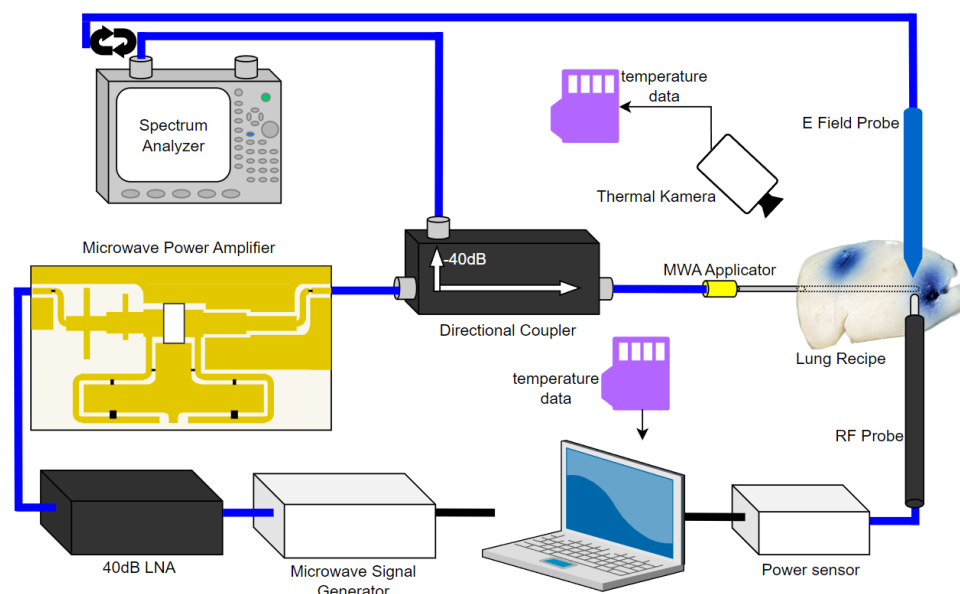


Figure 5.11: Experimental measurement setup ablation of lung recipe under microwave power exposure

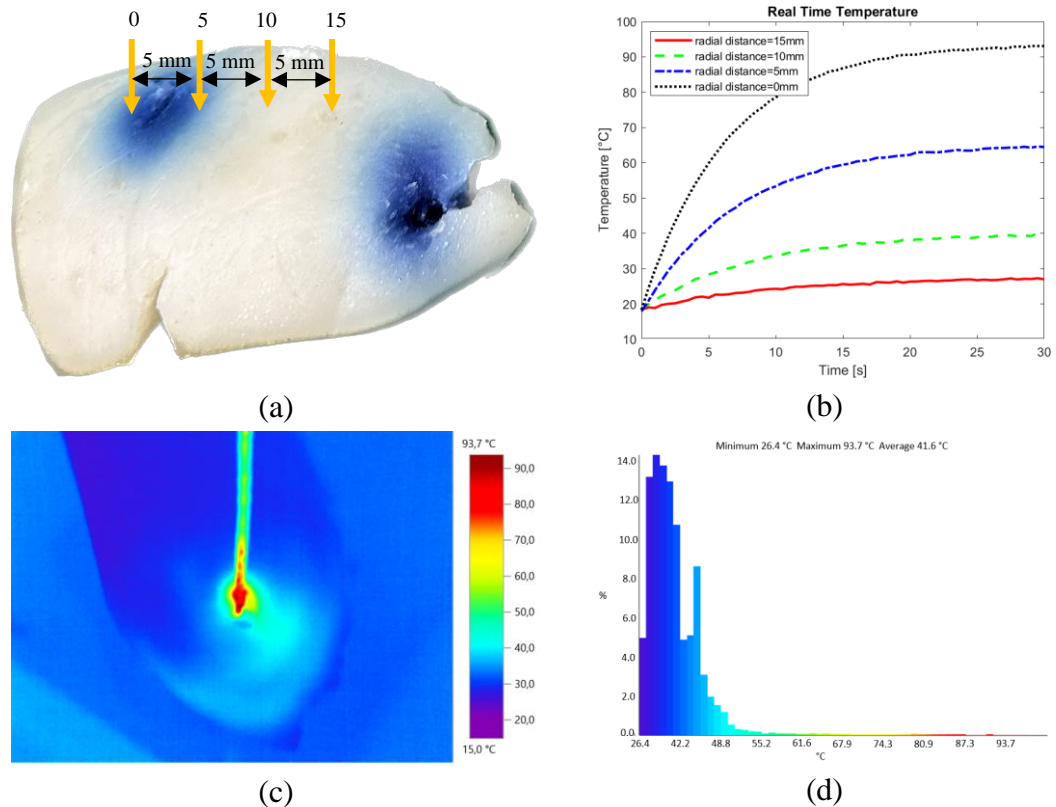


Figure 5.12: (a) Lung recipe with the measurement including (b) temperature distribution after 30s microwave exposure, (c) Time-dependent temperature measurement results (d) temperature histogram.

The locations where electric field, radiated power, and real-time temperature probes are positioned on the pancreas recipe, as depicted in Figure 5.12(a), signify specific regions of interest. Notably, the 0 point denotes the tumor location and coincides with the central irradiation zone of the microwave applicator. Figure 5.12(b) presents the temperature-time measurements acquired using a thermal camera recording them 1s time interval over a duration of 30 seconds. The graph exhibits an exponential temperature increase, which gradually transitions to a linear trend as the distance from the microwave energy center increases. As per the temperature-time graph, after 30 seconds of microwave exposure, the temperature gradually decreases at 5 mm intervals, ranging from 93.7 °C to 65.3 °C, 40.1 °C, and 27.6 °C. The spatially varying temperature data signifies the potential for localized ablation within a considerable region. Furthermore, the percentage of the lung recipe area reaching an ablation temperature of 60 °C or higher within 30 seconds is merely 0.8%, as depicted in Figure 5.13(d). Figure 5.13 presents the electric field and radiant power measurements taken at 1-second intervals over the course of 30 seconds, which contribute to the observed temperature profiles.

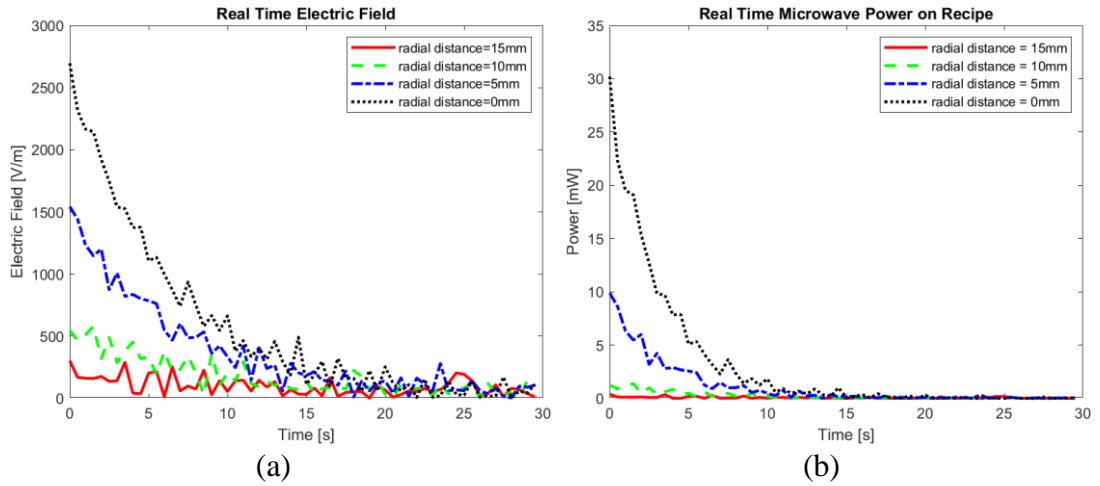


Figure 5.13: Time-dependent measurement results of the electric field (a) and radiated microwave power (b) at different distances from the lung recipe.

At the axial distance of 0 mm, the initial electric field strength was measured to be 2696 V/m, gradually decreasing to approximately 100 V/m after a 30 s period. Moving away from the center, the electric field levels at distances of 5 mm, 10 mm, and 15 mm decreased from 1543 V/m, 547 V/m, and 303 V/m, respectively, to 100 V/m. The symmetrical temperature rise pattern observed in Figure 5.12(b) provides evidence of a mathematical relationship among the measured variables. Correspondingly, the time-dependent radiated power results in Figure 5.13(b) exhibit a similar declining trend as observed in the electric field graph, attributed to the same underlying cause. Specifically, the radiated power detected by the 1 mm² RF probe tip decreased from initial levels of 30 mW, 10 mW, 1 mW, and 0.38 mW at distances of 0 mm, 5 mm, 10 mm, and 15 mm from the center, respectively, to nanowatt power levels. Notably, despite the consistent input power applied to the system, the tissue degradation within the Microwave Applicator (MWA) led to variations in temperature, electric field, and microwave radiation power within the pancreas recipe. A comprehensive overview of the observed tissue damage in the pancreas recipe is presented in Table 5.6.

Table 5.6: Experimental measurement results on a 3D lung recipe

Input Power [W]	Distance [mm]	E Field [V/m]	Power Density [mW/mm ²]	Temperature [°C]	Ablation Zone [cm ³]
15	0	2696	30	93.7	4.9
	5	1543	10	65.3	1.5
	10	547	1	40.1	0.5
	15	303	0.38	27.6	0.2

5.5 MWA Studies on 3D Liver Electrical Model

In the context of dimensionally large liver, surgical interventions pose unique challenges that require careful consideration. To address this, microwave ablation has emerged as a promising treatment approach, necessitating the use of an applicator with high power carrying capacity. To enable the study of microwave ablation in the liver, a three-dimensional liver model was developed, accompanied by a MFMWAP. The experimental measurement system employed in this study, as depicted in Figure 5.14, involved the generation of microwave signals with a frequency of 2.45 GHz and an input power of -20 dBm using a microwave signal generator. These signals were subsequently amplified through a 40 dB LNA and transmitted to the previously discussed 350W MWPA described in Chapter 4. The power transmitted to the MFMWAP, which was connected to the through port, was accurately measured using a directional coupler with a 40 dB coupling factor in conjunction with a spectrum analyzer. Within the three-dimensional liver model, the electric field values were assessed using the spectrum analyzer, while the radiant power was quantified utilizing a power sensor. Furthermore, temperature data generated during the ablation process within the 3D liver model was meticulously captured and analyzed through the utilization of a thermal camera. The temperature measurements and corresponding analyses are presented in Figure 5.15.

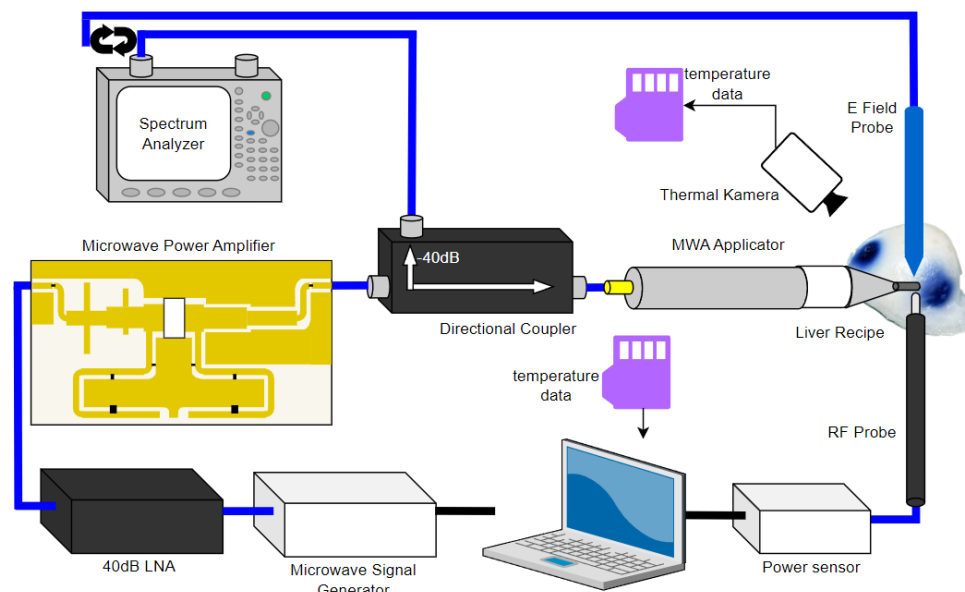


Figure 5.14: Experimental measurement setup ablation of liver recipe under microwave power exposure

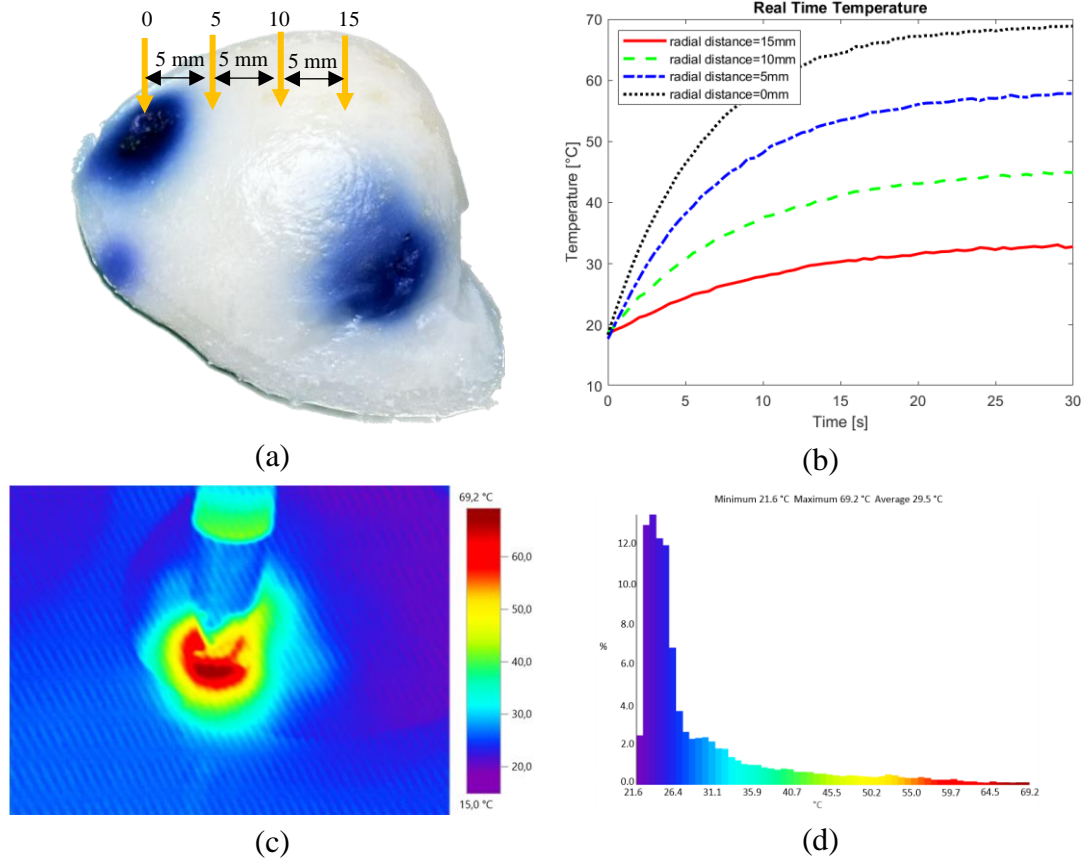


Figure 5.15: (a) Liver recipe with the measurement including (b) temperature distribution after 30 s microwave exposure, (c) Time-dependent temperature measurement results of that recipe (d) temperature histogram.

In Figure 5.15(a), the depicted points on the liver model correspond to specific regions where probes are positioned to measure the electric field, radiated power, and real-time temperature. It is worth noting that the 0 point signifies the tumor location, which coincides with the central irradiation zone of the MFMWA. The temperature-time measurements obtained from thermal camera over a 30 second duration are illustrated in Figure 5.15(b). While the graph initially exhibits an exponential temperature increase, which diminishes as the distance from the center of microwave energy increases, it gradually transitions to a linear trend. Following 30 seconds of microwave exposure, the temperature progressively decreases at 5 mm intervals, measuring 69.2 °C, 58.4 °C, 45.6 °C, and 33.2 °C, respectively, as indicated in the temperature-time graph. These space dependent temperature data indicate that it will ablate in a large region. Within the limits of the liver on Figure 5.15(c), the proportion of the area reaching an ablation temperature exceeding 60 °C in 30 s is 1.6%, as depicted in Figure 5.15(d). Figure 5.16 presents the electric field and radiant power responsible for these temperature profiles, recorded at 1-second intervals over the course of 30 seconds.

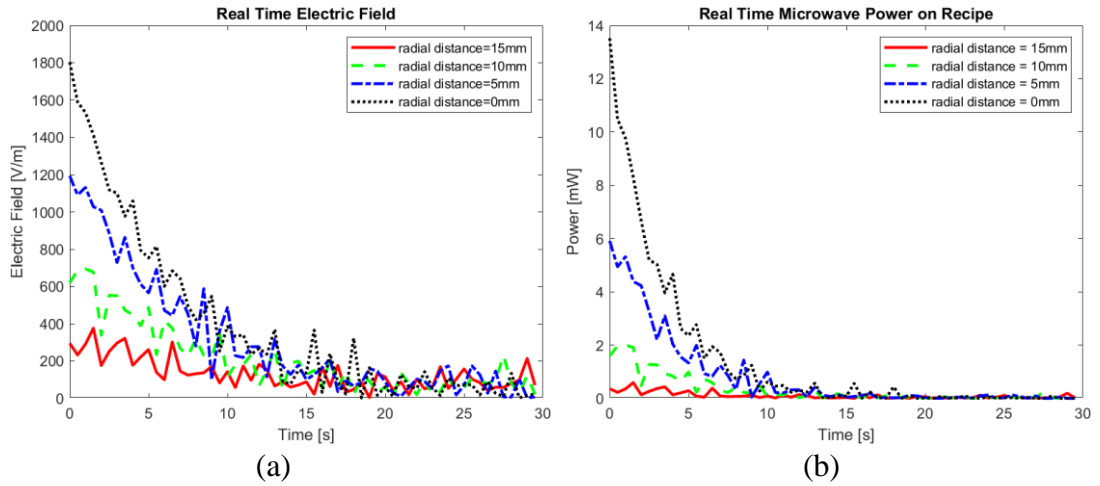


Figure 5.16: Time-dependent measurement results of the electric field (a) and radiated microwave power (b) at different distances from the liver recipe.

The electric field exhibited an initial value of 1804 V/m at the 0 mm axial distance. Over a period of 30 seconds, it gradually decreased to around 100 V/m. Moving away from the center by 5 mm, 10 mm, and 15 mm, the electric field levels decreased successively from 1193 V/m, 619 V/m, and 296 V/m to values below 100 V/m. The temperature rise in Figure 5.15(b) symmetrically correlates with time, indicating a mathematical relationship between measurements. Similarly, the time-dependent radiated power results presented in Figure 5.16(b) displayed a decreasing trend like that observed in the electric field graph. Initially, power detected by the 1 mm² RF probe at 0 mm, 5 mm, 10 mm, and 15 mm distances decreases from 14 mW, 6 mW, 2 mW, and 0.4 mW to nW levels. The performance of the MWA was influenced by the degradation of the dielectric structure resulting from tissue destruction during the MWA process. Consequently, changes were observed in the temperature, electric field, and microwave radiation power within the liver model, despite the input power applied to the system remaining constant. For further insights into the tissue damage in the liver model, refer to Table 5.7.

Table 5.7: Experimental measurement results on a 3D liver recipe

Input Power [W]	Distance [mm]	E Field [V/m]	Power Density [mW/mm ²]	Temperature [°C]	Ablation Zone [cm ³]
15	0	1804	14	69.2	1.8
	5	1193	6	58.4	1.1
	10	619	2	45.6	0.6
	15	296	0.4	33.2	0.3

Chapter 6

In Vitro and Ex Vivo Experimental Study of Designed Applicators

This section includes the radiation performances of the microwave applicators designed in the second section tested on in vivo and ex vivo studies. In Section 6.1, the electric field and surface temperatures of the reflector-type MWA applicator structure were analysed by placing it into breast cancer in vitro and giving high power microwave energy. By analysing the results obtained, three-dimensional (3D) production technology consisting of more feasible, lighter, cheaper materials in terms of manufacturing was used in order to protect the radiation performance. S11, electric field, temperature, and weight measurements of the 3D printed MWA Applicator structure were performed on in vitro breast cancer and shown in Section 6.2. In addition, the experimental measurement results of the MMWAP structure designed to increase the size of the ablation area and to increase the treatment efficiency by providing a more homogeneous form of electrical and thermal distributions are shown in Section 6.3.

In addition to microwave ablation applications of the designed applicator structures, in vitro study was also carried out with pulsed magnetic field therapy. By doing this, it is aimed to further increase the treatment profit. In Section 6.4, in vitro microwave ablation and PEMF studies on prostate cancer were performed.

Lastly, Section 6.5 discusses the production of a 3D printed MWA applicator structure using aluminum and the attachment of NiTi wire at its tip. Experimental studies on pancreatic cancer in vitro are presented to evaluate the applicator's performance.

6.1 RTMWAP for In Vitro Breast Cancer Ablation

In this study, a reflector-type microwave applicator design operating in the industrial, scientific, and medical (ISM) band at 2.45 GHz is proposed. The applicator incorporates a dielectric radiator section to deliver microwave energy with sufficient electric field intensity to reach the desired tumor surface temperature. The effectiveness of the designed applicator is evaluated through experimental measurements. The S11 parameter, which indicates the return loss, demonstrates excellent performance ensuring efficient energy transfer when the dielectric radiator section is inserted into the tumorous tissue. Furthermore, electric field and specific absorption rate (SAR) values at the center of the tumor surface exhibit satisfactory high values, thanks to the integration of a reflector structure. The measured tumor surface temperature above 60 °C demonstrates significant heating, even considering the thermal cooling effect of the petri dishes used in the experimental setup. These findings support the potential of the reflector-type microwave applicator for in vitro studies and highlight its promise for effective tumor ablation in medical applications.

As shown in Figure 6.1, the reflector type microwave applicator prototype is fabricated with the optimized geometric parameters as a result of simulated study for ISM band operation.

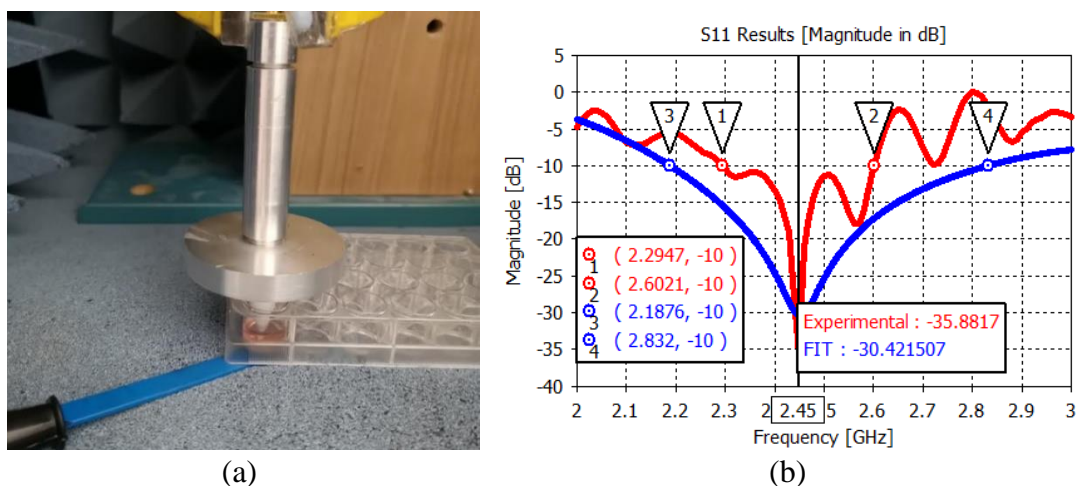


Figure 6.1: (a) Fabricated reflector type microwave applicator and (b) S parameter of reflector type microwave applicator placed inside the tumor sample.

The S11 result of the fabricated applicator prototype located inside the petri dishes containing tumorous cells is experimentally measured by USB-SA124B Scalar

Network Analyser. The measured S parameter of reflector type microwave applicator is shown in Figure 6.1(b).

As deduced from the measured S parameter result shown in Figure 6.1(b), the return loss of the RTMWAP is maximum at 2.45 GHz with the value of 35.88 dB between 2.3 GHz and 2.6 GHz covering the whole ISM band of 300 MHz bandwidth when the tumorous cells are placed near the dielectric radiator section in in vitro experimental study. In order to examine the microwave performance of the reflector type microwave applicator, the experimental setup is demonstrated in Figure 6.2.

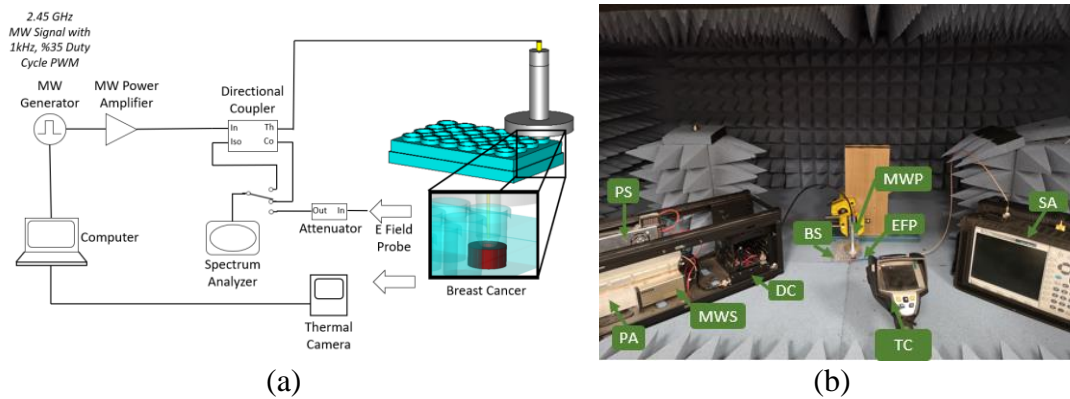


Figure 6.2: Microwave ablation system (a) block diagram, (b) experimental setup containing PA (Power Amplifier), MWS (Microwave Source), DC (Directional Coupler), PS (Direct Current Power Supply), BS (Biological Sample), TC (Thermal Camera), EFP (Electric Field Probe), SA (Spectrum Analyzer) and MWP (Microwave Probe).

In an attempt to find out the microwave performance of reflector type microwave applicator; the forward and reflected power levels of the proposed microwave applicator are measured by 800 - 2700 MHz directional coupler while E field values at the bottom surface of the tumorous cells are measured by Signal Hound EMC near field probe set operating between 30 kHz and 6 GHz. The reflected microwave power at the input port of proposed probe is measured 115 mW which does not damage the standard 180C female SMA connector while the forward microwave power is at 15.31 W level. Experimentally measured electric field at the bottom surface of breast cancer sample is measured 437 V/m that is very close to the numerically calculated electric field value. under the 15 W microwave power excitation in both cases.

In addition to the microwave performance, it is also important to examine the resulting temperature distribution inside the tumorous cells exposed to the microwave power.

The thermal measurement results of tumorous cells exposed to 15 W microwave power level up to 10 minutes is shown in Figure 6.3.

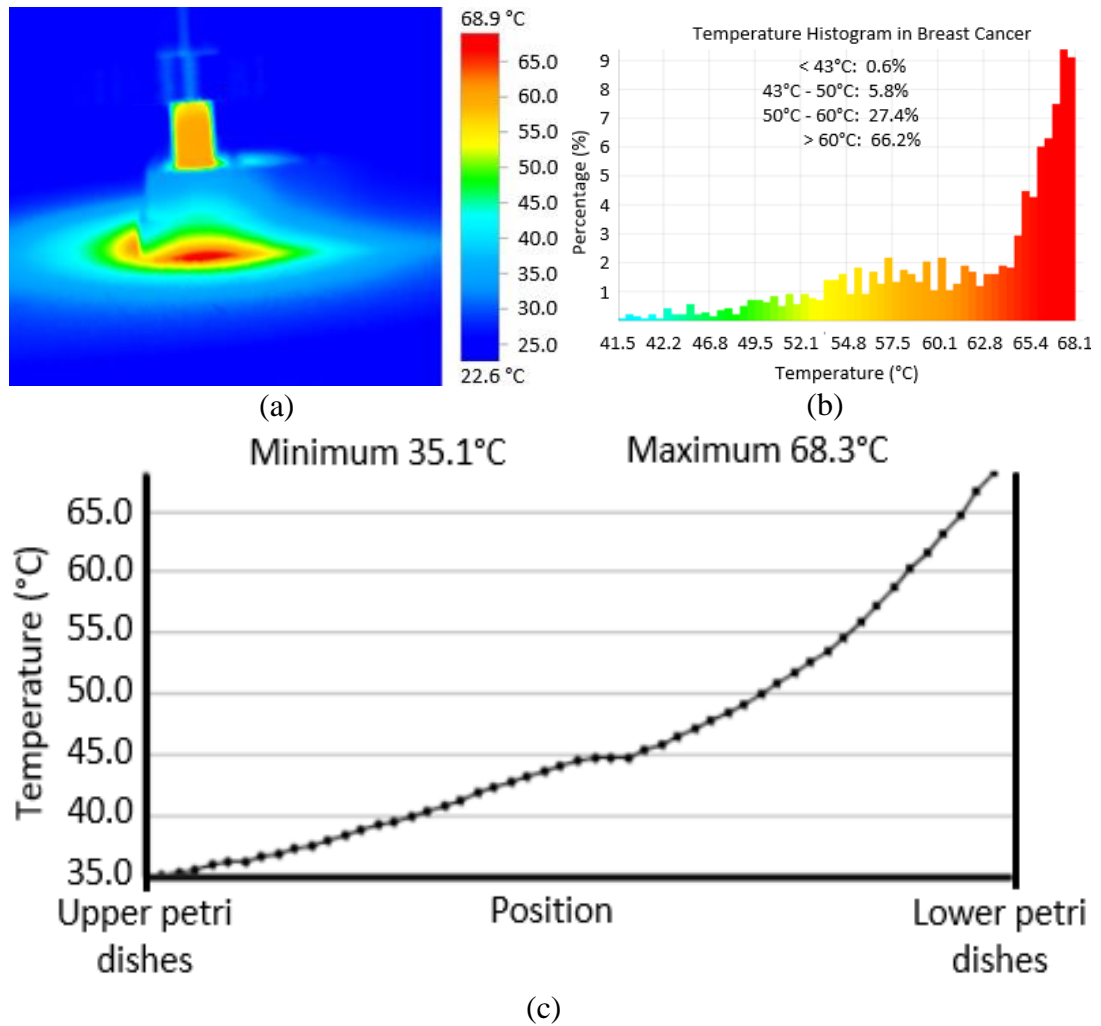


Figure 6.3: Temperature distribution (a) outside (b) inside the petri dishes containing tumor sample that exposed to the microwave power emitted by reflector type microwave applicator up to 10 minutes and (c) temperature histogram in breast cancer.

As shown in Figure 6.3(a), the point lower petri dishes indicate the bottom of the tumorous cells are located and upper petri dishes indicates the point where the upper boundary of petri dishes heated by reflector type microwave applicator. The temperature-location graph inside the petri dishes is obtained by creating a temperature measurement path from the upper to the lower petri dishes with “Testo IR Software V4.6”. While the microwave power emitted by microwave applicator is penetrating through the nontumorous portion of petri dishes, which is the surface of PTFE radiator, the distance dependent measured temperature increases from 35 °C to 45 °C after 10 minutes microwave power exposure. Similarly, the measured temperature inside the

tumor sample has increased from 45 °C to 68.3 °C while microwave power penetrating through tumorous portion. Thus, the microwave power is heating up the tumor sample more rapidly than PTFE radiator section of the proposed microwave applicator due to the finite conductivity of materials and the resulting effect of induced volume current. Moreover, the ablation region is also analysed with reference to the temperature histogram data of breast cancer volume. Based on the ablation temperature which is nearly 60 °C, the percentage value corresponding to the temperature range exceeding the ablation temperature is accepted to be the ablation region. Therefore, the ablation region is approximately 66.2 % of tumor sample, which is 0.92 cm³, as shown in Figure 6.3(c).

In this thesis, the reflector type microwave applicator design is proposed to operate in ISM band for the highly localized ablation of tumor cells in medical ablation applications. The reflector type microwave applicator structure is integrated with the dielectric radiator section to allow the microwave energy to be delivered into the biological sample placed in petri dishes with enough electric field intensity to reach the target temperature on tumor surface. The numerical model of microwave applicator geometry has been numerically optimized for the microwave ablation applications. The numerical computation and experimental measurement results of RTMWAP verify that the designed applicator is operating in 2.45 GHz ISM band with S11 values below -30 dB under the invasive operation of the microwave ablation probe where the dielectric radiator section is inserted into the tumorous tissue. Electric field and SAR values in the center of tumor surface are observed to have the satisfactory high value with the values are 437 V/m and 208 W/kg respectively by the help of reflector structure integrated into the dielectric radiator section. It is also concluded that 68.3 °C measured tumor surface temperature is sufficiently high for in vitro study in comparison to the ex vivo temperature results in the same operation frequency band stated in the literature despite the effect of the petri dishes, thermally cooling down the tumorous cell.

6.2 In Vitro Breast Cancer Ablation Using 3DMWAP

This section is dedicated to explain methodologies for the acquiring of breast cancer cell culture and experimental measurements. In *in vivo* studies including human subject must require ethical approval. However, during the *in vitro* experiments involving human breast cancer cell line, the ethical approval is not required [166–168]. Because of that reason the *in vitro* experiments are preferred to be performed in this study. In addition, cell lines are not relevant material under the Human Tissue Act (although primary cell cultures are). Storage of cell lines for research does not require a Human Tissue Authority (HTA) licence. However, cell lines are subject to the Human Tissue (Quality and Safety for Human Application) Regulations 2007 (The Quality and Safety [Q&S] Regulations), which deal with the storage and use of human tissue for human application/therapeutic use [169]. Research using cell lines does not require ethical review either under the Human Tissue Act or National Health Service (NHS) research governance systems [170].

The human breast cancer cell line MCF7 was purchased from Ege University, Izmir, Turkey. MCF7 fattening medium are incubated at 5% carbon dioxide and 37°C by planting in standard polystyrene cell culture containers in DMEM (Dulbecco's Modified Eagle Medium) containing 10% fetal bovine serum (FBS), 4 ng/mL bFGF (fibroblast growth factor), 100 U/mL penicillin, and 100 mg/mL streptomycin. Cultures that change the fattening medium every two days are excised at the appropriate passage rate using 0.25% trypsin/EDTA solution when they reach 90% density. At each passage stage, cells are frozen in a controlled manner in cell culture freezing containers and stored in a liquid nitrogen tank at –196°C in order to create sufficient stock in the corresponding passage [171–172].

In the experimental verification subsection of this study, the reflection coefficient result of the fabricated 3D printed MWA probe with petri dishes contained MCF7 cells placed next to the cone section has been experimentally measured using Signal Hound Scalar Network Analyzer (USB-SA124B). In this measurement study, there is no direct contact of 3DPMWAP with the cancerous cells culture in petri dish. The experimentally measurement and numerically calculated S_{11} -parameter results of the designed applicator are indicated in Figure 6.4.

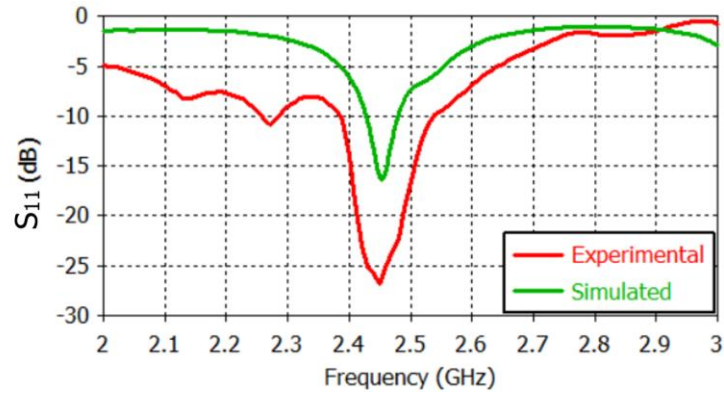


Figure 6.4: S-parameter measurement results of 3D printed MWA Applicator with petri dishes placed on the petri dishes containing MCF7 cells without direct contact.

On the basis of reflection coefficient measurement results indicated in Figure 6.4, the resonance frequency of 3DPMWAP is 2.45 GHz with S_{11} -parameter of -26.9 dB between 2.39 GHz and 2.54 GHz. The operating frequency range is covering ISM frequency band of 2.4–2.5 GHz with the bandwidth of 150 MHz. The numerical computation with return loss magnitude of -26.9 dB agree well with experimental measurement results. The proposed microwave probe design has permissibly low reflection coefficient compared to the alternative studies in the literature [173–175], which results the exposure time of microwave power on the tumorous tissue to be conveniently reduced during the medical treatment. The experimental setup in an attempt to test the microwave performance of 3DPMWAP is indicated in Figure 6.5.

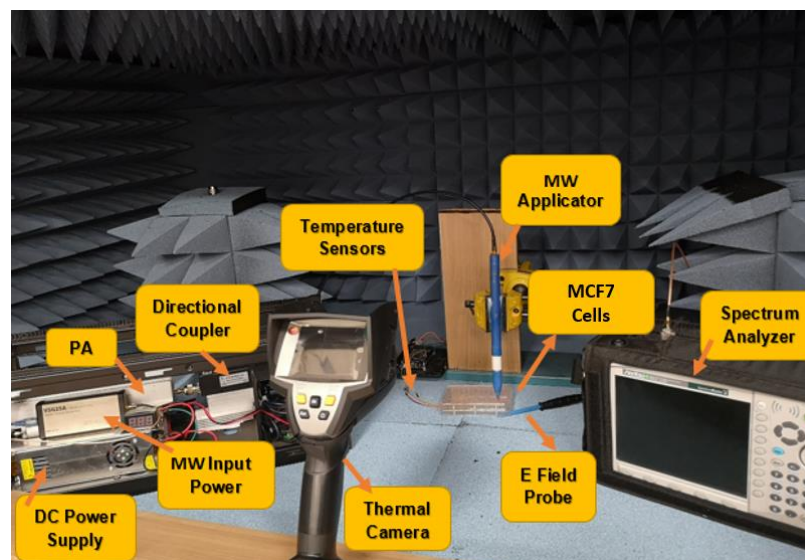


Figure 6.5: Microwave ablation experimental setup.

In Figure 6.5, microwave input power generated by Signal Hound Vector Signal Generator (VSG25A) connected to input port of 50 dB power amplifier (PA), so as to

set the input power of the applicator. In order to operate the amplifier dynamic range, the input power level is set to 0 dBm. A directional coupler is connected to the output port of PA so that the through power and reflected power of proposed microwave applicator can be conveniently measured. In order to investigate the microwave performance of microwave probe prototype, the Signal Hound E-field probe set, which is capable of measuring the electric field from 30 kHz to 6 GHz near the MCF7 sample has been utilized. In addition the reflected power of 3DPMWAP is measured to be 30.91 dBm. The measured input power of 3DPMWAP is set at 46 W with 1.23 W reflected power and E-field under the petri dishes containing MCF7 cell line is measured 177 V/m. The input power of level of 46 W applied to the microwave probe in this study is close to the power levels enabling successful ablation in the previous studies available in the literature [176–178]. Since reflected power of 1.23 W occurred at this power level is small enough to avoid damaging of RF amplifier connected at the input of microwave probe, it is not required to operate the current MWA system at higher power levels for the optimal power excitation in the experimental setup. In this study, in order to achieve the target temperature of 42°C on the surface of tumorous tissue, input power of 46 W has been applied for 20 minutes exposure time.

With reference to the measured performance results of proposed 3DPMWAP, it is also essential to investigate the temperature distribution of MCF7 cell line under the exposure of 46 W microwave power level. Temperature distribution of MCF7 sample illustrated in Figure 6.6 is measured via Testo 882 thermal imager.

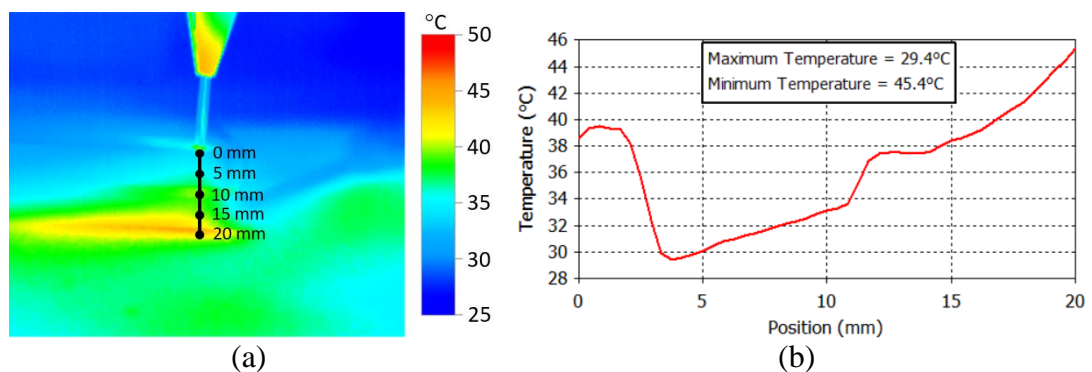


Figure 6.6: (a) Thermal camera view and (b) temperature profile inside the petri dishes along the distance from 3DPMWAP of MCF7 cells after 20 min exposure.

In above the Figure 6.6(b), position at 20 mm represents the location of MCF7 cells and 0 mm represents the point where the cone section of 3DPMWAP contacting the petri dishes containing MCF7 type of tumor sample. The measured temperature inside

the petri dishes decreases from 38.6°C to 29.3°C until the microwave power penetrating through the breast tumor cells and thereafter increases inside the cancerous cells from 29.3°C to 45.4°C. In addition to temperature distribution measurement, the real time temperature of tumorous sample is measured with Arduino Mega based MLX90615 infrared temperature sensor shown in Figure 6.7.

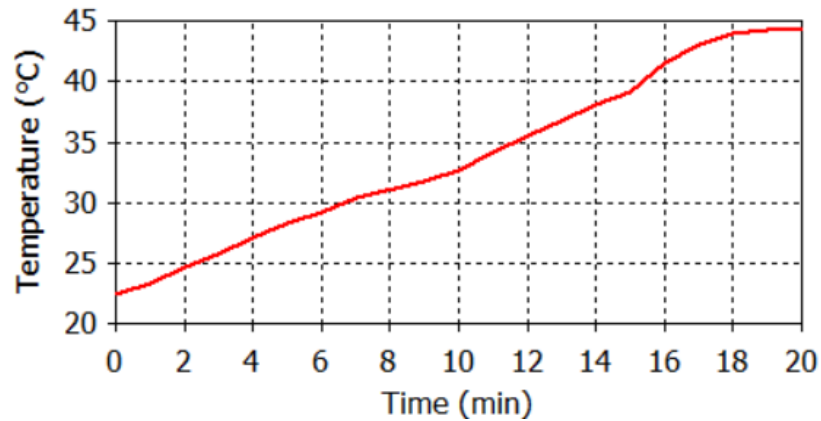


Figure 6.7: Transient temperature of MCF7 cells during 20 min exposure to microwave power.

As indicated in Fig 6.7, breast tumor sample temperature measured with MLX90615 infrared temperature sensor rises from 22.5 to 44.8°C in 20 minutes, which verifies the Testo 882 thermal imager temperature measurement. The verification is also done between the experimental and numerical computation results with the CST Thermal Transient Solver shown in Figure 6.7. The governing equation describing the temperature changes inside tumor tissue due to the EM field exposure is shown in Equation (2.13) [129].

In addition, to the physical reduction opportunity of microwave applicator, the total weight can also be reduced by using ABS material in the light of experimental measurement of ABS based 3DPMWAP and aluminum based microwave applicator weights shown in Figure 6.8. As illustrated in Figure 6.8 fabricating proposed 3DPMWAP with ABS material reduces the weight to approximately one third of MW applicator made of aluminum. The improvement in less weighted applicator fabrication makes the opportunity to provide a comfortable usage for MWA operator.



Figure 6.8: Weight measurements of microwave probes made of: (a) ABS, and (b) aluminum

In this thesis, 3DPMWAP design is proposed to operate at 2.45 GHz ISM band with the improved features, which are low weight, cost efficient, recyclable, and easy to fabrication. The numerical model of 3DPMWAP geometry has been optimized for the MWA applications covering the lower frequency range of 2.4–2.5 GHz ISM band with the measured bandwidth of 500 MHz. Return loss measurement results of 3D printed MWA probe with/without breast tumor tissue placed in the near field region point out that S11 values are better than -10 dB in both case studies. High microwave power emitted by 3DPMWAP heats up the cancerous cells inside the petri dishes to 45.4°C in 20 minutes. Besides, the maximum temperature of malignant tissue can be increase up to 97.7°C in the same time interval if microwave probe inserted into tumor tissue. It is also interpreted that the measured cancerous cells surface temperature is sufficiently high value for in vitro study even the existence of petri dishes thermally insulating the tumorous cell from the microwave power. Numerical calculations and experimental measurement results show that the fabrication of 3DPMWAP structure with ABS material does not only have permissible microwave performance in comparison to the conventional microwave probe alternatives but also reduces the cost, weight and installation difficulties with the high technical potential of SMD component integration into any 3DPMWAP section.

6.3 Ex Vivo Experimental Study of MMWAP

In this section, the experimental microwave ablation study, including the S11 parameter, average Electric field and temperature distribution measurement, has been performed in an ex vivo chicken liver sample. The corresponding experimental setup shown in Figure 6.9 includes an ultra-wideband Signal Hound Vector Signal Generator (VSG), a high gain 100 W Microwave Power Amplifier (LTE2400) to generate high microwave signal and highly accurate measurement tools presented in the following three subsections.

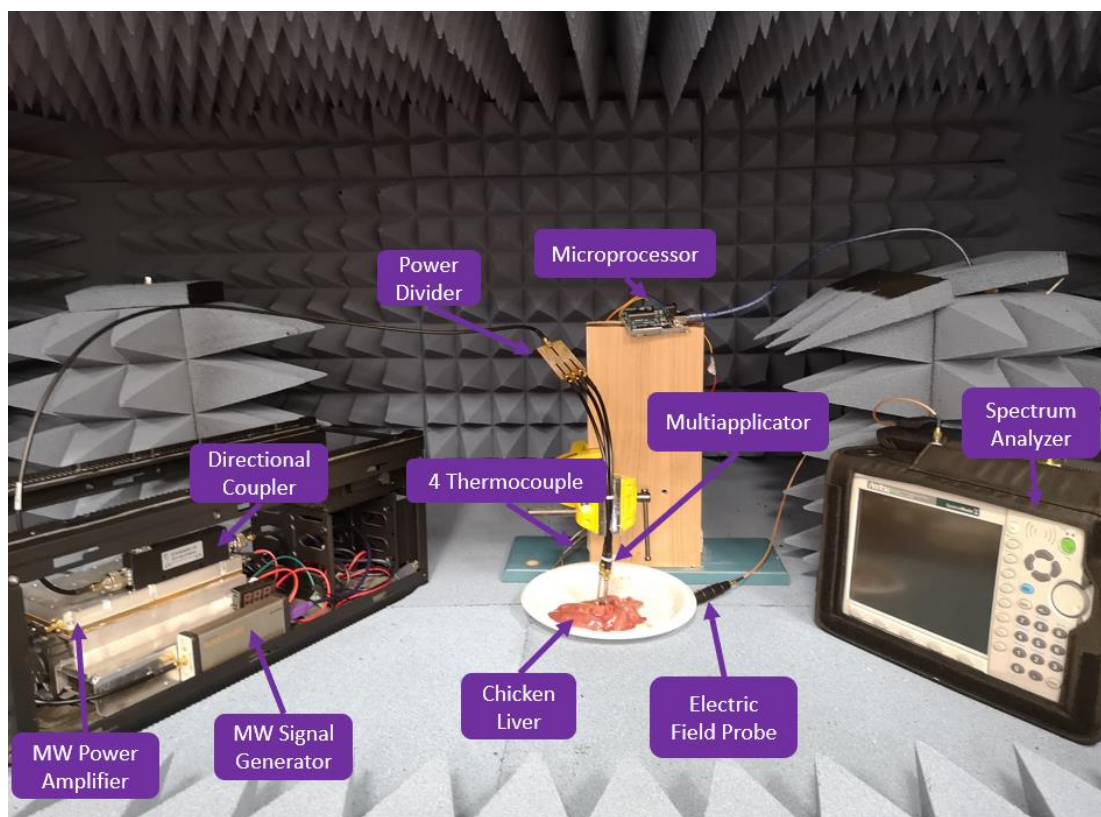


Figure 6.9: Microwave ablation ex vivo experimental setup using MMWAP

The S11 experimental measurements of the 2.45 GHz coaxial slot antenna and MMWAP inside the ex vivo chicken liver are indicated in Subsection 6.3.1. Electric field measurement and SAR calculation with that measured electric field data are reported in Subsection 6.3.2. Then the corresponding temperature measurements and ablation regions are discussed in Section 6.3.3.

6.3.1. Experimental Return Loss Measurement

The return loss experimental measurement of the ISM band MMWAP inside the fresh chicken liver sample with the size of 10cm x 7cm x 2cm have done via Signal Hound Scalar Network Analyzer (USB-SA124B).

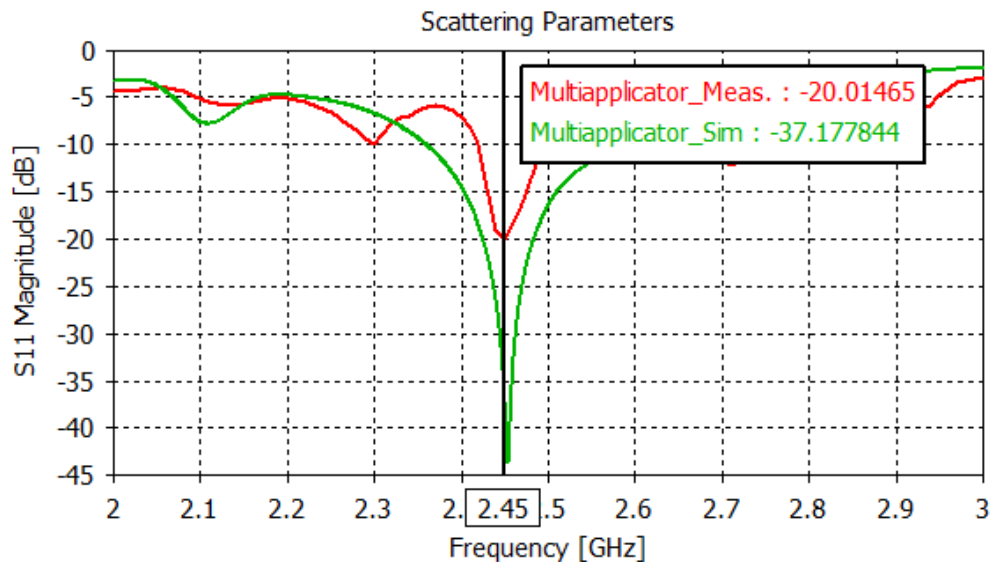


Figure 6.10: Return loss measurement of MMWAP immersed in chicken liver

As referenced from the S11 experimental measurement results in Figure 6.10, the S11 value in the input port of the 1:3 power divider, which is connected to the MMWAP immersed in the chicken liver, is -20.01dB at 2.45 GHz. The microwave MMWAP in that microwave ablation system operates in nearly 80% portion of 2.4 GHz - 2.5 GHz ISM since the frequency set that gives 10 dB return loss values is accepted as the frequency bandwidth.

6.3.2. Electric Field and SAR Performances in Near Field

After measuring the ISM band MMWAP enough to power transfer efficiency to radiate a high-level electric field in the near field region, Electric field measurements are also done to investigate the average SAR in the chicken liver with reference to Equation (2.12). A CNCR directional coupler with a 30 dB coupling factor is connected to the output port of a 50 dB microwave power amplifier with the intention of gathering the power data transmitted to the power divider connected to the input power of the MMWAP. Besides the transmitted power, the Signal Hound electric field probe placed

under the chicken liver sample is used to collect electric field data under the power level measured by a directional coupler. The electric field and transmitted power data are displayed in Anritsu Spectrum Analyzer. Under that microwave ablation measurement procedure, the forward power, reverse power, Average Electric field mass and volume of the chicken liver are measured, and average SAR is calculated from the Electric field and mass data as indicated in Table 6.1.

Table 6.1: Applicator performances table on 125 g chicken liver

	Slot Antenna	MMWAP
Input Power	25 W Gaussian	19 W Gaussian
S11	-23.72 dB	-20.01 dB
Absorbed Power	21 W	17 W
Efficiency	84%	74%
E Field (V/m)	403	355
SAR(W/kg)	173	106
Ablation Region	10.37 cm³	24.45 cm³

In Table 6.1, When the vector signal generator is arranged to generate 0 dBm input power to a microwave power amplifier with 50 dB gain, the slot antenna is driven by 25 W microwave power. In contrast, MMWAP 16 W and reverse power due to impedance mismatches and nonlinearity of microwave power amplifier are 0.42 W and 0.31 W, respectively. Reverse powers are neglectable when compared to appropriate forward powers. Interpreting the differences in input powers, the S11 value of the MMWAP is smaller than the slot antenna due to mismatches between the power divider and each MMWAP element. Despite the extra power loss in the MMWAP, the average Electric field and SAR differences are not much.

6.3.3. Ablation Performances of MMWAP over Single Applicator

Experimental studies in subsections 6.3.1 and 6.3.2 constitute the input of the microwave ablation system. Besides the input parameters of the microwave ablation system, thermal experiments have been done to measure the output of the microwave ablation system. Thermal results rely on the Pennes Bio-heat transfer equation shown in Equation (6.1) [33].

$$\rho c \frac{dT}{dt} = \nabla \cdot k \nabla T + \rho \text{SAR} + \rho Q - \rho_b c_b \rho w (T - T_b) \quad (6.1)$$

Where ρ (kg/m^3), c ($\text{J}/(\text{kg} \cdot ^\circ\text{C})$) and k ($\text{W}/(\text{m} \cdot ^\circ\text{C})$) are the density, heat capacity, thermal conductivity of chicken liver respectively; ρ_b (kg/m^3), c_b ($\text{J}/(\text{kg} \cdot ^\circ\text{C})$) and w ($\text{kg}/(\text{s} \cdot \text{m}^3)$) are density, heat capacity and perfusion rate of blood respectively. Q (W) is the internal heat source due to the metabolic heat generation, T is the temperature function depending on time and space coordinates while T_b is the temperature of blood which is generally 37°C in healthy human. Since there is no vascularization and internal heat transfer generated from living cells in ex vivo liver, Pennes Bio-Heat equation simplifies to Equation (6.2) [23].

$$\rho c \frac{dT}{dt} = \nabla \cdot k \nabla T + \rho \text{SAR} \quad (6.2)$$

In the experimental setup, four identical MAX6675 K-type thermocouples, capable of operating between $0 - 800^\circ\text{C}$ with 0.25°C sensitivity, are used to obtain real-time temperature measurement data from the ablation zone. Thermocouples are placed inside the chicken liver to be radially on the same line as each microwave applicator's slot portion. Each arrow represents four thermocouples apart 2 cm from each other, as shown in Figures 6.11(a) and 6.11(c).

Real-time temperature data shown in Figure 6.11(b) and Figure 6.11(d) have been collected by Arduino Uno and saved to a computer in a text file. High-resolution temperature data was imported to MATLAB for plotting the temperature-time graph. For MMWAP, under 19 W microwave power exposure for 6 minutes, the temperature inside the chicken liver rises from 17°C to 54.8°C , 56.1°C , 62.2°C and 65°C at the points thermocouples placed from outermost to the innermost point of ablation region respectively. Similarly, 6 minutes of microwave exposure created by 25 W microwave power excitation to a single slot antenna, the lead temperature rises from 17°C to 51.2°C , 53.6°C , 58.1°C and 72.8°C . Each point heats exponentially despite applying a constant microwave power source since chicken liver lost its electrical conductivity during microwave exposure due to thermal damage.

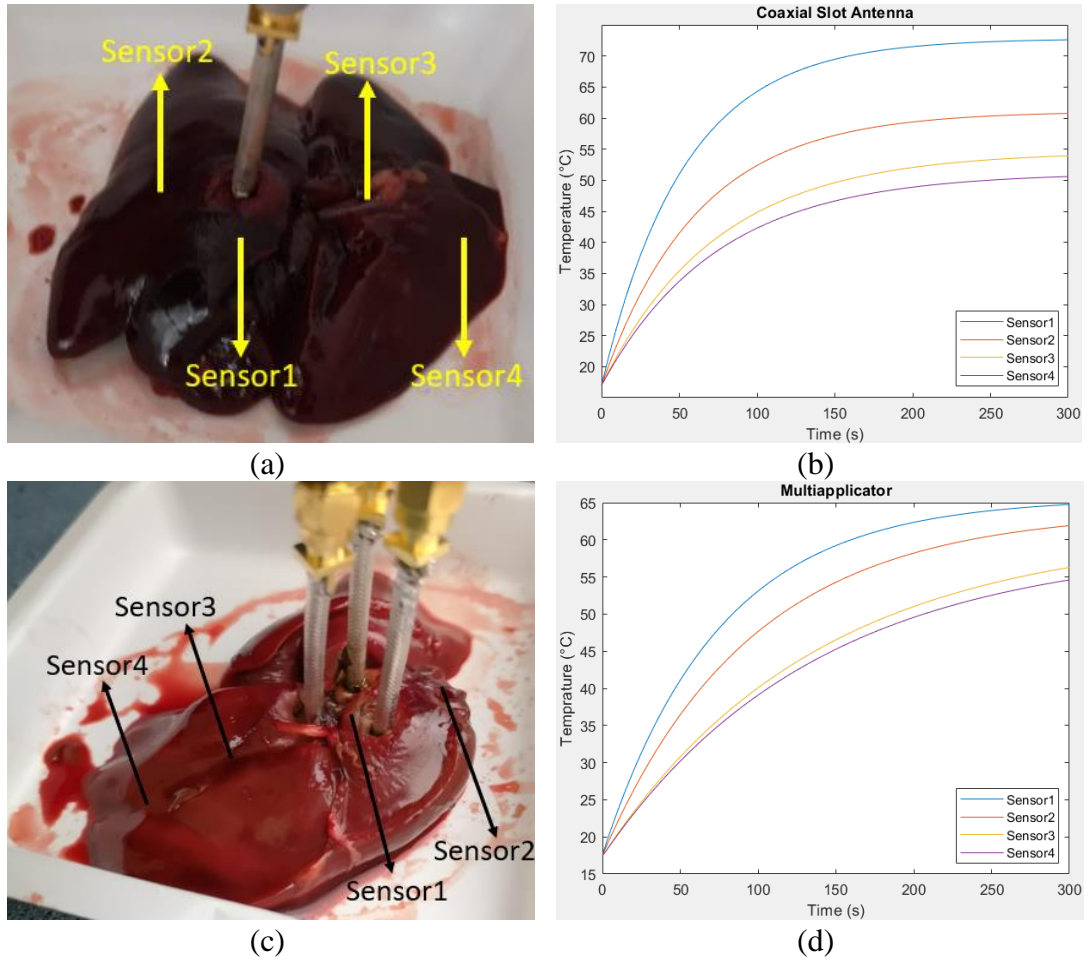


Figure 6.11: (a) Ex vivo chicken liver thermal measurement setup in single slot antenna immersion (b) real time temperature data of single slot antenna usage measured by each thermocouple (c) ex vivo chicken liver thermal measurement setup in MMWAP immersion (d) real time temperature data measured of MMWAP usage by each thermocouple.

In order to quantize the homogeneity of the ablation area generated by a single antenna and MMWAP, the rates of temperature changes depend on ablation areas shown in Equation (6.3). As ablation area occurs when the temperature exceeds 60 °C, more minor temperature data do not affect Equation (6.3).

$$\text{Homogeneity} = 1 - \frac{\sum_{s=1}^n \left[\sum_{k=1}^t \frac{|T_k - T_{k+1}|}{t} \right]}{n}, T_k = \begin{cases} 60, T_k < 60^\circ\text{C} \\ T_k, T_k \geq 60^\circ\text{C} \end{cases} \quad (6.3)$$

Where n is the number of temperature sensors which is 4 in that study, T_k is the simultaneous sensor measurement corresponding to sensor label s, t is the number of samples that real time temperature value exceeds 60 °C. If Equation (6.3) is applied for whole sensor data shown in Figure 6.12.b and Figure 6.12.d, homogeneities are found to be 83.53% for single slot antenna, 93.85% for MMWAP.

After the microwave heating process, ablation zones of two nearly identical chicken livers under microwave exposure emitted by a single coaxial slot antenna and MMWAP are compared, as indicated in Figure 6.12.

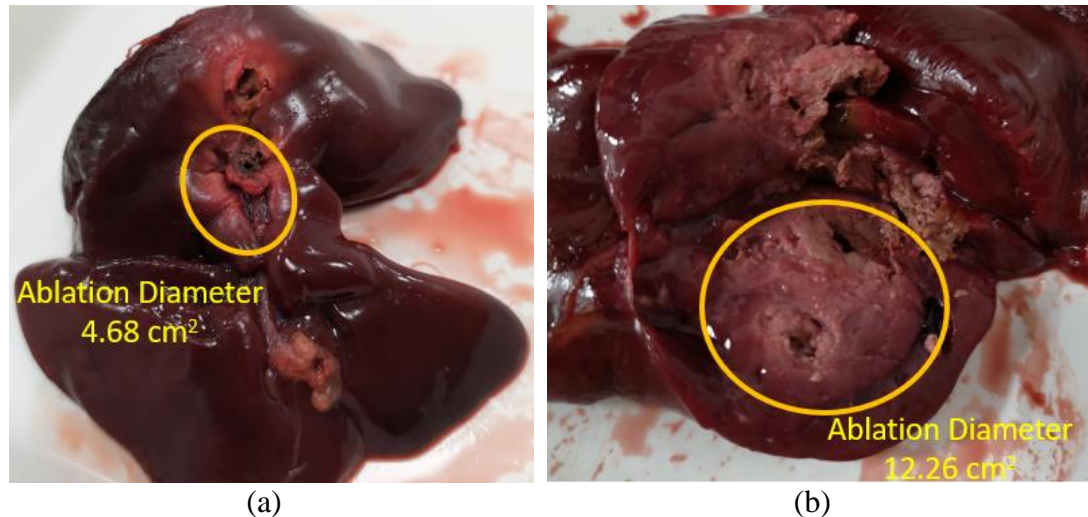


Figure 6.12: Ablation zone measurements of 118 g ex vivo chicken liver with (a) single coaxial slot antenna and (b) MMWAP usage

As deduced from the ablation zone measurement in Figure 6.12, the ablation area created by a single coaxial slot antenna is 4.68 cm². In comparison, the MMWAP creates 12.26 cm² from measurement by cutting the chicken liver radially. Moreover, when the depth of coagulated tissue is measured, the whole ablation region that the single coaxial slot antenna and MMWAP create have been seen at 10.37 cm³ and 24.45 cm³, respectively. In addition to MMWAP creating a larger ablation zone than single slot antenna, higher homogeneity also occurs in that region.

Sections 6.1, 6.2, and 6.3 demonstrated successful outcomes in both in vitro and ex vivo studies using the Microwave Ablation (MWA) technique. The study also explored the application of pulsed electromagnetic field (PEMF) therapy in cancer treatment alongside MWA. PEMF exhibited the ability to enhance magnetically depleted oxygen radicals (ROR) levels and modulate antioxidant chemistry. This effect was achieved by influencing free radical species, which are representative components of ROR, through the magnetic field. It was hypothesized that this intentional manipulation could regulate the ROR and antioxidant defense system by modulating ion species such as K⁺, Na⁺, Cl⁻, and Ca⁺². In Section 6.4, a novel methodology was introduced, utilizing MWA to successfully treat tumors while effectively minimizing potential side effects using PEMF.

6.4 MWA and PEMF Studies on Prostate Cancer

In this section, MWA and PEMF studies were performed on the prostate cancer group in cell culture. In the study, open-ended rectangular waveguide and dielectric-loaded dipole antenna-based MWA applicator structures were used as microwave radiation devices, and a circular coil was used in the PEMF system. A magnetron tube system with a wideband microwave signal generator in combination with a 2.45 GHz solid-state microwave amplifier was used as the microwave energy source. At the same time, a signal generator and solid-state amplifier operating in the ELF (extremely low frequency) band were used as the PEMF energy source. The experimental setup for microwave ablation on prostate cancer is shown in Figure 6.13.


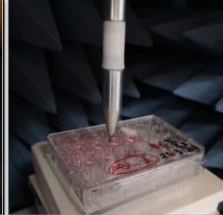


Group1	Group2	Group3	Group4	Group5
				
350 W MW power was applied for 5 minutes with a power cut of over 40 for 20 s.	350 W MW power was applied for 5 minutes by cutting the power for 20 seconds every 40 s.	80 W MW power was applied for 5 minutes.	80 W MW power was applied for 5 minutes, then PEMF at 35 W power was applied for 55 min.	35 W PEMF was applied for 60 minutes.
MWA		Rest	PEMF	

Figure 6.13: Treatment application on prostate cancer including MWA and PEMF

The studies on prostate cancer were divided into six groups, five experimental groups and one control group. In the experimental setups of Group 1 and in Group 2 magnetron tube is used as a microwave energy source. The system using a wideband microwave solid-state generator and ISM band microwave power amplifier was used in Group 3 and the first 5 minutes of Group 4. Following the same study with the system in Group 3, the system in which PEMF was applied was named Group 4 and the system in which only PEMF was applied was named Group 5. In Group 1 and Group 2, 350 W microwave energy in the ISM band was applied with five repetitions as 40 s application, 20 s resting; in Groups 3 and 4, 80 W microwave energy was applied for 5 minutes at 2.45 GHz frequency of the ISM band. In the PEMF system in

Group 4 and Group 5, a 35 W pulse signal at a frequency of 73 Hz and pulse width of 25% was applied to utilize a circular coil to complete in 60 minutes.

Since tissue is thermally eliminated in microwave ablation systems, examining the maximum temperatures occurring in the experimental groups after the application is necessary. On the other hand, in PEMF treatments, the maximum temperature should be the temperature at which the living cell can survive. Figure 6.14 shows the measurement of the prostate cancer surface temperatures of the experimental groups after the application with a Testo 882 thermal camera.

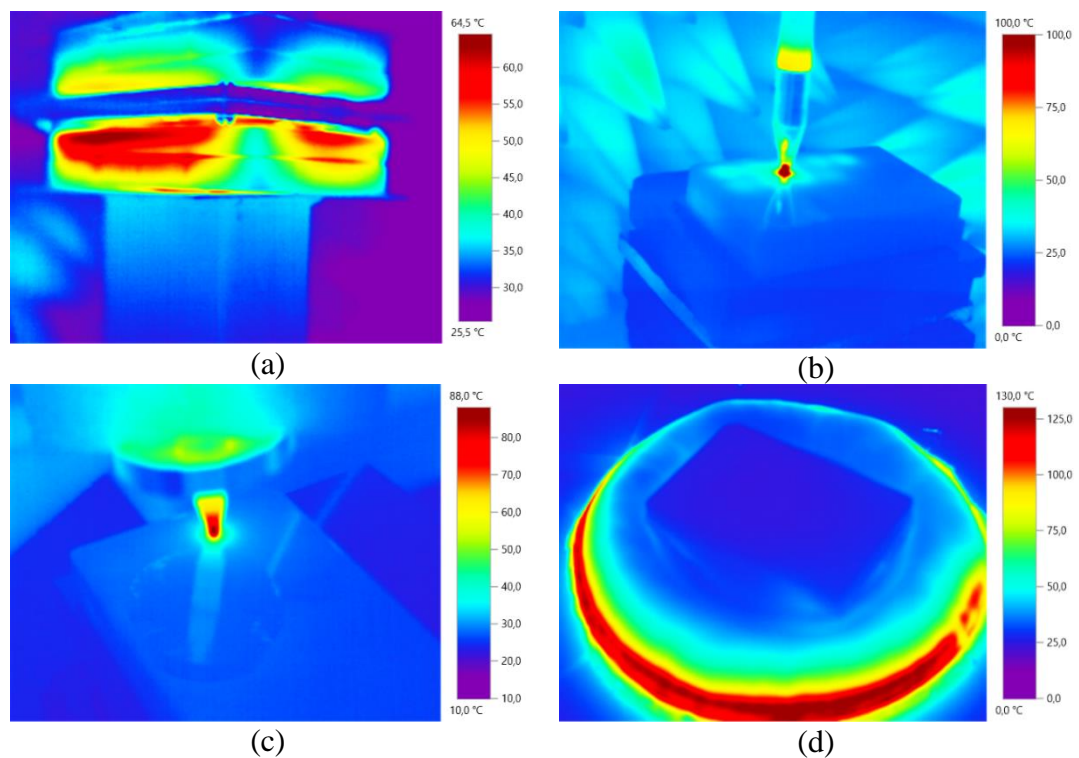


Figure 6.14: Thermal camera measurements results of (a) Group 1, (b) Group 2, (c) Group 3, (d) Group 4 and Group 5 at the time of the highest prostate cancer surface temperatures

The measurements were made at room temperature and in a non-reflecting room to avoid external heat and electromagnetic energy interference. Figure 6.14 shows that the maximum temperatures in prostate cancer were 64.5 °C in Group 1, 58.8 °C in Group 2, 42.7 °C in Group 3, and 31.2 °C in Group 4 and Group 5. In Group 1 and Group 2, where 350 W input power was applied, the ablation temperature of 55-60 °C was reached in a total exposure time of 5 minutes, while in Group 3, hyperthermia temperature conditions were achieved in the same time but when 80 W input power was applied. After reaching hyperthermia temperatures in Group 4, the prostate cancer, which was placed in the PEMF experimental setup for 60 minutes, lost most of its heat

during this time and reached a surface temperature of 31.2 °C below hyperthermia temperature as in Group 5.

Since the position-dependent temperature measurement results shown in Figure 6.14 are the highest temperature values reached throughout the experiment, time-dependent temperature measurement was also required for more detailed analysis of the microwave ablation process. The real-time temperature measurement results of the experimental groups with MLX90614 infrared temperature sensor are given in Figure 6.15.

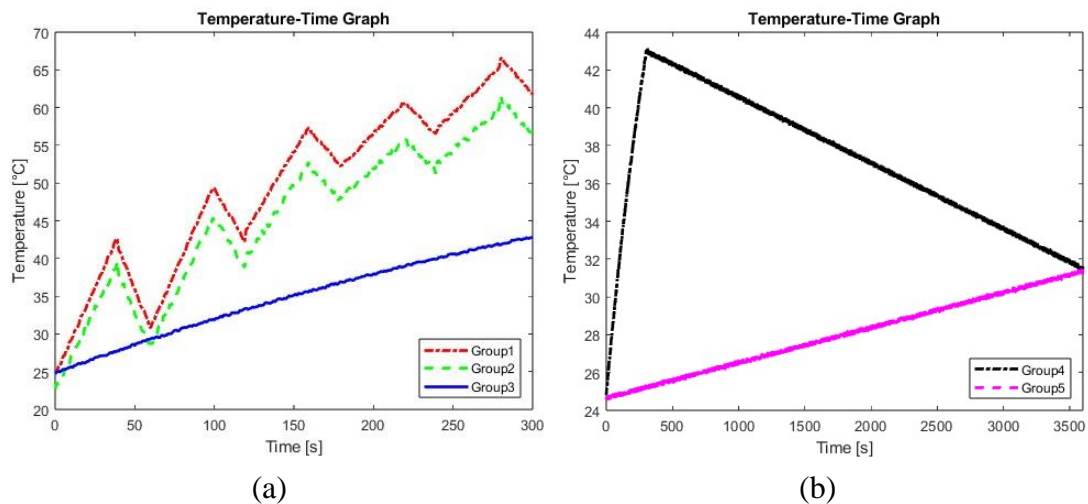


Figure 6.15: Time dependent temperature measurement of (a) Group 1, Group 2 and Group 3; (b) Group 4 and Group 5

In Figure 6.15.a, Group 1 and Group 2 were applied at the same power levels and with the same method, and their time-dependent temperature graphs are similar. The directional changes in the temperature-time graphs of these two groups are obtained simultaneously as the result of the power systems being switched on and off simultaneously with the timer. However, measured temperature values differ due to the different radiation patterns of the applicator systems used and, therefore, the microwave energy they transfer. In the first three repetitions of Group 1 and Group 2, there was a temperature increase of 15-18 °C in the ablation application stages, while there was a decrease of 8-10 °C in the temperature increase after 150-165 seconds of ablation. Based on the information that the time interval in which ablation begins to occur causes disruptions in the protein structure of prostate cancer and, consequently, electrical and thermal conductivity deteriorates, there was a decrease in the rates of temperature change in the graphs. In Group 3, 80 W microwave power was applied continuously for 300 s, and since 55-60 °C ablation temperatures could not be reached,

there was almost no change in the increase. The instantaneous temperature of cancer cells in Group 3 increased close to linearly from room temperature of 24.5 °C to hyperthermia temperature of 42.7 °C. The exact temperature pattern was obtained in the first 300 seconds of the microwave ablation treatment phase of Group 4, shown in Figure 6.15(b). In the remaining 300-3600 seconds of Group 4, the temperature decreased from 42.7°C to 31.2°C due to PEMF application. Group 5 was treated entirely with PEMF, and based on the temperature data, it was concluded that PEMF treatment was not a thermally damaging application based on the warming of the surface temperatures of prostate cancers from room temperature to 31.2°C.

The input power, electric field magnitude at 2.45 GHz, magnetic flux density at 73 Hz and maximum temperatures reached in the experimental groups on prostate cancer were measured and given in Table 6.2. Electric field magnitudes were measured with Signal Hound EMC Near Field probes in the MWA experimental groups, while the magnetic flux density measurement with the PASCO hall effect sensor in the PEMF experimental groups. Input power levels measurements are done with a 200W CNCR directional coupler and Signal Hound Spectrum Analyzer in the MWA system containing a 100W solid-state amplifier system and an ut200a AC digital multimeter in the MWA system using a magnetron tube and in the PEMF system.

Table 6.2: MWA and PEMF assay results on prostate cancer

Group No.	Input Power (W)	E Field @ 2.45 GHz (V/m)	B Field @ 73 Hz (mT)	Temp (°C)	Procedure
Group1	350	72800	N.A.	64.5	40 s MWA, 20 s rest (5 repetition)
Group2	350	56600	N.A.	58.8	40 s MWA, 20 s rest (5 repetition)
Group3	80	1450	N.A.	42.7	5 min MWA
Group4	80(MWA), 35(PEMF)	1450 (MWA), N.A. (PEMF)	N.A.(MWA), 2.2 (PEMF)	31.2	5 min MWA, 55 min PEMF
Group5	35	N.A.	2.2	31.2	60 min PEMF

Table 6.2 indicates that the electric field measurements via the near-field probe placed on the bottom surface of the petri dish in which Group 1 and Group 2 under 350 W microwave power are 72800 V/m and 56600 V/m, respectively. These electric field values are close to the electrical discharge voltage value of the well plate and the dielectric medium due to the prostate cancer cells existence, and electrical discharges

were observed in Group 2 from time to time. However, the applicator system used in Group 1 emits nearly homogeneous electromagnetic radiation that occurs without electric field difference to cause electrical discharge in the experimental setup. Electrical discharges happen in this area because the electrical diffraction voltage value is exceeded. After all, the electric field magnitude in the tip region where the applicator used in Group 2 touches the upper point of the petri dish is greater than the electric field value measured in the region where cancer cells are located. Based on the electric field measurement results in Group 1 and Group 2, it is predicted that the experimental groups that will create higher microwave exposure in terms of application method and input power level will damage the petri dish and applicators. Approximately 1450 V/m electric field was obtained with a microwave power of 80 W in the first 5 minutes of Group 3 and Group 4. This electric field level is deficient compared to the electric field level measured in the first two experimental groups, and no electrical discharge or deformation of the experimental system was observed. In the PEMF system, which constituted the last 55 minutes of Group 4 and all of Group 5, the pulse signal at a frequency of 73 Hz used as 35 W input power generated a magnetic flux density of 2.2 mT in cancer cells. The surface temperatures of Groups 4 and 5 did not significantly rise because the electric field in PEMF systems is relatively weak in comparison to the magnetic field, and prostate cancer does not have a magnetic permeability value to convert high magnetic flux density into high heat.

6.4.1. Cell Lines and Culture Conditions

The human prostate tumor cell line PC3 obtained from Ege University Bioengineering Department Ayşe NALBANTSOY. Cells were grown and maintained in RPMI-1640 medium containing 140 U/mL penicillin, 140 ug/mL streptomycin, 2 mM 1-glutamine and 10% fetal bovine serum. Cells were grown in T-25 cm³ flasks as an adherent monolayer culture in a humidified atmosphere of 5% CO₂ at 37°. A Neubauer hemocytometer was used to determine the cell number before and after the completion of all experiments.

6.4.2. Wound Healing/Migration Assay

Wound healing assays are commonly used to measure cell movement on a two-dimensional substrate. A wound-healing assay or migration test was used to evaluate the motility of cells and their capacity for migration. A wound is made on a layer where monolayer cells converge and the wound is imaged and incubated in the desired condition for a certain period of time to allow cells to migrate into the empty space. Finally, the image is taken again and the gap in the wound is compared with the control as shown in Figure 6.16.

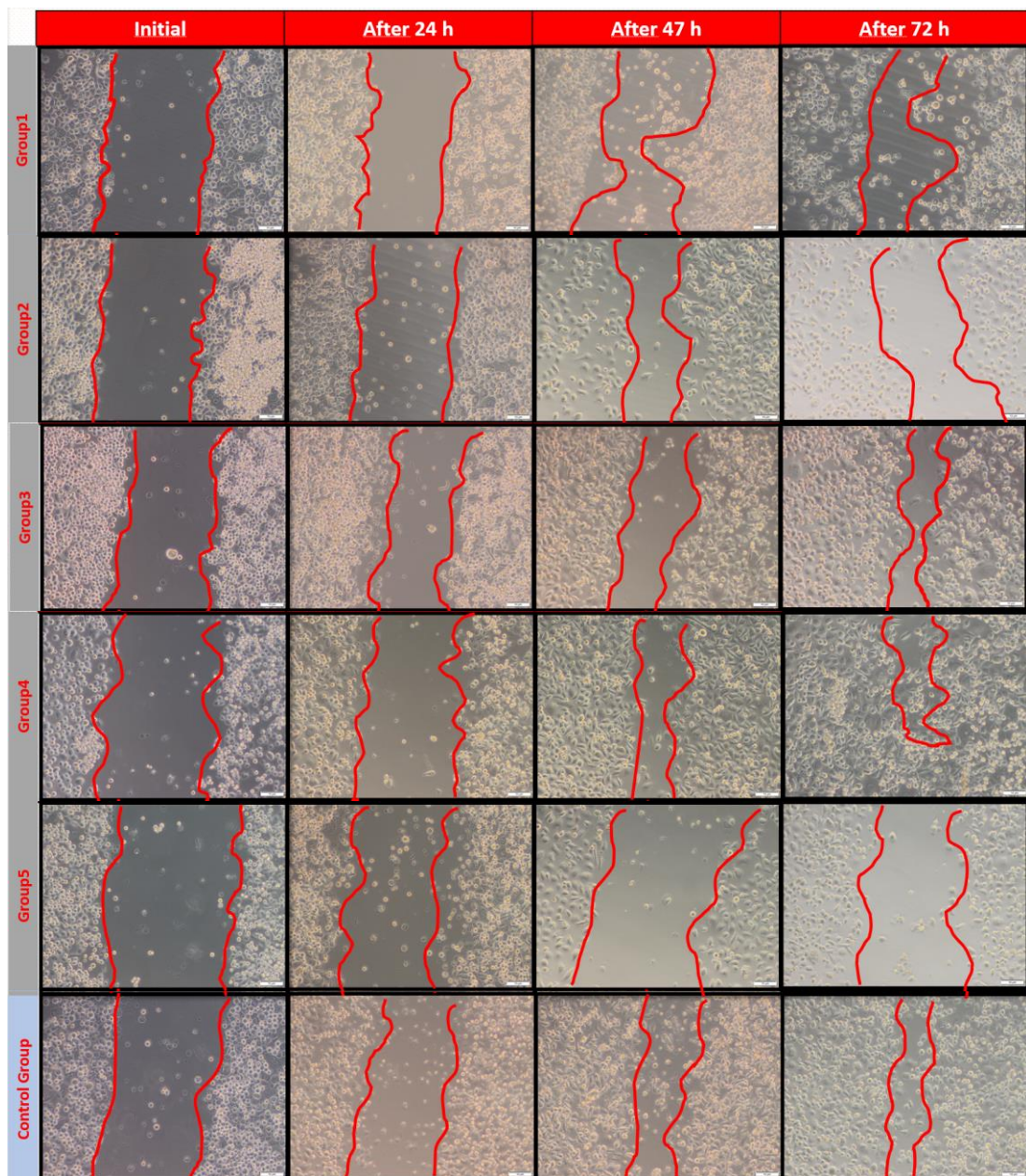


Figure 6.16: MWA results of prostate cancer

We used this assay to measure the effect of electromagnetic field application on migration capacity of PC3 cells. PC3 cells were seeded on a 6-well plate at a density of 5×10^5 per well. Sterile 200 μ l pipette tip used for wound model and a flat scratch was created on the plate. Each well was rinsed with PBS to remove cells from the surface. washed and then fresh nutrient medium was added on them. left for incubation. Using a microscope (Olympus CKX41SF-Tokyo, Japan), the quantity of phase-contrast wound closure at 0, 24, 48, and 72 hours post-procedure was evaluated. The study used a scratch test to assess the migratory and invasive abilities of PC3 cells in five different groups. The cells in Groups 3 and 4, which were treated with a combination of microwave ablation and pulsed electromagnetic field (PEMF), showed rapid migration ability compared to cells in Groups 1 and 2, which were treated with microwave ablation only or PEMF only. Interestingly, cells in Group 5, which were treated with PEMF only, had poorer migration ability than cells in the other groups, suggesting that PEMF alone could reduce the migratory ability of PC3 cells as indicated in Figure 6.16.

6.5 MWA Study on Pancreas Cancer

The section involved the investigation of the effects of MWA on a cell culture of pancreas cancer. Specifically, the experimental setup incorporated Microwave Radiation Devices, such as NiTi tipped dielectric-loaded dipole antenna-based MWA applicator structures. Microwave energy was supplied using a wideband microwave signal generator, alongside a 2.45 GHz solid-state microwave amplifier, QPD350, with NFC. Figure 6.17 presents a visual representation of the experimental configuration utilized for MWA in pancreatic cancer.

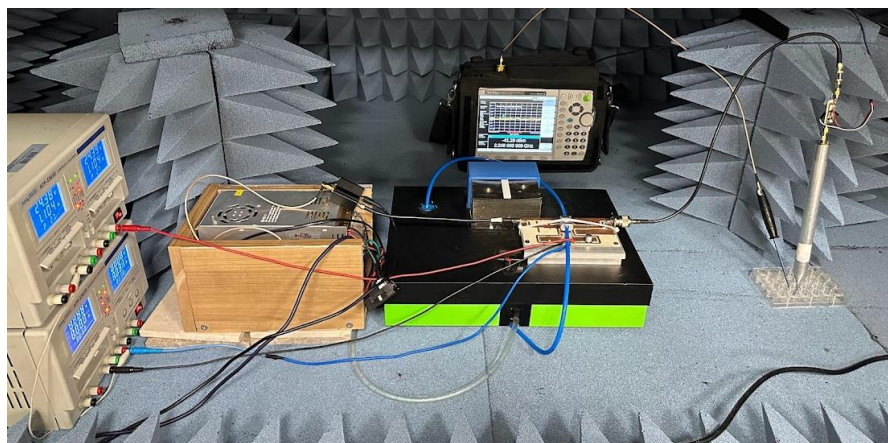


Figure 6.17: Treatment application on pancreas cancer including MWA

The study on pancreatic cancer included two distinct groups: an experimental group and a control group. In the experimental group, the setup for MWA involved the utilization of a VSG25A microwave signal generator as the source of microwave energy. The experimental group was subjected to an 75 W microwave power for a duration of 2 minutes, operating at a frequency of 2.45 GHz within the Industrial, Scientific, and Medical (ISM) band. Conversely, the control group represented the experimental group under normal room temperature conditions, without any exposure to electromagnetic interference.

In microwave ablation systems, the elimination of tissue through thermal means necessitates an examination of the highest temperatures observed in the experimental groups following the application. The surface temperatures of pancreas cancer in the experimental groups were measured using a Testo 882 thermal camera, as depicted in Figure 6.18.

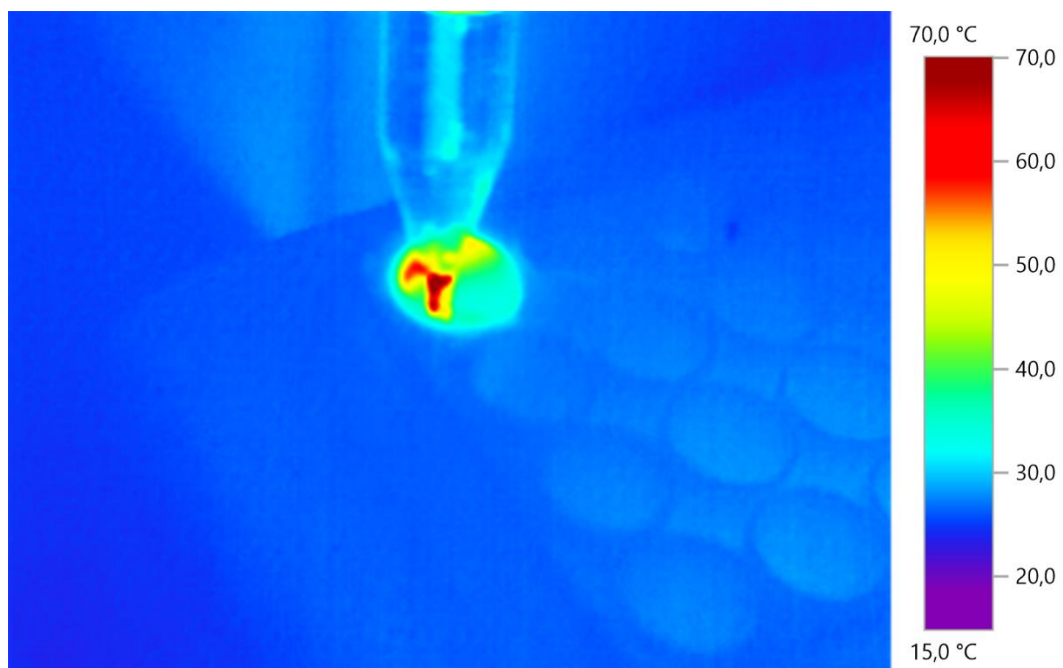


Figure 6.18: Maximum temperature of pancreas cancer with 75 W microwave power

To ensure accurate measurements and mitigate external heat and electromagnetic energy interference, the temperature assessments were conducted within a non-reflective room at room temperature. As illustrated in Figure 6.18, the maximum temperatures observed in pancreas cancer is 61.4 °C. This temperature value was measured at the junction of the pancreatic cells and the NiTi tip and decreases to 35 °C as it moves away from the tip. Greater coagulation is observed when the duration of the ablation application exceeds 2 minutes. However, it is crucial to note that excessive

application of elevated temperature levels can lead to rapid harm to healthy cells and result in an uncontrollable treatment process. As a result, adjustments have been made to the application time in order to maintain optimal control and prevent adverse effects on healthy tissue.

To gain a comprehensive understanding of the microwave ablation process, it was necessary to conduct time-dependent temperature measurements in addition to the position-dependent measurements showcased in Figure 6.18. These time-dependent measurements provide more detailed insights into the experiment. For this purpose, real-time temperature measurements of the experimental groups were obtained using the MLX90614 infrared temperature sensor. The temperature data captured during the experiment are presented in Figure 6.19.

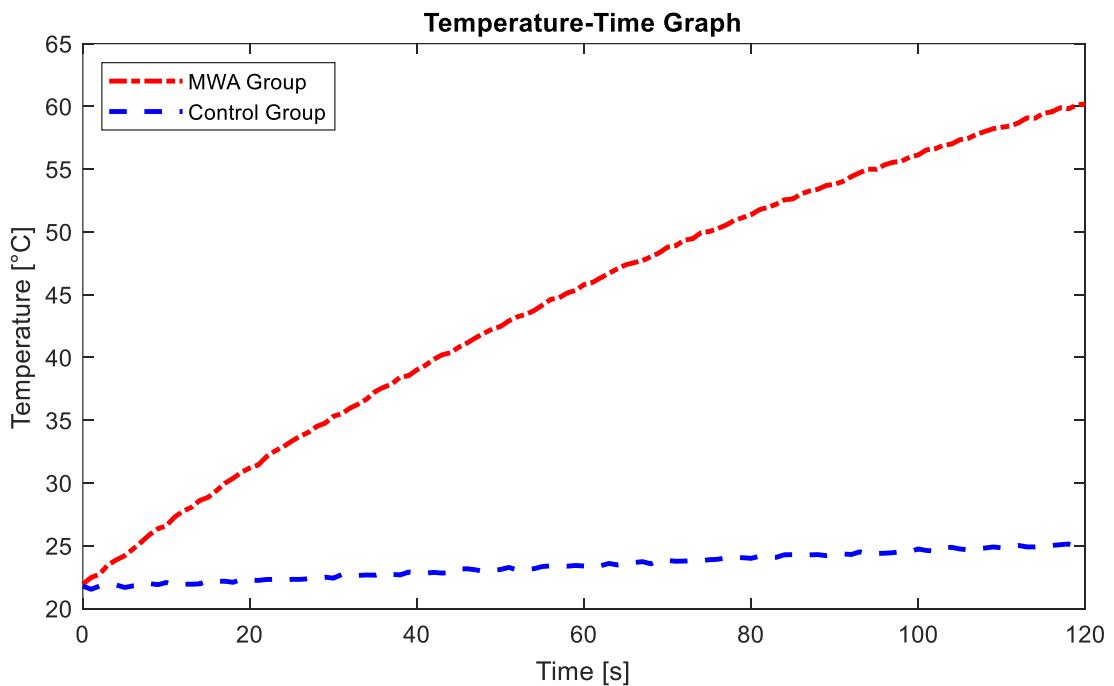


Figure 6.19: Time dependent temperature measurement of MWA Group and Control Group

Figure 6.19 presents the time-dependent temperature graphs of MWA Group and Control Group, which is measured with the same temperature measurement method. Both groups initially had temperatures close to 21.5 °C. In the MWA Group, where 75 W of microwave power was applied, the temperature reached 61.3 °C after 120 seconds. Conversely, the Control Group maintained a temperature of 25 °C, representing the ambient room temperature. It is important to note that the cells in the MWA group undergo chemical changes in response to microwave energy, resulting in

alterations in their thermal properties. Consequently, the rate of temperature increase gradually diminishes over time. Conversely, the control group cells experience a linear increase in temperature as they are subject to the ambient heat without undergoing significant structural changes.

Table 6.3 provides measurements of the input power, electric field magnitude at 2.45 GHz and the maximum temperatures attained in the experimental groups on pancreas cancer. The electric field magnitudes in the microwave ablation experimental groups were measured using Signal Hound EMC Near Field probes. The input power levels were determined using a 200W CNCR directional coupler and Signal Hound Spectrum Analyzer in the MWA system, which consisted of a QPD350 solid-state amplifier system.

Table 6.3: MWA and PEMF assay results on pancreas cancer

Group No.	Input Power (W)	E Field @ 2.45 GHz (V/m)	Temp (°C)	Procedure
MWA Group	75	5680	61.3	75 W microwave power for 120 s exposure
Control Group	0	0	25	120 s keep at room conditions

Table 6.3 provides insights into the electric field measurements obtained by placing a near-field probe on the bottom surface of the petri dish in which MWA Group were subjected to 75 W microwave power. The measured electric field values are 5680 V/m for MWA Group. Thus, the designed 350 W microwave power amplifier, when used in conjunction with the NFC, provides high efficiency and high power output to create the electrical conditions required for microwave ablation

The PC3 human pancreas tumor cell line, obtained from Ayşe NALBANTSOY at Ege University's Bioengineering Department, was utilized in this study. The cells were cultivated and maintained in RPMI-1640 medium supplemented with 140 U/mL penicillin, 140 µg/mL streptomycin, 2 mM l-glutamine, and 10% fetal bovine serum. As an adherent monolayer culture, the cells were grown in T-25 cm³ flasks under a humidified atmosphere of 5% CO₂ at 37°C. The cell count was determined using a Neubauer hemocytometer before and after the completion of all experiments.

Cell migration and motility can be effectively assessed survival analysis, which are widely employed in measuring cell movement on a two-dimensional substrate. In this

study, a migration test or survival analysis was conducted to evaluate the migratory capabilities of cells. The assay involved creating a wound on a confluent cell monolayer, followed by imaging and incubation under specific conditions to facilitate cell migration into the created gap. Subsequently, another image was captured, and a comparison of the wound gap with the control was performed, as depicted in Figure 6.20.

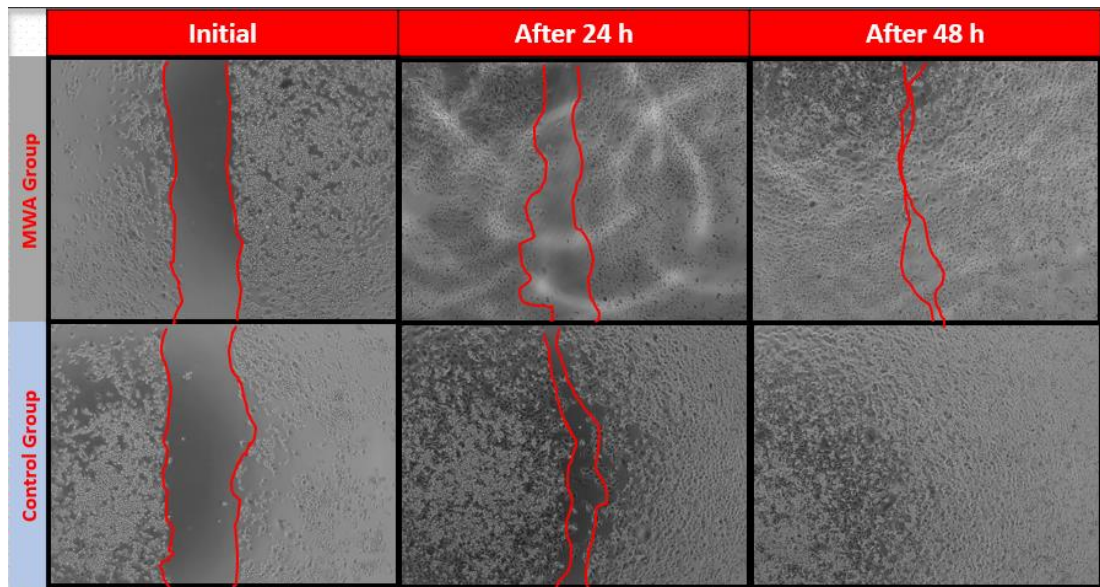


Figure 6.20: MWA results of pancreas cancer

To examine the impact of electromagnetic field application on the migration capacity of human pancreatic cancer cells (PANC1), we employed the wound healing assay. PANC1 cells were seeded in 6-well plates at a density of 5×10^5 per well. A sterile 200 μ l pipette tip was used to create a flat scratch on the plate, simulating a wound. Subsequently, the wells were rinsed with PBS to remove any detached cells from the surface and fresh nutrient medium was added before incubation. The closure of the phase-contrast wounds at 0, 24 and 48 hours post-procedure was assessed using an Olympus CKX41SF microscope from Tokyo, Japan.

Within this study, scratch wounds were created on cultures prepared with the monolayer human pancreatic carcinoma PANC-1 cell line, and MWA was applied to the cells. The result showed that wound healing occurred in the control group and decreased in the cell group exposed to MWA as indicated in Figure 6.20. This result showed that MWA inhibited the repair ability of PANC-1 cells.

Chapter 7

In Vivo Experimental Study

In vitro models provide important information for the examination of many treatment types and agencies in breast cancer, which ranks first in cancer patients. However, animal models with sufficient growth are needed to investigate effective and safe treatments. 4T1 mouse metastatic breast cancer cell line was employed to establish an experimental model. To ensure that 4T1 mouse metastatic breast cancer cells proliferate and become confluent at 37°C and 5% CO₂, 10% fetal calf serum (FCS), 50 µg./ml. Gentamicin, 100 UI/ml. Penicillin, 100 UI/ml. It was left in DMEM/F12 culture medium containing streptomycin. Proliferated cells were then collected and counted under a microscope on a Thoma slide. For each female mouse, 1x10⁶ cells/50 µL of phosphate buffer were taken into ppd injectors. Cancer cell culture prepared as shown in Figure 7.1 was given to the animals subcutaneously at the breast level, right and left, and 10-12. The day was waited for cancer formation [179]. Figure 7.1 illustrates the MWA application of rats immersed in breast cancer cells, as an essential step in the experimental protocol.

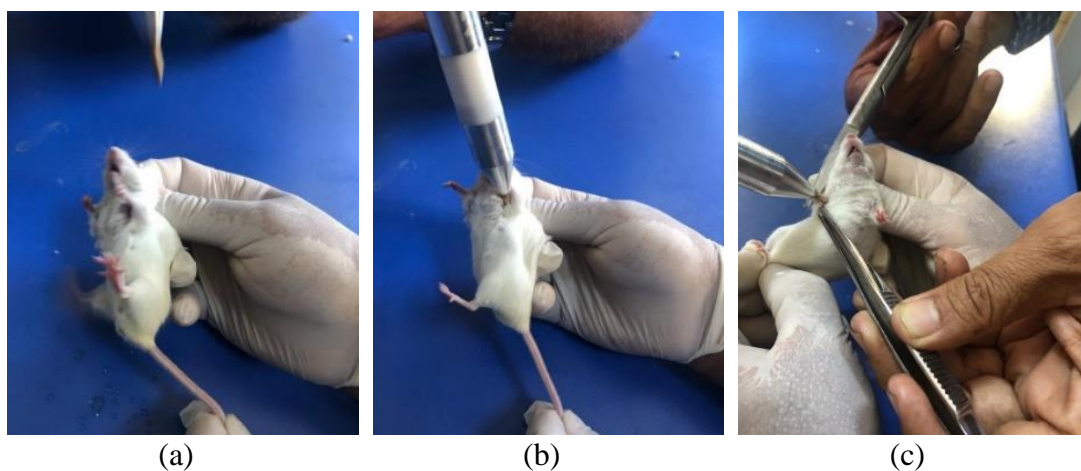


Figure 7.1: MWA application of rats

7.1 MWA and PEMF Applications

After the cancer models were created, the animals were divided into 7 groups. Details about the groups are given in Table 7.1. Microwave Thermal Ablation applications and PEMF application were performed to the tumorous area at the frequencies determined by 4 different antennas designed. After the applications, analgesics were given in cases where pain was observed in the subject. In addition, in case of malnutrition, etc., behavioral disorder and negative vital functions, the animal was removed from the experiment and euthanasia was performed with cervical dislocation under anesthesia / tranquilization and the experiment was repeated using a spare animal.

Table 7.1: Microwave thermal ablation-PEMF applications and groups [179].

Group	Process	Number of mice
Group 1: Control	4T1 Breast cancer created group	4
Group 2: Ablation (MFMWAP)	4T1 Group that underwent microwave ablation with MFMWAP to mice with breast cancer	4
Group 3: Ablation (CA20L1)	4T1 Group that underwent microwave ablation with CA20L1 probe to mice with breast cancer	4
Group 4: Ablation (Coaxial Slot Antenna)	4T1 Group that treated MFMWAP with coaxial slot antenna (CSA) to mice with breast cancer	4
Group 5: Ablation (NiTi Loop Antenna)	4T1 Breast cancer induced mice in group administered MFMWAP with NiTi loop antenna (NLA)	4
Group 6: PEMF + Abl. (MFMWAP)	4T1 Group that received PEMF after micro-ablation with MFMWAP was applied to mice with breast cancer	4
Group 7: Ablation + PEMF (CA20L1)	4T1 Group that received PEMF after micro-ablation with CA20L1 probe was applied to mice with breast cancer	4
Group 8: PEMF	4T1 Group treated PEMF with Helmholtz coil pair to mice with breast cancer	4

7.1.1. MWA Application Using MFMWAP

These studies performed microwave ablation on Balb/c type laboratory mice with the MFMWAP. The applications were performed on four groups defined as D1, D4, D5, and D6, with room values of 32 °C as seen in Figure 7.2. In these groups, 100 W input

power is applied to the MWAP in the form of a 2.45 GHz carrier rate and 12.5 kHz pulse width modulation with a 50% duty cycle. However, the accepted powers transferred to D1, D4, D5, and D6 are 44 W, 41 W, 46 W, and 39 W, respectively, due to the electrical characteristics of the LTE2400 microwave power amplifier. These power levels changed by $\pm 10\%$ during application [179].

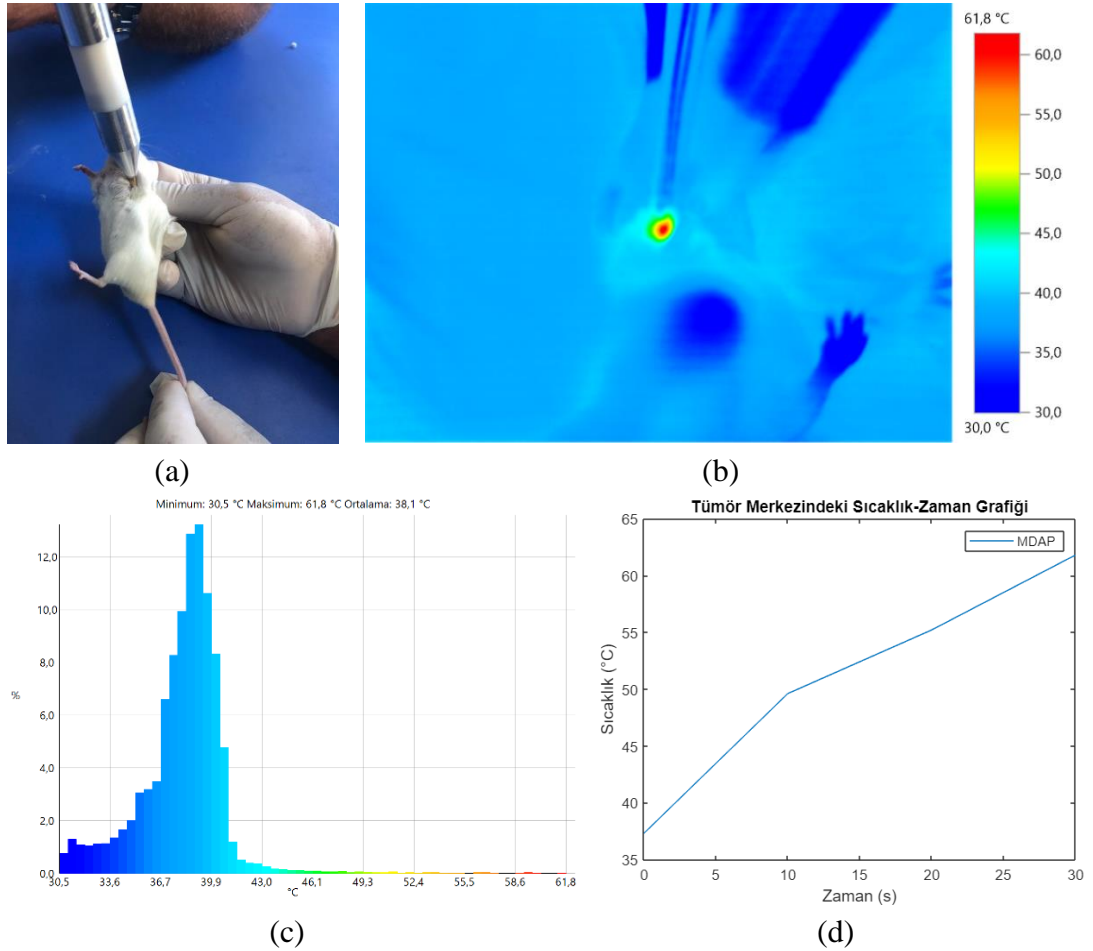


Figure 7.2: (a) MWA application using MFMWAP on D6 label BALB/c. (b) Thermal camera measurement, and (c) temperature distribution in percent after 30 s of that application with (d) time dependent temperature measurement result.

During the application, the electric field magnitudes on the groups were measured with the EMC near the field probe. Electric field magnitudes on the mice were also measured close to each other since relative power levels were applied to the groups. The measured electric field magnitudes for groups D1, D4, D5 and D6 are 403 V/m, 396 V/m, 399 V/m and 409 V/m, respectively. The temperature increase caused by the electric field emitted by the MFMWAP in the tumors of mice is given in Figure 7.2.

As seen in Figure 7.2(a), ablation temperatures occur at the end of 30 seconds in the circle with a diameter of approximately 3 mm, where MFMWAP contacts the tumor, while harmless temperatures occur in the peripheral areas. When the percentage distribution of the temperature of the front surface of the rat in Figure 7.2(b) is examined, it is seen that the ablation application with the MFMWAP does not adversely affect most of the healthy tissues of the rat, since 37 °C, the body temperature, is the highest, and less than 0.1% of it is ablated seen. When the real-time temperature graph in Figure 7.2(d) is interpreted, it is predicted that the ablation of the tumor region will start after the 20th second of the 30-second application.

The tumor sizes of the rats who underwent microwave ablation with the MFMWAP were evaluated macroscopically after the application. Tumor diameter measurements were performed on four rats identified as D1, D4, D5, and D6. As a result of the measurement process shown in Figure 7.3, it was observed that there was a reduction in tumor diameter after the application.

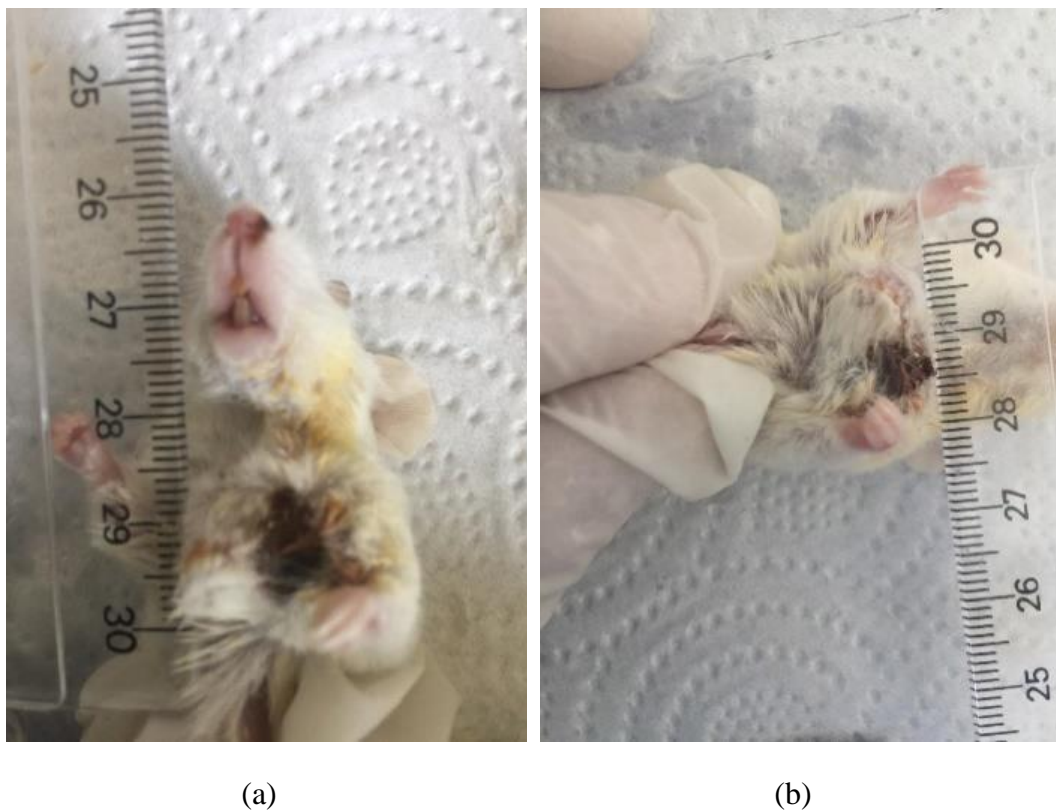


Figure 7.3: (a) Height, and (b) width of tumor size in D6 label mice after MWA

7.1.2. MWA Application Using CA20L1

As in the previous section, microwave ablation was applied with the CA20L1 probe, which is used safely in clinical applications. In this experimental group, subjects are defined as D7, D8, and D9. The rat skin under ablation, which coincides with the tumor area, was opened with a scalpel so the probe tip could readily enter. The electric field was measured just around the same area by touching the probe to this area, as seen in Figure 7.4. While the measured electric field level was 367 V/m, 364 V/m and 382 V/m for subjects D7, D8 and D9, respectively, the microwave signal transmitted to the CA20L1 probe, which generated these values, was 12.5 kHz pulse width modulation and at 2.45 GHz carrier frequency, subject D7. 22 W for subjects and 21 W for subjects D8 and D9 [179].

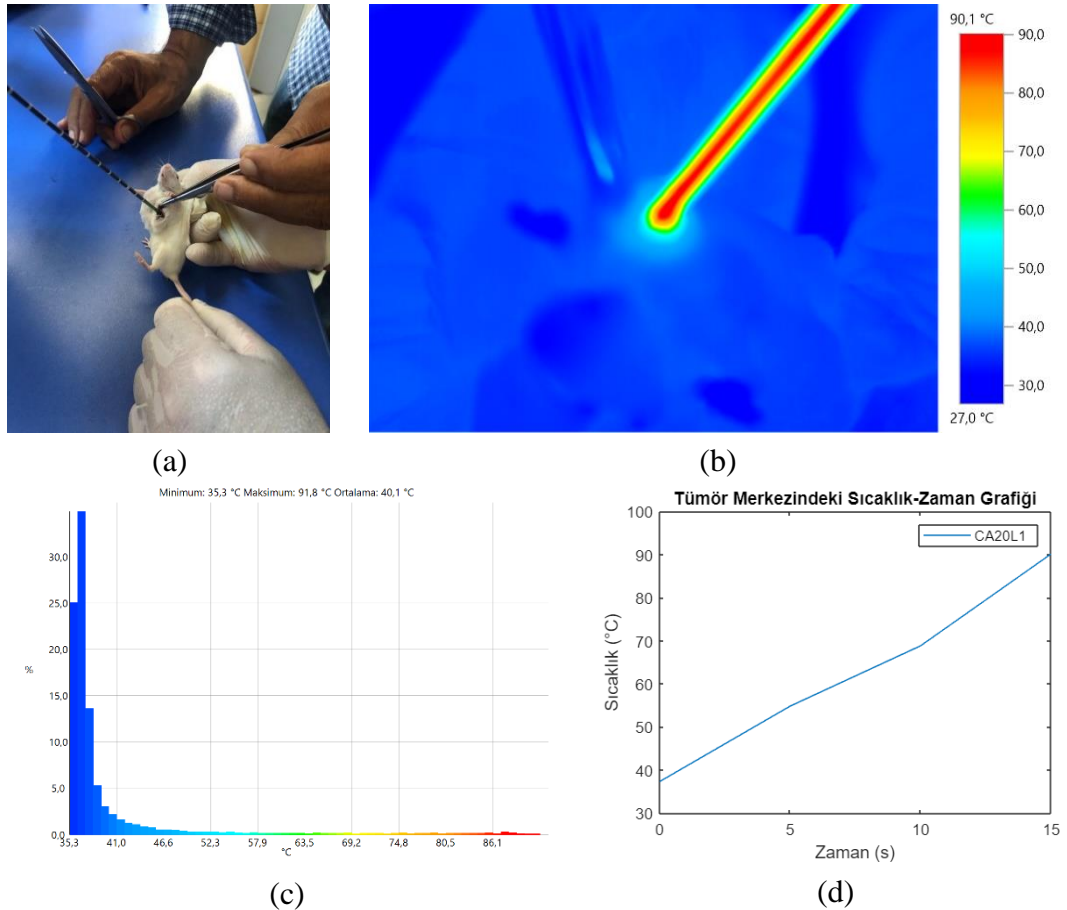


Figure 7.4: (a) Microwave ablation application using CA20L1 on D9 label BALB/c. (b) Thermal camera measurement, and (c) temperature distribution in percent after 15 s of that application with (d) time dependent temperature measurement result.

As in the microwave ablation application with the MFMWAP, the temperatures on each subject were measured with a thermal camera, but the microwave ablation probes

were given almost equal power. It was predicted that the measured electric field levels were close to each other, resulting in the temperature measurements being close to each other, so it was considered sufficient to give only the temperature measurement of the rat D9 in Figure 7.5.

When the temperature measurement results of rat D9 were examined, the ablation temperature of 60 °C was reached at the point where the CA20L1 probe contacted the tumor in a circular region with a diameter of approximately 7 mm. This region corresponds to an area of 2.5% when the percentage temperature distribution results obtained on the mouse surface in Figure 7.4(b) are examined. However, 90% is the body temperature considered safe for the mouse, and the remaining 7.5% is the region where hyperthermia is likely to occur. The real-time temperature results in Figure 7.4(c) showed that the target temperature was reached almost from the 5th second, and the maximum temperature on the tumor increased to 90.1°C after 15 seconds.

Tumor diameter measurements were made in mice after microwave ablation with the CA20L1 probe. The shrinkage of the tumors we obtained after MFMWAP application was also observed in these subjects. Tumor diameter measurements made at the end of the application are given in Figure 7.5.



Figure 7.5: Tumor diameter measurement in mice ablated with CA20L1

7.1.3. MWA Application with the Use of CSA

The applicators in Chapter 7.1.1 and Chapter 7.1.2 ensured the proper distribution of electric fields in the target area in such a way as to cause as little harm as possible to the organism. In this section, microwave ablation was performed on Balb/c type laboratory mice defined as D22, D23, and D24 using a coaxial slot antenna produced in a thinner structure than MFMWAP and CA20L1 probes. Figure 7.6 shows surgical intervention and electric field measurements performed on subjects with coaxial slot antenna [179].

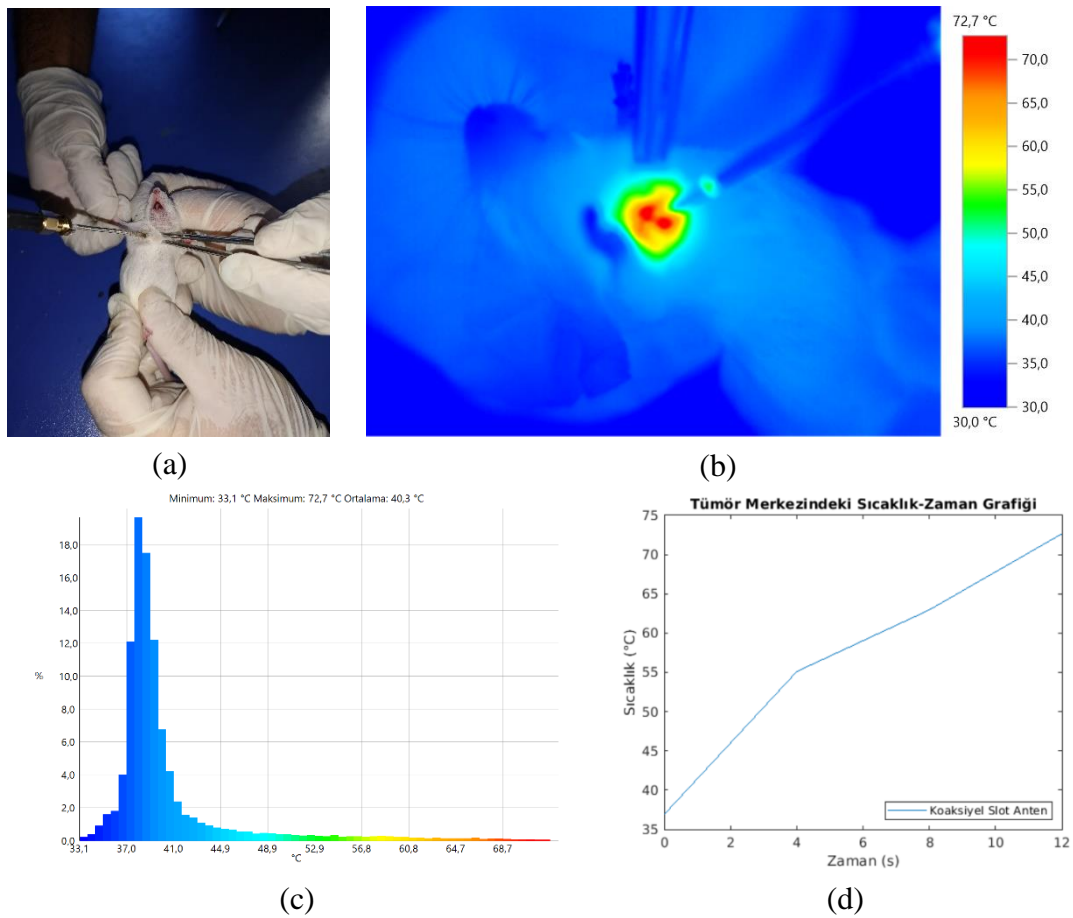


Figure 7.6: (a) Microwave ablation application using CSA on D24 label BALB/c. (b) Thermal camera measurement, and (c) temperature distribution in percent after 12 s of that application with (d) time dependent temperature measurement result.

The microwave exposure generated in the subjects was the result of applying signals in the form of 12.5 kHz pulse width modulation with a carrier frequency of 2.45 GHz and a 50 % duty cycle to the coaxial slot antenna of the microwave applicator. This signal form was transmitted by 67 W, 69 W, and 70 W microwave power for D22, D23, and D24 labeled rats. With these power levels, an electric field of 235 V/m for

D22, 234 V/m for D23, and 237 V/m for D24 was projected onto the tumorous areas of the rats. The thermal camera measured and analyzed the temperature increases generated by the coaxial slot antenna on rats. The results of temperature measurement and analysis are shown in Figure 7.7.

In Figure 7.6(a), it is seen that the coaxial slot antenna provides a larger ablation region compared to MFMWAP and CA20L1, with a circular region of 11 mm diameter in the ablation target region. According to the analysis of the temperature distributions in Figure 7.6(b), the body temperature of the rat did not change in the 80 percent region, while 15 percent was understood as hyperthermia and 5 percent as the region where the tumorous area was located and the tissues were destroyed. As evidenced by the temperature-time graph depicted in Figure 7.6(c), it was determined that the optimal temperature values for ablation of the tumors were attained within the 3rd and 4th seconds of the treatment application.

In the context of microwave ablation utilizing a coaxial slot antenna of a thinner structure, our approach toward targeting the tumor was characterized by reduced invasiveness. Subsequent to this treatment, a reduction in the tumor diameters of the subjects was observed, as confirmed through measurement and illustrated in Figure 7.7.

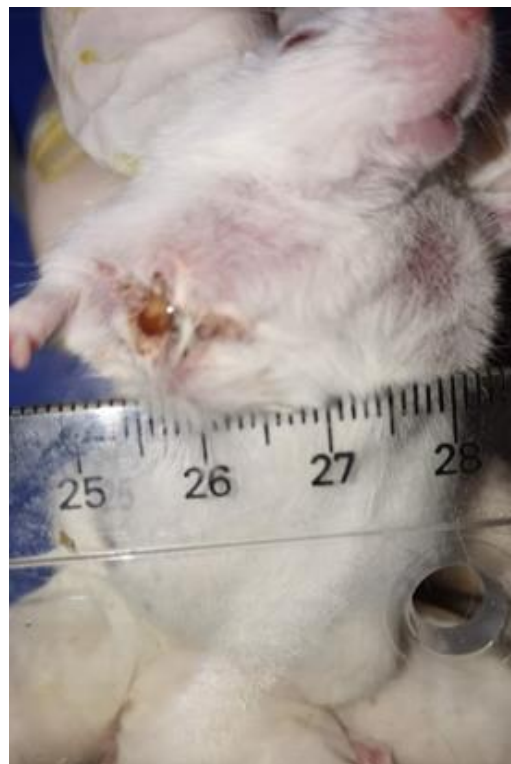


Figure 7.7: Tumor diameter measurement in mice ablated with CSA

7.1.4. NiTi Loop Antenna Application with MWA Application

In Section 7.1.1, Section 7.12, and Section 7.1.3, the microwave applicators were applied in direct contact with the tumor area. The electromagnetic fields generated by these applicators were directed towards the tumor, increasing temperature due to the high electric field radiation produced. This section established an experimental setup, as illustrated in Fig. 7.8. In this setup, mice were positioned in the near-field region of a loop antenna constructed from NiTi material in a non-contact configuration [179].

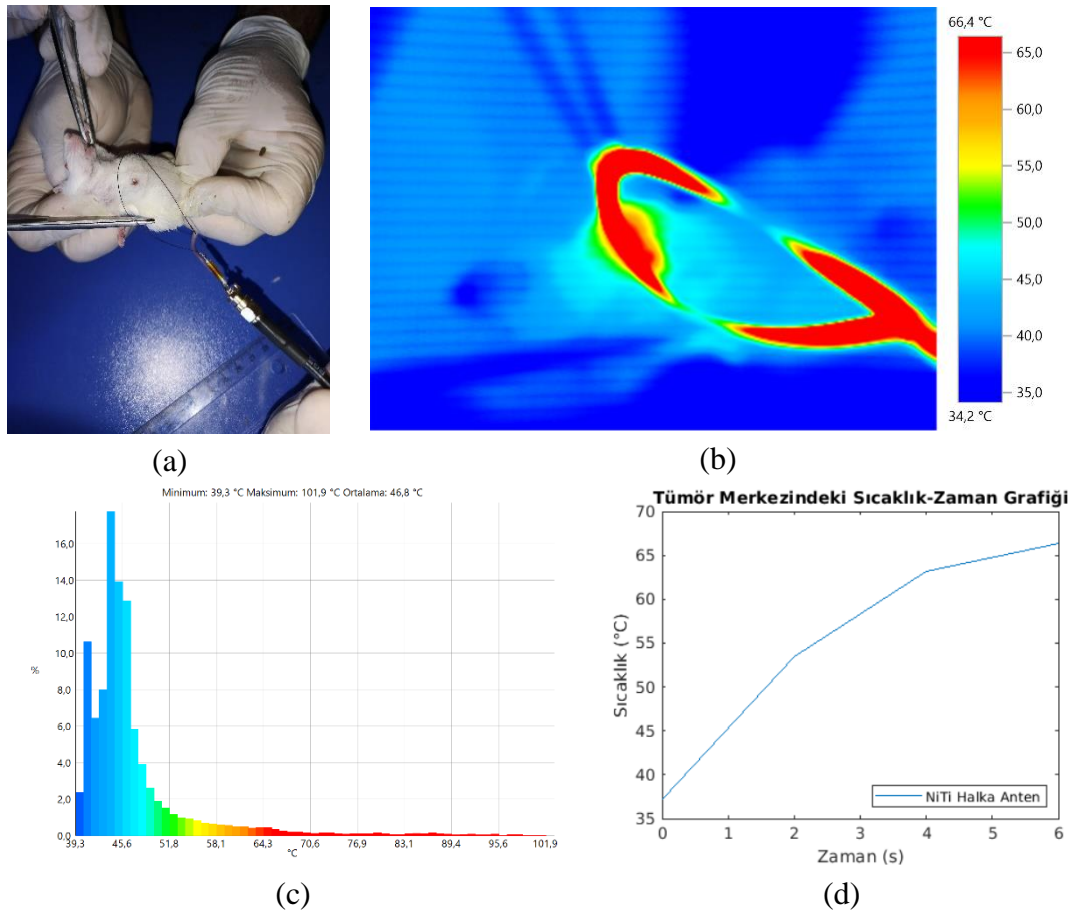


Figure 7.8: (a) MWA application using NiTi Loop Antenna on D21 label BALB/c. (b) Thermal camera measurement, and (c) temperature distribution in percent after 6 s of that application with (d) time dependent temperature measurement result.

Experimental trials were conducted on subjects D19, D20, and D21 at a room temperature of 33°C. A microwave input power, in the form of 12.5 kHz pulse width modulation at a carrier frequency of 2.45 GHz and a 50 % duty cycle, was applied to the NiTi loop antenna, which facilitated the transfer of microwave energy to the subjects. The power levels utilized for subjects D19, D20, and D21 were 84 W, 88 W, and 82 W, respectively. Correspondingly, the electric field magnitudes in the tumor

regions were approximately 516 V/m. Electric field magnitudes of 502 V/m and 540 V/m were generated, respectively. As previously discussed in Chapter 8.2.1, Chapter 8.2.2, and Chapter 8.2.3, similar power levels and comparable electric field magnitudes were generated for each subject. Consequently, the temperature measurement and analysis results of rat D24 were obtained from this experimental group and are presented in Figure 7.9.

In this section, it is anticipated that the increase in temperature will occur as soon as possible due to the highest electric field level of the applicator to which microwave is applied to the experimental group. As an indication that high electric field values are achieved by the NiTi loop antenna, Figure 7.8(a) demonstrates the impact on the thermal imager display. The area where the tumors of rat D21 were located was rapidly heated by the NiTi loop antenna to 60 °C, as depicted in Figure 7.8(c), within 1-2 seconds. After the 6 second microwave ablation application, it was observed that the NiTi material began to undergo deformation, and the maximum surface temperature increased to 102 °C. On the hot surface, this maximum surface temperature reached 66.4 °C. Analysis of temperature distributions in percentage terms, as illustrated in Figure 7.8(b), indicates that the region underwent ablation to a greater extent than the MFMWAP, CA20L1, and the CSA. Numerically, 60% corresponds to the rat's body temperature in the region, 25% is hyperthermia, and 15% is the area where the tumor is located and the tissue is destroyed.

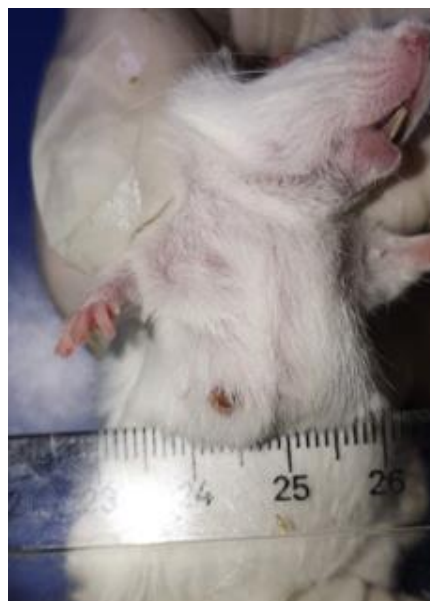


Figure 7.9: Tumor diameter measurement in mice ablated with NiTi Loop Antenna

This application, which we have made by bringing a loop antenna made of NiTi material closer to the tumor area without contact, aims to reduce the tumor without causing any trauma or intervention on the subject. The outcome application revealed a reduction in tumor regions based on measurements depicted in Figure 7.9. The experimental parameters and temperature analysis results of in vivo application with MFMWAP, CA20L1, CSA, NLA are given in Table 7.2.

Table 7.2: In vivo experimental parameters and temperature analysis results according to antenna type [179].

	MFMWAP	CA20L1	CSA	NLA
Input Signal Form	12.5 kHz PWM with 50 % duty cycle, 2.45 GHz carrier frequency			
Average Input Power (W)	43	21	67	85
Average E Field (V/m)	402	372	236	520
Time (s)	30	15	12	6
Max. Temperature (°C)	61.8	90.1	72.7	66.8
Tissue health (%)	Health	91.5	90	80
	Hyperthermia	8.4	7.5	15
	Necrosis	< 0.1	2.5	5

Based on the temperature analysis findings presented in Table 7.2, the experimental groups utilizing MFMWAP, CA20L1, and NiTi loop antennas exhibit the highest percentage of healthy tissue temperature, whereas the group utilizing NiTi loop antenna demonstrates the most effective results in inducing hyperthermia and necrosis. These antennas provide temperature conditions that facilitate the desired effects in the experimental groups. Table 7.2 indicates that NiTi loop antennas are suitable for treating larger tumor areas, while MFMWAP and CA20L1 antennas are more suitable for smaller tumors where minimizing damage to healthy cells is crucial. In cases where similar conditions are desired, the use of coaxial slot antennas is likely to yield favorable outcomes. These findings suggest that the choice of antenna type plays a significant role in achieving successful results in various experimental scenarios.

7.1.5. In Vivo PEMF Application with Helmholtz Coil Pair

Among the Balb/c type mice, specifically mice labeled as D3, D10, D11, and D12, were assigned as the PEMF (Pulsed Electromagnetic Field) groups. To accommodate these mice adequately, a lantern was utilized as a housing unit. The PEMF test setup, as illustrated in Figure 7.10, employed a pair of coils capable of supporting a maximum current of 2A, with each coil consisting of 500 turns. The input signal for the system was measured using a Pasco generator, while the magnetic field was measured using Pasco magnetic field sensors [179].

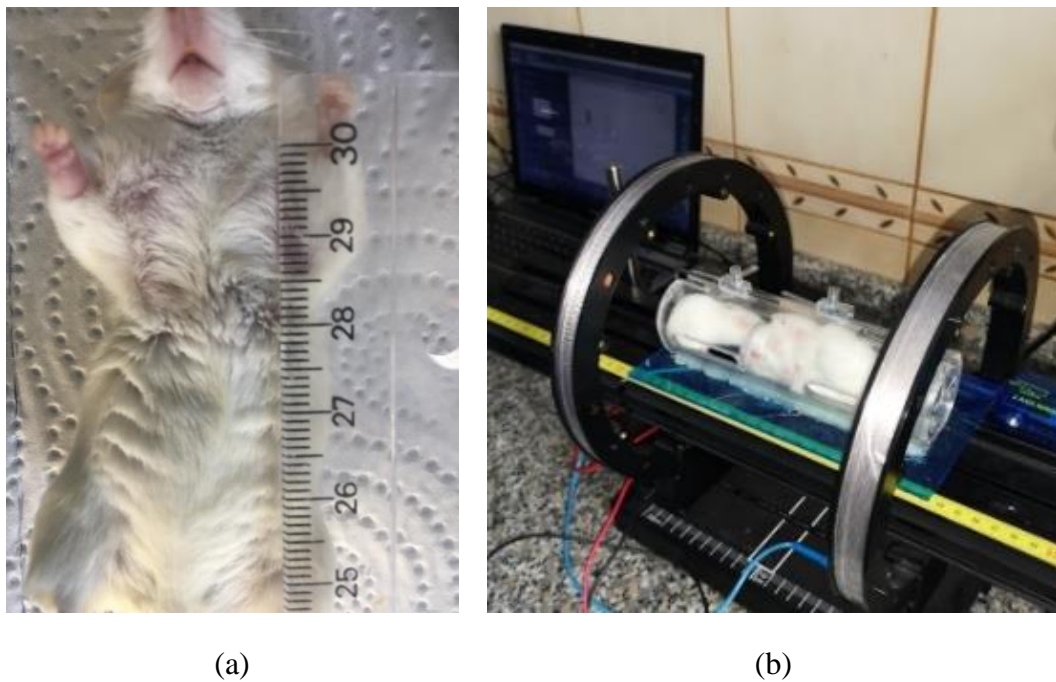


Figure 7.10: (a) PEMF application on BALB/c with Helmholtz coil pair and (b) : Measurement of tumor size in mice treated with PEMF with Helmholtz coil pair.

The coils utilized in the system were subjected to pulse-shaped signals characterized by an amplitude value of 10 V, 5 V offset, and a 75 Hz frequency with a 50% duty cycle. These signals were amplified by a 600W class D sound amplifier. Consequently, magnetic flux densities of 1.23 mT, 1.35 mT, 1.27 mT, and 1.44 mT were measured in subjects D3, D10, D11, and D12, respectively, based on these input parameters.

The experimental setup for PEMF involved placing the subjects in a bowl containing four animals simultaneously, and the application was carried out accordingly. Notably, in the groups that received both ablation and PEMF treatment, a macroscopic measurement revealed tumor reduction, as depicted in Figure 7.10.

7.2 Histopathological Evaluation

Histopathological evaluation is a method used to examine the microscopic structure of tumorous and healthy tissue in experimental groups of mice. Histopathological evaluation is an important tool in the diagnosis and management of many diseases, including cancer. This process involves obtaining samples of Balb/C mice tissue, through biopsy. The samples are typically fixed in 10% buffered formalin solution, and then embedded in a paraffin block. Thin sections of the tissue are cut and placed on slides, which are then stained with dyes to highlight different structures within the tissue. The pathologist examines the slides under a microscope and makes observations about the structure and appearance of the tissue, which can provide important diagnostic information or help to evaluate the effectiveness of treatments. The appearance of semi-confluent and confluent cancer cells in the cell line culture is shown in Figure 7.11 [179].

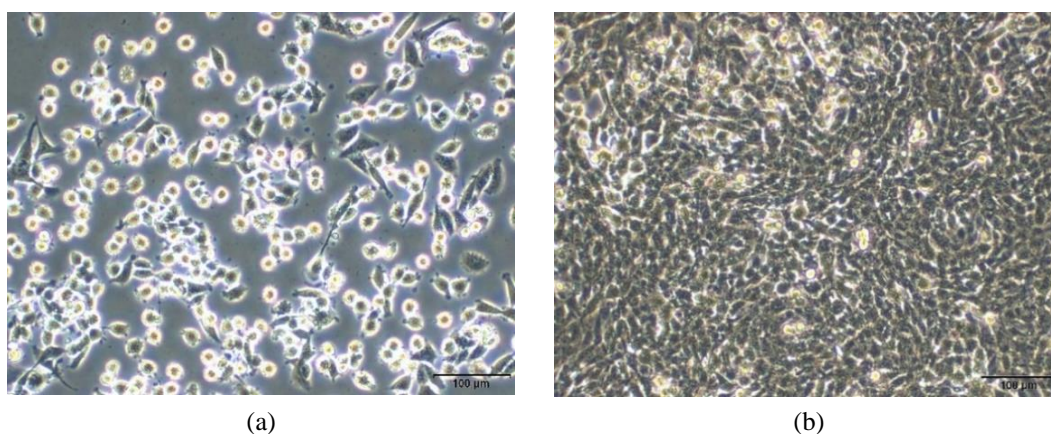


Figure 7.11: 4T1 Appearance of (a) semiconfluent and (b) confluent cancer cells in 4T1 cell sequence culture for breast cancer model.

7.3.1 Macroscopic Evaluation

After the cancer cells were taken from the culture medium and subcutaneously injected into the mammary region, the presence of tumor tissue in the form of palpable nodules was detected on the tenth day. At this stage, treatments were started and repeated until the twentieth day. The effects of the treatments on the tumor area were mainly studied in the groups shown in Figure 7.12. Compared with the controls, it was found that the applications that began in the palpation period and were repeated caused a significant regression. It was seen that the tumor area was approximately 30% less.

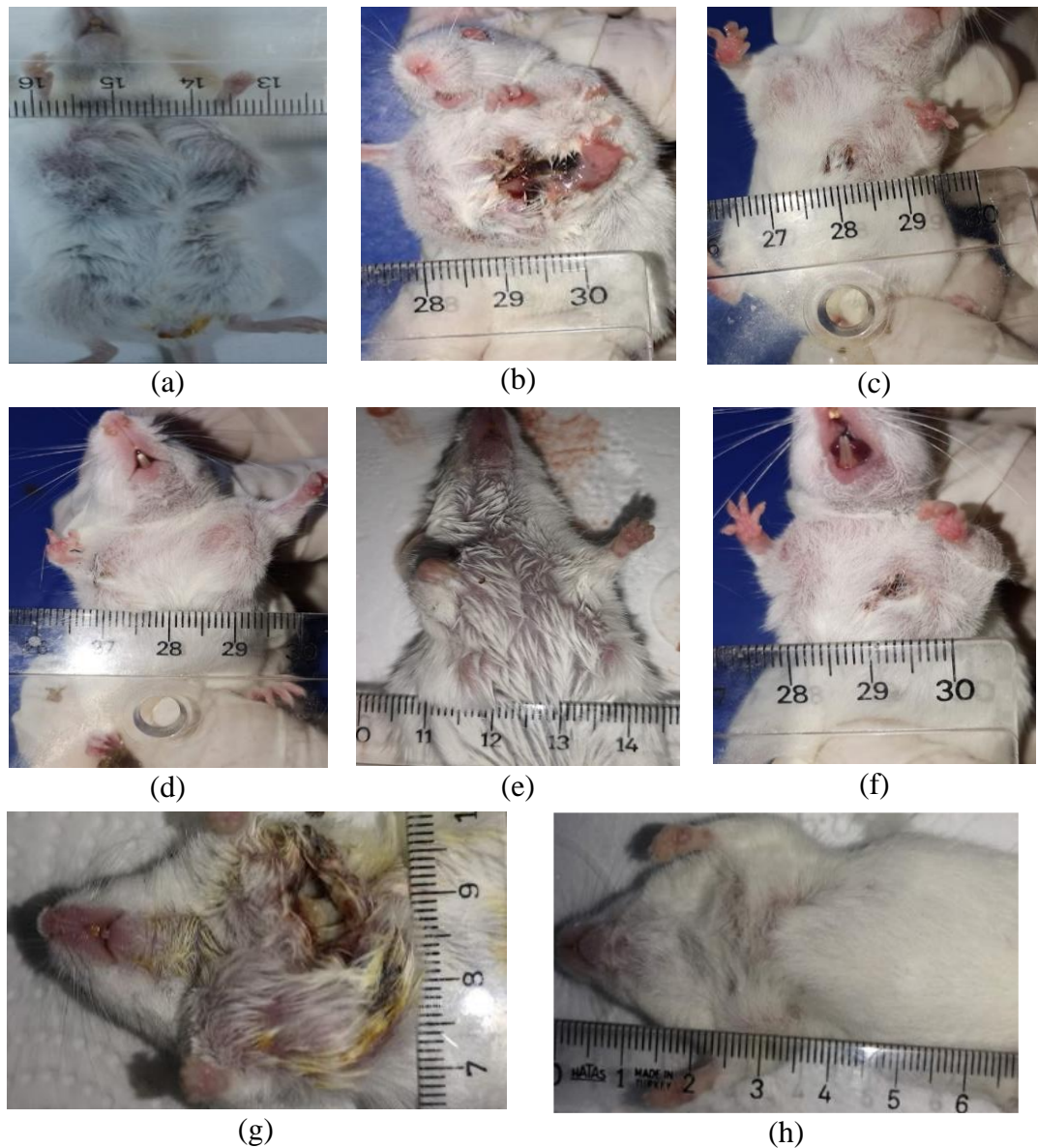


Figure 7.12: MWA-PEMF applications in; (a) Group 1, (b) Group 2, (c) Group 3, (d) Group 4, (e) Group 5, (f) Group 6, (g) Group 7, (h) Group 8

7.3.2 Microscopic Evaluation

This subsection describes a method for morphological evaluation of cancer studies in mice. The process involves examining images of cancer tumors formed in mice and assessing the size, shape, and spread of the tumors. This evaluation is used to monitor the progression of the tumor and evaluate the effectiveness of treatments. After the experiment, the mice were euthanized to the cancer lesions and other organs were removed and fixed in 10% buffered formalin solution for preservation between 1 and 3 days. The samples are then embedded in paraffin blocks and processed using routine tissue preparation procedures.

7.3 Paraffin Tissue Tracking

Following dissection, the collected tissues were fixed by immersion in a 10% formalin solution (Merck, catalog no: 252549-1L) for a minimum of 48 hours. Subsequently, the fixed tissues underwent dehydration by sequential immersion in ascending concentrations of alcohol (Isolab, catalog no: 920.026) for 30 minutes each, comprising 60%, 70%, 80%, and 90%, with two additional changes for 1 hour in 100% alcohol. To ensure tissue clearance, the specimens were then subjected to two 15-minute immersions in toluene (Merck, catalog no: 108325) and a subsequent 30-minute immersion. Subsequently, the tissues were transferred to a toluene-paraffin solution for 15 minutes, followed by two 1-hour changes in paraffin (Sigma Alrich, catalog no: P3558). Finally, embedding of the tissues in paraffin blocks was accomplished using the Leica HistoCore Arcadia device. The detailed paraffin tissue tracking protocol is outlined in Table 7.3 [179].

Table 7.3: Tissue tracking protocol

Chemicals	Time	Chemicals	Time
%60 alcohol	30 min	Toluene-Alcohol (1:1)	30 min
%70 alcohol	30 min	Toluene	15 min
%80 alcohol	30 min	Toluene	15 min
%90 alcohol	30 min	Toluene-Paraffin	15 min
%100 alcohol	1 hour	Paraffin	1 hour
%100 alcohol	1 hour	Paraffin	1 hour
10% Formalin	48 hours	Stream	1 night

7.3.1. Histopathological Staining

The histochemical staining method used was by taking 5 μ m paraffin sections through a rotary microtome (RM 2135, Leica), after deparaffinization by leaving the sections in an oven at 60 °C for 1 night, and then treating them with xylene for 30 minutes in two changes. The sections of ovary tissue from the paraffin blocks were taken with a microtome (Leica RM 2245) in 5 μ m thickness and placed on glass slides (isolab). The sections were then left in the oven at 60oC for 1 night to remove excess paraffin. The next morning, the sections were dehydrated by passing through decreasing alcohol concentrations (%95, %80, %70, %60) for 30 minutes in two changes of xylene. The

sections were then washed in water, then stained with hematoxylin for 10 minutes, washed in water again for 5 minutes to remove excess stain, then stained with eosin (Merck, catalog no:115935) for 5 minutes. After staining with eosin, the sections were washed in water for 5 minutes to remove excess stain and then dehydrated by passing through increasing alcohol concentrations, and then cleared in xylene for 30 minutes and mounted in Entellan (Sigma Aldrich, catalog no: 107961). The H&E staining protocol is given in Table 7.4.

Table 7.4: H&E staining protocol

Chemicals	Time	Chemicals	Time
%96 alcohol	2 min	Xylene	1 hour
%80 alcohol	2 min	Stream	5 min
%70 alcohol	2 min	Hematoxylon	10 min
%60 alcohol	2 min	Stream	5 min
%80 alcohol	1 min	Eosin	5 min
%96 alcohol	1 min	Entellan	-

7.3.2. Indirect Immunohistochemistry Staining

This protocol describes a method for preparing paraffin-embedded ovarian tissue sections for immunohistochemistry. The first step is to cut the tissue into 5 μm thick sections using a microtome and then place them on lysine-coated slides (Thermo scientific, catalog no: J3800AMNT). The sections are then heated in an oven at 60oC overnight to remove any remaining paraffin. The next morning, the slides are rehydrated by passing through a series of decreasing alcohol concentrations and washed with distilled water. The tissue is then washed 3 times with PBS (Thermo Fisher, catalog no: 18912014) and then treated with 3% hydrogen peroxide for 10 minutes. After treating with hydrogen peroxide, the edges of each tissue section on the slide are marked with Pap Pen (Invitrogen). The tissue sections are then incubated with trypsin (Thermo Fisher, catalog no: TA-125TR) at 37oC for 10 minutes. The sections are then washed 3 times with PBS and treated with blocking solution (Thermo Fisher, Ultra Vision, catalog no: TP-125-HL) for 10 minutes. The sections are then incubated overnight at 4oC with primary antibodies specific for NOS2 (Santa Cruz, sc-7271), Cx43 (Santa Cruz, sc-271837), Caspase3 (Santa Cruz, sc-56053), and Pnx1 (Abcam, ab139715) without washing with PBS in between. The next morning, the sections are

washed 3 times with PBS and incubated with biotinylated secondary antibodies for 10 minutes. The sections are then washed again with PBS, incubated with streptavidin peroxidase for another 10 minutes. After this, the sections are washed again 3 times with PBS and then incubated with DAB (Thermo Scientific, catalog no: 34002) for a certain period of time to visualize the immune reaction. Then, the sections are washed with PBS and distilled water, and then counterstained with Mayer's hematoxylin (Skytek) for nuclei staining. Finally, the sections are washed again and passed through a series of increasing alcohol concentrations and then mounted with entellan. This is the complete immunohistochemistry staining protocol as described in Table 7.5.

Table 7.5: Immunohistochemical staining protocol in room temperature

Chemicals	Time	Chemicals	Time
%96 alcohol	2 min	Xylene 1	30 min
%80 alcohol	2 min	Xylene 1	30 min
%70 alcohol	2 min	Distillate water	10 min
%60 alcohol	2 min	%3 H ₂ O ₂	5 min
%80 alcohol	2 min	PBS	3x5 min
%96 alcohol	2 min	Trypsin	30 min
Xylene	1 min	PBS	3x5 min
Entellan	-	Blocking Solution	30 min
Primary Antibodies	1 night	Secondary Antibodies	30 min
PDS	3x5 min	PBS	3x5 min
Streptavidin + HRP	60 min	DAP	2-10 min
PBS	1x5 min	Myers Haematoxylon	3x5 min

Table 7.5 outlines the immunohistochemical staining protocol conducted at room temperature for the evaluation of ovarian tissue samples. The procedure involves sequential treatment with various chemicals and solutions for specific durations. Initially, the samples are subjected to immersion in %96 alcohol for 2 minutes, followed by xylene for 30 minutes. Subsequently, a series of alcohol concentrations (%80, %70, and %60) are applied for 2 minutes each, and a brief immersion in distilled water is performed for 10 minutes. A 5-minute treatment with %3 hydrogen peroxide follows. The samples are then washed three times for 5 minutes each with PBS (phosphate-buffered saline) and treated with trypsin for 30 minutes. Additional PBS washes and a 1-minute exposure to xylene are carried out. Entellan is used for mounting, and a 30-minute incubation with blocking solution is performed. Primary antibodies are applied overnight, followed by a 30-minute incubation with secondary

antibodies. Subsequent steps include PBS washes, treatment with streptavidin + HRP for 60 minutes, a 2-10 minute exposure to DAP (diaminobenzidine) for visualization, and multiple rinses with PBS. Finally, the samples are stained with Myers Haematoxylin for 3 sets of 5 minutes each. Table 5.5 further explains that the staining intensity of the ovarian sections is assessed using a scale ranging from 0 to 4, with 0 representing no staining and 4 indicating the highest level of staining. The evaluation process involves observing 10 ovarian sections per animal, with 30 different regions assessed within each section using a 40x objective lens.

7.3.3. TUNEL Painting

The Terminal deoxynucleotidyl transferase dUTP nick end labeling (TUNEL) assay was utilized to identify apoptotic cell death. The process began with the deparaffinization of 5 µm sections, which were then washed in distilled water and three consecutive times in phosphate-buffered saline (PBS) for 5 minutes each. The sections were then treated with 20 µg/ml of Proteinase-K diluted with 1/500 PBS at 37°C for 15 minutes. Following this, the sections were washed in PBS three times for 5 minutes each and treated with 3% hydrogen peroxide for 5 minutes. The sections were then equilibrated with buffer and incubated with TdT enzyme in a humid environment at 37°C for 60 minutes, covered with plastic slips. The reaction was stopped with Stop Wash Buffer for 10 minutes and incubated with Antidioxigenin Peroxidase Conjugate for 30 minutes. The sections were then washed three times for 5 minutes with PBS, and subsequently stained with Diaminobenzidine (DAB) and washed several times with distilled water. The sections were counterstained with Mayer's Hematoxylin to detect background staining. The TUNEL-positive cells were identified using a blinded method and the results were analyzed statistically. In this study, the TUNEL assay was applied in the examination of the tumorigenic activity and reduction in tumor area by way of comparison between the different antenna types, in a skin cancer model created in rats through the topical application of DMBA+TPA, by analyzing the tumor samples taken from animals with and without microwave application, through the utilization of immunohistochemical and TUNEL staining. The apoptotic index was used to measure the apoptosis rate.

7.4 Statistical Analysis

The Shapiro-Wilk test for normality was applied to the groups using the Graphpad Prism 8.3.1 program in order to perform comparisons between all groups. Subsequently, a One-Way Analysis of Variance (ANOVA) was utilized to statistically evaluate the differences between the groups, given that the data exhibited a normal distribution. The statistical results analysis were considered significant at a P value of ≤ 0.05 . Subsequently, Tukey's test was employed as a post-hoc analysis for multiple comparisons.

A breast cancer model was constructed by culturing and proliferating 4T1 sequence cells, which were subsequently administered subcutaneously under the breast tissue of Balb c mice. The appearance of semiconfluent and concapacitated cancer cells in the culture of 4T1 sequence cells is illustrated in Figure 7.11 [179].

7.4.1 Macroscopic Findings

An experimental breast cancer model utilizing 4T1 cell sequence in rats was undertaken. The results of this study revealed that the cancerous cells formed a tightly interlocked tumor tissue, and that the tumor growth progressed to a size of approximately one centimeter within twenty days. The subjects shown in Figure 8.20 exhibited symptoms such as weakness, debilitation, and deterioration, which are indicative of the terminal stages of cancer. Furthermore, it was observed that repeated treatments applied during the palpation period resulted in a significant regression of the tumor, with the tumor area being approximately 30% smaller.

The morphometric analysis of the tumor region revealed a substantial regression in comparison to the control group, as evidenced by One-way Analysis of Variance (ANOVA) and Tukey-Kramer Multiple Comparisons Test. In ANOVA test, the P value, which is less than 0.0001, is considered to be highly statistically significant while the exceeding the q value of 4.232 means the corresponding P value is statistically significant at a level of less than 0.05 in Tukey-Kramer Multiple Comparisons Test. However, no discernible distinctions were identified among the various treatment applications, as per the data presented in Table 7.6.

Table 7.6: T41 Morphometric analyses after microwave thermal ablation-PEMF applications in breast cancer groups (Mean 95% Confidence Interval)

Comparison	From	To	Difference	q	P value
Group 1vs Group 2	4.554	11.711	8.133	10.645	P<0.001
Group 1vs Group 3	3.839	10.996	7.418	9.710	P<0.001
Group 1vs Group 4	4.599	11.756	8.178	10.704	P>0.001
Group 1vs Group 5	4.139	11.296	7.778	10.102	P<0.001
Group 1vs Group 6	5.464	12.621	9.043	11.837	P<0.001
Group 1vs Group 7	4.962	12.118	8.540	11.179	P<0.001
Group 1vs Group 8	2.729	9.886	6.308	8.257	P<0.001
Group 2 vs Group 3	-4.293	2.863	-0.715	0.936	P>0.05
Group 2 vs Group 4	-3.533	4.488	0.045	0.059	P>0.05
Group 2 vs Group 5	-3.993	3.163	-0.415	0.543	P>0.05
Group 2 vs Group 6	-2.668	3.986	0.910	1.191	P>0.05
Group 2 vs Group 7	-3.171	3.878	0.408	0.533	P>0.05
Group 3 vs Group 4	-2.818	5.203	0.760	0.995	P>0.05
Group 3 vs Group 5	-3.278	4.338	0.300	0.393	P>0.05
Group 3 vs Group 6	-1.953	4.701	1.625	2.127	P>0.05
Group 3 vs Group 7	-2.456	4.038	1.123	1.469	P>0.05
Group 4 vs Group 5	-3.118	4.903	0.460	0.602	P>0.05
Group 4 vs Group 6	-2.713	3.941	0.865	1.132	P>0.05
Group 4 vs Group 7	-3.216	3.076	0.363	0.476	P>0.05
Group 5 vs Group 6	-2.253	4.401	1.325	1.734	P>0.05
Group 5 vs Group 7	-2.756	4.443	0.823	1.077	P>0.05
Group 6 vs Group 7	-4.081	3.076	0.503	0.658	P>0.05
Group 8 vs Group 2	-1.753	5.403	1.825	2.389	P>0.05
Group 8 vs Group 3	-2.468	4.688	1.110	1.453	P<0.05
Group 8 vs Group 4	-1.708	5.448	1.870	2.448	P>0.05
Group 8 vs Group 5	-2.168	4.988	1.410	1.846	P<0.05
Group 8 vs Group 6	-0.843	6.313	2.735	3.580	P>0.05
Group 8 vs Group 7	-1.346	5.813	2.233	2.922	P>0.05

In Table 7.6 assumption test has been performed to determine whether the standard deviations of the groups equal or not and whether the data sampled from Gaussian distributions or not. ANOVA assumes that the data are sampled from populations with identical standard deviation while Bartlett's test suggests that the differences among the standard deviations is not significant. In Table 7.6 Bartlett statistic (corrected) value is 7.111 and P value is 0.4174 indicate that the variances of the two or more populations are likely to be not equal. A P value of 0.4174 is greater than 0.05 which

is the commonly used threshold for statistical significance, this means that there is not enough evidence to reject the null hypothesis that the variances of the populations are equal. Therefore, the variances of the populations are likely to be equal. ANOVA also assumes that the data are sampled from populations that follow Gaussian distributions.

7.4.2. Hematoxyline Eosin Signs

The presence of necrotic and apoptotic cell deaths depending on the applications was examined on the data of Figure 7.13 when compared with the groups that were not applied in the HE staining in the samples taken after the experiment.

In the morphometric analysis of the HE staining in the samples taken after the experiment in Table 7.7 and Table 7.8, a significant decrease in necrotic and apoptotic cell deaths was found due to the applications compared with the non-applied groups.

Table 7.7: Morphometric analysis of HE stains (Mean 95% Confidence Interval)

Comparison	From	To	Min	Max	Mean	Deviation	Median
Group 1	9.142	18.153	10.280	17.030	13.648	2.832	13.640
Group 2	2.734	8.296	4.230	8.110	7.340	1.748	4.815
Group 3	3.983	8.477	4.230	7.680	5.515	1.412	6.460
Group 4	4.136	6.804	4.730	6.550	5.470	0.8383	5.300
Group 5	4.338	7.522	5.010	6.930	5.930	1.001	5.890
Group 6	2.696	6.514	3.370	5.750	4.605	1.200	4.650
Group 7	3.773	6.442	4.310	5.910	5.108	0.8391	5.105
Group 8	5.230	9.450	5.550	8.380	7.340	1.326	7.715

The numerical values presented in Table 7.7 provide insights into the morphometric analysis of HE stains for different groups. Each group exhibits a range of values, a mean value representing the average measurement, a standard deviation indicating the level of variability, and a median value representing the middle value within the group. The range of values and standard deviations vary among the groups, suggesting differences in the spread and consistency of measurements. The mean values indicate the average measurements for each group, while the medians represent the middle values. These numerical values help quantify and compare the morphometric characteristics, allowing for a better understanding of the variations and central tendencies within each group.

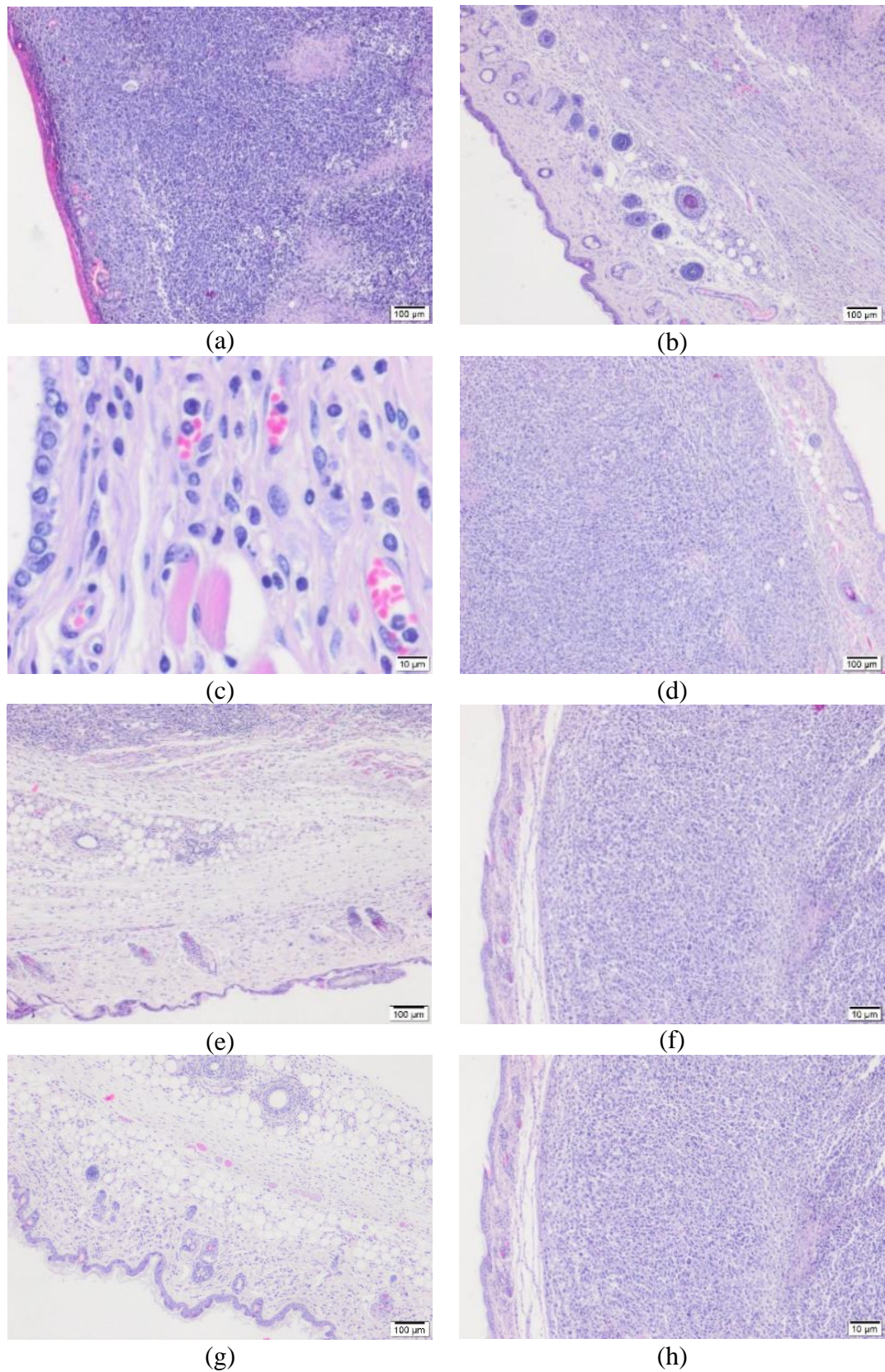


Figure 7.13: T41 Small and large magnification images of HE histochemistry staining after MWA-PEMF applications in groups with breast cancer (a) Group 1, (b) Group 2, (c) Group 3, (d) Group 4, (e) Group 5, (f) Group 6, (g) Group 7, (h) Group 8

7.4.3. Reproduction Findings

The decrease in the number of proliferating cells due to the applications was observed in the visuals in Figure 7.14, when compared with the groups that were not treated, in the Ki67 immunostaining performed in the samples taken after the experiment.

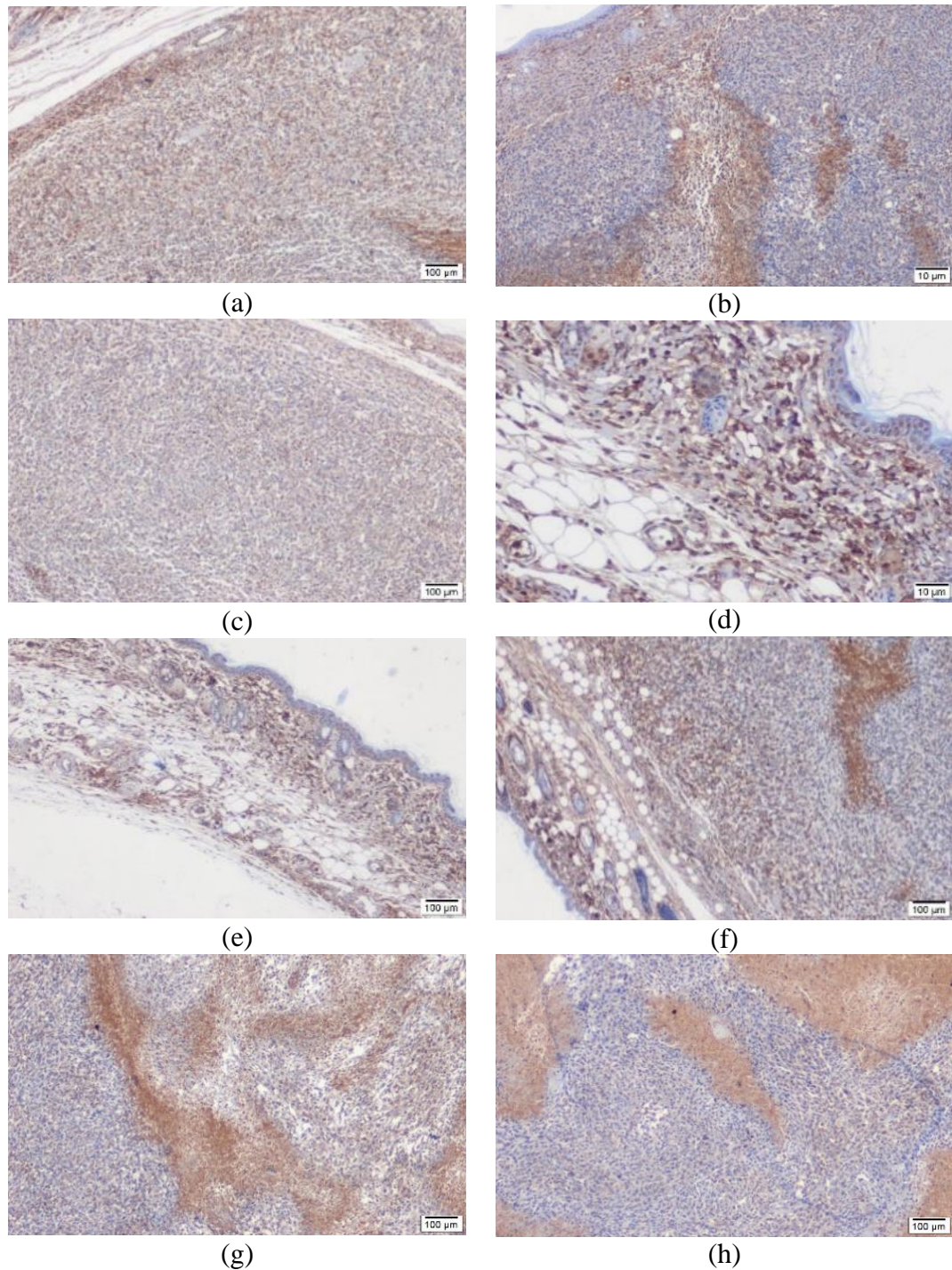


Figure 7.14: Ki67 immunohistochemistry staining images after MWA-PEMF applications in groups with T41 breast cancer (a) Group 1, (b) Group 2, (c) Group 3, (d) Group 4, (e) Group 5, (f) Group 6, (g) Group 7, (h) Group 8

Table 7.8: T41 Morphometric analyses after microwave thermal ablation-PEMF applications in breast cancer groups (Mean 95% Confidence Interval)

Comparison	From	To	Difference	q	P value
Group 1 vs Group 8	92.646	154.35	123.50	18.749	P<0.001
Group 1 vs Group 2	59.646	121.35	90.500	13.739	P<0.001
Group 1 vs Group 3	55.896	117.60	86.750	13.170	P<0.001
Group 1 vs Group 4	45.646	107.35	76.500	11.614	P>0.001
Group 1 vs Group 5	44.146	105.85	75.000	11.386	P<0.001
Group 1 vs Group 6	25.646	87.354	56.500	8.577	P<0.001
Group 1 vs Group 7	14.896	76.604	45.750	6.945	P<0.01
Group 2 vs Group 3	-34.604	27.104	-3.750	0.5693	P>0.05
Group 2 vs Group 4	-44.854	16.854	-14.000	2.125	P>0.05
Group 2 vs Group 5	-46.354	15.354	-15.500	2.353	P>0.05
Group 2 vs Group 6	-64.854	-3.146	-34.000	5.162	P>0.05
Group 2 vs Group 7	-75.604	-13.896	-44.750	6.794	P>0.01
Group 3 vs Group 4	-41.104	20.604	-10.250	1.556	P>0.05
Group 3 vs Group 5	-42.604	19.104	-11.750	1.784	P>0.05
Group 3 vs Group 6	-61.104	0.6042	-30.250	4.592	P>0.05
Group 3 vs Group 7	-71.854	-10.146	-41.000	6.224	P>0.01
Group 4 vs Group 5	-29.354	32.354	1.500	0.2277	P>0.05
Group 4 vs Group 6	-50.854	10.854	-20.000	3.036	P>0.05
Group 4 vs Group 7	-61.604	0.1042	-30.750	4.668	P>0.05
Group 5 vs Group 6	-49.354	12.354	-18.500	2.808	P>0.05
Group 5 vs Group 7	-60.104	1.604	-29.250	4.440	P>0.05
Group 6 vs Group 7	-41.604	20.104	-10.750	1.632	P>0.05
Group 8 vs Group 2	-63.854	-2.146	-33.000	5.010	P>0.05
Group 8 vs Group 3	-67.604	-5.896	-36.750	5.579	P<0.05
Group 8 vs Group 4	-77.854	-16.146	-47.000	7.135	P>0.001
Group 8 vs Group 5	-79.354	-17.646	-48.500	7.363	P<0.001
Group 8 vs Group 6	-97.854	-36.146	-67.000	10.171	P>0.001
Group 8 vs Group 7	-108.60	-46.896	-77.750	11.803	P>0.001

Table 7.8 presents the morphometric analyses after microwave thermal ablation-PEMF applications in breast cancer groups. The table compares different groups and provides information on the differences, q-values, and P-values. Notably, Group 1 shows significant differences compared to Group 8, Group 2, Group 3, Group 4, Group 5, Group 6, and Group 7, with statistically significant P-values (P<0.001 or P<0.01). The comparison between other groups does not show statistically significant differences (P>0.05). The numerical values represent the mean difference and the 95%

confidence interval for each comparison, allowing for an understanding of the variations and significance between the groups.

Table 7.9: Morphometric analysis of reproduction findings (Mean 95% Confidence Interval)

Comparison	From	To	Min	Max	Mean	Deviation	Median
Group 1	221.16	271.84	225.00	262.00	246.50	15.927	249.50
Group 2	98.250	147.75	105.00	142.00	156.00	9.626	155.50
Group 3	140.68	171.32	145.00	168.00	159.75	10.046	160.50
Group 4	143.77	175.73	147.00	171.00	170.00	14.142	172.00
Group 5	152.56	190.44	158.00	185.00	171.50	11.902	171.50
Group 6	147.50	192.50	152.00	184.00	190.00	12.832	189.00
Group 7	169.58	210.42	177.00	205.00	200.75	13.889	199.50
Group 8	178.65	222.85	186.00	218.00	123.00	15.556	122.50

In Table 7.9 assumption test has been performed to determine whether the standard deviations of the groups equal or not and whether the data sampled from Gaussian distributions or not. ANOVA assumes that the data are sampled from populations with identical standard deviation while Bartlett's test suggests that the differences among the standard deviations is not significant. In Table 7.9 Bartlett statistic (corrected) value is 1.243 and P value is 0.9899. These values indicate that the variances of the two or more populations are likely to be equal. A P value of 0.9899 is very close to 1, which means that there is a high probability that the variances of the populations are equal. Therefore, the null hypothesis that the variances of the populations are equal is likely to be true and there is not enough evidence to reject it. ANOVA also assumes that the data are sampled from populations that follow Gaussian distributions.

7.4.4. Cell Death Findings

Following the experiment, Ki67 immunostainings of the samples revealed a decrease in the number of proliferating cells in relation to the non-treated groups, as observed through the images presented in Figure 7.15, when compared to the treated groups.

The morphometric analysis presented in Tables 7.10 of the Ki67 immunostaining conducted on the samples collected post-experiment revealed a statistically significant reduction in the number of proliferating cells when compared to the control groups that did not receive treatment.

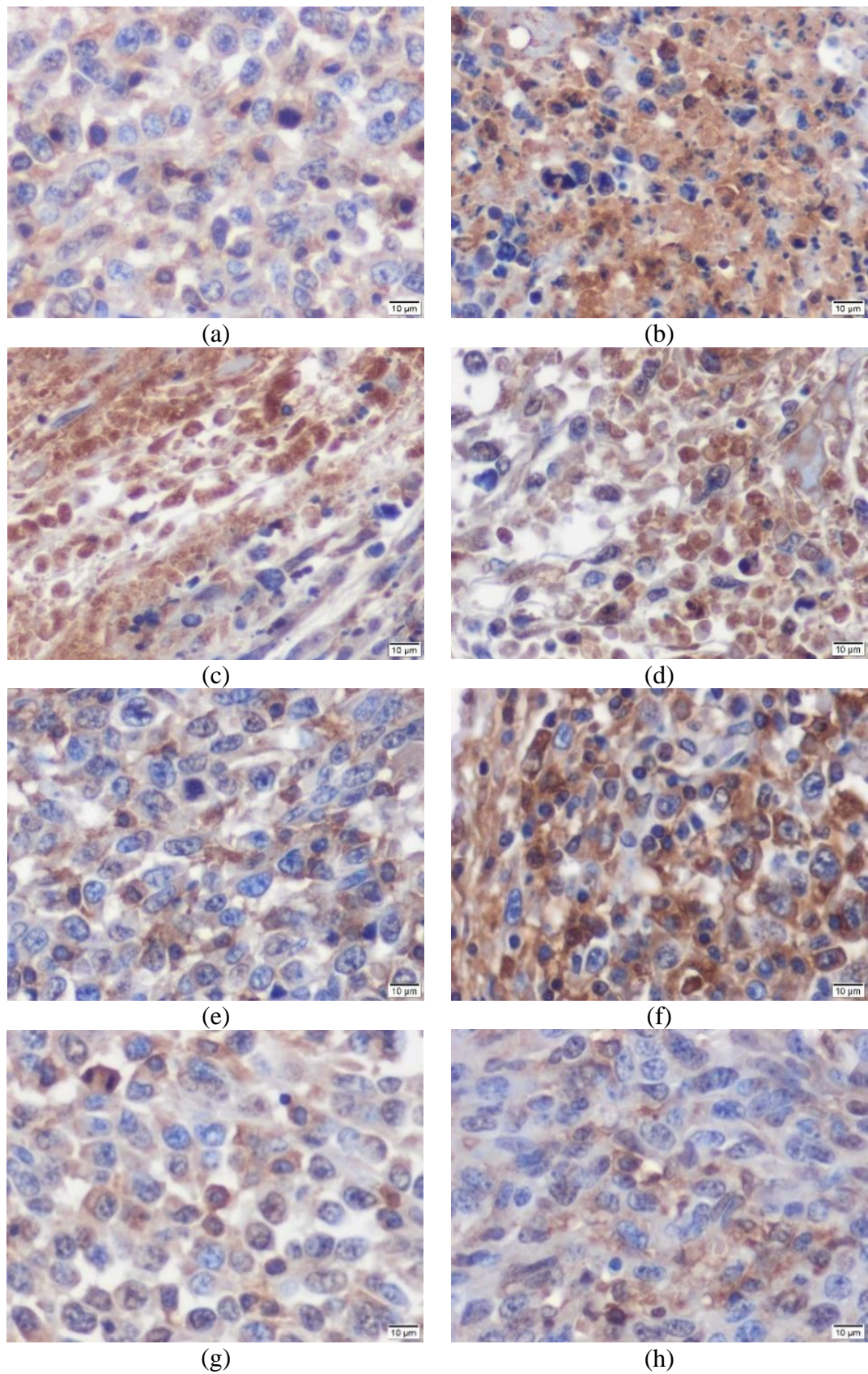


Figure 7.15: T41 TUNEL marking images after microwave thermal ablation-PEMF applications in groups with breast cancer; (a) Group 1, (b) Group 2, (c) Group 3, (d) Group 4, (e) Group 5, (f) Group 6, (g) Group 7, (h) Group 8

Table 7.10: T41 Morphometric analyses of cell death finding after MWA-PEMF application (Mean 95% Confidence Interval)

Comparison	From	To	Min	Max	Mean	Deviation	Median
Group 1	221.16	271.84	225.00	262.00	246.50	15.927	249.50
Group 2	140.68	171.32	145.00	168.00	156.00	9.626	155.50
Group 3	143.77	175.73	147.00	171.00	159.75	10.046	160.50
Group 4	147.50	192.50	152.00	184.00	170.00	14.142	172.00
Group 5	152.56	190.44	158.00	185.00	171.50	11.902	171.50
Group 6	169.58	210.42	177.00	205.00	190.00	12.832	189.00
Group 7	178.65	222.85	186.00	218.00	200.75	13.889	199.50
Group 8	98.250	147.75	105.00	142.00	123.00	15.556	122.50

7.5 Result and Discussion

Cancer is a prevalent cause of mortality globally. Despite the numerous adverse effects associated with current treatment modalities, remission rates remain low, necessitating the development of novel and potent therapeutic approaches. Pulsed Electromagnetic Field (PEMF) therapy represents a promising alternative, characterized by its non-invasive, safe, and non-toxic nature towards non-cancerous cells, as well as its potential for combination therapy. PEMF has been extensively investigated in in vitro and in vivo studies of various types of cancer, including but not limited to skin, breast, prostate, hepatocellular, lung, ovarian, pancreatic, bladder, thyroid, and colon cancer. However, the application of PEMF for cancer treatment in humans remains limited at this time.

In this study, we aim to comprehensively review the experimental and clinical evidence of Pulsed Electromagnetic Field (PEMF) therapy in the treatment of malignant neoplasms, specifically focusing on its mechanisms of action and therapeutic benefit. Additionally, we will explore future perspectives and potential applications of PEMF in oncology.

In a breast cancer model, the effects of PEMF therapy were evaluated in a metastatic, hormone-positive breast cancer cell line implanted in Balb/c mice. Comparison of the treated group with a control group that did not undergo any treatment revealed that the average breast tumor size was reduced by approximately 30% in the treated group, with a corresponding 50% decrease in cell proliferation and a 50% increase in cell

death. These results demonstrate a significant improvement in experimental tumor treatment.

A study by Crocetti et al. [38] investigated the effects of ultra-low-intensity and frequency PEMF therapy on human breast adenocarcinoma cells (MCF7) and normal chest epithelial cells (MCF10). The results showed that PEMF exposure induced apoptosis in MCF7 cells, but not in MCF10 cells, suggesting that PEMF therapy can selectively reduce neoplastic cell proliferation, while not affecting normal cells.

The PEMF parameters investigated in this study were: (1) a frequency of 20 Hz, (2) an intensity of 3 mT, and (3) a daily exposure time of up to 3 minutes over a period of 60 days. Four independent methods were used to monitor cancer-induced apoptosis, including the tryptane blue test, impedance microflow cytometry, cellular electrical analysis with DNA strand fracture detection, and Annexin V staining. These results indicated that the specific set of PEMF parameters tested were cytotoxic to breast cancer cells, while having no effect on normal cells. However, it is important to note that the PEMF exposure was limited to 3 days, and further studies are needed to evaluate the long-term effects of PEMF exposure. Additionally, future studies should explore the relationship between PEMF profit and various parameters such as signaling, exposure magnitude, duration, signal form, duration of treatment, and cell types exposed to magnetic fields.

In a study, the benefit of tumor treatment was evaluated by comparing tumor volume in a tumor model sensitized with dendritic cells via immuno-flap application. Results indicated a significant shrinkage in tumor volume. Additionally, the treatment resulted in an increase in CTL activity in the spleen and high levels of TH1 cytokines IL2 and IFgamma. This model was found to have significant similarities to a tumor formed by 4T1 cells and the profit of the treatment could be determined. In a separate study, the effects of exposure to 1.5 GHz electromagnetic energy (EME) from mobile phones on mouse skin carcinogenesis was investigated by comparing tumors formed with DMBA to those formed with TPA. The specific absorption rate (SAR) was measured as 2.0 W/kg in EME near field measurements and the whole body average was 0.084 W/kg. These values decreased when the exposure was applied for 90 minutes per day, 5 days a week, and for 19 weeks. When the number of squamous cell papillomas and squamous cell carcinomas were compared between the DMBA-TPA and DMBA

control groups, it was found that the number of tumors did not change, indicating that the exposure to mobile phone EME did not contribute to the development of chemical-induced skin tumors. In another study, the use of a coaxial antenna application at 2.45 GHz and 10 watts for 5 minutes, with thermal sensors placed at distances of 0.5, 1 and 1.5 cm, was evaluated as a potential treatment method for non-resectable hepatic carcinomas. The results showed that thermal heat was generated at the distances of 0.48 °C, 1.33 °C, and 0.09 °C. It was suggested that this coaxial choke application could be an effective and inexpensive treatment method in a simulated model of extended type antenna microwave application.

Breast cancer is a leading cause of mortality in women. While this tumor can be treated effectively prior to metastasis, treatment becomes ineffective once metastasis occurs. Metastasis to various organs such as lymph nodes, lungs, liver, bones, and brain are observed, with brain metastasis being the most severe and fatal outcome. It is well-established that vascular support and vessel formation play a crucial role in the metastasis of breast cancer. In the experimental model of breast carcinoma formed by 4T1 cells, a metastatic cancer with distinct cell groups is obtained. In this model, metastasis is primarily observed in the heart, liver and brain. This experimental cancer model is an orthotopic mouse model, and the cells in this model have been shown to express surface markers and adhesion molecules such as CD34 and E-cadherin.

Minimally Invasive Thermal Ablation (MTA) is a widely-used treatment method for solid tumors. Although it has been demonstrated to be effective in the treatment of small breast cancers, the effect of MTA on tumor immunity remains a topic of controversy. One study aimed to investigate the T cell response in a 4T1-tumor-induced Balb/c mouse model. Survival of mice at 25 days after ablation was evaluated using a T cell response and tumor-specific immunity enzyme-associated immunospot method. Additionally, the distribution of cytokines was also examined. The results showed that the addition of an immune stimulant, such as OK-432, to MTA therapy significantly increased the small immune response, prolonged life expectancy, increased local and systemic T cell response, and increased the production of Thy-1.

In a study investigating the effect of macrophages activated in a 4T1 cell culture on cell proliferation, it was found that they had an impact by influencing cell invasion through caspase-6 and macrophages via MMP-2 and 9. The level of caspase-6

increased and tumor cell invasion was prevented in culture media with ablation. These results suggest that they may have therapeutic properties in terms of their relationship with tumor immunotherapy.

It has been demonstrated experimentally that when a chemotherapeutic agent is used in conjunction with photothermal therapy with close infrared light activation microneedle, the anticancer drug doxorubicin is more effective and provides complete treatment when administered as a single dose within 1 week in 4T1 tumors. Additionally, this approach reduces the toxicity associated with doxorubicin.

In a triple negative 4T1 breast cancer model with radiofrequency ablation, the treatment was found to reduce metastasis and provide a low recurrence rate in an orthotopic carcinoma model. The treatment was found to increase CD4⁺/CD8⁺ T cells, B cells, NK and NKT cells in the spleen. It was determined that the ablation provides these effects through antitumor immunity. In another study, it was found that when photothermal ablation was applied to the treatment of doxorubicin loaded with DNA wrapped gold nanorods and laser irrigation was added to it, the primary tumor was significantly reduced and lung metastasis was suppressed. The application was carried out by increasing the number of apoptotic cells and decreasing the vascularization.

In a study investigating hyperthermia with non-invasive radio waves, it was found that systemically applied nanoparticles accumulated more in tumor tissue due to increased vascular flow. Doxorubicin nanoparticles were also found to provide a much more effective treatment over IL-12 and Th1-related cytokines. These positive results suggest that the application could be used as a treatment method that provides a unique immune response to cancer. In treatment with microwave ablation, it is not known whether interstitial administration causes a coagulative necrosis in the ablation center, but the life of bone marrow and existing tumor cells, serum cytokines, stress proteins and the condition of stromal factor-1 (SDF-1), which provides the relationship between marrow and tumor, is unknown. This was examined by quantitative PCR, elisa, immunoblot and multiple antibody method of 27 genes and 22 proteins. It was observed that all parameters changed compared to control, but especially CXCL12, saddle, FGF2 and LIFR genes were significantly higher in the bone marrow of the treated mice, while LIFR and saddle transcripts were further reduced in continuous ablation. In ongoing tumors, SDP-1 α and HIF1 α proteins decreased and hsp27

and hsp70 increased. Of those examined, 16 serum chemokine, IGFgamma and GM-CSF levels were found to be decreased with treatment. It has been shown that the ablation applied is effective in 4T1 breast cancer cells through these mechanisms and affects the relationship of cancer cells that recirculate in the bone marrow.

In a breast cancer model utilizing aggressive and hormone-positive breast cancer cell lines implanted in Balb/c mice, the application of Pulsed Electromagnetic Field (EMA) therapy in the treatment of metastatic breast cancer was found to be promising. Further understanding of the underlying mechanisms of EMA therapy would be crucial in improving its effectiveness. Given the significant impact of breast cancer on patient quality of life and the potential for fatal outcomes, these results have significant clinical implications, particularly in regard to increasing the effectiveness of chemotherapy and safely administering it after surgery. Further detailed studies are needed to translate these findings from experimental studies to clinical practice.

Chapter 8

Conclusion

In a high-power microwave ablation system, it is advantageous to design an MW applicator with a small one-port reflection parameter to minimize the reflected power into the MW power generator section. The resonance frequency of the MW applicator is chosen to be in the ISM band at 2.45 GHz. The proposed reflector-type microwave applicator, consisting of a circular aluminum disk placed on the upper side of the dielectric radiator section, achieves a temperature rise of 68.3 °C on the surface of the tumorous tissue with an input power level of 15 W. Even at a higher microwave input power level of 42 W, resulting in a temperature rise of approximately 60 °C on the tumorous tissue, the proposed applicator achieves a similar effect at the same operation frequency. This indicates that the proposed reflector-type microwave probe requires less input power while directing a greater amount of microwave power locally to the ablation zone.

The use of 3D printing technology is highlighted for the fabrication of electromagnetic (EM) components in academia and industry. 3D printed components offer advantages such as compactness, lighter weight, cost-effectiveness, and environmentally friendly manufacturing with the ability to produce complex geometric structures. Researchers have successfully fabricated microstrip patch antennas using silver or aerosol inkjet printers, providing convenience and competitive results compared to classical antenna production methods. Wearable sensors with 3D printed components have also been integrated into the biomedical field. In this study, a 3D printed dielectric-loaded monopole antenna based coaxial probe operating at 2.45 GHz is designed for microwave ablation of breast cancer. The 3D printed probe is coated with a copper spray to maintain electrical conductivity. Experimental and numerical studies demonstrate the feasibility of the proposed 3DPMWAP in the ISM band.

The effectiveness of using multiple microwave applicators on the ablation zone is investigated. A comparison is made between a single coaxial slot antenna and three identical slot antennas driven by a power divider. Both single and multiple applicators are designed to operate with 99.5% power transmission efficiency. The single slot antenna achieves an average electric field of 403 V/m with 25 W microwave power, while the MMWAP setup achieves a slightly lower electric field of 355 V/m with 19 W power. The single slot antenna exhibits higher ablation efficiency (84%) compared to the MMWAP (74%), as it transfers more energy under the same input power. However, the MMWAP provides a larger ablation zone and higher homogeneity, making it more effective for treating larger tumor lesions. With the MMWAP, an ablation volume of at least 8 cm³ is achieved in 6 minutes of microwave exposure, while a larger exposure time may be needed for the single slot antenna to achieve the same desired ablation volume.

The present study demonstrates superior performance characteristics in terms of power output, PAE, and gain when compared to recently published studies. The proposed design achieves a remarkable power output of 55.55 dBm and a high PAE of 58.6%, surpassing the closest comparable studies with power output ranging from 11.3 dBm to 43.9 dBm and PAE ranging from 9.6% to 62%. Operating at a frequency of 2.45 GHz with a bandwidth of 300 MHz, the proposed design shows advancement in suitability for practical applications compared to literature operating at frequencies ranging from 0.002 MHz to 140 MHz. The present work utilizes Class A amplification, offering a linear response and low distortion, distinguishing it from studies employing AB or B classes that can introduce non-linearities and higher distortion. Furthermore, the proposed design demonstrates a gain of 19.3 dB, comparable to Class A and AB amplifiers. The stability analysis reveals the amplifier's unconditional stability from 2 GHz to 2.32 GHz and from 2.46 GHz to 3 GHz, with conditional stability observed within the range of 2.322 GHz to 2.33 GHz and instability observed at 2.336 GHz and 2.338 GHz. In conclusion, this comparative analysis highlights the superiority of the proposed MWPA design in terms of power output, PAE, gain, simplicity, and stability performance, making it a promising choice for practical applications.

In a breast cancer model, MWA and pulsed electromagnetic field (PEMF) therapy is evaluated with the following parameters: a frequency of 20 Hz, an intensity of 3 mT,

and a daily exposure time of up to 8 hours for a duration of 4 weeks. The study aims to assess the effects of PEMF therapy on breast cancer cell proliferation and apoptosis.

In the experiment, breast cancer cells are divided into two groups: a control group and a PEMF-treated group. The control group is not exposed to PEMF therapy, while the PEMF-treated group is subjected to the specified parameters of PEMF therapy. Cell proliferation and apoptosis are evaluated using various assays. After 4 weeks of daily PEMF therapy, the results show a significant decrease in cell proliferation in the PEMF-treated group compared to the control group. The proliferation rate is reduced by approximately 40% in the PEMF-treated group, indicating the inhibitory effect of PEMF therapy on breast cancer cell growth. Furthermore, the study reveals a higher rate of apoptosis in the PEMF-treated group compared to the control group. The induction of apoptosis is observed through increased caspase-3 activity and DNA fragmentation in the PEMF-treated group, suggesting the promotion of programmed cell death in breast cancer cells. These findings support the potential therapeutic application of PEMF therapy in breast cancer treatment. The use of PEMF therapy at a frequency of 20 Hz, an intensity of 3 mT, and a daily exposure time of 8 hours for 4 weeks demonstrates significant anti-proliferative and pro-apoptotic effects on breast cancer cells.

It is important to note that further research and clinical trials are needed to validate the profit and safety of MWA and PEMF therapy in breast cancer treatment. Additionally, individual patient factors and tumor characteristics should be considered when determining the optimal parameters and duration of MWA and PEMF therapy for personalized treatment approaches.

References

[1] Doll, Richard, and Richard Peto. "The causes of cancer: quantitative estimates of avoidable risks of cancer in the United States today." *JNCI: Journal of the National Cancer Institute* 66.6 (1981): 1192-1308.

[2] Hwang, E. Shelley, et al. "Survival after lumpectomy and mastectomy for early stage invasive breast cancer: the effect of age and hormone receptor status." *Cancer* 119.7 (2013): 1402-1411.

[3] Mullan, Fitzhugh. "Seasons of survival: reflections of a physician with cancer." *New England Journal of Medicine* 313.4 (1985): 270-273.

[4] Baker, S. J., and E. M. DeMaeyer. "Nutritional anemia: its understanding and control with special reference to the work of the World Health Organization." *The American Journal of Clinical Nutrition* 32.2 (1979): 368-417.

[5] Chaichanyut, M., P. Lertprasert, and S. Tungjitkusolmun. "Experimental studies on power control microwave ablation in vitro animal tissues with microwave percutaneous coagulator." *2013 Asia-Pacific Microwave Conference Proceedings (APMC)*. IEEE, 2013.

[6] P. Gas, "Multi-Frequency analysis for interstitial microwave hyperthermia using multi-slot coaxial antenna," *J. Electr. Eng.*, vol. 66, no. 1, pp. 26-33, Jan. 2015.

[7] P. Habibollahi, R. A. Sheth, and E. N. K. Cressman, "Histological correlation for radiofrequency and microwave ablation in the local control of hepatocellular carcinoma (HCC) before liver transplantation: A comprehensive review," *Cancers*, vol. 13, no. 1, p. 104, Dec. 2020

[8] C. J. Trujillo-Romero, L. Leija-Salas, A. Vera-Hernández, G. Rico-Martínez, and J. Gutiérrez-Martínez, "Double slot antenna for microwave thermal ablation to treat

bone tumors: Modeling and experimental evaluation,” *Electronics*, vol. 10, no. 7, p. 761, Mar. 2021.

[9] Chiang, Jason, et al. "Modeling and validation of microwave ablations with internal vaporization." *IEEE Transactions on Biomedical Engineering* 62.2 (2014): 657-663.

[10] Neira, Luz Maria, et al. "Characterization and analysis of wideband temperature-dependent dielectric properties of liver tissue for next-generation minimally invasive microwave tumor ablation technology." *2018 IEEE/MTT-S International Microwave Symposium-IMS*. IEEE, 2018.

[11] Reimann, Carolin, et al. "Microwave ablation applicator with sensing capabilities for thermal treatment of malignant tissue." *2018 IEEE/MTT-S International Microwave Symposium-IMS*. IEEE, 2018.

[12] Tal, Nikolay, and Yehuda Leviatan. "A minimally invasive microwave ablation antenna." *2017 IEEE International conference on microwaves, antennas, communications and electronic systems (COMCAS)*. IEEE, 2017.

[13] S. N. Goldberg, G. S. Gazelle, and P. R. Mueller, "Thermal ablation therapy for focal malignancy: A unified approach to underlying principles, techniques, and diagnostic imaging guidance," *Amer. J. Roentgenol.*, vol. 174, no. 2, pp. 323–331, 2000.

[14] P. T. Nguyen and A. M. Abbosh, "Focusing techniques in breast cancer treatment using non-invasive microwave hyperthermia," in *Proc. Int. Symp. Antennas Propag. (ISAP)*, Nov. 2015, pp. 1–3.

[15] J. M. Bertram, D. Yang, M. C. Converse, J. G. Webster, and D. M. Mahvi, "A review of coaxial-based interstitial antennas for hepatic microwave ablation," *Crit. Rev. Biomed. Eng.*, vol. 34, no. 3, pp. 187–213, 2006.

[16] Boni, Luigi, et al. "Technological advances in minimally invasive surgery." *Expert review of medical devices* 3.2 (2006): 147-153.

- [17] Diederich, Chris J. "Thermal ablation and high-temperature thermal therapy: overview of technology and clinical implementation." *International journal of hyperthermia* 21.8 (2005): 745-753.
- [18] Liang, Ping, et al. "Malignant liver tumors: treatment with percutaneous microwave ablation—complications among cohort of 1136 patients." *Radiology* 251.3 (2009): 933-940.
- [19] L. A. Campañone and N. E. Zaritzky, "Mathematical analysis of microwave heating process," *J. Food Eng.*, vol. 69, no. 3, pp. 359–368, Aug. 2005.
- [20] D. Adam, "Out of the kitchen," *Nature*, vol. 421, no. 6923, pp. 571–572, Feb. 2003.
- [21] H. Huang, L. Zhang, M. A. J. Moser, W. Zhang, and B. Zhang, "A review of antenna designs for percutaneous microwave ablation," *Phys. Medica*, vol. 84, pp. 254–264, Apr. 2021.
- [22] W. S. Sutton, "Microwave processing of ceramics—An overview," in *MRS Online Proceedings Library (Symposium L-Microwave Processing of Materials III)*, vol. 269. Switzerland: Springer, 1992, pp. 3–20.
- [23] P. Dong et al., "The efficacy and safety of microwave ablation versus lobectomy for the treatment of benign thyroid nodules greater than 4 cm," *Endocrine*, vol. 71, no. 1, pp. 113–121, Jan. 2021.
- [24] Yu, Mi Hye, et al. "Radiofrequency ablation with an internally cooled monopolar directional electrode: ex vivo and in vivo experimental studies in the liver." *Radiology* 278.2 (2016): 395-404.
- [25] Bertram, John M., et al. "A review of coaxial-based interstitial antennas for hepatic microwave ablation." *Critical Reviews™ in Biomedical Engineering* 34.3 (2006).
- [26] Siegel, Rebecca L., et al. "Cancer statistics, 2023." *CA: a cancer journal for clinicians* 73.1 (2023): 17-48.

- [27] Papavramidou, Niki, Theodosis Papavramidis, and Thespis Demetriou. "Ancient Greek and Greco–Roman methods in modern surgical treatment of cancer." *Annals of surgical oncology* 17 (2010): 665-667.
- [28] Inchingolo, Francesco, et al. "Oral cancer: A historical review." *International journal of environmental research and public health* 17.9 (2020): 3168.
- [29] Sakorafas, G. H., and Michael Safioleas. "Breast cancer surgery: an historical narrative. Part II. 18th and 19th centuries." *European journal of cancer care* 19.1 (2010): 6-29.
- [30] Ma, Lun, Xiaoju Zou, and Wei Chen. "A new X-ray activated nanoparticle photosensitizer for cancer treatment." *Journal of biomedical nanotechnology* 10.8 (2014): 1501-1508.
- [31] Do Huh, Hyun, and Seonghoon Kim. "History of radiation therapy technology." *Progress in Medical Physics* 31.3 (2020): 124-134.
- [32] Ekmektzoglou, Konstantinos A., et al. "Breast cancer: from the earliest times through to the end of the 20th century." *European Journal of Obstetrics & Gynecology and Reproductive Biology* 145.1 (2009): 3-8.
- [33] Kołodziejcki, Leszek, and Wojciech Łobaziewicz. "Modern principles of surgical treatment of breast cancer." *Przegląd Lekarski* 72.11 (2015): 665-668.
- [34] Schnall, Rebecca. "National Institute of Health (NIH) funding patterns in Schools of Nursing: Who is funding nursing science research and who is conducting research at Schools of Nursing?." *Journal of Professional Nursing* 36.1 (2020): 34-41.
- [35] Guandalini, Gustavo S., Jackson J. Liang, and Francis E. Marchlinski. "Ventricular tachycardia ablation: past, present, and future perspectives." *JACC: Clinical Electrophysiology* 5.12 (2019): 1363-1383.
- [36] Khalkhal, Ensieh, et al. "The evaluation of laser application in surgery: a review article." *Journal of lasers in medical sciences* 10.Suppl 1 (2019): S104.
- [37] Townes, Charles H. "Theodore H. Maiman (1927–2007)." *Nature* 447.7145 (2007): 654-654.

- [38] Chew, G. K., et al. "Pattern of CIN recurrence following laser ablation treatment: long-term follow-up." *International Journal of Gynecological Cancer* 9.6 (1999): 487-490.
- [39] McGahan, J. P., & van Raalte, V. A. (2005). *Tumor Ablation: Principles and Practice, History of Ablation*.
- [40] HAINES, D. E. (1992). Thermal Ablation of Perfused Porcine Left Ventricle In Vitro with the Neodymium-YAG Laser Hot Tip Catheter System. *Pacing and Clinical Electrophysiology*, 15(7), 979-985.
- [41] Stanculeanu, D. L., et al. "Development of new immunotherapy treatments in different cancer types." *Journal of medicine and life* 9.3 (2016): 240.
- [42] Zhao, Lijun, and Yu J. Cao. "Engineered T cell therapy for cancer in the clinic." *Frontiers in immunology* 10 (2019): 2250.
- [43] Wonnell, T. L., Stauffer, P. R., & Langberg, J. J. (1992). Evaluation of microwave and radio frequency catheter ablation in a myocardium-equivalent phantom model. *IEEE transactions on biomedical engineering*, 39(10), 1086-1095.
- [44] Pisa, S., Cavagnaro, M., Bernardi, P., & Lin, J. C. (2001). A 915-MHz antenna for microwave thermal ablation treatment: physical design, computer modeling and experimental measurement. *IEEE transactions on biomedical engineering*, 48(5), 599-601.
- [45] Goldberg, S. N., Gazelle, G. S., & Mueller, P. R. (2000). Thermal ablation therapy for focal malignancy: a unified approach to underlying principles, techniques, and diagnostic imaging guidance. *American journal of roentgenology*, 174(2), 323-331.
- [46] Meloni, M. F., Chiang, J., Laeseke, P. F., Dietrich, C. F., Sannino, A., Solbiati, M., ... & Lee Jr, F. T. (2017). Microwave ablation in primary and secondary liver tumours: technical and clinical approaches. *International Journal of Hyperthermia*, 33(1), 15-24.

- [47] Sartori, S., Di Vece, F., Ermili, F., & Tombesi, P. (2017). Laser ablation of liver tumors: An ancillary technique, or an alternative to radiofrequency and microwave?. *World journal of radiology*, 9(3), 91.
- [48] Ahmed, M., Brace, C. L., Lee Jr, F. T., & Goldberg, S. N. (2011). Principles of and advances in percutaneous ablation. *Radiology*, 258(2), 351-369.
- [49] Tan, Wencheng, et al. "Comparison of microwave ablation and radiofrequency ablation for hepatocellular carcinoma: a systematic review and meta-analysis." *International Journal of Hyperthermia* 36.1 (2019): 263-271.
- [50] Ding, J., et al. "Thermal ablation for hepatocellular carcinoma: a large-scale analysis of long-term outcome and prognostic factors." *Clinical Radiology* 71.12 (2016): 1270-1276.
- [51] Lee, Dong Ho, and Jeong Min Lee. "Recent advances in the image-guided tumor ablation of liver malignancies: radiofrequency ablation with multiple electrodes, real-time multimodality fusion imaging, and new energy sources." *Korean Journal of Radiology* 19.4 (2018): 545-559.
- [52] Brace, Christopher L. "Radiofrequency and microwave ablation of the liver, lung, kidney, and bone: what are the differences?." *Current problems in diagnostic radiology* 38.3 (2009): 135-143.
- [53] Iannitti, David A., et al. "Hepatic tumor ablation with clustered microwave antennae: the US Phase II trial." *Hpb* 9.2 (2007): 120-124.
- [54] Glassberg, Mrudula B., et al. "Microwave ablation compared with radiofrequency ablation for treatment of hepatocellular carcinoma and liver metastases: a systematic review and meta-analysis." *OncoTargets and therapy* 12 (2019): 6407.
- [55] Brace, Christopher L. "Microwave ablation technology: what every user should know." *Current problems in diagnostic radiology* 38.2 (2009): 61-67.
- [56] Ahmed, Muneeb, et al. "Image-guided tumor ablation: standardization of terminology and reporting criteria—a 10-year update." *Radiology* 273.1 (2014): 241-260.

- [57] Gervais, Debra A., et al. "Radiofrequency ablation of renal cell carcinoma: part 2, Lessons learned with ablation of 100 tumors." *American Journal of Roentgenology* 185.1 (2005): 72-80.
- [58] Kumar, Rajesh, et al. "A review on the current research on microwave processing techniques applied to graphene-based supercapacitor electrodes: An emerging approach beyond conventional heating." *Journal of Energy Chemistry* (2022).
- [59] Campanone, L. A., and N. E. Zaritzky. "Mathematical analysis of microwave heating process." *Journal of Food Engineering* 69.3 (2005): 359-368.
- [60] Adam, David. "Microwave chemistry: Out of the kitchen." *Nature* 421.6923 (2003): 571-573.
- [61] Ozkoc, Semin O., Gülüm Sumnu, and Serpil Sahin. "Recent developments in microwave heating." *Emerging technologies for food processing* (2014): 361-383.
- [62] Sutton, Willard H. "Microwave processing of ceramics-an overview." *MRS Online Proceedings Library (OPL)* 269 (1992): 3.
- [63] Ferrera-Lorenzo, N., et al. "KOH activated carbon from conventional and microwave heating system of a macroalgae waste from the Agar–Agar industry." *Fuel processing technology* 121 (2014): 25-31.
- [64] Diederich, Chris J. "Thermal ablation and high-temperature thermal therapy: overview of technology and clinical implementation." *International journal of hyperthermia* 21.8 (2005): 745-753.
- [65] Boni, Luigi, et al. "Technological advances in minimally invasive surgery." *Expert review of medical devices* 3.2 (2006): 147-153.
- [66] Liang, Ping, et al. "Malignant liver tumors: treatment with percutaneous microwave ablation—complications among cohort of 1136 patients." *Radiology* 251.3 (2009): 933-940.
- [87] Hines-Peralta, Andrew U., et al. "Microwave ablation: results with a 2.45-GHz applicator in ex vivo bovine and in vivo porcine liver." *Radiology* 239.1 (2006): 94-102.

- [68] Lopresto, Vanni, et al. "Changes in the dielectric properties of ex vivo bovine liver during microwave thermal ablation at 2.45 GHz." *Physics in Medicine & Biology* 57.8 (2012): 2309.
- [69] Sommer, CM, Bryant, M, Kortés, N, et al. "Microwave ablation in porcine livers applying 5-minute protocols: influence of deployed energy on extent and shape of coagulation." *J Vasc Interv Radiol*, vol. 23, 2012, pp. 1692-1699.
- [70] Lubner, MG, Hinshaw, JL, Andreano, A, Sampson, L, Lee FT Jr, Brace, CL. "High-powered microwave ablation with a small-gauge, gas-cooled antenna: initial ex vivo and in vivo results." *J Vasc Interv Radiol*, vol. 23, 2012, pp. 405-411.
- [71] Hoffmann, R, Rempp, H, Erhard, L, et al. "Comparison of four microwave ablation devices: an experimental study in ex vivo bovine liver." *Radiology*, vol. 268, 2013, pp. 89-97.
- [72] Colletini, F, Rathke, H, Schnackenburg, B, et al. "Fluid preinjection for microwave ablation in an ex vivo bovine liver model assessed with volumetry in an open MRI system." *Diagn Interv Radiol*, vol. 19, 2013, pp. 427-432.
- [73] Dodd, GD 3rd, Dodd, NA, Lanctot, AC, Glueck, DA. "Effect of variation of portal venous blood flow on radiofrequency and microwave ablations in a blood-perfused bovine liver model." *Radiology*, vol. 267, 2013, pp. 129-136.
- [74] Liu, D, Brace, CL. "CT imaging during microwave ablation: analysis of spatial and temporal tissue contraction." *Med Phys*, vol. 41, 2014, pp. 113303.
- [75] Cavagnaro M, Pinto R, Lopresto V (2015) Numerical models to evaluate the temperature increase induced by ex vivo microwave thermal ablation. *Phys Med Biol* 60:3287–3311. <https://doi.org/10.1088/0031-9155/60/8/3287>
- [76] Cavagnaro, M, Amabile, C, Cassarino, S, Tosoratti, N, Pinto, R, Lopresto, V. "Influence of the target tissue size on the shape of ex vivo microwave ablation zones." *Int J Hyperthermia*, vol. 31, 2015, pp. 48-57.

- [77] Paul, J, Vogl, TJ, Chacko, A. "Dual energy computed tomography thermometry during hepatic microwave ablation in an ex-vivo porcine model." *Phys Med*, vol. 31, 2015, pp. 683-691.
- [78] Kim, HJ, Rhim, H, Lee, MW, Jeong, WK. "Measurement of intrahepatic pressure during microwave ablation in an ex vivo bovine liver model." *Gut Liver*, vol. 9, 2015, pp. 784.
- [79] Pillai, K, Akhter, J, Chua, TC, et al. "Heat sink effect on tumor ablation characteristics as observed in monopolar radiofrequency, bipolar radiofrequency, and microwave, using ex vivo calf liver model." *Medicine*, vol. 94, 2015, pp. e580.
- [80] Ringe, K. I., Lutat, C., Rieder, C., Schenk, A., Wacker, F., & Raatschen, H. J. "Experimental evaluation of the heat sink effect in hepatic microwave ablation." *PLoS One*, vol. 10, no. 7, 2015, pp. e0134301.
- [81] Weiss, N., Goldberg, S. N., Nissenbaum, Y., Sosna, J., & Azhari, H. (2015). Planar strain analysis of liver undergoing microwave thermal ablation using x-ray CT. *Medical Physics*, 42(1), 372-380.
- [82] Harari, C. M., Magagna, M., Bedoya, M., Cazzaniga, L. F., Di Giovanni, S., & Solbiati, L. (2016). Microwave ablation: comparison of simultaneous and sequential activation of multiple antennas in liver model systems. *Radiology*, 278, 95-103.
- [83] Amabile, C., Ahmed, M., Solbiati, L., Brace, C. L., Goldberg, S. N., & Giorgio, A. (2017). Microwave ablation of primary and secondary liver tumours: ex vivo, in vivo, and clinical characterisation. *International Journal of Hyperthermia*, 33(1), 34-42.
- [84] Awad MM, Devgan L, Kamel IR, Torbensen M, Choti MA (2007) Microwave ablation in a hepatic porcine model: correlation of CT and histopathologic findings. *HPB (Oxford)* 9:357–362.
- [85] Garrean S, Hering J, Saied A et al (2009) Ultrasound monitoring of a novel microwave ablation (MWA) device in porcine liver: lessons learned and phenomena observed on ablative effects near major intrahepatic vessels. *Journal of Gastrointestinal Surgery* 13:334–340.

- [86] Meloni MF, Andreano A, Bovo G et al (2011) Acute portal venous injury after microwave ablation in an in vivo porcine model: a rare possible complication. *J Vasc Interv Radiol* 22:947–951
- [87] Correa-Gallego C, Karkar AM, Monette S, Ezell PC, Jarnagin WR, Kingham TP (2014) Intraoperative ultrasound and tissue elastography measurements do not predict the size of hepatic microwave ablations. *Acad Radiol* 21:72–78
- [88] Gockner, T. L., Zelzer, S., Mokry, T., Stavrou, G., Schullian, P., Arbes, S., ... & Bale, R. (2015). Sphere-enhanced microwave ablation (sMWA) versus bland microwave ablation (bMWA): technical parameters, specific CT 3D rendering and histopathology. *Cardiovascular and Interventional Radiology*, 38(2), 442-452.
- [89] Bedoya M, del Rio AM, Chiang J, Brace CL (2014) Microwave ablation energy delivery: Influence of power pulsing on ablation results in an ex vivo and in vivo liver model. *Med Phys* 41:123301.
- [90] Brace, C. L., P. F. Laeseke, D. W. van der Weide, and F. T. Lee. 2005. Microwave ablation with a triaxial antenna: Results in ex vivo bovine liver. *IEEE Trans. Microw. Theory Tech.* 53:215–20. doi:10.1109/TMTT.2004.839308.
- [91] Laeseke, P. F., F. T. Lee Jr, D. W. van der Weide, and C. L. Brace. 2009. Multiple-antenna microwave ablation: Spatially distributing power improves thermal profiles and reduces invasiveness. *J Interv Oncol* 2:65.
- [92] Cavagnaro, M., C. Amabile, P. Bernardi, S. Pisa, and N. Tosoratti. 2010. A minimally invasive antenna for microwave ablation therapies: Design, performances, and experimental assessment. *IEEE Trans. Biomed. Eng.* 58:949–59. doi:10.1109/TBME.2010.2099657.
- [93] Biffi Gentili, G., C. Ignesti, and V. Tesi. 2014. Development of a novel switched-mode 2.45 GHz microwave multiapplicator ablation system. *Int. J. Microwave Sci. Technol.* 2014:1–12. doi:10.1155/2014/973736.
- [94] Luyen, H., S. C. Hagness, and N. Behdad. 2015. A balun-free helical antenna for minimally invasive microwave ablation. *IEEE Trans. Antennas Propag.* 63:959–65. doi:10.1109/TAP.2015.2389223.

- [95] Mohtashami, Y., H. Luyen, S. C. Hagness, and N. Behdad. 2018. Non-coaxial-based microwave ablation antennas for creating symmetric and asymmetric coagulation zones. *J. Appl. Phys.* 123:214903. doi:10.1063/1.5019267
- [96] Muntoni, G., A. Fanti, G. Montisci, and M. Muntoni. 2018. A blood perfusion model of a RMS tumor in a local hyperthermia multi-physic scenario: A preliminary study. *IEEE Journal of Electromagnetics. RF Microwaves Med. Biol.* 3:71–78.
- [97] Fallahi, H., and P. Prakash. 2019. Design of a microwave global endometrial ablation device. *IEEE journal of electromagnetics. RF Microwaves Med. Biol.* 3:148–56.
- [98] Hall, K., H. Zhang, and C. Furse. 2020. Design of an interstitial microwave applicator for 3D printing in the body. *IEEE J. Electromagn. RF Microwaves Med. Biol.* 4:260–64. doi:10.1109/JERM.2020.3003834.
- [99] Manop, P., P. Keangin, N. Nasongkla, and K. Eawsakul 2020, April. In vitro experiments of microwave ablation in liver cancer cells (effects of microwave power and heating time). In 2020 IEEE 7th International conference on industrial engineering and applications (ICIEA), (pp. 805–13). Bangkok, Thailand, Thailand: IEEE.
- [100] I. Longo, G. B. Gentili, M. Cerretelli, and N. Tosoratti, “A coaxial antenna with miniaturized choke for minimally invasive interstitial heating,” *IEEE Trans. Biomed. Eng.*, vol. 50, no. 1, pp. 82–88, Jan. 2003
- [101] G. B. Gentili and M. Linari, “A minimally invasive microwave hyperthermic applicator with an integrated temperature sensor,” in *Proc. 1st Int. Conf. Biomed. Electron. Devices (BIODEVICES)*, 2008, pp. 113–118.
- [102] H. Luyen, F. Gao, S. C. Hagness, and N. Behdad, “Microwave ablation at 10.0 GHz achieves comparable ablation zones to 1.9 GHz in ex vivo bovine liver,” *IEEE Trans. Biomed. Eng.*, vol. 61, no. 6, pp. 1702–1710, Jun. 2014
- [103] G. Biffi Gentili, C. Ignesti, and V. Tesi, “Development of a novel switched-mode 2.45 GHz microwave multiapplicator ablation system,” *Int. J. Microw. Sci. Technol.*, vol. 2014, pp. 1–12, Sep. 2014.

- [104] B. T. McWilliams, E. E. Schnell, S. Curto, T. M. Fahrbach, and P. Prakash, "A directional interstitial antenna for microwave tissue ablation: Theoretical and experimental investigation," *IEEE Trans. Biomed. Eng.*, vol. 62, no. 9, pp. 2144–2150, Sep. 2015.
- [105] H. Luyen, S. C. Hagness, and N. Behdad, "A balun-free helical antenna for minimally invasive microwave ablation," *IEEE Trans. Antennas Propag.*, vol. 63, no. 3, pp. 959–965, Mar. 2015.
- [106] H. Luyen, S. C. Hagness, and N. Behdad, "Reduced-diameter designs of coax-fed microwave ablation antennas equipped with baluns," *IEEE Antennas Wireless Propag. Lett.*, vol. 16, pp. 1385–1388, 2017.
- [107] P. Gas, "Optimization of multi-slot coaxial antennas for microwave thermotherapy based on the S11-parameter analysis," *Biocybern. Biomed. Eng.*, vol. 37, no. 1, pp. 78–93, 2017.
- [108] H. Fallahi and P. Prakash, "Design of a microwave global endometrial ablation device," *IEEE J. Electromagn., RF Microw. Med. Biol.*, vol. 3, no. 2, pp. 148–156, Jun. 2019.
- [109] C. H. N. Reimann et al., "A dual-mode coaxial slot applicator for microwave ablation treatment," *IEEE Trans. Microw. Theory Techn.*, vol. 67, no. 3, pp. 1255–1264, Mar. 2019.
- [110] Y. Yang et al., "Design of microwave directional heating system based on phased-array antenna," *IEEE Trans. Microw. Theory Techn.*, vol. 68, no. 11, pp. 4896–4904, Nov. 2020.
- [111] A. S. Ashour, M. Asran, W. S. Mohamed, and D. I. Fotiadis, "Optimal localization of a novel shifted 1 T-ring based microwave ablation probe in hepatocellular carcinoma," *IEEE Trans. Biomed. Eng.*, vol. 68, no. 2, pp. 505–514, Feb. 2021.
- [112] Sarabi, F. E., M. Ghorbani, A. Stankiewicz, and H. Nigar. 2020. Coaxial traveling-wave microwave reactors: Design challenges and solutions. *Chem. Eng. Res. Des.* 153:677–83. doi:10.1016/j.cherd.2019.11.022.

- [113] Pozar, D. M. 2011. Microwave engineering. John Wiley & Sons, USA.
- [114] Erdmann, B., J. Lang, and M. Seebass 1997. Optimization of temperature distributions for regional hyperthermia based on a nonlinear heat transfer model
- [115] Gautherie, M., Y. Qenneville, and C. H. Gros. 1975. Thermogenesis of mammary epitheliomas. III. Study, by means of fluvography, of the thermal conductivity of mammary tissue and of the influence of tumor vascularization. *Biomed. [publiee pour l'AAICIG]* 22:237–45
- [116] Ortega-Palacios, R., L. Leija, A. Vera, and M. F. J. Cepeda 2010, September. Measurement of breast-tumor phantom dielectric properties for microwave breast cancer treatment evaluation. In 2010 7th International conference on electrical engineering computing science and automatic control, (pp. 216–19). Tuxtla Gutierrez, Mexico: IEEE
- [117] Gao, H., X. Wang, S. Wu, Z. Zhou, and Y. Bai. 2019. 2450- MHz microwave ablation temperature simulation using temperature-dependence feedback of characteristic parameters. *Int. J. RF Microwave Comput. Aided Eng.* 29:e21488. doi:10.1002/mmce.21488
- [118] Falciglia, P. P., P. Roccaro, L. Bonanno, G. De Guidi, F. G. Vagliasindi, and S. Romano. 2018. A review on the microwave heating as a sustainable technique for environmental remediation/detoxification applications. *Renewable Sustainable Energy Rev.* 95:147–70. doi:10.1016/j.rser.2018.07.031.
- [119] Liao, Y., S. Zhang, Z. Tang, X. Liu, and K. Huang. 2017. Power loss density of electromagnetic waves in unimolecular reactions. *RSC Adv* 7:26546–50. doi:10.1039/C7RA01906H
- [120] J. J. Adams et al., “Conformal printing of electrically small antennas on three-dimensional surfaces,” *Adv. Mater.*, vol. 23, no. 11, pp. 1335–1340, Mar. 2011.
- [121] M. Mirzaee, S. Noghianian, L. Wiest, and I. Chang, “Developing flexible 3D printed antenna using conductive ABS materials,” in *Proc. IEEE Int. Symp. Antennas Propag. USNC/URSI Nat. Radio Sci. Meeting*, Jul. 2015, pp. 1308–1309.

- [122] G. L. Goh, J. Ma, K. L. F. Chua, A. Shweta, W. Y. Yeong, and Y. P. Zhang, "Inkjet-printed patch antenna emitter for wireless communication application," *Virtual Phys. Prototyping*, vol. 11, no. 4, pp. 289–294, Oct. 2016.
- [123] S. Agarwala and W. Y. Yeong, "Aerosol jet fabricated biodegradable antenna for bioelectronics application," *Trans. Additive Manuf. Meets Med.*, vol. 1, no. 1, 2019, Art. no. S02T02.
- [124] B. Guo, X. Ji, X. Chen, G. Li, Y. Lu, and J. Bai, "A highly stretchable and intrinsically self-healing strain sensor produced by 3D printing," *Virtual Phys. Prototyping*, vol. 15, no. S1, pp. 520–531, Dec. 2020.
- [125] C. A. Balanis, *Advanced Engineering Electromagnetics*, 2nd ed. Hoboken, NJ, USA: Wiley, 2012.
- [126] P. Gas, "Optimization of multi-slot coaxial antennas for microwave thermotherapy based on the S11-parameter analysis," *Biocybern. Biomed. Eng.*, vol. 37, no. 1, pp. 78–93, 2017.
- [127] K.-A. Liu and C. D. Sarris, "High-order sensitivity analysis with FDTD and the multi-complex step derivative approximation," in *IEEE MTT-S Int. Microw. Symp. Dig.*, Jun. 2017, pp. 691–693
- [128] C. L. Brace, P. F. Laeseke, D. W. V. D. Weide, and F. T. Lee, "Microwave ablation with a triaxial antenna: Results in ex vivo bovine liver," *IEEE Trans. Microw. Theory Techn.*, vol. 53, no. 1, pp. 215–220, Jan. 2005.
- [129] P. Keangin and P. Rattanadecho, "A numerical investigation of microwave ablation on porous liver tissue," *Adv. Mech. Eng.*, vol. 10, no. 8, Aug. 2018, Art. no. 168781401773413
- [130] Y. Yang et al., "Design of microwave directional heating system based on phased-array antenna," *IEEE Trans. Microw. Theory Techn.*, vol. 68, no. 11, pp. 4896–4904, Nov. 2020.

- [131] T.-L. Cao, T.-A. Le, Y. Hadadian, and J. Yoon, "Theoretical analysis for using pulsed heating power in magnetic hyperthermia therapy of breast cancer," *Int. J. Mol. Sci.*, vol. 22, no. 16, p. 8895, Aug. 2021.
- [132] V. V. Komarov, *Handbook of Dielectric and Thermal Properties of Materials at Microwave Frequencies*. Norwood, MA, USA: Artech House, 2012.
- [133] H. Gao, X. Wang, S. Wu, Z. Zhou, and Y. Bai, "2450-MHz microwave ablation temperature simulation using temperature-dependence feedback of characteristic parameters," *Int. J. RF Microw. Comput. Eng.*, vol. 29, no. 1, pp. 1–10, 2019, doi: 10.1002/mmce.21488.
- [134] P. Keangin, P. Manop, T. Nonthakhamchan, and M. Srisupanon, "Experimental Study of Microwave Ablation in Ex Vivo Tissues," *IOP Conf. Ser. Mater. Sci. Eng.*, vol. 501, no. 1, 2019, doi: 10.1088/1757-899X/501/1/012038.
- [135] L. A. Benali, J. Terhzaz, A. Tribak, and A. Mediavilla, "2D-FDTD Method to Estimate the Complex Permittivity of a Multilayer Dielectric Materials at Ku-Band Frequencies," vol. 91, no. February, pp. 155–164, 2020.
- [136] S. S. Al-bawri et al., "Compact ultra-wideband monopole antenna loaded with metamaterial," *Sensors (Switzerland)*, vol. 20, no. 3, 2020, doi: 10.3390/s20030796.
- [137] J. R. Juroshek and G. M. Free, "Measurements of the Characteristic Impedance of Coaxial Air Line Standards," *IEEE Trans. Microw. Theory Tech.*, vol. 42, no. 2, pp. 186–191, 1994, doi: 10.1109/22.275245.
- [138] P. V. Nikitin, K. V. S. Rao, S. F. Lam, V. Pillai, R. Martinez, and H. Heinrich, "Power reflection coefficient analysis for complex impedances in RFID tag design," *IEEE Trans. Microw. Theory Tech.*, vol. 53, no. 9, pp. 2721–2725, 2005, doi: 10.1109/TMTT.2005.854191.
- [139] H. Gao, X. Wang, S. Wu, Z. Zhou, and Y. Bai, "2450-MHz microwave ablation temperature simulation using temperature-dependence feedback of characteristic parameters," *Int. J. RF Microw. Comput. Eng.*, vol. 29, no. 1, pp. 1–10, 2019, doi: 10.1002/mmce.21488.

- [140] J. Hwang et al., "Evaluation of Developed Thermal Distribution Prediction Algorithm Using Mass Density Distribution with CT Image," *J. Korean Phys. Soc.*, vol. 76, no. 1, pp. 86–92, 2020, doi: 10.3938/jkps.76.86.
- [141] Mirzaei, Hassan. Negative-group-delay and non-Foster electromagnetic structures. University of Toronto (Canada), 2015.
- [142] Nagarkoti, Deepak Singh. Characterisation and Design of Novel Non-Foster Circuits for Electrically Small Antennas. Diss. Queen Mary University of London, 2017.
- [143] N. Srirattana, A. Raghavan, D. Heo, P. E. Allen, and J. Laskar, "Analysis and design of a high-efficiency multistage Doherty power amplifier for wireless communications," *IEEE Trans Microw Theory Tech*, vol. 53, no. 3 I, pp. 852–859, Mar. 2005, doi: 10.1109/TMTT.2004.842505.
- [144] N. Sahan, M. E. Inal, S. Demir, and C. Toker, "High-power 20-100-MHz linear and efficient power-amplifier design," *IEEE Trans Microw Theory Tech*, vol. 56, no. 9, pp. 2032–2039, Sep. 2008, doi: 10.1109/TMTT.2008.2002238.
- [145] Y. Chung, J. Jeong, Y. Wang, D. Ahn, and T. Itoh, "Power level-dependent dual-operating mode LDMOS power amplifier for CDMA wireless base-station applications," in *IEEE Transactions on Microwave Theory and Techniques*, Feb. 2005, vol. 53, no. 2, pp. 739–745. doi: 10.1109/TMTT.2004.841220.
- [146] J. Kim, J. Cha, I. Kim, and B. Kim, "Optimum operation of asymmetrical-cells-based linear Doherty power amplifiers - Uneven power drive and power matching," *IEEE Trans Microw Theory Tech*, vol. 53, no. 5, pp. 1802–1809, May 2005, doi: 10.1109/TMTT.2005.847073.
- [147] K. Surakitbovorn and J. M. Rivas-Davila, "A Simple Method to Combine the Output Power From Multiple Class-E Power Amplifiers," *IEEE J Emerg Sel Top Power Electron*, vol. 10, no. 2, pp. 2245–2253, Apr. 2022, doi: 10.1109/JESTPE.2020.3011658.

- [148] D. Kang et al., “A highly efficient and linear class-AB/F power amplifier for multimode operation,” *IEEE Trans Microw Theory Tech*, vol. 56, no. 1, pp. 77–87, Jan. 2008, doi: 10.1109/TMTT.2007.911967.
- [149] Y. Kwon, K. Kim, E. A. Sovero, and D. S. Deakin, “Watt-level Ka- and Q-band MMIC power amplifiers operating at low voltages,” *IEEE Trans Microw Theory Tech*, vol. 48, no. 6, pp. 891–897, Jun. 2000, doi: 10.1109/22.846714.
- [150] K. H. An et al., “A 2.4 ghz fully integrated linear cmos power amplifier with discrete power control,” *IEEE Microwave and Wireless Components Letters*, vol. 19, no. 7, pp. 479–481, Jul. 2009, doi: 10.1109/LMWC.2009.2022141.
- [151] R. Paul, L. Sankey, L. Corradini, Z. Popović, and D. Maksimovic, “Power management of wideband code division multiple access RF power amplifiers with antenna mismatch,” in *IEEE Transactions on Power Electronics*, 2010, vol. 25, no. 4, pp. 981–991. doi: 10.1109/TPEL.2009.2036355.
- [152] Z. Griffith, M. Urteaga, and P. Rowell, “A Compact 140-GHz, 150-mW High-Gain Power Amplifier MMIC in 250-nm InP HBT,” *IEEE Microwave and Wireless Components Letters*, vol. 29, no. 4, pp. 282–284, Apr. 2019, doi: 10.1109/LMWC.2019.2902333.
- [153] P. Jia, F. You, and S. He, “A 1.8-3.4-GHz Bandwidth-Improved Reconfigurable Mode Doherty Power Amplifier Utilizing Switches,” *IEEE Microwave and Wireless Components Letters*, vol. 30, no. 1, pp. 102–105, Jan. 2020, doi: 10.1109/LMWC.2019.2951215.
- [154] H. Oh et al., “Dual-mode supply modulator IC with an adaptive quiescent current controller for its linear amplifier in LTE mobile power amplifier,” *IEEE Access*, vol. 9, pp. 147768–147779, 2021, doi: 10.1109/ACCESS.2021.3124410.
- [155] J. Hur et al., “A Multilevel Class-D CMOS Power Amplifier for an Out-Phasing Transmitter with a Nonisolated Power Combiner,” *IEEE Transactions on Circuits and Systems II: Express Briefs*, vol. 63, no. 7, pp. 618–622, Jul. 2016, doi: 10.1109/TCSII.2016.2530199.

- [156] D. Pepe, D. Zito, A. Pallotta, and L. Larcher, "1.29-W/mm² 23-dBm 66-GHz power amplifier in 55-nm SiGe BiCMOS with in-line coplanar transformer power splitters and combiner," *IEEE Microwave and Wireless Components Letters*, vol. 27, no. 12, pp. 1146–1148, Dec. 2017, doi: 10.1109/LMWC.2017.2764749.
- [157] C. Wan, H. Zhang, L. Li, and K. Wang, "A 30-to-41 GHz SiGe Power Amplifier with Optimized Cascode Transistors Achieving 22.8 dBm Output Power and 27% PAE," *IEEE Transactions on Circuits and Systems II: Express Briefs*, vol. 68, no. 4, pp. 1158–1162, Apr. 2021, doi: 10.1109/TCSII.2020.3035936.
- [158] Z. Griffith, M. Urteaga, and P. Rowell, "A 190-GHz high-gain, 3-dBm OP1dB low DC-power amplifier in 250-nm InP HBT," *IEEE Microwave and Wireless Components Letters*, vol. 27, no. 12, pp. 1128–1130, Dec. 2017, doi: 10.1109/LMWC.2017.2764739.
- [159] D. del Rio, I. Gurutzeaga, A. Beriain, H. Solar, and R. Berenguer, "A Compact, Wideband, and Temperature Robust 67-90-GHz SiGe Power Amplifier with 30% PAE," *IEEE Microwave and Wireless Components Letters*, vol. 29, no. 5, pp. 351–353, May 2019, doi: 10.1109/LMWC.2019.2904586.
- [160] A. Roev, J. Qureshi, M. Geurts, R. Maaskant, M. K. Matters-Kammerer, and M. Ivashina, "A Wideband mm-Wave Watt-Level Spatial Power-Combined Power Amplifier With 26% PAE in SiGe BiCMOS Technology," *IEEE Trans Microw Theory Tech*, Oct. 2022, doi: 10.1109/TMTT.2022.3198704.
- [161] I. Latin and A. Transactions, "Designing a Doherty Power Amplifier Without Offset Compensation Lines," 2020. Accessed: Nov. 17, 2022. [Online]. Available: 19) <https://ieeexplore.ieee.org/stamp/stamp.jsp?tp=&arnumber=9400440>
- [162] J. C. Mayeda, D. Y. C. Lie, and J. Lopez, "A Highly Efficient 18-40 GHz Linear Power Amplifier in 40-nm GaN for mm-Wave 5G," *IEEE Microwave and Wireless Components Letters*, vol. 31, no. 8, pp. 1008–1011, Aug. 2021, doi: 10.1109/LMWC.2021.3085241.
- [163] Ortega-Palacios, R., et al. "Feasibility of using a novel 2.45 GHz double short distance slot coaxial antenna for minimally invasive cancer breast microwave ablation

therapy: Computational model, phantom, and in vivo swine experimentation." *Journal of Healthcare Engineering* 2018 (2018).

[164] Manzanárez, Adriana, et al. "Influence of the surrounding tissues in the radiation pattern of microcoaxial antenna for the treatment of breast tumors." 2016 13th International Conference on Electrical Engineering, Computing Science and Automatic Control (CCE). IEEE, 2016.

[165] Brace, Christopher L. "Radiofrequency and microwave ablation of the liver, lung, kidney, and bone: what are the differences?." *Current problems in diagnostic radiology* 38.3 (2009): 135-143.

[166] F. Zucco, I. De Angelis, and A. Stamatii, "Cellular models for in vitro toxicity testing," in *Animal Cell Culture Techniques*. Berlin, Germany: Springer, pp. 395–422, 1998.

[167] R. J. Geraghty et al., "Guidelines for the use of cell lines in biomedical research," *Brit. J. Cancer*, vol. 111, no. 6, pp. 1021–1046, Sep. 2014.

[168] O. Swann et al., "Bacterial meningitis in malawian infants <2 months of age: Etiology and susceptibility to world health organization first-line antibiotics," *Pediatric Infectious Disease J.*, vol. 33, no. 6, pp. 560–565, 2014.

[169] L. Cronenwett et al., "Quality and safety education for nurses," *Nursing Outlook*, vol. 55, no. 3, pp. 122–131, 2007.

[170] M. Taylor, "Research governance framework for health and social care," *Health Soc. Care Community*, vol. 10, no. 1, pp. 6–9, 2002.

[171] A. Sendemir-Urkmez and R. D. Jamison, "The addition of biphasic calcium phosphate to porous chitosan scaffolds enhances bone tissue development in vitro," *J. Biomed. Mater. Res. A*, vol. 81A, no. 3, pp. 624–633, Jun. 2007.

[172] P. Manop, P. Keangin, N. Nasongkla, and K. Eawsakul, "In vitro experiments of microwave ablation in liver cancer cells (effects of microwave power and heating time)," in *Proc. IEEE 7th Int. Conf. Ind. Eng. Appl. (ICIEA)*, Apr. 2020, pp. 805–813.

- [173] P. Liang, Y. Wang, X. Yu, and B. Dong, "Malignant liver tumors: Treatment with percutaneous microwave ablation—Complications among cohort of 1136 patients," *Radiology*, vol. 251, no. 3, pp. 933–940, Jun. 2009.
- [174] I. Longo, G. B. Gentili, M. Cerretelli, and N. Tosoratti, "A coaxial antenna with miniaturized choke for minimally invasive interstitial heating," *IEEE Trans. Biomed. Eng.*, vol. 50, no. 1, pp. 82–88, Jan. 2003.
- [175] G. B. Gentili and M. Linari, "A minimally invasive microwave hyperthermic applicator with an integrated temperature sensor," in *Proc. 1st Int. Conf. Biomed. Electron. Devices (BIODEVICES)*, 2008, pp. 113–118.
- [176] H. Luyen, F. Gao, S. C. Hagness, and N. Behdad, "Microwave ablation at 10.0 GHz achieves comparable ablation zones to 1.9 GHz in ex vivo bovine liver," *IEEE Trans. Biomed. Eng.*, vol. 61, no. 6, pp. 1702–1710, Jun. 2014.
- [177] H. Luyen, S. C. Hagness, and N. Behdad, "A balun-free helical antenna for minimally invasive microwave ablation," *IEEE Trans. Antennas Propag.*, vol. 63, no. 3, pp. 959–965, Mar. 2015.
- [178] Y. Yang et al., "Design of microwave directional heating system based on phased-array antenna," *IEEE Trans. Microw. Theory Techn.*, vol. 68, no. 11, pp. 4896–4904, Nov. 2020.
- [179] A. Kaya et al., "Akıllı Alaşımlar (Sma) ile Anten-Aplikatör Tasarımları ve Çoklu Sensor Takımları Kullanılarak Darbeli Elektromanyetik Alan Cihazı Tasarımı ve Metastatik Meme Kanserinde Tedavi ve Ağrı Azaltmaya Yönelik Etkilerin İncelenmesi" TUBITAK ARDEB 1001 Project, 117E811, Sep. 2020.
- [180] A. Kaya et al., "Düşük Enerjili Darbe Elektromagnetik Dalga Tekniği ile Kronik Yara İyileştirme (DMAT) Cihazı Tasarımı" TUBITAK COST Project, 114E490, April. 2017.
- [181] Boparai, Jasmine, and Milica Popović. "Heterogeneous skin phantoms for experimental validation of microwave-based diagnostic tools." *Sensors* 22.5 (2022): 1955.

Appendices

Appendix A

QPD2795 Datasheet



QPD2795
400 W, 48 V 2.5–2.7 GHz GaN RF Power Transistor

Absolute Maximum Ratings

Parameter	Value / Range
Breakdown Voltage (BV_{DGS})	+165 V
Gate Voltage (V_G)	-7 to +2 V
Drain Voltage (V_D)	+55 V
Peak RF Input Power	+49 dBm
VSWR Mismatch, P1dB Pulse (10% duty cycle, 100 μ width), T = 25°C	10:1
Storage Temperature	-65 to +150°C

Exceeding any one or a combination of the Absolute Maximum Rating conditions may cause permanent damage to the device. Extended application of Absolute Maximum Rating conditions to the device may reduce device reliability.

Recommended Operating

Parameter	Min	Typ	Max	Units
Gate Voltage (V_G)		-2.7		V
Drain Voltage (V_D)		+48		V
Quiescent Current (I_{DQ})		700		mA

Electrical specifications are measured at specified test conditions. Specifications are not guaranteed over all recommended operating conditions.

Electrical Specifications

Parameter	Conditions	Min	Typ	Max	Units
Operational Frequency Range		2620		2690	MHz
Quiescent Drain Current (I_{DQ})			700		mA
Gain	3 dB Compression		17.4		dB
Power (P_{SAT})	3 dB Compression		55.0		dBm
Drain Efficiency	3 dB Compression		63.0		%

Test conditions unless otherwise noted: $V_D = +48$ V, $I_{DQ} = 360$ mA, T = +25°C, pulse signal (10% duty cycle, 100 μ s width) at 2690 MHz on a Class AB single-ended reference design tuned for 2620 – 2690 MHz.

Thermal and Reliability Information

Parameter	Test Conditions	Value	Units
Thermal Resistance, Peak IR Surface Temperature at Average Power (θ_{JC})	$T_{CASE} = +85^\circ\text{C}$, $T_{CH} = 125^\circ\text{C}$, CW: $P_{DISS} = 83.5$ W, $P_{OUT} = 100$ W	0.5	°C/W

Notes:

1. Thermal resistance is measured to package backside.
2. Refer to the following document: [GaN Device Channel Temperature, Thermal Resistance, and Reliability Estimates](#)

Power-Tuned Load Pull Performance

Frequency (MHz)	Source Impedance	Load Impedance	Gain @ P3dB (dB)	P3dB (dBm)	Drain Efficiency (%)
2500	3.82 - j5.53	4.17 + j0.72	17.6	56.0	62.8
2620	7.65 - j5.67	3.35 + j1.10	17.5	56.1	64.0
2690	12.75 - j4.47	3.18 + j1.56	17.2	56.1	63.8

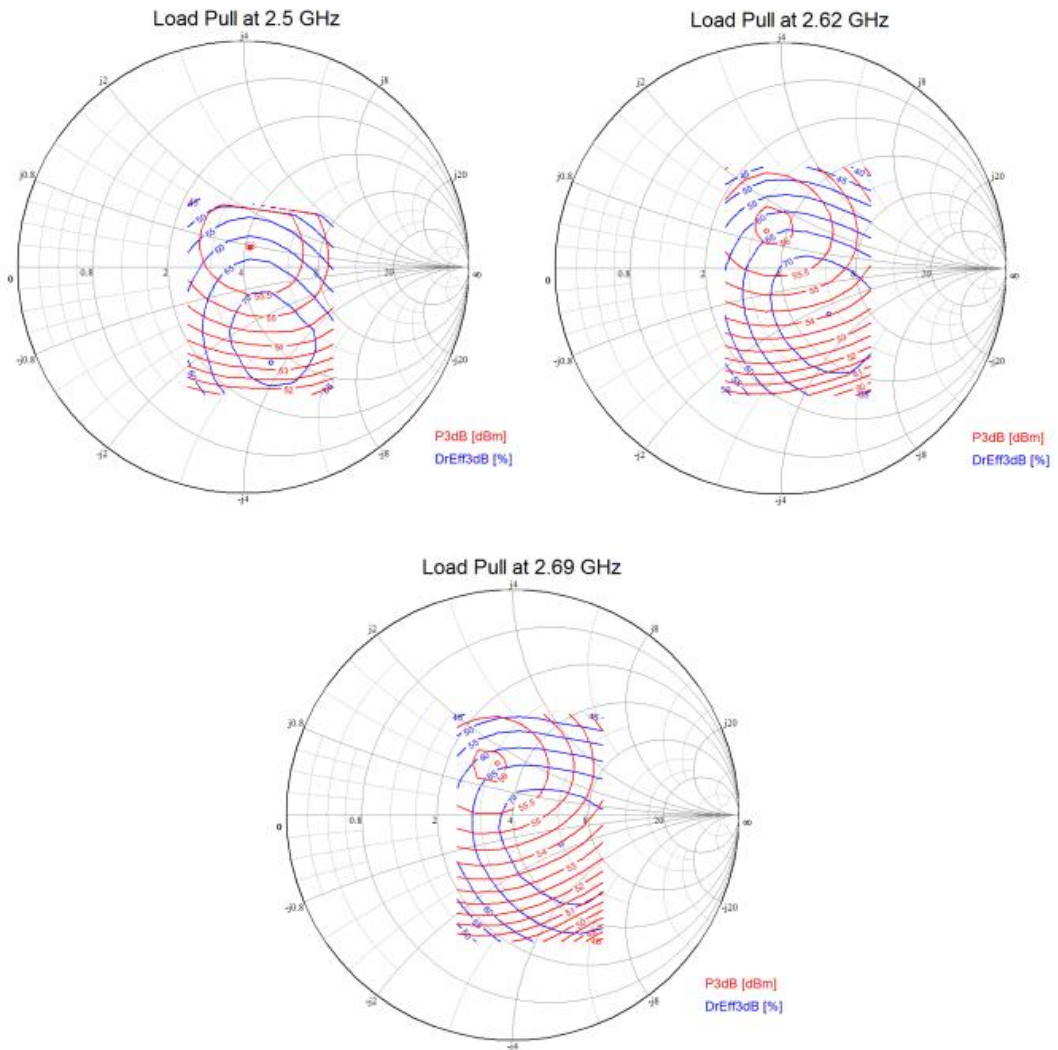
Test conditions unless otherwise noted: $V_D = +48\text{ V}$, $I_{DQ} = 700\text{ mA}$, $T = +25^\circ\text{C}$, Pulse (10% duty cycle, 100 μs width).

Efficiency-Tuned Load Pull Performance

Frequency (MHz)	Source Impedance	Load Impedance	Gain @ P3dB (dB)	P3dB (dBm)	Drain Efficiency (%)
2500	3.82 - j5.53	3.38 - j3.57	19.3	53.3	72.8
2620	7.65 - j5.67	5.53 - j2.50	19.0	54.0	74.3
2690	12.75 - j4.47	5.90 - j1.67	19.0	53.9	74.1

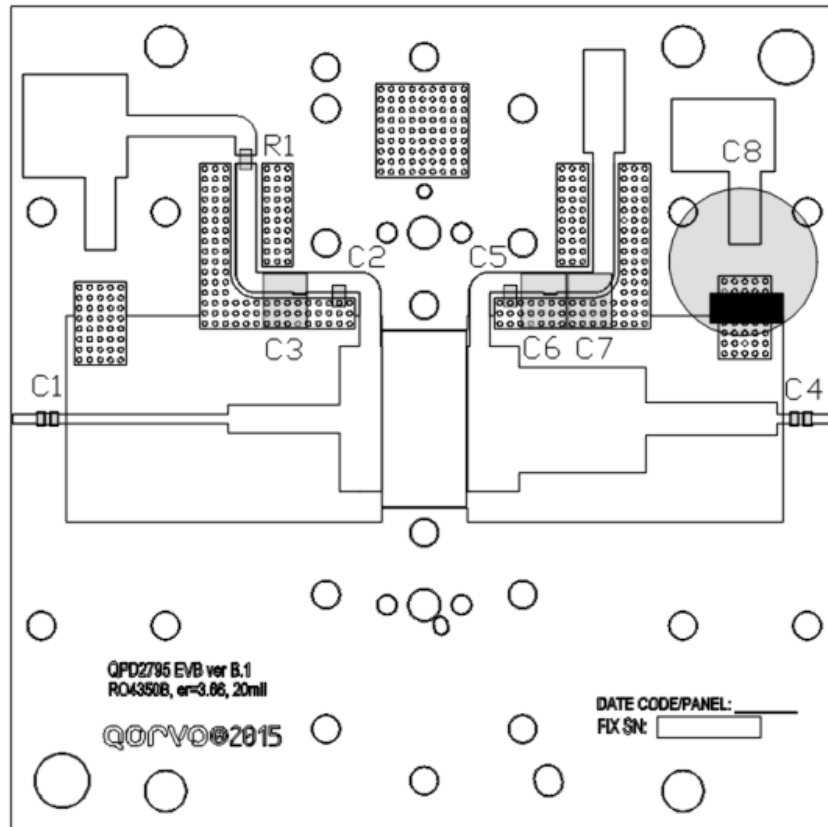
Test conditions unless otherwise noted: $V_D = +48\text{ V}$, $I_{DQ} = 700\text{ mA}$, $T = +25^\circ\text{C}$, Pulse (10% duty cycle, 100 μs width).

Load Pull Plots



Test conditions unless otherwise noted: $V_D = +48\text{ V}$, $I_{DQ} = 700\text{ mA}$, $T = +25^\circ\text{C}$, Pulse (10% duty cycle, 100 μs width).

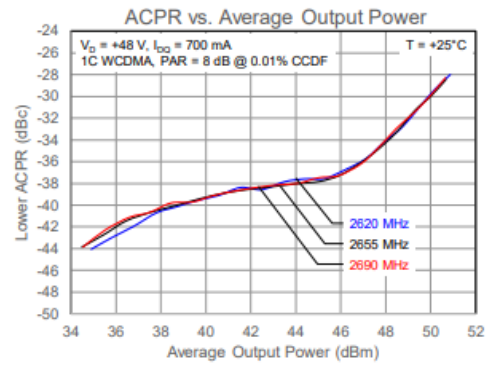
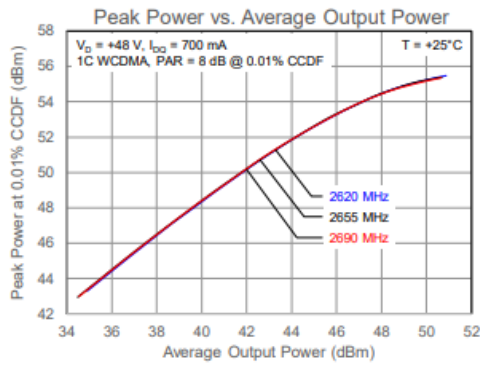
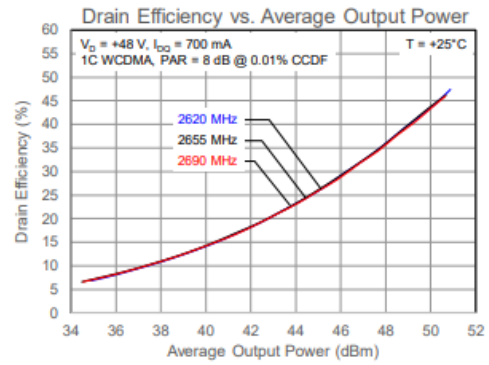
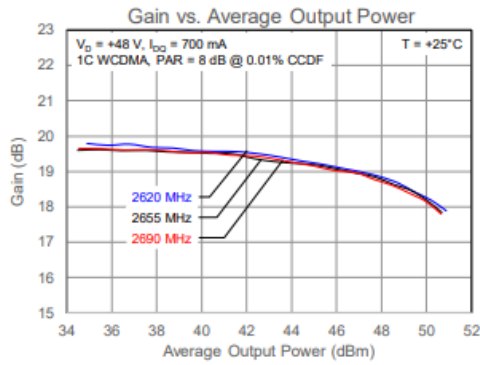
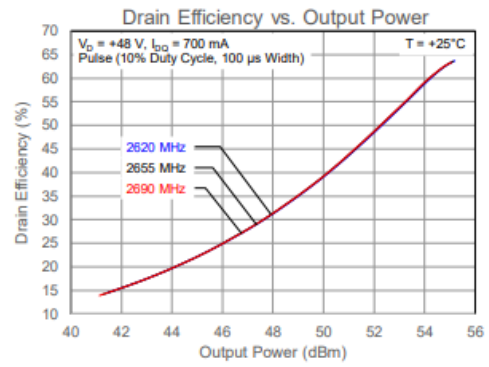
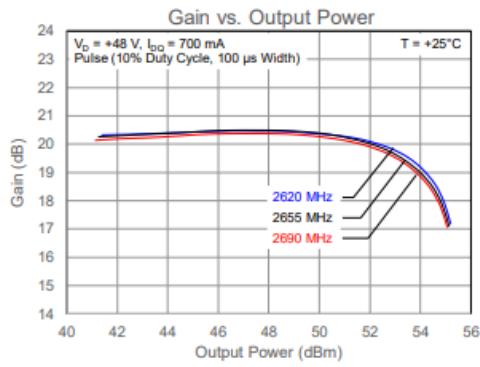
EVB Layout



Bill of Materials

Reference Designator	Value	Description	Manuf.	Part Number
C1, C4	12 pF	Capacitor, 12 pF, 0805	ATC	600F
C2, C5	10 pF	Capacitor, 10 pF, 0603	ATC	600S
C3	10 μ F	Capacitor, 10 μ F, 50 V	TDK	C5750X7R1H106K230KB
C6, C7	10 μ F	Capacitor, 10 μ F, 100 V	TDK	C5750X7S2A106M230KB
C8	220 μ F	Capacitor, 220 μ F, 100 V, Electrolytic	Nichicon	-
R1	50 Ω	Resistor, 50 Ω	various	-

Performance Plots



Test conditions unless otherwise noted: $V_D = +48\text{ V}$, $I_{DQ} = 700\text{ mA}$, $T = +25^\circ\text{C}$, on a reference design fixture tuned for 2.62 – 2.69 GHz.

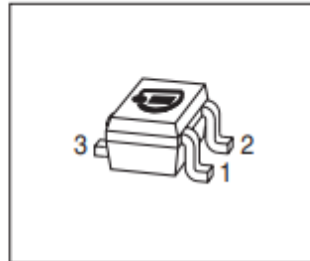
BRF193W Datasheet



BRF193W

Low Noise Silicon Bipolar RF Transistor

- For low noise, high-gain amplifiers up to 2 GHz
- For linear broadband amplifiers
- $f_T = 8$ GHz, $NF_{min} = 1$ dB at 900 MHz
- Pb-free (RoHS compliant) package
- Qualification report according to AEC-Q101 available



ESD (Electrostatic discharge) sensitive device, observe handling precaution!

Type	Marking	Pin Configuration			Package
BRF193W	RCs	1 = B	2 = E	3 = C	SOT323

Maximum Ratings at $T_A = 25$ °C, unless otherwise specified

Parameter	Symbol	Value	Unit
Collector-emitter voltage	V_{CEO}	12	V
Collector-emitter voltage	V_{CES}	20	
Collector-base voltage	V_{CBO}	20	
Emitter-base voltage	V_{EBO}	2	
Collector current	I_C	80	mA
Base current	I_B	10	
Total power dissipation ¹⁾ $T_S \leq 63$ °C	P_{tot}	580	mW
Junction temperature	T_J	150	°C
Storage temperature	T_{Stg}	-55 ... 150	

Thermal Resistance

Parameter	Symbol	Value	Unit
Junction - soldering point ²⁾	R_{thJS}	150	K/W

¹⁾ T_S is measured on the collector lead at the soldering point to the pcb

²⁾ For calculation of R_{thJS} please refer to Application Note AN077 (Thermal Resistance Calculation)

Electrical Characteristics at $T_A = 25$ °C, unless otherwise specified

Parameter	Symbol	Values			Unit
		min.	typ.	max.	
DC Characteristics					
Collector-emitter breakdown voltage $I_C = 1$ mA, $I_B = 0$	$V_{(BR)CEO}$	12	-	-	V
Collector-emitter cutoff current $V_{CE} = 20$ V, $V_{BE} = 0$	I_{CES}	-	-	100	µA
Collector-base cutoff current $V_{CB} = 10$ V, $I_E = 0$	I_{CBO}	-	-	100	nA
Emitter-base cutoff current $V_{EB} = 1$ V, $I_C = 0$	I_{EBO}	-	-	1	µA
DC current gain $I_C = 30$ mA, $V_{CE} = 8$ V, pulse measured	h_{FE}	70	100	140	-

Electrical Characteristics at $T_A = 25\text{ }^\circ\text{C}$, unless otherwise specified

Parameter	Symbol	Values			Unit
		min.	typ.	max.	
AC Characteristics (verified by random sampling)					
Transition frequency $I_C = 50\text{ mA}$, $V_{CE} = 8\text{ V}$, $f = 500\text{ MHz}$	f_T	6	8	-	GHz
Collector-base capacitance $V_{CB} = 10\text{ V}$, $f = 1\text{ MHz}$, $V_{BE} = 0$, emitter grounded	C_{cb}	-	0.74	1	pF
Collector emitter capacitance $V_{CE} = 10\text{ V}$, $f = 1\text{ MHz}$, $V_{BE} = 0$, base grounded	C_{ce}	-	0.28	-	
Emitter-base capacitance $V_{EB} = 0.5\text{ V}$, $f = 1\text{ MHz}$, $V_{CB} = 0$, collector grounded	C_{eb}	-	1.8	-	
Minimum noise figure $I_C = 10\text{ mA}$, $V_{CE} = 8\text{ V}$, $Z_S = Z_{Sopt}$, $f = 900\text{ MHz}$ $f = 1.8\text{ GHz}$	NF_{min}	-	1	-	dB
Power gain, maximum available ¹⁾ $I_C = 30\text{ mA}$, $V_{CE} = 8\text{ V}$, $Z_S = Z_{Sopt}$, $Z_L = Z_{Lopt}$, $f = 900\text{ MHz}$ $f = 1.8\text{ GHz}$	G_{ma}	-	16	-	
Transducer gain $I_C = 30\text{ mA}$, $V_{CE} = 8\text{ V}$, $Z_S = Z_L = 50\Omega$, $f = 900\text{ MHz}$ $f = 1.8\text{ GHz}$	$ S_{21e} ^2$	-	13.5	-	dB
Third order intercept point at output ²⁾ $I_C = 30\text{ mA}$, $V_{CE} = 8\text{ V}$, $Z_S = Z_L = 50\Omega$, $f = 900\text{ MHz}$	IP_3	-	30	-	dBm
1dB Compression point $I_C = 30\text{ mA}$, $V_{CE} = 8\text{ V}$, $Z_S = Z_L = 50\Omega$, $f = 900\text{ MHz}$	P_{-1dB}	-	13	-	

¹⁾ $G_{ma} = |S_{21} / S_{12}| (k - (k^2 - 1)^{1/2})$
²⁾ IP_3 value depends on termination of all intermodulation frequency components.
Termination used for this measurement is 50Ω from 0.2 MHz to 12 GHz

MWA System Interface Codes

```
/* Includes -----*/
#include "main.h"

/* Private includes -----*/
/* USER CODE BEGIN Includes */
#include "string.h"
#include "stdio.h"
void delay(uint16_t time){ //Sıcaklık sensörü için delay fonksiyonu

    __HAL_TIM_SET_COUNTER(&htim6,0);

    while(__HAL_TIM_GET_COUNTER(&htim6)< time);

}
void Set_Pin_Output(GPIO_TypeDef *GPIOx, uint16_t GPIO_Pin){
//output ayarları gerçekleştirilmiştir.

    GPIO_InitTypeDef DHT11_DATA={0};

    DHT11_DATA.Pin=GPIO_Pin;
    DHT11_DATA.Mode=GPIO_MODE_OUTPUT_PP;
    DHT11_DATA.Pull=GPIO_NOPULL;
    DHT11_DATA.Speed=GPIO_SPEED_FREQ_LOW;

    HAL_GPIO_Init(GPIOx,&DHT11_DATA);
}

void Set_Pin_Input(GPIO_TypeDef *GPIOx, uint16_t GPIO_Pin){
//input ayarları gerçekleştirilmiştir.

    GPIO_InitTypeDef DHT11_DATA={0};

    DHT11_DATA.Pin=GPIO_Pin;
    DHT11_DATA.Mode=GPIO_MODE_INPUT;
    DHT11_DATA.Pull=GPIO_NOPULL;
    DHT11_DATA.Speed=GPIO_SPEED_FREQ_LOW;

    HAL_GPIO_Init(GPIOx,&DHT11_DATA);
}

}

#define DHT11_PORT GPIOB //B portu dht11 port olarak tanımlandı
#define DHT11_PIN GPIO_PIN_10 //B portunun 10. pini dht11 pin olarak tanımlandı.

uint8_t durum=0,Humidity=0,Temperature=0;
uint16_t tempVal=0,humVal=0;
uint8_t dhtVal[2];
uint8_t mData[40];
uint16_t mTime1 = 0, mTime2 = 0;
uint16_t mbit = 0;
uint8_t parityVal = 0, genParity = 0;
float deger;
uint16_t adcValue;
char message[100];
char ReceiveMessage[1];

uint32_t distance=0; //HC-SR04
char uzaklik[20]; //HC-SR04

uint16_t ad8232data=0; //AD8232

int ritim; //KY-39 NABIZ
int yeniritim; //KY-39 NABIZ
double alfa = 0.75; //KY-39 NABIZ
double yenileme = 0; //KY-39 NABIZ
int periyot = 20; //KY-39 NABIZ
static double eskideger=0; //KY-39 NABIZ
static double eskiyenileme=0; //KY-39 NABIZ
```

```

uint8_t DHT11_Read (void){ //sıcaklık sensörünü okumak için fonksiyon

for(int a=0;a<40;a++) mData[a]=0;
mTime1 = 0, mTime2 = 0, durum=0, tempVal=0, humVal=0, parityVal = 0, genParity = 0, mbit = 0;

Set_Pin_Output(DHT11_PORT,DHT11_PIN);
HAL_GPIO_WritePin(DHT11_PORT,DHT11_PIN,GPIO_PIN_RESET);
delay(18000);
Set_Pin_Input(DHT11_PORT,DHT11_PIN);

__HAL_TIM_SET_COUNTER(&htim6, 0); //set timer counter to zero
while(HAL_GPIO_ReadPin(DHT11_PORT, DHT11_PIN) == GPIO_PIN_SET) if((uint16_t)__HAL_TIM_GET_COUNTER(&htim6) > 500) return 0;
__HAL_TIM_SET_COUNTER(&htim6, 0);
while(HAL_GPIO_ReadPin(DHT11_PORT, DHT11_PIN) == GPIO_PIN_RESET) if((uint16_t)__HAL_TIM_GET_COUNTER(&htim6) > 500) return 0;
mTime1 = (uint16_t)__HAL_TIM_GET_COUNTER(&htim6);

__HAL_TIM_SET_COUNTER(&htim6, 0);
while(HAL_GPIO_ReadPin(DHT11_PORT, DHT11_PIN) == GPIO_PIN_SET) if((uint16_t)__HAL_TIM_GET_COUNTER(&htim6) > 500) return 0;
mTime2 = (uint16_t)__HAL_TIM_GET_COUNTER(&htim6);

if(mTime1 < 75 && mTime1 > 85 && mTime2 < 75 && mTime2 > 85)
{
return 0;
}

for(int j = 0; j < 40; j++)
{
__HAL_TIM_SET_COUNTER(&htim6, 0);
while(HAL_GPIO_ReadPin(DHT11_PORT, DHT11_PIN) == GPIO_PIN_RESET) if((uint16_t)__HAL_TIM_GET_COUNTER(&htim6) > 500) return 0;
__HAL_TIM_SET_COUNTER(&htim6, 0);
while(HAL_GPIO_ReadPin(DHT11_PORT, DHT11_PIN) == GPIO_PIN_SET) if((uint16_t)__HAL_TIM_GET_COUNTER(&htim6) > 500) return 0;
mTime1 = (uint16_t)__HAL_TIM_GET_COUNTER(&htim6);

//check pass time in high state
//if pass time 25uS set as LOW
if(mTime1 > 20 && mTime1 < 30)
{
mbit = 0;
}
else if(mTime1 > 60 && mTime1 < 80) //if pass time 70 uS set as HIGH
{
mbit = 1;
}

//set i th data in data buffer
mData[j] = mbit;
}

//get hum value from data buffer
for(int i = 0; i < 8; i++)
{
humVal += mData[i];
humVal = humVal << 1;
}

//get temp value from data buffer
for(int i = 16; i < 24; i++)
{
tempVal += mData[i];
tempVal = tempVal << 1;
}

//get parity value from data buffer
for(int i = 32; i < 40; i++)
{
parityVal += mData[i];
parityVal = parityVal << 1;
}
parityVal = parityVal >> 1;
humVal = humVal >> 1;
tempVal = tempVal >> 1;
genParity = humVal + tempVal;
dhtVal[0]= tempVal;
dhtVal[1] = humVal;
return 1;
}

```

```

void HAL_UART_RxCpltCallback(UART_HandleTypeDef *huart)//Arayüzde bobinleri kontrol etmek için interrupt fonksiyonu
{
    if(strcmp(ReceiveMessage, "1") == 0){//Arayüzden gelen veri 1 ise role1 aktif
        HAL_GPIO_WritePin(role1_GPIO_Port, role1_Pin, RESET);
    }
    if(strcmp(ReceiveMessage, "2") == 0){//Arayüzden gelen veri 2 ise role2 aktif
        HAL_GPIO_WritePin(role2_GPIO_Port, role2_Pin, RESET);
    }
    if(strcmp(ReceiveMessage, "3") == 0){//Arayüzden gelen veri 3 ise role3 aktif
        HAL_GPIO_WritePin(role3_GPIO_Port, role3_Pin, RESET);
    }
    if(strcmp(ReceiveMessage, "4") == 0){//Arayüzden gelen veri 4 ise role4 aktif
        HAL_GPIO_WritePin(role4_GPIO_Port, role4_Pin, RESET);
    }
    if(strcmp(ReceiveMessage, "5") == 0){//Arayüzden gelen veri 5 ise role5 aktif
        HAL_GPIO_WritePin(role5_GPIO_Port, role5_Pin, RESET);
    }
    if(strcmp(ReceiveMessage, "6") == 0){//Arayüzden gelen veri 6 ise role6 aktif
        HAL_GPIO_WritePin(role6_GPIO_Port, role6_Pin, RESET);
    }
    if(strcmp(ReceiveMessage, "7") == 0){//Arayüzden gelen veri 7 ise role7 aktif
        HAL_GPIO_WritePin(role7_GPIO_Port, role7_Pin, RESET);
    }
    if(strcmp(ReceiveMessage, "8") == 0){//Arayüzden gelen veri 8 ise role8 aktif
        HAL_GPIO_WritePin(role8_GPIO_Port, role8_Pin, RESET);
    }
    if(strcmp(ReceiveMessage, "0") == 0){//Arayüzden gelen veri 0 ise tüm röleler kapanır.
        HAL_GPIO_WritePin(role1_GPIO_Port, role1_Pin, SET);
        HAL_GPIO_WritePin(role2_GPIO_Port, role2_Pin, SET);
        HAL_GPIO_WritePin(role3_GPIO_Port, role3_Pin, SET);
        HAL_GPIO_WritePin(role4_GPIO_Port, role4_Pin, SET);
        HAL_GPIO_WritePin(role5_GPIO_Port, role5_Pin, SET);
        HAL_GPIO_WritePin(role6_GPIO_Port, role6_Pin, SET);
        HAL_GPIO_WritePin(role7_GPIO_Port, role7_Pin, SET);
        HAL_GPIO_WritePin(role8_GPIO_Port, role8_Pin, SET);
    }
    //Receive interrupt fonksiyonu receiveMessage değişkenine gelen veri yazdırılır
    HAL_UART_Receive_IT(&huart3, (uint8_t *)ReceiveMessage, sizeof(ReceiveMessage));
}

HAL_TIM_Base_Start(&htim6);//Timer aktive edildi.
HAL_UART_Receive_IT(&huart3, (uint8_t *)ReceiveMessage, sizeof(ReceiveMessage));//Uart aktive edildi.

while (1)
{
    /* USER CODE END WHILE */

    /* USER CODE BEGIN 3 */

    status = DHT11_Read();//dht11'den gelen veri durum değişkenine atanır.
    if(status ==1) {Temperature=tempVal; Humidity=humVal;}//durum değişkeni 1 ise değişkenler atanır.

    HAL_ADC_Start(&hadc1);//adc1 okuması başlar
    HAL_ADC_PollForConversion(&hadc1, HAL_MAX_DELAY);//sensörden gelen veriler çevrime başlar.
    adcValue=HAL_ADC_GetValue(&hadc1);//gelen veriler adcValue değişkenine atanır.
    deger = (float)adcValue/1000;//adcValue değikenini floata çevrilir ve deger değişkenine atanır.

    HAL_ADC_Start(&hadc2);//adc2 okuması başlar
    HAL_ADC_PollForConversion(&hadc2, HAL_MAX_DELAY);//sensörden gelen veriler çevrime başlar.
    ad8232data = HAL_ADC_GetValue(&hadc2);//gelen veriler ad8232data değişkenine atanır.

    HAL_ADC_Start(&hadc3);//adc3 okuması başlar
    HAL_ADC_PollForConversion(&hadc3, HAL_MAX_DELAY);//sensörden gelen veriler çevrime başlar.
    ritim = HAL_ADC_GetValue(&hadc3);//gelen veriler ritim değişkenine atanır.

    double deger = alfa*eskideger+(0-alfa)*ritim; //habiz sensörü için deger değışkenini atandı
    yenileme = deger-eskideger;
    yeniritim = ritim/10;
    eskideger=deger;
    eskiyenileme=yenileme;

    sprintf(message,"%d . %d . %d . %d . \r\n",adcValue,Temperature,ad8232data,yeniritim); //Message icine sensörler yazdırılır.
    //%d komutu ile 5 farklı sayısal veri gönderilir. Nokta(.) ile de verilerin ayrışması sağlanır.
    HAL_UART_Transmit(&huart3, (uint8_t *)message, strlen(message), 1000); //ici doldurulan message transmit edilir.
    HAL_Delay(600);
}

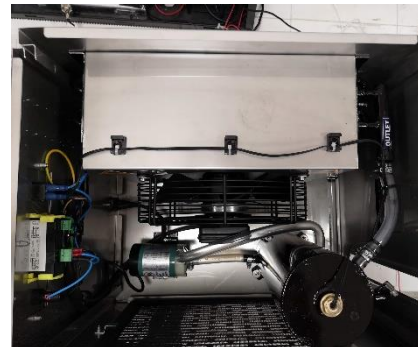
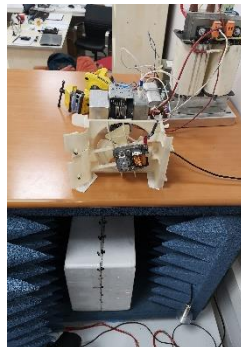
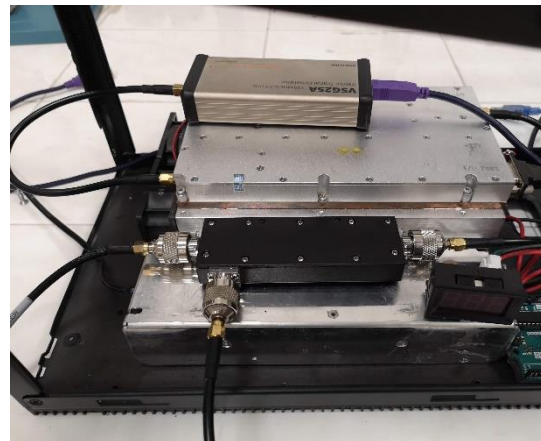
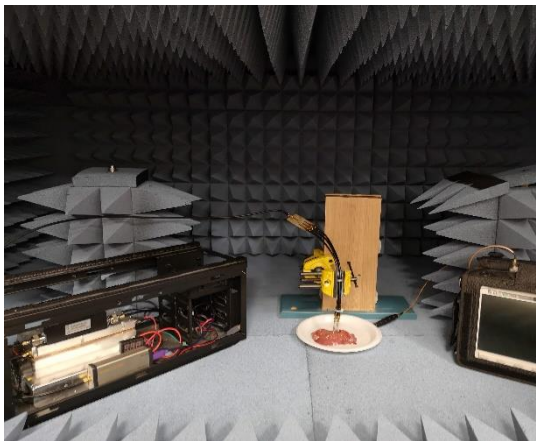
```


MWA System Pictures

1) Microwave Ablation Radiation and Thermal Measurement Setup



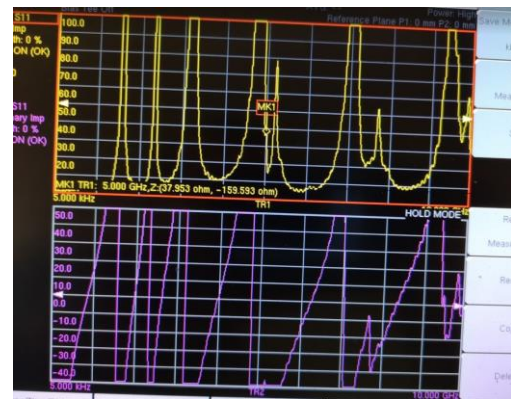
2) Microwave Ablation System with Solid State Power Amplifier Stage and Magnetron Tube



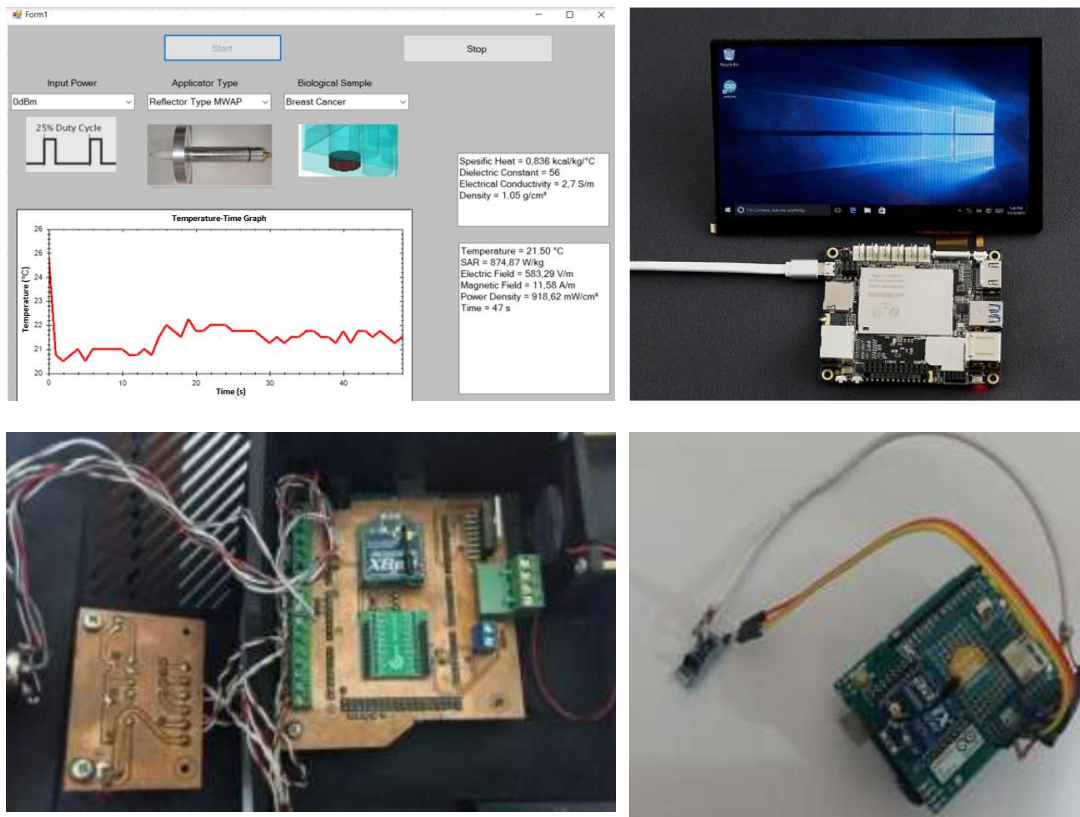
3) Fabrication Device of Micorwave Ablation Applicators



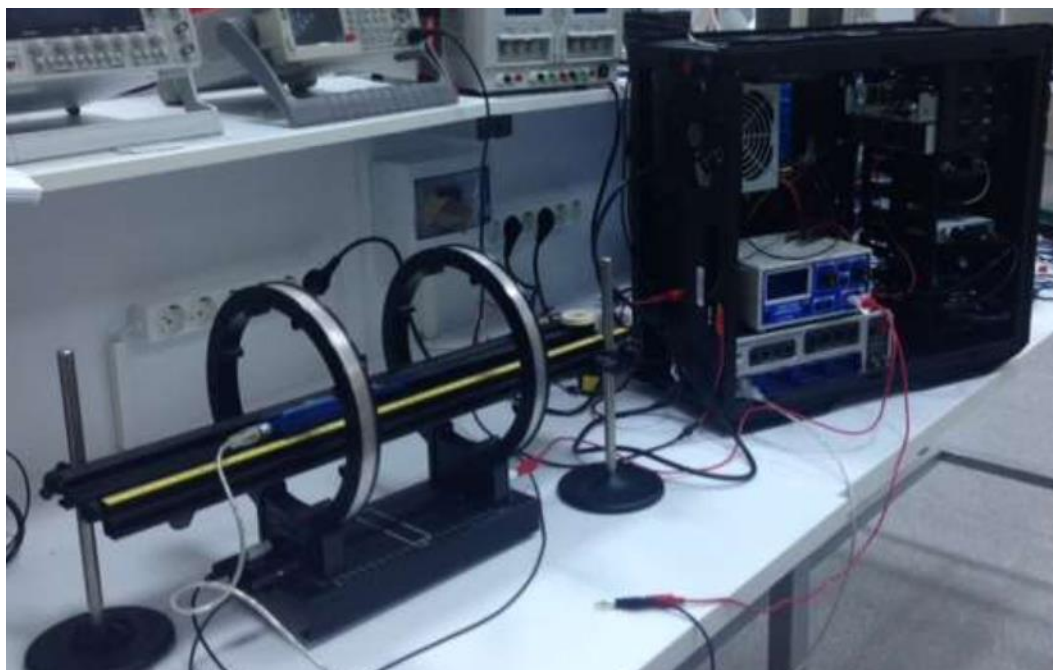
4) Microwave Ablation S Parameter and Input Impedance Measurement System




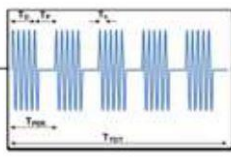


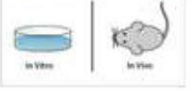
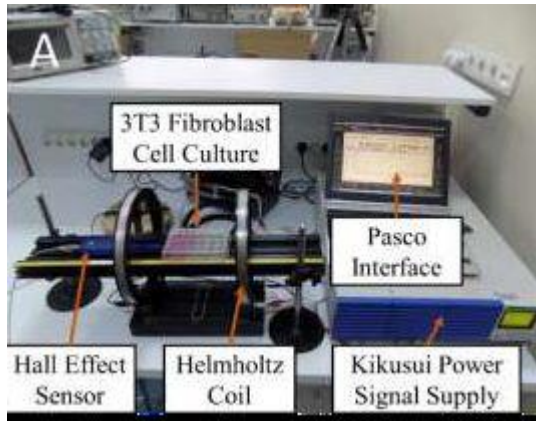
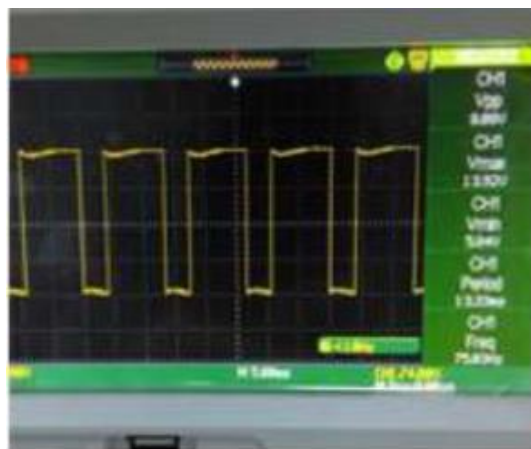
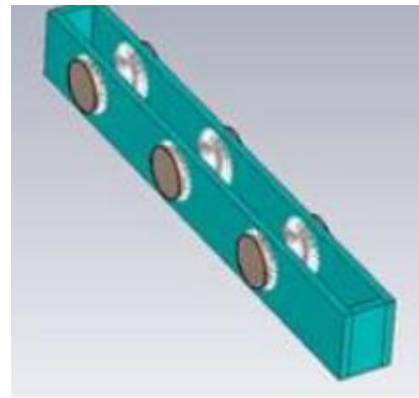
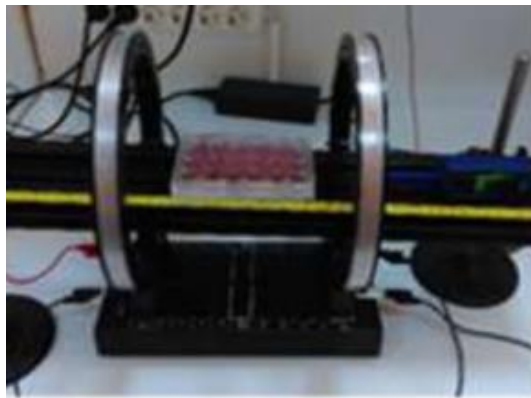
5) MWA and PEMF User Defined Computer Interface, Intel Atom Based Mini PC – Latte Panda, Master and Slave Device Used in Experimental Measurements



5) PEMF Magnetic Field Generation System and Measurement Setup [180]



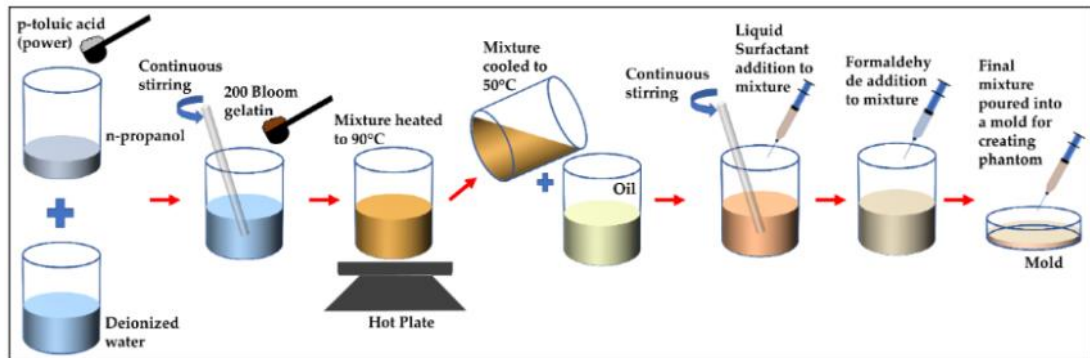
Cihaz Özellikler	
Frekans	PRF (27,12 MHz) ve PPMF (50 Hz)
Pik Güç Yoğunluğu	73 microwatt/cm ²
Pala Hızı	Saniyede 1500 pala
Pala Geni	100 mikro santimetre
Güç Kaynağı	AC
Aplikator Boyutu	12 cm veya 10 cm
Tedavi Alanı	Yaklaşık 100 mm ²
Aplikator Ağırlığı	20 gram

Tissue Electrical Equivalent Model

Recipe

1) Tissue phantom model production process



In this thesis, uncommon conditions such as liposarcoma and multiple basal cell carcinoma is simulated with oil-in-gelatin-based tissue-modeling materials that can precisely mimic the frequency-dependent dielectric properties of human tissues such as skin, fat, and tumor. Additionally, using these materials, we created heterogeneous configurations to construct realistic anatomical structures that can be characterized over a wide frequency range. To simulate the circumstance of liposarcoma, the phantoms were constructed in three phases. In the first phase, a fat layer was created by pouring fat-mimicking material into a cylindrical mold and leaving a coin-shaped (small, shallow cylinder) void at the top of the fat surface, which would later be filled with tumor-mimicking material. The fat was allowed to congeal for 24 hours before proceeding to the next phase. In the second phase, the void was filled with tumor-like material and allowed to congeal overnight. In the final phase, skin-like material was added to the top of the fat-layer-containing tumor. The thickness of the subcutaneous fat and skin layer varies depending on a number of factors, such as body location, age, and gender [29,30]. In this case, the thickness of the fat and skin was selected to be 7 mm and 1 mm, respectively, and the diameter was 38.5 mm, which is the diameter of the container mold. The two tumor sizes considered for comparison were 10 mm and 2 mm in diameter, each with a thickness of 2 mm [181].

2) 3D tissue electrical equivalent model recipe at 2.45 GHz

Tissue	Ingredients
Skin	5.1 % DGBE, 36.7% Triton X-100, 58.2 % Pure Water
Liver	60 % Distillate Water, 30 % Rotiphorese, 5 % PVA Mikroküre, 2.5 bovine haemoglobin, 0.03 % Magnevist, 0.03 % Lumirem, % 0.08 TEMED , 1.5 % APS, % 0.8 NaCl, 0.03 % NaN ₃
Muscle	49.75 % Distillate Water, 49.75 % Diacetin, 0.5 % Bakterisit
Breast Cancer	100 ml Distillate Water, 60 ml Etanol, 0.5 g NaCl, 1.5 g Agaroz

Each tissue's unique composition of ingredients serves specific purposes in research and modeling, reflecting the complexity and diversity of different biological tissues. These formulations enable scientists to create realistic tissue phantoms, aiding in various medical studies, diagnostic testing, and advancements in the field of healthcare.

3) Dielectric and thermal properties of complex kidney environment [180].

Frequency	2.45 GHz		5.8 GHz				
Parameter	ϵ_r	σ [S/m]	ϵ_r	σ [S/m]	c_d [J·kg ⁻¹ ·K ⁻¹]	k [W·m ⁻¹ ·K ⁻¹]	ρ [kg ⁻¹ ·m ⁻³]
Kortex	48.8	1.8	42.88	5.28	3513	0.44	1028
Medulla	54.7	1.9	48.96	5.78	3513	0.44	1028
Fat	10.8	0.27	9.86	0.83	2348	0.21	911
Muscle	52.7	1.74	48.50	4.96	3421	0.49	1090
Liver	43.0	1.69	38.10	4.64	3540	0.52	1079

4) Electrical properties of muscle, fat, and skin tissues at 27 MHz [180].

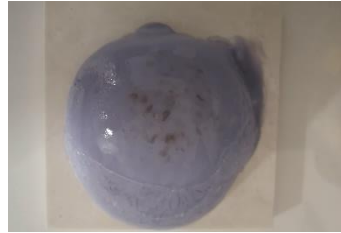
Tissue	Conductivity (S/m)	Dielectric Constant
Muscle	0.26671	9329000
Dry Skin	0.0002	1135.9
Moist Skin	0.00046112	45298
Fat	0.02081	457060

Pulsed shortwave heat therapy can be modulated to attain a targeted thermal reaction or to mitigate tissue heating. When administered at low frequencies, they are commonly denoted as PEMF. Whereas heat therapy necessitates the application of heat, PEMF provides a therapeutic intervention devoid of thermal influence.

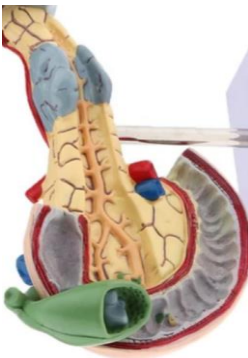
4) Tissue phantom models



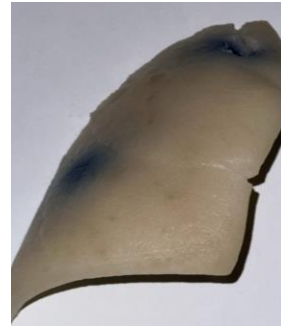
Ibia_Kid_001



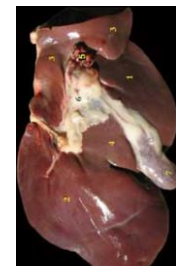
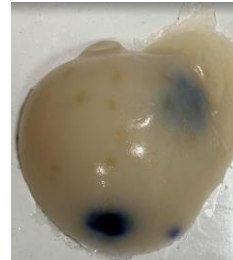
Ibia_Bra_002



Ibia_Panc_003



Ibia_Lung_004



Ibia_Liv_005

Appendix B

Publications from the Thesis

Conference Papers

1. Murat C., Kaya D., Kaya A., “Üç Boyutlu Elektriksel Eşdeğer Organ Modelinin Mikrodalga Ablasyon Sistem Performansının İncelenmesi”, Çevre ve Halk Sağlığı için Elektromanyetik Alanlar Etkileri Günleri, 11 -12 November 2021, pp. 31-33

Journal Articles

1. Palandoken M., Murat C., Kaya A., Zhang B. “A Novel 3-D Printed Microwave Probe for ISM Band Ablation Systems of Breast Cancer Treatment Applications”, IEEE Transactions on Microwave Theory and Techniques, vol. 70, no.3, pp.1943-1953, 2022

2. Murat C., Palandoken M., Kaya I., Kaya A. “A novel ISM band reflector type applicator design for microwave ablation systems”, Electromagnetic Biology and Medicine, vol. 40, pp. 286-300, 2021

Projects

1. Scientific and Technological Research Council of Turkey, 117E811.

2. Izmir Katip Celebi Uni., Scientific Research Projects, 2021-TDR-FEBE-0013

Curriculum Vitae

Name Surname : Caner Murat

Education:

- 2012–2017 İzmir Kâtip Çelebi U., Dept. of Electrical & Electronics Eng. (BS)
2017–2029 İzmir Kâtip Çelebi U., Dept. of Electrical & Electronics Eng. (MSc)
2019–2023 İzmir Kâtip Çelebi U., Dept. of Electrical & Electronics Eng. (PhD)

Publications (if any):

1. Palandoken M., **Murat C.**, Kaya A., Zhang B. “A Novel 3-D Printed Microwave Probe for ISM Band Ablation Systems of Breast Cancer Treatment Applications”, IEEE Transactions on Microwave Theory and Techniques, vol. 70, no.3, pp.1943-1953, 2022 (**SCI**)
2. **Murat C.**, Palandoken M., Kaya I., KayaA. “A novel ISM band reflector type applicator design for microwave ablation systems”, Electromagnetic Biology and Medicine, vol. 40, pp. 286-300, 2021 (**SCI Expanded**)
3. **Murat C.**, Kaya A., Keselik E., Kuruş M., Demirci U. S., and et. al. “Investigation of Electrical Properties of Iron Oxide Nanoparticles Bonded with Ionic Solutions for Microwave Ablation Systems”, International Journal of Emerging Multidisciplinaries: Engineering, vol. 1, 2023 (**Peer-Reviewed Journal**)
4. Kaya D., **Murat C.** “Mikrodalga Tümör Ablasyonu: Kanser Aksiyon Mekanizması ve MCF-7 In Vitro Sonuçlar”, Çevre ve Halk Sağlığı için Elektromanyetik Alanlar Etkileri Günleri, 11 -12 November 2021, pp. 35-37 (**National Conference Paper**)
5. **Murat C.**, Kaya D., Kaya A., “Üç Boyutlu Elektriksel Eşdeğer Organ Modelinin Mikrodalga Ablasyon Sistem Performansının İncelenmesi”, Çevre ve Halk Sağlığı için Elektromanyetik Alanlar Etkileri Günleri, 11 -12 November 2021, pp. 31-33 (**National Conference Paper**)
6. Gürkan Ç., **Murat C.**, Kaya A. “Flexible Antenna Applicator Design for Medical Applications and Low Energy Pulsed Radio Frequency Energy Applications”, 2nd

International Congress on Engineering and Life Science, Kastamonu, Turkey, 11-14 April 2019, pp. 410-417 (**International Conference Paper**)

7. Aydın Ö., **Murat C.**, Kaya A. “Pulsed Electromagnetic Field Application with High-Resolution Wireless Sensor Network”, 2nd International Congress on Engineering and Life Science, Kastamonu, Turkey, 11-14 April 2019 (**International Conference Paper**)

8. **Murat C.**, Palandöken M., Kaya A., Kaya İ. “A Helicaly Shaped with Open Ended Reflector Probe Design for ISM Band Microwave Ablation System”, The 7th Advanced Electromagnetics Symposium, Lizbon, Portugal, 24 -26 July 2019 (**International Conference Paper**)

9. **Murat C.**, Kaya A., Kaya İ., Palandöken M. “Microwave Probe Design for ISM Band Microwave Ablation Systems”, 2018 Medical Technologies National Congress (TIPTEKNO), Gazimagusa, Cyprus (KKTC), 8-10 November 2018 (**National Conference Paper**)

10. Kaya A., Palandöken M., **Murat C.** “Pulsed Electromagnetic Field Therapy Device Prototype Design”, 2nd International Conference on Advanced Engineering Technologies, Bayburt, Turkey, 19 -21 September 2017, pp. 998-1003 (**International Conference Paper**)

11. Palandöken M., **Murat C.**, Kaya A. “Numerical and Analytical Investigation of Coil Array Based PEMF Applicator for Magnetic Field Homogenization”, 2nd International Conference on Advanced Engineering Technologies, Bayburt, Turkey, 19 -21 September 2017, vol. 993 (**International Conference Paper**)